

# Modeling the (proto)neutron star crust : toward a controlled estimation of uncertainties

Thomas Carreau

▶ **To cite this version:**

Thomas Carreau. Modeling the (proto)neutron star crust : toward a controlled estimation of uncertainties. Physics [physics]. Normandie Université, 2020. English. NNT : 2020NORMC206 . tel-03019954

**HAL Id: tel-03019954**
**https://theses.hal.science/tel-03019954**

Submitted on 23 Nov 2020

**HAL** is a multi-disciplinary open access archive for the deposit and dissemination of scientific research documents, whether they are published or not. The documents may come from teaching and research institutions in France or abroad, or from public or private research centers.

L'archive ouverte pluridisciplinaire **HAL**, est destinée au dépôt et à la diffusion de documents scientifiques de niveau recherche, publiés ou non, émanant des établissements d'enseignement et de recherche français ou étrangers, des laboratoires publics ou privés.

Normandie Université

# THÈSE

## Pour obtenir le diplôme de doctorat

**Spécialité PHYSIQUE**

**Préparée au sein de l'Université de Caen Normandie**

# Modeling the (proto)neutron star crust: toward a controlled estimation of uncertainties

## Présentée et soutenue par
## Thomas CARREAU

| Thèse soutenue publiquement le 25/09/2020 devant le jury composé de | | |
|---|---|---|
| Mme MICAELA OERTEL | Directeur de recherche au CNRS, LUTH, CNRS/Observatoire de Paris | Rapporteur du jury |
| Mme CONSTANCA PROVIDENCIA | Professeur, Université de Coïmbra | Rapporteur du jury |
| M. NICOLAS CHAMEL | Maître de recherches, Fonds de la Recherche Scientifique | Membre du jury |
| Mme ANTHEA FANTINA | Chargé de recherche au CNRS, 14 GANIL de CAEN | Membre du jury |
| M. JEROME MARGUERON | Directeur de recherche au CNRS, Institut de Physique des 2 Infinis | Président du jury |
| Mme FRANCESCA GULMINELLI | Professeur des universités, Université Caen Normandie | Directeur de thèse |

**Thèse dirigée par FRANCESCA GULMINELLI, Laboratoire de physique corpusculaire (Caen)**

UNIVERSITÉ CAEN NORMANDIE

ED 591 PSIME

lpc caen
Laboratoire de physique corpusculaire

# Remerciements/Acknowledgements

Je souhaite tout d'abord remercier le directeur du LPC Caen, Gilles Ban, de m'avoir accueilli au sein du laboratoire.

I would like to thank the jury members Nicolas Chamel, Anthea F. Fantina, Jérôme Margueron, Micaela Oertel, and Constança Providência who carefully read this manuscript. I have appreciated the referees Micaela Oertel and Constança Providência having shown interest in my work during the defense. I thank them and Nicolas Chamel for their useful comments and corrections.

Je tiens à exprimer tout mon estime à Francesca par qui j'ai eu la chance d'être encadré pendant trois ans et demi, en tenant compte du stage de deuxième année de master. J'ai énormément appris de nos nombreux échanges. Francesca a toujours pris le temps de répondre à mes questions et m'a accordé une grande liberté concernant l'encadrement de stages, l'enseignement, la participation aux conférences ou encore la médiation scientifique. Pour toutes ces raisons, je la remercie sincèrement.

Je remercie vivement Anthea pour les discussions intéressantes que nous avons pu avoir et d'avoir été ma guide à Bruxelles lors de nos visites rendues à Nicolas. Je remercie par ailleurs Nicolas pour son accueil chaleureux à l'ULB et ses conseils. J'ai grandement apprécié travailler avec Anthea et Nicolas.

Je remercie également Jérôme avec qui j'ai eu la chance de collaborer. J'ai apprécié nos échanges lors de nos rencontres en conférence ou à l'IP2I.

Je souhaite remercier l'ensemble des membres du LPC de contribuer à l'ambiance conviviale qui reigne au sein du laboratoire. Y Préparer ma thèse pendant ces trois ans fut un grand plaisir.

Un grand merci aux thésards (et ex-thésards !) ainsi qu'aux postdocs du laboratoire pour tous les très bons moments passés ensemble au labo et lors des soirées. Merci à Daniel d'avoir fait le déplacement depuis Cherbourg pour venir assister à ma soutenance. Joël, j'espère que je ne te manquerai pas trop lors des trajets quotidiens*. Bon courage à notre rugbyman Edgar pour la dernière ligne droite ! Je souhaite également bon courage à Cyril et Joël ainsi qu'à la jeune génération Alexandre, Chloé, Savitri et William pour la suite jusqu'à la soutenance. Yoann, j'ai adoré être ton collègue de bureau†. Merci d'avoir contrôlé la caméra le jour de la soutenance.

*J'espère que tu sauras faire la différence entre un panneau stop et un feu rouge à l'avenir !

†à mi-temps !

Valérian, on a fait toutes nos années d'études ensemble et on va maintenant être séparés par plus que quelques mètres pendant les années à venir. Nos discussions et après-midi musique vont me manquer[‡]. Bonne chance à Marie et toi en Allemagne, on passera vous voir !

Merci à mon ami d'enfance Alexis qui m'a suivi tout le long de ce parcours (depuis la maternelle !).

Enfin, je remercie naturellement mon petit frère Alexis et mes parents de m'avoir toujours soutenu dans mes choix. Pour la même raison, je tiens également à remercier Catherine.

Ces derniers mots sont destinés à Manon qui m'accompagne depuis le début. Merci pour ton soutien et tes encouragements sans failles, particulièrement durant ces derniers mois où nous étions confinés tous les deux et que je rédigeais. Tu es merveilleuse et je suis heureux de partager cette réussite avec toi.

[‡]Heureusement, on pourra toujours s'envoyer des WAV !

# Contents

**List of Figures** **ix**

**List of Tables** **xi**

**General introduction** **1**

**1 Structure and equation of state of cold nonaccreting neutron stars 9**
1.1 Ground state of the outer crust . . . . . 11
1.1.1 Wigner-Seitz cell energetics . . . . . 11
1.1.1.1 Nuclear mass tables . . . . . 12
1.1.1.2 Relativistic electron gas . . . . . 12
1.1.2 The BPS model . . . . . 13
1.1.3 Equilibrium composition and equation of state . . . . . 15
1.2 Ground state of the inner crust . . . . . 19
1.2.1 Modeling the nuclear energy . . . . . 20
1.2.1.1 Metamodeling of homogeneous nuclear matter . . . . . 22
1.2.1.2 From homogeneous nuclear matter to finite nuclei in the CLD approximation . . . . . 27
1.2.2 Variational formalism . . . . . 31
1.2.3 Results . . . . . 35
1.2.3.1 Numerical code . . . . . 35
1.2.3.2 Equilibrium composition . . . . . 36
1.2.3.3 Equation of state . . . . . 38
1.2.4 Strutinsky shell corrections to the CLD energy . . . . . 39
1.2.5 Nonspherical pasta phases . . . . . 42
1.2.6 Crust-core transition from the crust side . . . . . 45
1.3 Matter of the core . . . . . 47
1.3.1 Outer core: homogeneous $npe\mu$ matter . . . . . 48
1.3.1.1 Variational equations . . . . . 49
1.3.1.2 Equilibrium composition and equation of state . . . . . 50
1.3.2 Inner core . . . . . 51
1.4 Unified metamodeling of the equation of state . . . . . 52
1.5 Conclusions . . . . . 54

**2 Bayesian inference of neutron star observables 57**
2.1 From the equation of state to neutron star observables . . . . . 59
2.1.1 Masses and radii . . . . . 59
2.1.1.1 Mass-radius relation . . . . . 59
2.1.1.2 Crust thickness and mass . . . . . 62
2.1.2 Moment of inertia within the slow rotation approximation . . . 63
2.1.2.1 Total moment of inertia and fraction contained in the crust . . . . . 64
2.1.2.2 Connection to pulsar glitches . . . . . 66
2.1.3 Tidal deformability . . . . . 68
2.2 Bayesian determination of the equation of state parameters . . . . . 70
2.2.1 Principle of Bayesian inference . . . . . 70
2.2.2 Prior distribution of equation of state parameters . . . . . 72
2.2.2.1 Flat prior compatible with empirical constraints . . . . 72
2.2.2.2 Sensitivity analysis of the crust-core transition point . 73
2.2.3 Determination of the likelihood function . . . . . 76
2.2.3.1 Constraints on nuclear physics observables . . . . . 76
2.2.3.2 Physical requirements and constraints on neutron star observables . . . . . 78
2.2.4 Posterior distribution of equation of state parameters . . . . . 78
2.2.4.1 Marginalized one-parameter posterior distributions of empirical parameters . . . . . 79
2.2.4.2 Correlations among empirical parameters . . . . . 82
2.3 General predictions for neutron star observables . . . . . 84
2.3.1 Global properties: confrontation with popular models and the GW170817 event . . . . . 84
2.3.1.1 Equation of state . . . . . 85
2.3.1.2 Masses and radii . . . . . 86
2.3.1.3 Tidal deformability . . . . . 88
2.3.2 Bayesian analysis of the crust-core transition . . . . . 91
2.3.3 Pulsar glitches: answering the question "*Is the crust enough?*" . 96
2.4 Conclusions . . . . . 102

**3 Crystallization of the crust of protoneutron stars 105**
3.1 Model of the crust at finite temperature . . . . . 107
3.1.1 One-component Coulomb plasma approximation . . . . . 107
3.1.1.1 OCP in a liquid phase . . . . . 108
3.1.1.2 OCP in a solid phase . . . . . 109
3.1.1.3 Crystallization of a OCP . . . . . 110
3.1.2 Multicomponent Coulomb plasma in a liquid phase . . . . . 112
3.1.2.1 Nuclear statistical equilibrium . . . . . 112
3.1.2.2 Evaluation of the chemical potentials . . . . . 114
3.1.2.3 Evaluation of the rearrangement term . . . . . 115
3.1.3 Nuclear free energy functional in the free neutron regime . . . . 116
3.1.3.1 Thermodynamics of nuclear matter . . . . . 117

3.1.3.2 Energetics of clusters at finite temperature in the CLD approximation . . . 120
3.2 Study of the outer crust at crystallization . . . 120
3.2.1 Crystallization temperature . . . 122
3.2.2 Equilibrium composition . . . 122
3.2.3 Impurity parameter . . . 126
3.2.4 Abundancies of odd nuclei . . . 126
3.3 Study of the inner crust at crystallization . . . 129
3.3.1 Influence of shell effects in the OCP approximation . . . 130
3.3.1.1 Temperature dependence of shell corrections . . . 130
3.3.1.2 Equilibrium composition of the OCP at crystallization for modern BSk functionals . . . 133
3.3.2 MCP results . . . 136
3.3.2.1 Equilibrium composition of the MCP . . . 137
3.3.2.2 Impurity parameter . . . 139
3.4 Conclusions . . . 140

**General conclusions and outlooks** **143**

**A Energy density of a relativistic electron gas** **147**

**B Neutron and proton chemical potentials in the metamodel** **149**

**C Partie en français** **151**
C.1 Introduction générale . . . 151
C.2 Structure et équation d'état des étoiles à neutrons froides non accrétantes 157
C.3 Inférence bayésienne des observables des étoiles à neutrons . . . 158
C.4 Cristallisation de la croûte des protoétoiles à neutrons . . . 160
C.5 Conclusions générales et perspectives . . . 162

**Bibliography** **167**

# List of Figures


1 Schematic representation of the inside of a neutron star . . . . . 2
2 Masses measured from pulsar timing . . . . . 4

1.1 Ground-state composition versus baryon density in the outer crust . . . 18
1.2 Pressure versus baryon density in the outer crust . . . . . 19
1.3 r-cluster and e-cluster representations . . . . . 20
1.4 Accuracy of the metamodeling technique for SLy4 . . . . . 26
1.5 Fit of surface and curvature parameters . . . . . 29
1.6 Surface plus curvature energy per surface nucleon versus asymmetry . . 30
1.7 Ground-state composition versus baryon density in the inner crust . . . 36
1.8 Energy per nucleon and pressure versus baryon density in the inner crust, and symmetry energy at subsaturation densities . . . . . 38
1.9 Perturbative implementation of proton shell corrections for BSk24 . . . 40
1.10 Equilibrium value of $Z$ versus baryon density in the inner crust with Strutinsky shell corrections . . . . . 41
1.11 Pasta phases in the inner crust . . . . . 44
1.12 Crust-core transition density versus surface parameter $p$ for SLy4 . . . 46
1.13 Crust-core transition density and pressure for several interactions . . . 48
1.14 Equilibrium composition, pressure, and symmetry energy versus baryon density in the outer core . . . . . 50
1.15 Unified metamodeling of the equation of state . . . . . 53

2.1 Mass-radius relation for several popular equations of state . . . . . 61
2.2 Crust thickness and mass versus neutron star mass for several popular equations of state . . . . . 63
2.3 Moment of inertia and fraction of crust moment of inertia versus neutron star mass for several popular equations of state . . . . . 65
2.4 Tidal Love number and dimensionless tidal deformability versus neutron star mass for several popular equations of state . . . . . 69
2.5 Sensitivity analysis of the crust-core transition point for BSk24 and BSk22 75
2.6 Energy per nucleon and pressure of nuclear matter versus density from chiral effective field theory caclulations . . . . . 77
2.7 Marginalized posteriors for isoscalar empirical parameters assuming different filters . . . . . 80
2.8 Marginalized posteriors for isovector empirical parameters assuming different filters . . . . . 81

2.9 Correlations among empirical parameters for the sets passing through the low-density filter . . . 82
2.10 Correlations among empirical parameters for the sets passing through both low-density and high-density filters . . . 83
2.11 Posterior equation of state confronted with popular models and the GW170817 event . . . 85
2.12 Posterior mass-radius relation confronted with popular models and the GW170817 event . . . 87
2.13 Posterior $\Lambda_1 - \Lambda_2$ relation confronted with popular models and the GW170817 event . . . 89
2.14 Marginalized posterior probability distribution for the dimensionless tidal deformability of a $1.4M_\odot$ neutron star . . . 90
2.15 Prior and posterior distribution for the surface plus curvature energy per surface nucleon versus isospin asymmetry . . . 91
2.16 Correlation of the crust-core transition density and pressure with the equation of state parameters for different filters . . . 93
2.17 Marginalized probability distributions for the crust-core transition density and pressure for different filters . . . 95
2.18 Correlation of the crust thickness and fractional crust moment of inertia of a $1.4M_\odot$ neutron star with the equation of state parameters for different filters . . . 97
2.19 Marginalized probabilities for the crust thickness and fraction of crust moment of inertia of a $1.4M_\odot$ neutron star . . . 99
2.20 Marginalized posterior for the neutron star mass and radius of Vela . . 100
2.21 Marginalized posterior for the fraction of crust moment of inertia as a function of the neutron star mass . . . 101

3.1 Free energy density difference between liquid and solid phases versus temperature . . . 111
3.2 Crystallization temperature versus pressure for the one-component plasma in the outer crust . . . 121
3.3 Equilibrium OCP composition versus baryon density in the outer crust at finite temperature . . . 123
3.4 Normalized probability distribution of the atomic number $Z$ in the outer-crust regime . . . 124
3.5 Equilibrium composition of the multicomponent plasma versus pressure in the outer-crust regime . . . 125
3.6 Impurity parameter versus pressure in the outer-crust regime . . . 127
3.7 Fraction of odd-$A$ and odd-$Z$ nuclei versus pressure in the outer crust regime . . . 128
3.8 Equilbrium value of proton number versus baryon density in the inner crust for BSk14 at finite temperature . . . 131
3.9 Free energy density versus proton number $Z$ for different thermodynamic conditions in the free neutron regime . . . 132
3.10 Crystallization temperature and equilibrium value of $Z$ of the one-component plasma versus baryon density in the inner crust . . . 134

3.11 Crystallization temperature and equilibrium value of $Z$ of the one-component plasma versus baryon density in the inner crust . . . . . 135
3.12 Equilibrium proton fraction of the one-component plasma versus temperature in the inner-crust regime . . . . . 136
3.13 Equilibrium composition of the multicomponent plasma versus baryon density in the inner-crust regime . . . . . 137
3.14 Normalized probability distribution of the atomic number $Z$ in the inner-crust regime . . . . . 138
3.15 Impurity parameter versus baryon density in the inner-crust regime . . 139

# List of Tables


1.1 Ground state of the outer crust . . . . . 16
1.2 Ground state of matter at the neutron-drip point . . . . . 19
1.3 Empirical parameters for SLy4, BSk24, BSk22, and DD-ME$\delta$, and extracted from nuclear experiments . . . . . 23

2.1 Empirical parameters for BSk14, PKDD, and TM1 . . . . . 60
2.2 Minimum value and maximum value of each of the empirical parameters for the prior distribution . . . . . 73
2.3 68% confidence intervals for the crust-core transition density and pressure for different filters . . . . . 94
2.4 68% confidence intervals for the crust thickness and fractional crust moment of inertia of $1.4M_\odot$ neutron star for different filters . . . . . 98

3.1 Value of the fraction and baryon mass fraction of odd nuclei in the outer crust for three selected temperatures . . . . . 129

# General introduction

## Astrophysical context

The existence of dense stars was hypothesized as early as 1931 by Landau [Lan32], a year before the discovery of neutrons by Chadwick [Cha32]. Landau anticipated that the stellar matter density may become "so great that atomic nuclei come in close contact, forming one gigantic nucleus". In 1934, Baade and Zwicky introduced the term *supernova* (SN) to designate a "remarkable type of giant novae", a rare and very energetic phenomenon, characterized by a sudden and ephemeral burst in luminosity followed by a slow decay, and they predicted that "supernovae represent the transitions from ordinary stars to *neutron stars*" [BZ34]. The presence of neutron stars (NS) in the Universe remained purely theoretical until 1968, when a rapidly pulsating source, a *pulsar*, was observed for the first time by Jocelyn Bell, a graduate student supervised by Antony Hewish [Hew+68]. Several weeks after this observation, and motivated by the discovery of the Crab pulsar in 1968 which could not be identified as a white dwarf on account of a very short pulsation period [Com+69], pulsars were identified as "rotating neutron stars" by Gold [Gol68], paving the way for important theoretical development and observations in the following decades.

### Formation and structure of neutron stars

During their life, stars of mass greater than $\sim 10 M_\odot$ ($M_\odot$ being the mass of the Sun), can ignite their core elements up to silicon burning into iron, then the fusion of elements is no longer possible since iron is the most stable nuclide in nature. The chain of reactions in their core ends, and in their final stage the stars exhibit an onion-like structure, their core being composed of iron and neutron-rich iron-group nuclei [Bet+79], surrounded by shells of lower and lower burning elements up to possible inert hydrogen, at progressively lower temperatures and densities [WHW02]. At this point, the stratified core is essentially sustained by the electron degeneracy pressure, and its mass keeps increasing through accretion as silicon shells are consumed, until it overtakes the Chandrashekar mass limit, $M_{Ch} \sim 1.44 M_\odot$, when the gravitational force overcomes the electron degeneracy pressure [Cha31], which has the effect of triggering a core-collapse supernova (CCSN) explosion [Jan+07]. In the aftermath of a CCSN, a warm protoneutron star (PNS) is left behind, with temperatures exceeding $10^{10}$ K, and two outcomes are possible: either the PNS will end up as a cold NS, or into a black hole if its mass is larger than the NS maximum mass, which is uncertain up to the present. Few minutes after the formation of the hot PNS, it transforms into an ordinary NS

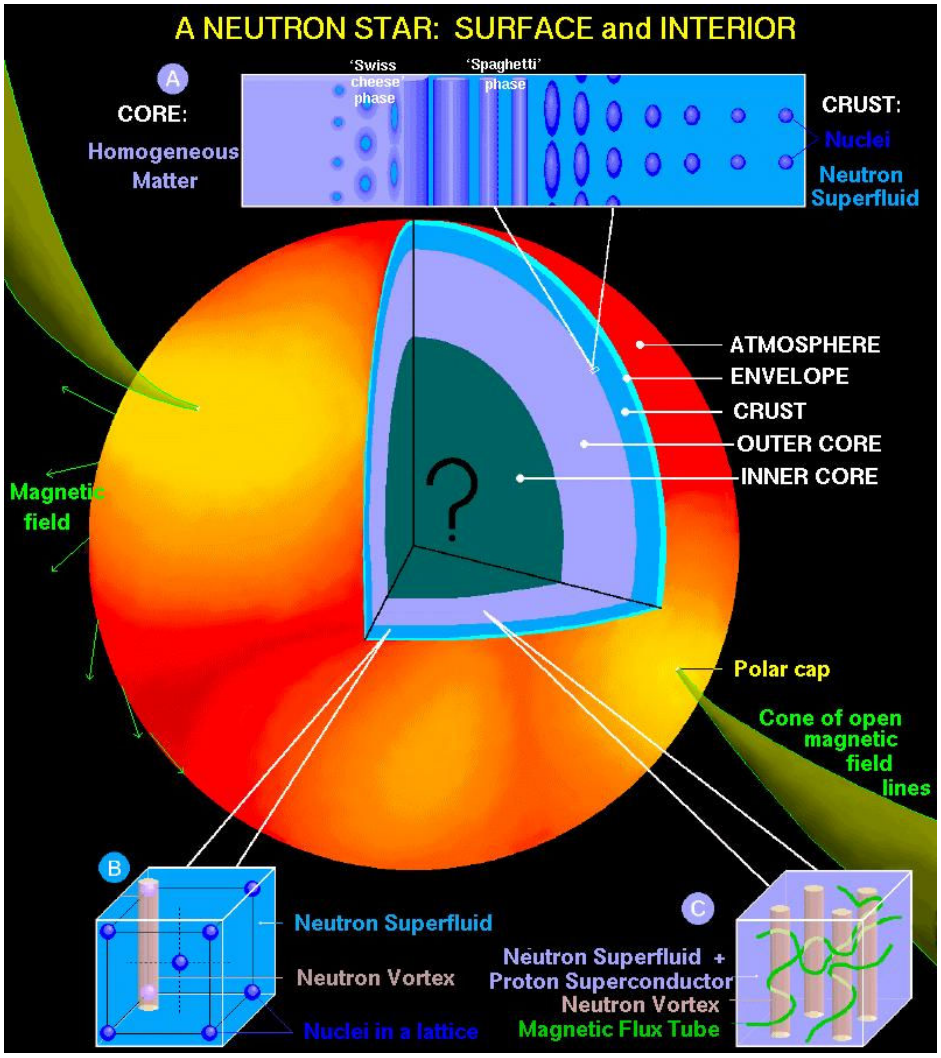



**Figure 1:** *Schematic representation of the inside of an NS. Figure taken from [PR06].*

which is transparent for neutrinos.

The star cools down by emitting neutrinos and photons, and at approximately $10^8$ K matter is catalyzed, that is in its ground state. A schematic representation of the internal structure of a cold NS is given in Fig. 1. The outermost surface of an NS consists of a very thin atmosphere of only a few centimeters and an envelope of few meters, where the spectrum of thermal electromagnetic radiation is formed. The analysis of the thermal emission from the surface layers of isolated NS can provide useful information on the surface temperatures, and the detection of gravitationally redshifted spectral lines can yield the NS mass-to-radius ratios. Unfortunately, the nonthermal component dominates in the majority of very young pulsars, and for NS older than $\tau \sim 1$ Myr the surface temperature is generally too low to detect the thermal radiation. The thermal radiation from the entire NS surface can dominate at soft x-ray energies for middle-aged pulsars, $\tau \sim 10 - 100$ kyr [HPY07]. The inhomogeneous crust is situated just below the outermost surface and is about 1 km thick. The

crust is generally subdivided into two regions: the outer crust and the inner crust, and the border between them is situated at the neutron drip surface, a few hundred meters from the atmosphere bottom. Inside the crust, atoms are fully ionized and form a lattice immersed in a relativistic electron gas, and if the neutron chemical potential is larger than the neutron rest mass, additionally in a neutron gas. Due to electron capture, matter is more neutron-rich with increasing density, further toward the interior of the star. In the bottom layers of the inner crust, nuclei are expected to exhibit nonspherical shapes. As the temperature of the inner crust falls below the critical temperature $T_c \sim 10^{10}$ K, free neutrons with anti-aligned spins and zero orbital angular momentum form Cooper pairs and behave in a superfluid state, characterized by the absence of viscosity. At about half the saturation density $n_{sat}$, corresponding to the equilibrium density of symmetric homogeneous nuclear matter, the crust-core interface is reached and nuclei disappear. Once again, we can distinguish the outer core, corresponding to the density range $0.5n_{sat} \lesssim n_B \lesssim 2n_{sat}$, and the inner core, where $n_B \gtrsim 2n_{sat}$ ($n_B$ being the baryon density). In the outer core, matter consists of a mixture of neutrons, protons, electrons, and possibly muons. The composition of the inner core is however uncertain, and several hypotheses have been put forward, such as the appearance of hyperons, boson condensates, and/or a phase transition to quark matter.

## Observables of (proto)neutron stars

Pulsars were identified to rotating NS which produce pulsed emission, soon after their chance discovery in 1967 by Jocelyn Bell [Hew+68]. Five decades later, we have now observed about 3000 of them, and numerous techniques have been developed to measure their characteristic observables.

### Global properties

It is easier for astronomers to measure the mass of an NS belonging to a binary system. There are several types of binaries: x-ray binaries, double NS binaries, radio pulsar–white dwarf binaries, and pulsars in binaries with nondegenerate stars (main-sequence stars). Depending on the type of binary, different techniques are used to infer the NS mass [HPY07]. For example, in double NS binaries the relativistic Shapiro delay [Sha64] can be exploited to infer the mass via pulsar timing, which consists in the regular monitoring of the rotation of a pulsar over long time periods. The relativistic Shapiro delay is a phenomenon from which precise masses for both a millisecond pulsar and its companion can be inferred [Dem+10; Cro+20]. Let us notice however that it is only observed in a small subset of high-precision, highly inclined binary pulsar systems. Measured NS masses via pulsar timing are displayed in Fig. 2.

Measuring NS radii with high precision is a more challenging task. The basic principle of the radius extraction relies in the measurement of the the x-ray spectrum (flux and frequency), from which both the surface temperature and the star radius can be extracted using the equation of black-body emission. In particular, accurate estimations of the star radius are believed to be provided by spectral fits in low-mass x-ray binaries

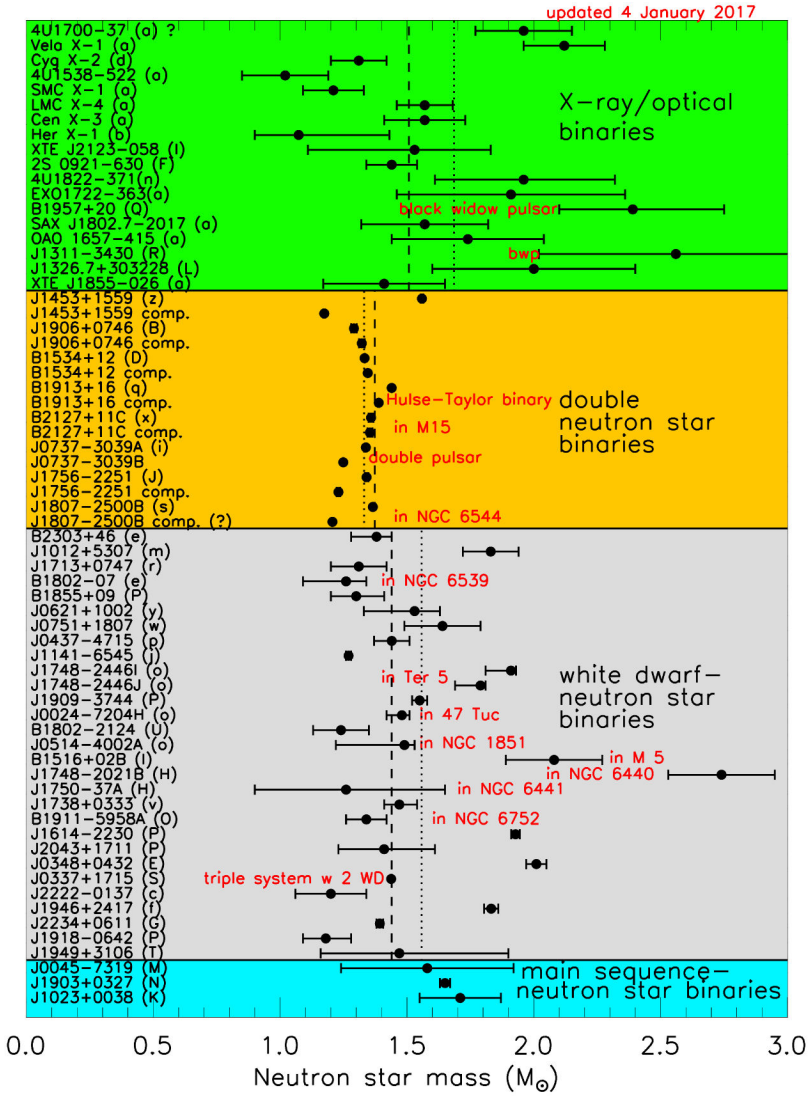



**Figure 2:** *Masses measured from pulsar timing. Vertical dashed (dotted) lines indicate category error-weighted (unweighted) averages. Figure taken from [Lat19].*

(LMXBs) during periods of little to no accretion, called quiescence [BBR98]. A number of quiescent LMXBs have been studied with the Chandra and/or XMM–Newton observatories [Hei+14; Ser+12; GR14; Gui+13]. However, the results strongly depend on the assumptions made on the composition of the neutron star atmosphere which is poorly known [Ste+18]. An important improvement is expected from the analysis of the recent NICER mission, whose first results start to be available [Bog+19a; Bog+19b; Mil+19; Raa+19; Ril+19], even if complications in the interpretation of the data arise due to the nonuniformity of the temperature over the surface (hot spots) [Bog+19a; Bog+19b; Mil+19; Raa+19; Ril+19]. Typical values for the NS masses and radii are $M = 1.4 M_\odot$ and $R = 10 - 14$ km, respectively.

Very recently, the first detection of gravitational waves (GW) from the coalescence of two NS, the GW170817 event, has yielded important constraints for the tidal de-

formability of NS [Abb+18]. The tidal deformability describes how much a body is deformed by tidal forces, which arise when two massive bodies are in orbit around each other. The simplest and best known example corresponds to the Moon causing the tides observed in Earth's oceans. The detection of gravitational radiation emitted by inspiraling binary NS is possible using ground-based GW detectors such as LIGO and Virgo. Shortly before merging, once the relative distance between the stars is small enough, the tidal distortion of the NS become so large that, in some cases (in strongest signals corresponding to closest merging events), it becomes possible to infer the tidal deformability from the GW signal.

### Pulsar glitches

The so-called pulsar glitches are sudden jumps in the rotational frequency of a compact star. They are thought to originate from an abrupt transfer of angular momentum from the superfluid components of the NS, acting as an angular momentum reservoir, to the solid crust of the star, and all the normal fluid components which are strongly coupled to the crust by mutual dissipation. This sudden transfer is thought to be due to the unpinning of the superfluid vortices from the crystal lattice [AI75]. Indeed, a rotating superfluid, such as the superfluid neutrons in the inner crust of the NS, produces individual quantized vortices, with a density proportional to the rotational rate. Those vortices migrate towards the surface of the star due to quantization of the macroscopic vorticity, where they get pinned to the ions of the lattice that constitutes the solid crust of the NS. Since the star experiences a spin-down due to the emission of electromagnetic radiation, a differential lag develops between the faster superfluid vortices and the slower crust, leading to crustal stress. When the differential lag between the slower solid crust and faster superfluid vortices reach some threshold and can no longer be sustained, the vortices suddenly unpin from the lattice sites, leading to an angular momentum transfer to the crust, and the rest of the star which is entangled with the crust by mutual friction, so as to recover a close equilibrium between the normal and superfluid components. Since the electromagnetic slowing down is a continuous process, this is not a final equilibrium situation, and eventually stresses start to build up again, ultimately leading to another glitch event. At the time of writing, 555 glitches have been observed in 190 pulsars through high-precision pulsar timing [Esp+11; Jod]. The Vela pulsar (PSR B0833-45) is one of the most active glitchers known, with glitches occurring four times per decade on average.

## Microphysics of the (proto)neutron star crust

A theoretical description of the different phenomena mentioned above requires the modeling of dense baryonic matter, specifically the nuclear equation of state (EoS). The EoS relates, in given conditions of temperature and densities, the thermodynamic quantities of the system, such as the mass density and the pressure, at the equilibrium. Its determination allows us to compute among others the mass-radius relation of NS, obtained by solving the hydrostatic equilibrium equation in general relativity [Tol39; OV39]. Since quantum chromodynamics (QCD) in the nonperturbative

regime cannot be exactly solved, the EoS is strongly model dependent, which induces considerable uncertainties in the prediction of astrophysical observables. In this thesis, we are particularly interested in the modeling of the (P)NS crust, where matter is inhomogeneous. From the modeling point of view, the regime of subsaturation matter constitutes a challenging part of the nuclear EoS. Indeed, the uncertainties do not only concern the nuclear energy functional, but also the many-body method used to model inhomogeneous matter. Indeed, the evaluation of the EoS implies to know the microscopic composition at each point in the star. At finite temperature, an extra complication arises from the statistical mechanics treatment of the problem. Historically, the stellar EoS at subsaturation densities was first calculated within the so-called single-nucleus approximation (SNA) [BBP71; NV73], based on the assumption that matter can be represented by the most probable nucleus given by the minimization of the free energy density of matter. While this approximation is exact at zero temperature, a full distribution of clusters should be considered at finite temperature, as is it the case in nuclear statistical equilibrium (NSE) models. Again, the exact solution of the many-body problem at finite temperature being out of scope, modeling cannot be avoided, which induces a model dependence on the calculation of observables.

One could naively consider that an optimal nuclear model can be extracted by confronting the theoretical predictions with the observational data. However, a major issue when considering characteristic EoS is that some observables are better reproduced by a particular model (or a class of models), while they fail to reproduce other observables. In addition, each observable is associated with uncertainties and the ability to reproduce or not a determined measurement does not have the same impact on the reliability of the model, depending on which observable is considered. In addition to astrophysical constraints, there are also constraints coming from nuclear experiments, and recent developments in *ab initio* calculations based on chiral effective field theory (EFT) [DHS16], which consists in the determination of the nuclear energy functional from a systematic power expansion which respects the fundamental symmetries of low-energy QCD [ME11], that is the theory of strong interactions. The different models that can be considered have not been confronted to all those constraints, and not on the same level. In these circumstances, it is very arduous to validate (or invalidate) a model. A solution for this impasse is provided by the use of Bayesian inference principle, which allows to update our prior beliefs on the EoS with the constraints arising from the multiple sources mentioned above. It has been shown that the (P)NS observables are sensitive to the microphysics entering the EoS, for instance to the high-order derivatives of the nuclear symmetry energy and to the surface properties of finite nuclei. It is therefore essential to constrain these inputs in order to control the uncertainties in the observables. In this thesis, we are interested in making realistic predictions and to investigate the sources of uncertainties in the observables of nonaccreting cold NS and warm PNS, using the present day constraints provided by nuclear experiments, theoretical developments in chiral EFT, and astrophysical observations. This general argument applies to the total modeling of the NS, and also to the NS crust, which is the main focus of this work.

While the crust only represents a very small percentage of the total NS mass, knowledge of it is important in order to understand NS dynamics, notably glitches

and cooling. In addition to the nuclear EoS, the determination of crustal observables requires the knowledge of the density and pressure at the transition point from the solid crust to the liquid core [PFH14]. In order to validate the full crustal origin of the large glitches observed in some pulsars, such as Vela, the neutron star crust must be sufficiently thick to store a significant amount of angular momentum. The corresponding fraction of the crust moment of inertia can be estimated [LEL99; And+12; Del+16] in a range going from 1.6% up to 15%, depending on the importance of the effect of crustal entrainment, which is currently under debate [MU16; WP17]. A reliable estimation of the crust thickness and of the associated moment of inertia is thus crucially needed to validate the crustal origin of pulsar glitches. For all these applications, it is essential to have objective criteria allowing to validate or invalidate the different models, and possibly correlate the residual uncertainty of model predictions to well-defined parameters that can be constrained in the future by more precise experiments or *ab initio* calculations. The first part of the present thesis is aimed at providing a step forward in this direction. This will be done by introducing a flexible metamodeling procedure which will allow us to confront a very large set of models of catalyzed nuclear matter to the different constraints coming from both low-energy nuclear physics and astrophysical observations of mature NS.

The second part of the thesis will deal with the modeling of the crust at finite temperature. Again, the focus will be put on the determination of reliable error bars on the determination of astrophysical quantities due to the uncertainties of the modeling. This finite temperature modeling is not only essential to describe PNS dynamics, but it might also be relevant for the description of crustal observables of mature neutron stars. Indeed, the crust of an NS is unlikely to be in full thermodynamic equilibrium at zero temperature: NS are born hot, and if their core cools down sufficiently rapidly, the composition might be frozen at a finite temperature [Gor+11]. Deviations from the ground-state composition in the cooled crust around the neutron-drip density were already considered in [BC79], but simple extrapolations of semiempirical mass formulae were used at that time. The value of the freeze-out temperature is difficult to evaluate, but a lower limit is given by the crystallization temperature, since we can expect that nuclear reactions will be fully inhibited in a Coulomb crystal. For these reasons, the last part of this thesis will be dedicated to the study of the structure of the crust at the temperature of crystallization. The possible presence of amorphous and heterogeneous phases in the inner crust of a neutron star is expected to reduce the electrical conductivity of the crust, with potentially important consequences on the magneto-thermal evolution of the star. The study of cooling processes is important for comparing the theoretical calculations with surface temperature as measured by satellites. In cooling simulations, the disorder is quantified by an impurity parameter which is often taken as a free parameter. This parameter is directly related to the electron–impurity conductivity, which contributes to the total thermal conductivity [FI76].

## Structure of the thesis

The thesis is divided into three chapters. In Chapter 1, we consider a unified metamodeling approach in order to calculate the composition and EoS of cold non accreting

NS for any functional of nuclear matter (NM). The cluster energy in the inner crust is calculated within the compressible liquid drop (CLD) approximation. In Chapter 2, we carry out the Bayesian determination of the EoS parameters, leading to realistic predictions for the observables of cold NS, which we compare to the constraints of the LIGO/Virgo collaborations. Valuable information arising from nuclear physics experiments, chiral EFT calculations, and astrophysical observations are incorporated into the likelihood probability. Correlations among EoS parameters are explored. The crust-core transition quantities and fraction of crustal moment of inertia are computed for the posterior distribution of EoS parameters, and we discuss the full crustal origin of Vela pulsar glitches. In Chapter 3, we consider an NSE approach to model the crust of PNS at finite temperature. The equilibrium composition at the crystallization temperature is calculated, and the so-called impurity parameter, which is an important input for NS cooling simulations is evaluated for different realistic functionals. The presence of odd-mass and odd-charge nuclei in the outer crust is also investigated.

# Chapter 1

# Structure and equation of state of cold nonaccreting neutron stars

This chapter deals with the structure and EoS of NS within the framework of the "cold catalyzed matter" (CCM) hypothesis.

With typical temperature of about $T \sim 10^8$ K $\sim 0.01$ MeV, NS are very cold systems from the nuclear physics viewpoint, therefore the CCM hypothesis is commonly used to predict their internal composition and pressure. In this limit, thermal, nuclear, and beta equilibrium are established at zero temperature, meaning that the energy cannot be lowered by weak, strong, or electromagnetic processes, thus the matter is in its ground state. It is reasonable to expect these equilibrium conditions to be valid in any NS as far as it is not accreting matter from a neighbor. Indeed, in the accretion scenario, the typical timescale of the process are such that the matter composition is believed to be out of equilibrium.

As already discussed in the general introduction, the evaluation of the EoS implies to know the microscopic composition at each point in the star. At subsaturation densities, the solid crust consists mainly of clusterized matter, arranged in a body-centered cubic lattice [HPY07]. The relevant degrees of freedom in the crust are the Wigner-Seitz (WS) cells, containing exactly one lattice point [WS33]. At zero temperature, WS cells are supposed to be identical, thus the SNA, which considers a unique configuration for a given thermodynamic condition of temperature and pressure $(P, T)$, becomes exact. The ground state of the outer crust is almost entirely characterized by experimental nuclear masses, which are available up to $(N-Z)/A \lesssim 0.3$, $N$ being the number of neutrons, $Z$ the number of protons, and $A = N + Z$ the number of nucleons constituting atomic nuclei. The determination of inner-crust ground state is however more challenging because the crust is permeated by free neutrons, a situation which cannot be achieved in terrestrial conditions. Therefore, different treatments, from microscopic [NV73] to classical [BBP71], can be envisaged to estimate the energy of matter, and the EoS in this region depends on the nucleon-nucleon (NN) effective interaction or energy functional. At suprasaturation densities, matter consists of a uniform plasma of neutrons, protons, electrons, and eventually muons, in both strong and weak equilibrium. The development of a unified EoS, that is such that matter at subsaturation and supersaturation densities are treated within a unique model, is

essential if one wants to make realistic predictions on NS observables [For+16].

The plan of the chapter is as follows. In Section 1.1, the ground state of the outer crust is determined by application of the method introduced by Baym, Pethick, and Sutherland (BPS) [BPS71], using experimental masses supplemented by state-of-the-art microscopic theoretical mass tables. Section 1.2 is devoted to the determination of the inner-crust ground state using a compressible liquid drop model (CLDM) based on the metamodeling technique [MHG18a; CGM19a]. The phase transition from the solid crust to the liquid core, occuring at some $\approx 1$ km from the surface of the star, is investigated. In Section 1.3, we calculate the ground state of matter in the outer core, and we address the problem of the inner-core composition. In Section 1.4, a unified metamodeling of the EoS is proposed. Finally, conclusions are given in Section 1.5.

## Contents

**1.1 Ground state of the outer crust . . . . . 11**
1.1.1 Wigner-Seitz cell energetics . . . . . 11
1.1.1.1 Nuclear mass tables . . . . . 12
1.1.1.2 Relativistic electron gas . . . . . 12
1.1.2 The BPS model . . . . . 13
1.1.3 Equilibrium composition and equation of state . . . . . 15
**1.2 Ground state of the inner crust . . . . . 19**
1.2.1 Modeling the nuclear energy . . . . . 20
1.2.1.1 Metamodeling of homogeneous nuclear matter . . 22
1.2.1.2 From homogeneous nuclear matter to finite nuclei in the CLD approximation . . . . . 27
1.2.2 Variational formalism . . . . . 31
1.2.3 Results . . . . . 35
1.2.3.1 Numerical code . . . . . 35
1.2.3.2 Equilibrium composition . . . . . 36
1.2.3.3 Equation of state . . . . . 38
1.2.4 Strutinsky shell corrections to the CLD energy . . . . . 39
1.2.5 Nonspherical pasta phases . . . . . 42
1.2.6 Crust-core transition from the crust side . . . . . 45
**1.3 Matter of the core . . . . . 47**
1.3.1 Outer core: homogeneous $npe\mu$ matter . . . . . 48
1.3.1.1 Variational equations . . . . . 49
1.3.1.2 Equilibrium composition and equation of state . . 50
1.3.2 Inner core . . . . . 51
**1.4 Unified metamodeling of the equation of state . . . . . 52**
**1.5 Conclusions . . . . . 54**

## 1.1 Ground state of the outer crust

At zero temperature, the matter inside the outer crust corresponds to a lattice of strongly bound nuclei, immersed in a sea of electrons. The mass density at which nuclei are fully ionized and electron completely degenerated is of the order of $\rho_B \gg 6AZ \sim 10^4$ g/cm$^3$ for $^{56}$Fe, which is the ground state of matter at very low density. Below $10^4$ g/cm$^3$, some electrons are still bound to the nuclei and one must rely on the EoS calculated by Feynman, Metropolis, and Teller from 15 to $10^4$ g/cm$^3$, suitable for the envelope of neutron stars [FMT49].

This section deals with the determination of the outer-crust ground state. In 1.1.1, we detail the different terms entering the WS cell energy, with emphasis on the relativistic electron gas energy as well as nuclear masses. The ground state of the outer crust is calculated by application of the variational BPS method [BPS71], which is presented in 1.1.2. Finally, using current knowledge on experimental masses [Hua+17] supplemented by different microscopic theoretical mass tables, we compute the equilibrium composition and EoS. Our results are presented in 1.1.3.

### 1.1.1 Wigner-Seitz cell energetics

In the outer crust, a WS cell is composed of a strongly bound nucleus at the center, immersed in a relativistic electron gas of density $n_e$. Charge neutrality is assured in each unit cell, $n_e = n_p$, with $n_p$ the proton density inside the cell.

The energy of a WS cell in the outer crust can therefore be written as

$$E_{WS} = E_i + V_{WS}\varepsilon_e, \tag{1.1}$$

with $E_i$ the ion energy, $V_{WS}$ the volume of the cell, and $\varepsilon_e$ the energy density of the free electron Fermi gas. The ion energy reads

$$E_i = M'(A,Z)c^2 + E_L + E_{zp}, \tag{1.2}$$

where $M'(A,Z)c^2$ is the nuclear mass of a nucleus with associated mass number $A$ and charge number $Z$, $E_L$ the temperature-independent static-lattice term, and $E_{zp}$ the zero-point quantum vibration term given by

$$E_{zp} = \frac{3}{2}\hbar\omega_p u_1, \tag{1.3}$$

where $u_1 = 0.5113875$ is a numerical constant for a body-centered cubic lattice (see Table 2.4 of [HPY07]), which is assumed to be the geometry minimizing the lattice energy. This assumption was recently confirmed in [CF16]. The ion plasma frequency $\omega_p$ is given by

$$\hbar\omega_p = \sqrt{\frac{(\hbar c)^2 4\pi n_N (Ze)^2}{M'(A,Z)c^2}}, \tag{1.4}$$

$e$ being the elementary charge, $c$ the speed of light, $\hbar = h/2\pi$ the reduced Planck constant, and where the ion density $n_N = 1/V_{WS}$ has been introduced. The lattice energy reads

$$E_L = -C_M \frac{(Ze)^2}{a_N}, \tag{1.5}$$

with $C_M = 0.895929255682$ the Mandelung constant for a body-centered cubic lattice (see Table 2.4 of [HPY07]), and $a_N = (4\pi n_N/3)^{-1/3}$ the ion-sphere radius.

#### 1.1.1.1 Nuclear mass tables

An essential input for Eq. (1.2) is the nuclear mass table. When available, that is for $I = (N - Z)/A \lesssim 0.3$, we use experimental masses from the 2016 Atomic Mass Evaluation (AME) [Hua+17]. For more neutron-rich nuclei and until we reach the neutron drip line, the use of a model is required, thus a model dependence arises. A possibility is to rely on microscopic Hartree-Fock-Bogoliubov (HFB) theoretical mass tables [Sam+02], which are based on the nuclear energy-density functional theory.

In general, atomic masses are tabulated instead of the nuclear ones which can be calculated as

$$M'(A, Z)c^2 = M(A, Z)c^2 - Zm_e c^2 + B_e(Z), \tag{1.6}$$

with $M(A, Z)c^2 = \Delta\epsilon + Am_u c^2$ the atomic mass ($\Delta\epsilon$ is the mass excess and $m_u$ is the atomic mass unit), $m_e$ the electron mass, and $B_e$ the binding energy of atomic electrons depending solely on the number of protons $Z$ according to the approximation proposed in [LPT03] (see their Eq. (A4)),

$$B_e(Z) = 1.44381 \times 10^{-5} Z^{2.39} + 1.55468 \times 10^{-12} Z^{5.35}. \tag{1.7}$$

#### 1.1.1.2 Relativistic electron gas

In the cold outer crust, the mass densities are above $\sim 10^4$ g/cm$^3$ therefore the electrons are essentially free. In this regime, it was shown in [WI03] that electron-charge screening effects are negligible and that the electron density is essentially homogeneous. This is explained from the fact that the electron Thomas-Fermi screening length is larger than the lattice spacing. The expression of the energy density of a relativistic electron gas, with rest mass energy, at zero temperature can be calculated as

$$\begin{aligned} \varepsilon_e(n_e) &= \int_0^{k_e} \frac{k^2 dk}{\pi^2} c\sqrt{\hbar^2 k^2 + {m_e}^2 c^2} \\ &= \frac{P_r}{8\pi^2}\left[x_r(1 + 2{x_r}^2)\gamma_r - \ln(x_r + \gamma_r)\right], \end{aligned} \tag{1.8}$$

with $P_r = {m_e}^4 c^5/\hbar^3$ the relativistic unit of the electron pressure, $x_r = \hbar k_e/(m_e c)$ the relativity parameter, and $\gamma_r = \sqrt{1 + {x_r}^2}$. $k_e$ is the electron Fermi wave number given by

$$k_e = (3\pi^2 n_e)^{1/3}. \tag{1.9}$$

The derivation of Eq. (1.8) is given in Appendix A. Above $10^7$ g/cm$^3$, $x_r \gg 1$, thus electrons can be considered ultrarelativistic and Eq. (1.8) becomes

$$\varepsilon_e(n_e) = \frac{3}{4} n_e m_e c^2 x_r. \tag{1.10}$$

Taking the derivative of Eq. (1.8) with respect to the electron gas density yields the pressure,

$$\begin{aligned} P_e &= -\frac{\partial(V_{WS}\varepsilon_e)}{\partial V_{WS}} = n_e \frac{\partial \varepsilon_e}{\partial n_e} - \varepsilon_e \\ &= \frac{P_r}{8\pi^2}\left[x_r\left(\frac{2}{3}x_r^2 - 1\right)\gamma_r + \ln(x_r + \gamma_r)\right]. \end{aligned} \tag{1.11}$$

The electron exchange energy, which is a direct consequence of the Pauli exclusion principle, and the electron correlation energy, which is due to the fact that the motion of each electron is affected by the motion and position of the other electrons, are neglected since they are known to be small in comparison with the kinetic energy of relativistic electrons. The expression of the electron exchange correction to the free energy density for a strongly degenerate electron gas is given in [HPY07] (see their Eq. (2.151)). We have checked that the inclusion of these corrections does not modify the results presented in this chapter.

### 1.1.2 The BPS model

The variational technique which is currently used to calculate the ground state of the outer crust was introduced by Baym, Pethick, and Sutherland in [BPS71].

The thermodynamic potential to be minimized is the zero-temperature Gibbs free energy per nucleon at fixed pressure $P$ under the condition of charge neutrality $n_e = Zn_N$, until the neutron drip sets in, the condition for which is $\mu_n = m_n c^2$, with $\mu_n$ the neutron chemical potential, and $m_n$ the neutron mass.

The definition of the zero-temperature Gibbs free energy per nucleon is

$$g = \frac{\varepsilon_{WS} + P}{n_B}, \tag{1.12}$$

where $\varepsilon_{WS} = E_{WS}/V_{WS}$ is the energy density of the WS cell, and $n_B$ is the baryon density given by $n_B = n_N A = A/V_{WS}$. We can calculate the pressure as

$$P = {n_B}^2 \frac{\partial(\varepsilon_{WS}/n_B)}{\partial n_B}\bigg|_{Z,A}, \tag{1.13}$$

yielding, using Eq. (1.1),

$$P = P_e + \frac{1}{3}E_L n_N + \frac{1}{2}E_{zp} n_N. \tag{1.14}$$

Thus the expression of the zero-temperature Gibbs free energy per nucleon can be rewritten as

$$g = \frac{M'(A,Z)c^2 + \frac{4}{3}E_L + \frac{1}{2}E_{zp} + Z\mu_e}{A}, \tag{1.15}$$

where $\mu_e$ is the electron chemical potential given by

$$\mu_e = \frac{\partial \varepsilon_e}{\partial n_e}. \tag{1.16}$$

Essentially, one fixes the pressure $P$, calculates for each nucleus $(A, Z)$ the electronic density by solving numerically Eq. (1.14), then constructs a table $g(A, Z)$. The ground state of the outer crust at pressure $P$ then corresponds to the nucleus associated to the minimum value of $g$.

As explained in [Pea+18], the neutron chemical potential can be calculated through

$$\mu_n = g, \tag{1.17}$$

because the beta equilibrium equation $\mu_n = \mu_p + \mu_e$ holds throughout the star. Indeed, by exploiting the thermodynamic relation

$$\mathcal{G} = \varepsilon + P = \mu_n n_n + \mu_p n_p + \mu_e n_e, \tag{1.18}$$

together with the charge neutrality condition $n_e = n_p$, we obtain

$$\mathcal{G} = \mu_n n_n + (\mu_e + \mu_p) n_p, \tag{1.19}$$

where $\mathcal{G}$ is the zero-temperature Gibbs free energy density, and $\mu_p$ the proton chemical potential. In the case where the chemical equilibrium is established, that is if weak processes are at equilibrium, we finally get

$$\mathcal{G} = \mu_n n_B. \tag{1.20}$$

One should stress that while minimizing the zero-temperature Gibbs free energy per nucleon at fixed pressure is less practical than simply minimizing the total energy density at constant baryon density, it makes it easier to study the transitions between layers. The pressure increases continuously with increasing depth in the star, thus a discontinuity in the density is the signature of a transition from a layer $(A, Z)$ to another $(A', Z')$. Noting that the pressure in the outer crust is approximately equal to the pressure of the electron gas (the lattice and zero-point terms contribute to less than 5% to the total pressure in the bottom layers of the outer crust), we know that $n_e = n_p$ is continuous across the transition thus

$$\Delta n_B = n'_B - n_B \simeq n_p \left( \frac{A'}{Z'} - \frac{A}{Z} \right), \tag{1.21}$$

and the fractional change in the baryon mass density results

$$\frac{\Delta \rho_B}{\rho_B} \simeq \frac{\Delta n_B}{n_B} \simeq \frac{Z/A}{Z'/A'} - 1. \tag{1.22}$$

For this reason, it is more convenient to choose the pressure as the independent variable. In this way we avoid to make a Maxwell construction to estimate the pressure at which the transition from $(A, Z)$ to $(A', Z')$ occurs.

The BPS model is still widely used to determine the ground state of the outer crust. However, at that time the authors took the values of nuclear binding energies from the outdated phenomenological macroscopic model of Myers and Swiatecki [MS65] and considered only 150 even-even nuclei. Moreover, they did not take into account the zero-point vibration energy, Eq. (1.3). In the last decades, considerable efforts have

been made to measure nuclear masses near the neutron drip line [LPT03], as well as theoretical developments were achieved to construct microscopic mass tables [Sam+02; GCP13]. It is therefore important to reevaluate the ground state of the outer crust considering those experimental and theoretical advances. In this line, Haensel and Pichon studied the consequences of progress concerning the experimental determination of atomic masses in 1994 [HP94]. The authors found that the ground state of the outer crust can be determined exclusively by experimental masses in a fully model independent way up to $\rho_B \approx 10^{11}$ g/cm$^3$. From this density up to the neutron drip point, the phenomenological, liquid-drop based mass formula of Möller was used, the formalism of which is described in [MN88].

In the same spirit as [HP94], we calculate, in the following, the ground state of the outer crust using the present day knowledge on experimental masses of neutron rich nuclei [Hua+17; Wel+17] combined with state-of-the-art microscopic theoretical mass tables [GCP13].

### 1.1.3 Equilibrium composition and equation of state

We turn to the numerical results obtained applying the BPS method presented in 1.1.2. The ground state of the outer crust is calculated, beginning at $P = 3\times10^{-11}$ MeV/fm$^3$, corresponding approximately to $n_B \approx 10^{-9}$ fm$^{-3}$, in order to ensure complete ionization and electron degeneracy. The pressure is increased from steps of $0.02P$ until the neutron drip point, defined by $\mu_n - m_n c^2 = 0$, is reached.

The ground-state composition and EoS of the outer crust of a cold nonaccreting NS is reported in Table 1.1. The upper part of the table, $n_B < 3.84 \times 10^{-5}$ fm$^{-3}$, corresponding to $\rho_B < 6.39 \times 10^{10}$ g/cm$^3$, is exclusively determined by experimental data from the AME2016 [Hua+17]. Let us notice that the maximum mass density at which experimentally studied nucleus $^{80}$Zn was present was found to be slightly lower in [HP94], $\rho_B = 5.44 \times 10^{10}$ g/cm$^3$. This is due to the fact that the determination of this density depends on the mass formula used, here HFB-24, for the neutron rich nuclides present in the bottom layers of the outer crust. From $3.84\times10^{-5}$ fm$^{-3}$, matter becomes so neutron rich that the nuclear masses cannot be measured experimentally for now, thus a model dependence is expected to arise because the nuclear masses have to be extrapolated from laboratory nuclei. The nuclear mass model used to calculated the ground state here is HFB-24 [GCP13], constructed from the BSk24 functional following the Hartree-Fock-Bogoliubov method [Sam+02]. The BSk24 functional is part of a family of functionals labeled BSk22 to BSk26, consisting of unconventional effective Skyrme forces with extra $t_4$ and $t_5$ terms that behave as density-dependent generalizations of the usual $t_1$ and $t_2$ terms present in traditional Skyrme forces [VB72; Cha+97]. The functionals BSk22-26 were fitted to the 2353 experimental masses of the AME2012 [Aud+12] and differ mainly by their symmetry energy $S$, defined here as the difference between the energy per nucleon of pure neutron matter (PNM) $e_{PNM}$ and the energy per nucleon of symmetric nuclear matter (SNM) $e_{SNM}$,

$$S(n_B) = e_{PNM}(n_B) - e_{SNM}(n_B). \tag{1.23}$$

At the saturation density of nuclear matter $n_B = n_{sat} \approx 0.16$ fm$^{-3}$, $S(n_B)$ coincides

| element | $Z$ | $N$ | $Y_p$ | $n_{B,max}$ (fm$^{-3}$) | $P_{max}$ (MeV/fm$^3$) | $\mu_n - m_n c^2$ (MeV) | $\mu_e$ (MeV) |
|---|---|---|---|---|---|---|---|
| $^{56}$Fe | 26 | 30 | 0.4643 | $4.97 \times 10^{-9}$ | $3.40 \times 10^{-10}$ | -8.96 | 0.95 |
| $^{62}$Ni | 28 | 34 | 0.4516 | $1.56 \times 10^{-7}$ | $4.09 \times 10^{-8}$ | -8.26 | 2.57 |
| $^{64}$Ni | 28 | 36 | 0.4375 | $8.07 \times 10^{-7}$ | $3.60 \times 10^{-7}$ | -7.52 | 4.34 |
| $^{66}$Ni | 28 | 38 | 0.4242 | $9.27 \times 10^{-7}$ | $4.16 \times 10^{-7}$ | -7.46 | 4.50 |
| $^{86}$Kr | 36 | 50 | 0.4186 | $1.85 \times 10^{-6}$ | $1.03 \times 10^{-6}$ | -7.01 | 5.63 |
| $^{84}$Se | 34 | 50 | 0.4048 | $6.85 \times 10^{-6}$ | $5.64 \times 10^{-6}$ | -5.87 | 8.59 |
| $^{82}$Ge | 32 | 50 | 0.3902 | $1.67 \times 10^{-5}$ | $1.77 \times 10^{-5}$ | -4.82 | 11.41 |
| $^{80}$Zn | 30 | 50 | 0.3750 | $3.84 \times 10^{-5}$ | $5.10 \times 10^{-5}$ | -3.58 | 14.86 |
| $^{78}$Ni | 28 | 50 | 0.3590 | $6.68 \times 10^{-5}$ | $1.01 \times 10^{-4}$ | -2.63 | 17.61 |
| $^{126}$Ru | 44 | 82 | 0.3492 | $7.52 \times 10^{-5}$ | $1.12 \times 10^{-4}$ | -2.47 | 18.15 |
| $^{124}$Mo | 42 | 82 | 0.3387 | $1.21 \times 10^{-4}$ | $2.04 \times 10^{-4}$ | -1.54 | 21.05 |
| $^{122}$Zr | 40 | 82 | 0.3279 | $1.56 \times 10^{-4}$ | $2.75 \times 10^{-4}$ | -1.03 | 22.69 |
| $^{121}$Y | 39 | 82 | 0.3223 | $1.63 \times 10^{-4}$ | $2.84 \times 10^{-4}$ | -0.98 | 22.86 |
| $^{120}$Sr | 38 | 82 | 0.3167 | $1.95 \times 10^{-4}$ | $3.52 \times 10^{-4}$ | -0.60 | 24.12 |
| $^{122}$Sr | 38 | 84 | 0.3115 | $2.37 \times 10^{-4}$ | $4.49 \times 10^{-4}$ | -0.15 | 25.62 |
| $^{124}$Sr | 38 | 86 | 0.3065 | $2.56 \times 10^{-4}$ | $4.87 \times 10^{-4}$ | 0.00 | 26.14 |

**Table 1.1:** *Ground state of the outer crust of a cold nonaccreting neutron star. Experimental data from the 2016 Atomic Mass Evaluation [Hua+17] are used when available. Mass excesses of $^{77-79}$Cu are taken from [Wel+17]. Experimental masses are supplemented with masses from microscopic HFB-24 theoretical mass table [GCP13] (lower part). The last line corresponds to the neutron drip point. The following quantities are reported in the table: the element, the atomic number $Z$, the neutron number $N$, the proton fraction $Y_p = Z/A$ ($A$ is the number of nucleons), the maximum baryon density $n_{B,max}$ at which the nuclide is found, the associated pressure $P_{max}$, the neutron chemical potential minus rest mass $\mu_n - m_n c^2$, and the electron chemical potential $\mu_e$.*

with the so-called symmetry energy parameter $E_{sym}$. This quantity is constrained to 32, 31, 30, and 29 MeV for BSk22, BSk23, BSk24, and BSk25, respectively. For BSk26, $E_{sym} = 30$ MeV as well but the functional is fitted to the APR EoS of PNM [APR98], unlike BSk22-25 that are fitted to the stiffer LS2 EoS [LS08].

The first layer of the outer crust consists of a crystal lattice of $^{56}$Fe, the mass per nucleon of which is the lowest among all nuclides. The sequence of nuclides is in good agreement with the results of [HP94]. One can note the persistence of magic numbers $Z = 28$ and $N = 50$ at low density, and $Z = 82$ at higher density. In particular, in [HP94] the $N = 82$ shell is found from $\rho_B = 9.64 \times 10^{10}$ g/cm$^3$ to $4.32 \times 10^{11}$ g/cm$^3$, point of neutron drip (see Table 3.1 of [HPY07]). It is explained in [HPY07] that the apparent strong effect of the $N = 82$ shell in the bottom layers could be an artifact of the extrapolation using the mass formula of [MN88] and that further investigations on nuclear shell structure in the vicinity of the neutron drip point were required. Here we

find two additional layers of strontium ($N = 84$ and $N = 86$) with respect to [HP94] results, and the layer of $^{118}$Kr before the neutron drip is not observed.

At high density, a thin layer of odd-mass nuclei $^{121}$Y is found with the HFB-24 mass model. It is interesting since the possibility of having odd nuclei in the ground state of the outer crust was not considered in the original calculation of BPS [BPS71]. Also, it is reported in [Pea+18] that $^{79}$Cu is favored over $^{76}$Ni, found for HFB-22 and HFB-25, in the case where the recent mass excess measurements of [Wel+17] are not included. This highlights the importance of measuring the mass of odd-nuclei. Indeed, one could expect that the presence of odd-nuclei in the outer crust of NS might lead to a ferromagnetic phase transition at low temperature, which would generate a magnetic field and alter the existing field, and so the electron gas.

It can also be observed in Table 1.1 that the proton fraction $Y_p = Z/A$ always decreases with increasing depth. The neutronization of matter can be understood by the following reason. Neglecting the static-lattice energy as well as the zero-point quantum vibrations terms, we can write the zero-temperature Gibbs energy per nucleon as

$$g \simeq \frac{M'(A,Z)c^2 + V\varepsilon_e}{n_B V} + \frac{P}{n_B}. \tag{1.24}$$

Since the lattice does not contribute to the pressure, we have $P \simeq P_e = n_e\mu_e - \varepsilon_e$, yielding

$$g \simeq \frac{M'(A,Z)c^2}{A} + \frac{n_e}{n_B}\mu_e. \tag{1.25}$$

The charge neutrality is ensured in the unit cell, therefore $n_e/n_B = Z/A$ and we finally get

$$g \simeq \frac{M'(A,Z)c^2}{A} + \frac{Z}{A}\mu_e. \tag{1.26}$$

For $\rho_B \gg 10^{-7}$ g/cm$^3$, electrons are ultrarelativistic and the electron chemical potential is calculated by taking the derivative of Eq. (1.10),

$$\mu_e = \frac{\partial \varepsilon_e}{\partial n_e} = \frac{3}{4}\hbar c(3\pi^2)^{1/3} n_e^{1/3}. \tag{1.27}$$

Therefore, the electron chemical potential $\mu_e$ scales as $P^{1/4}$ ($P \propto n_e^{4/3}$). Then it appears that, with increasing pressure, it is energetically favorable to decrease the proton fraction $Y_p = Z/A$ in order to compensate the increase in the term $M'(A,Z)c^2/A$. The neutron chemical potential monotonously increases with increasing density and at $n_B = 2.56 \times 10^{-4}$ fm$^{-3}$, corresponding to $P = 4.87 \times 10^{-4}$ MeV/fm$^3$, the neutron drip is finally reached. It should be mentioned that the neutron drip density as well as pressure depend on the mass model, here chosen to be HFB-24.

The model dependence of the composition in the bottom layers of the outer crust (bottom part of Table 1.1) can be seen in Figure 1.1, where we represent the proton number $Z$ and the neutron number $N$ as a function of the baryon density $n_B$ for four different mass models that reproduce with comparable accuracy the present experimental mass information: HFB-14 [GSP07], HFB-24, HFB-26 [GCP13], and FRDM [Mol+95] that supplement the experimental data. The model dependence is

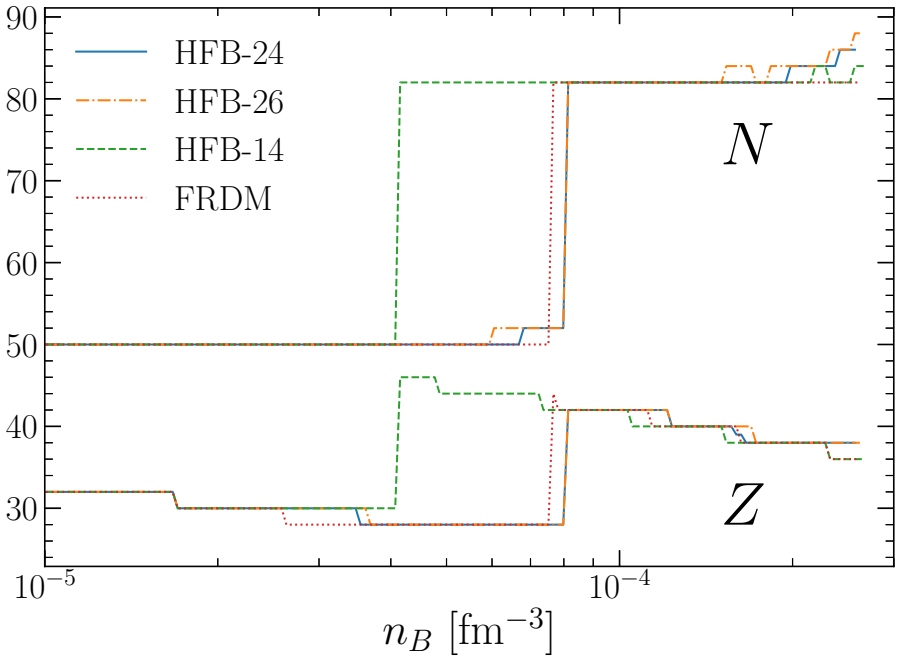



**Figure 1.1:** *Variation with baryon density $n_B$ of the equilibrium value of atomic number $Z$ and neutron number $N$ in the bottom layers of the outer crust for four different models: HFB-24, HFB-26 [GCP13], HFB-14 [GSP07], and FRDM [Mol+95].*

observed from $n_B \approx 2.5 \times 10^{-5}$ fm$^{-3}$, where the experimental mass data are not available. We recover similar sequences of nuclides with the different mass models, with the strong shell effect associated to $N = 50$ at low density and $N = 82$ in the bottom layers. A thin layer with $N = 52$ is also found for HFB-24 and HFB-26 just before the transition to $N = 82$. While this transition occurs in the vicinity of $8 \times 10^{-5}$ fm$^{-3}$ for HFB-24, HFB-26, and FRDM, it is found to happen at approximately $4 \times 10^{-5}$ fm$^{-3}$ for HFB-14. Different nuclides are found close to the neutron drip, depending on the model: $^{124}$Sr is found for HFB-24, $^{126}$Sr for HFB-26, $^{120}$Kr for HFB-14, and $^{122}$Kr for FRDM. Let us note that most of the mass of the outer crust is actually concentrated in those densest layers. The neutron drip density $n_{ND}$ and pressure $P_{ND}$ slightly depend on the model as well. These values are reported in Table 1.2.

The variation of pressure with baryon density, namely the EoS, is shown in Fig. 1.2 for the four mass models. The selected models give the same value of pressure up to $\approx 2.5 \times 10^{-5}$ fm$^{-3}$, as it is the case for the composition. At higher densities, we can perceive the small effect of the model, in particular at the transitions from a layer to another at which the pressure stays constant, but where a discontinuity is observed in the density.

| model | element | $Z$ | $N$ | $n_{ND}$ (fm$^{-3}$) | $P_{ND}$ (MeV/fm$^3$) |
|---|---|---|---|---|---|
| HFB-24 | $^{124}$Sr | 38 | 86 | $2.56 \times 10^{-4}$ | $4.87 \times 10^{-4}$ |
| HFB-26 | $^{126}$Sr | 38 | 88 | $2.62 \times 10^{-4}$ | $4.91 \times 10^{-4}$ |
| HFB-14 | $^{120}$Kr | 36 | 84 | $2.67 \times 10^{-4}$ | $5.01 \times 10^{-4}$ |
| FRDM | $^{122}$Kr | 36 | 82 | $2.62 \times 10^{-4}$ | $4.99 \times 10^{-4}$ |

**Table 1.2:** *Chemical element, atomic number $Z$, neutron number $N$, density $n_{ND}$, and pressure $P_{ND}$ at the neutron drip point for four different mass models: HFB-24, HFB-26 [GCP13], HFB-14 [GSP07], and FRDM [Mol+95].*

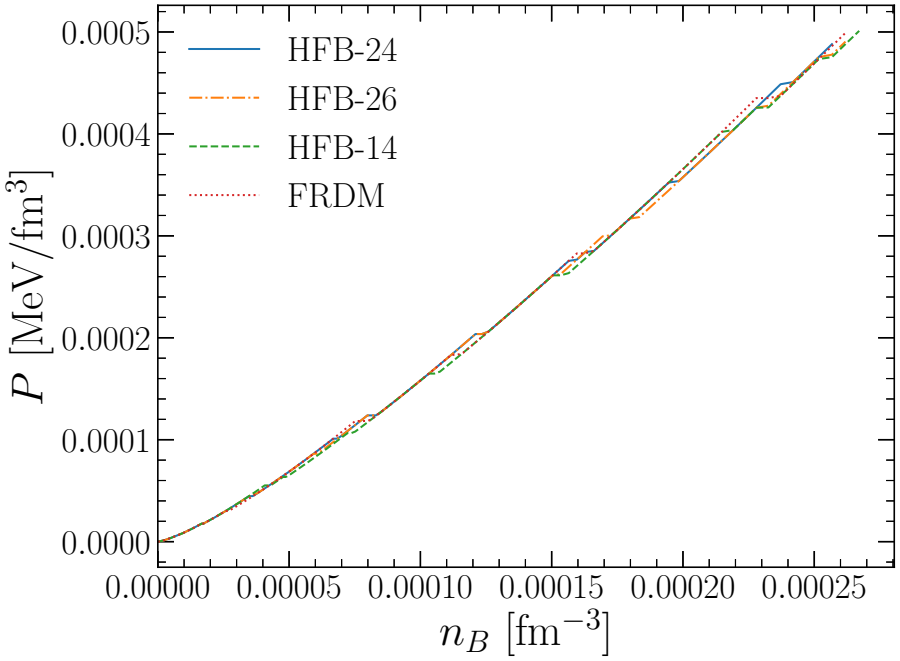



**Figure 1.2:** *Variation with baryon density $n_B$ of pressure $P$ for four different models: HFB-24, HFB-26 [GCP13], HFB-14 [GSP07], and the FRDM [Mol+95].*

## 1.2 Ground state of the inner crust

The neutron drip marks the onset of the inner crust, which is a system that cannot be reproduced in the laboratory since the dripped neutrons would evaporate, while they stay confined in the WS cell due the gravitational pressure. For this reason, the equilibrium composition and so the EoS in the inner crust are fully model dependent.

This section deals with the determination of the ground state of the inner crust. In 1.2.1, we present the metamodeling of the infinite nuclear matter EoS used to calculate the energy of the neutron gas, and extended to finite nuclei within the so-called compressible liquid drop (CLD) approximation so as to describe the cluster energetics. The derivation of the system of equilibrium equations for the determination of

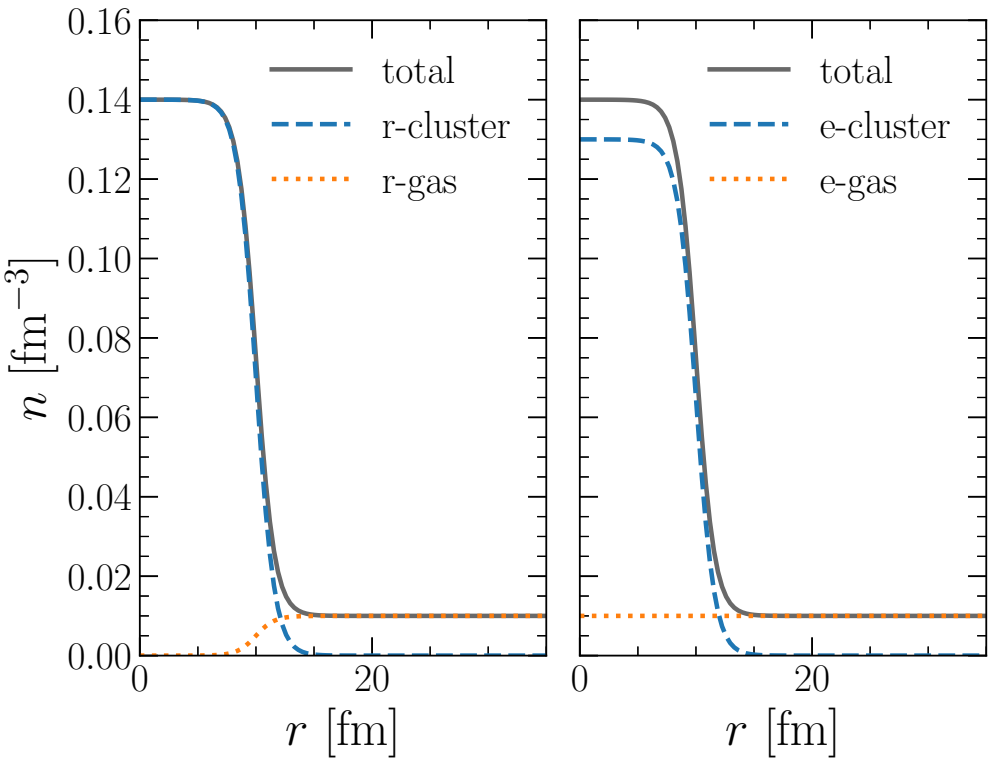



**Figure 1.3:** *Wood-Saxon density profiles, for arbitrary values, within a WS cell in the regime of the inner crust. Blue dashed lines correspond to the cluster density with different decompositions between cluster and gas (left, r-cluster; right, e-cluster), and orange dotted lines to the gas density. The total density profile is represented in gray solid lines.*

the inner-crust ground state is detailed in 1.2.2. The numerical method as well as results are presented afterwards, in 1.2.3. In 1.2.4 we add Strutinsky shell corrections on top of the CLD energy as an attempt to recover magic numbers in the free neutron regime. Nonspherical pasta phases in the bottom layers of the inner crust are considered in 1.2.5. Finally, the phase transition from the solid crust to the liquid core is investigated in 1.2.6.

### 1.2.1 Modeling the nuclear energy

Once the neutron dripline is reached, neutrons start to drip out of nuclei but stay confined in the WS cell because of the gravitational pressure, whereas they would have been emitted in the laboratory. In the regime of the inner crust, we thus have, in each unit cell, a cluster immersed in an electron sea, and an ambient neutron gas.

There is an ambiguity regarding the characterization of the cluster-gas interface. One should ask whether the neutron gas penetrates the cluster or not. Hence, two classical representations can be introduced, namely the r-cluster and e-cluster representations [Pap+13], to interpret the distribution of the $N_{WS}$ neutrons and $Z_{WS}$

protons in the unit cell. In the former, the cluster occupies a volume at the center of the cell and is surrounded by the neutron gas. Evidently, there is a thin region where cluster and gas overlap given the fact that a sharp interface would be unrealistic. The r-cluster representation naturally emerges in the local density approximation in density functional theory. Indeed, if the energy is expressed as a function of the local density, then the cluster corresponds to the dense part and the gas to the dilute one. This interpretation is used in most of the calculations at finite temperature to model SN, see for example the renowned Lattimer and Swesty EoS [LS91]. In the e-cluster representation, the gas penetrates the cluster. This interpretation appears spontaneously in single-particle developments. Indeed, in very neutron-rich clusters, beyond the neutron dripline, the bound states are occupied as well as the resonant and continuum states. All the unbound single-particle states that are occupied thus represent the neutron gas, characterized by a quasihomogeneous spatial distribution, the continuum wave functions being very similar to plane waves. The difference between the two representations is illustrated in Fig. 1.3. The cluster and gas density profiles, described by Woods-Saxon profiles with arbitrary values, are plotted along the WS cell radius in the r-cluster representation (left) and e-cluster representation (right). Woods-Saxon profiles are known to give a good description of medium-mass and heavy nuclei density profiles, and are commonly used in Thomas-Fermi (TF) and extended Thomas-Fermi (ETF) calculations [Ons+08; Pea+18]. In both representations, the total density profile (solid gray line) is the same, and so must therefore be the total energy in a TF or ETF framework. One can switch between the two representations using the simple geometric relations

$$A_e = A\left(1 - \frac{n_g}{n_0}\right), \quad Z_e = A\left(1 - \frac{n_{g,p}}{n_{0,p}}\right), \tag{1.28}$$

where $A_e$ ($Z_e$) is the number of nucleons (protons) in the e-cluster, $A$ ($Z$) the number of nucleons (protons) in the r-cluster, $n_g$ ($n_{g,p}$) the total (proton) gas density, and $n_0$ ($n_{0,p}$) the average total (proton) density inside the cluster. Since we do not consider the possibility of proton drip in the inner crust, we have $n_{g,p} = 0$, yielding $Z_e = Z$ and implying that the total gas density is equal to that of the neutron gas. Indeed, while free protons are expected at non-zero temperature, their presence at zero temperature remains uncertain [BBP71] and depends on the nuclear model. For some models, the proton drip could set in the very bottom layers of the crust [Pea+18]. However, if nonspherical shapes are considered then it is found that protons remain in the cluster for most models.

At zero temperature, we define the mass of the cluster in the e-cluster representation as

$$M_{i,e}c^2 = (A - Z)m_n c^2 + Zm_p c^2 + E_{cl} - V_{cl}(\varepsilon_g + n_g m_n c^2), \tag{1.29}$$

where $\varepsilon_g$ represents the energy density of the neutron gas of density $n_g$, $V_{cl} = A/n_0$ the volume of the cluster, and $E_{cl}$ the energy of the cluster, which will be specified lower in this chapter. The WS cell energy $E_{WS}$ can be written as

$$\begin{aligned} E_{WS} &= M_{i,e}c^2 + V_{WS}\varepsilon_e + V_{WS}(\varepsilon_g + n_g m_n c^2) \\ &= E_{cl} + V_{WS}\varepsilon_e + (V_{WS} - V_{cl})\varepsilon_g + Z_{WS}(m_p - m_n)c^2 + A_{WS}m_n c^2, \end{aligned} \tag{1.30}$$

with $V_{WS}$ the volume of the cell. The total number of protons $Z_{WS}$ and nucleons $A_{WS}$ inside the WS cell are given respectively by

$$Z_{WS} = A\frac{1-I}{2} \quad \text{and} \quad A_{WS} = A\left(1-\frac{n_g}{n_0}\right) + n_g V_{WS}, \tag{1.31}$$

where the cluster asymmetry $I = (N-Z)/A$ has been introduced. Let us notice that the number of protons inside the cell remains an integer number, as in the outer crust, unlike the number of neutrons that is noninteger because of the outside neutron gas.

As for the bottom layers of the outer crust, the determination of the ground state of the inner crust is model dependent. Therefore, the two necessary ingredients of the WS cell energy are the equation of state of PNM, and the energy of the cluster, which will be treated in the CLD approximation introduced by Baym, Bethe, and Pethick (BBP) in their pioneering work [BBP71].

#### 1.2.1.1 Metamodeling of homogeneous nuclear matter

The ambient neutron gas in the WS cell is treated as homogeneous nuclear matter. In this limit, a large number of nucleons $A \longrightarrow \infty$ is contained in a large box. The system is entirely characterized by the neutron density $n_n$ and the proton density $n_p$. Let us also introduce the total density $n = n_n + n_p$ and the asymmetry $\delta = (n_n - n_p)/n$. Two limit cases can be distinguished: pure neutron matter, where $n = n_p$, and symmetric nuclear matter, where $n_n = n_p$. Beta-equilibrated matter corresponds to the matter inside the core of neutron stars and is treated in Section 1.3. Different methods have been proposed in order to evaluate the energy per nucleon of homogeneous nuclear matter. While considerable theoretical efforts have been devoted to *ab initio* approaches in the recent years [Gan+14], these calculations might become unreliable at suprasaturation densities. Also, the treatment of three-body forces, which are known to play a major role in the determination of the saturation properties of nuclear matter, remains a challenge [DHS16]. Another possibility is to derive the nuclear EoS from phenomenological forces [Cha+98]. This approach however suffers from the possible introduction of artificial correlations among the parameter space. In the following we present the metamodeling technique [MHG18a; MHG18b]. As we will see, this technique allows to parametrize in a simple analytical way the energy per nucleon obtained in the different *ab initio* or effective approaches, as well as interpolate continuously between them. By largely exploring the parameter space of this metamodel (or model of models), constraints coming from experimental measurements can be directly implemented. Indeed, nuclear experiments give us knowledge on the properties of nuclear matter around the saturation density of symmetric nuclear matter $n_{sat}$, which is roughly the density of laboratory nuclei. For instance, the isoscalar Giant Monopole Resonance energy is correlated with the empirical parameter $K_{sat}$, which corresponds to the compression modulus of SNM. The well-known nuclear EoS empirical parameters correspond in fact to the successive density derivatives of nuclear matter energy per particle of SNM and symmetry energy at saturation density, associated to the isoscalar ($E_{sat}$, $K_{sat}$, $Q_{sat}$, and $Z_{sat}$) and isovector channel ($E_{sym}$, $L_{sym}$, $K_{sym}$, $Q_{sym}$,

| Parameter | Unit | $N$ | SLy4 | BSk24 | BSk22 | DD-ME$\delta$ | Average | Uncertainty |
|---|---|---|---|---|---|---|---|---|
| $E_{sat}$ | MeV | 0 | -15.97 | -16.05 | -16.09 | -16.12 | -15.8 | 0.3 |
| $n_{sat}$ | fm$^{-3}$ | 1 | 0.1595 | 0.1578 | 0.1578 | 0.1520 | 0.155 | 0.005 |
| $K_{sat}$ | MeV | 2 | 230 | 246 | 246 | 219 | 230 | 20 |
| $Q_{sat}$ | MeV | 3 | -363 | -274.5 | -276 | -748 | 300 | 400 |
| $Z_{sat}$ | MeV | 4 | 1587 | 1184 | 1190 | 3950 | -500 | 1000 |
| $E_{sym}$ | MeV | 0 | 32.01 | 30.00 | 32.00 | 32.35 | 32 | 2 |
| $L_{sym}$ | MeV | 1 | 46.0 | 46.4 | 68.5 | 52.8 | 60 | 15 |
| $K_{sym}$ | MeV | 2 | -120 | -38 | 13 | -118 | -100 | 100 |
| $Q_{sym}$ | MeV | 3 | 521 | 711 | 563 | 846 | 0 | 400 |
| $Z_{sym}$ | MeV | 4 | -3197 | -4031 | -3174 | -3545 | -500 | 1000 |
| $m^*_{sat}/m$ | | | 0.69 | 0.80 | 0.80 | 0.69 | 0.75 | 0.1 |
| $\Delta m^*_{sat}/m$ | | | -0.19 | 0.20 | 0.20 | -0.17 | 0.1 | 0.1 |

**Table 1.3:** *Value of each of the empirical parameters, associated unit, and derivative order $N$ for SLy4 [Cha+98], BSk24, BSk22 [GCP13], and DD-ME$\delta$ [Roc+11] functionals. Average values and uncertainties extracted from experimental analysis are taken from [MHG18a].*

and $Z_{sym}$), respectively. The symmetry energy is generally defined as

$$e^{sym}_{HM}(n) = \frac{1}{2}\frac{\partial^2 e_{HM}(n,\delta)}{\partial \delta^2}\bigg|_{\delta=0}, \tag{1.32}$$

where $e_{HM}$ is the energy per nucleon in nuclear matter. In Table 1.3 are listed the value of each empirical parameter for the Skyrme-type SLy4 [Cha+98], BSk22, and BSk24 [GCP13], and relativistic DD-ME$\delta$ [Roc+11] functionals. Average values and associated uncertainties extracted from experimental analysis are also provided. It can be seen that the isovector parameters are in general less known than the isoscalar ones for the same derivative order. For instance, the relative uncertainty on $K_{sym}$ is about 100% while that of $K_{sat}$ is less than 10%. It should also be stressed that the high-order parameters $Q_{sat(sym)}$ and $Z_{sat(sym)}$ are poorly constrained by nuclear experiments.

The empirical parameters can be used in a Taylor expansion to estimate the nuclear matter EoS analytically up to $n \approx 2 - 3n_{sat}$ [MHG18a; MHG18b]. Limiting us to derivative order $N = 2$, we obtain

$$e^{N=2}_{HM}(n,\delta) = E_{sat} + \frac{1}{2}K_{sat}x^2 + \delta^2(E_{sym} + L_{sym}x + \frac{1}{2}K_{sym}x^2), \tag{1.33}$$

with $x = (n - n_{sat})/(3n_{sat})$ a function of the density. However, we should stress already that $N = 2$ is not sufficient for describing the EoS at subsaturation densities, and even less for suprasaturation densities. The high-order parameters $Q_{sat(sym)}$ and $Z_{sat(sym)}$ are essential and carry the largest uncertainty as far as the bulk part of the EoS is concerned.

In a mean field approach, we can treat nucleons as independent particles, thus the kinetic part of the energy per particle of nuclear matter is given by the same functional form as a nonrelativistic Fermi gas (FG), that is

$$t_{HM}^{FG}(n,\delta) = \frac{1}{2} t_{sat}^{FG}(1+3x)^{2/3}\left[(1+\delta)^{5/3}\frac{m}{m_n^*} + (1-\delta)^{5/3}\frac{m}{m_p^*}\right], \tag{1.34}$$

where $t_{sat}^{FG} = 3\hbar^2/(10m)(3\pi^2/2)^{2/3}n_{sat}^{2/3}$ is the kinetic energy of SNM at the saturation density, $m = (m_n + m_p)/2$ is the mean nucleon mass, and $m_n^*$ ($m_p^*$) is the neutron (proton) effective mass. The Landau effective mass is introduced in order to take into account the in-medium nuclear interaction that alters the mass of nucleons. It can be parametrized as ($q = n, p$)

$$\frac{m}{m_q^*} = \sum_{\alpha=0}^{1} m_{q,\alpha}(\delta)\frac{x^\alpha}{\alpha!} = 1 + (\kappa_{sat} + \tau_3\kappa_{sym}\delta)(1+3x), \tag{1.35}$$

with $\tau_3 = 1$ ($\tau_3 = -1$) for neutrons (protons). Two additional parameters $\kappa_{sat}$ and $\kappa_{sym}$, related to the effective mass $m_{sat}^*$ and isospin splitting $\Delta m_{sat}^*$ at saturation density, are then introduced. They are defined at $n = n_{sat}$ as

$$\kappa_{sat} = \frac{m}{m_{sat}^*} - 1, \tag{1.36}$$

$$\kappa_{sym} = \frac{1}{2}\left(\frac{m}{m_n^*} - \frac{m}{m_p^*}\right). \tag{1.37}$$

In principle, it is possible to reproduce any EoS model with a Taylor expansion, considering an infinite number of parameters, $N \to \infty$, however the convergence would be very slow. In order to fasten the series convergence, one can add extra functional dependencies, which correspond to the true EoS in the limit of simplistic cases, but which allow, by judicious choices of empirical parameters, to reproduce with precision realistic functionals. With this observation in mind, a $\delta^{5/3}$ dependence is added as in Eq. (1.33), by decomposing the energy per particle into a potential and kinetic part, yielding

$$e_{HM}^N(x,\delta) = t_{HM}^{FG}(n,\delta) + v_{MM}^N(n,\delta), \tag{1.38}$$

where $v_{MM}^N$ is the potential energy per particle expressed as a Taylor expansion in the parameter $x$ at $n = n_{sat}$,

$$v_{MM}^N(n,\delta) = \sum_{\alpha\geq 0}^{N}(v_\alpha^{is} + \delta^2 v_\alpha^{iv})\frac{x^\alpha}{\alpha!}. \tag{1.39}$$

The quadratic approximation for the isospin dependence of the potential energy has been made in Eq. (1.39), as suggested by microscopic calculations in [Vid+09]. The coefficients $v_\alpha^{is}$ and $v_\alpha^{iv}$ are mapped to the empirical parameters following

$$v_\alpha^{is} = \left.\frac{\partial^\alpha e_{HM}}{\partial x^\alpha}\right|_{n=n_{sat},\delta=0} \quad \text{and} \quad v_\alpha^{iv} = \left.\frac{\partial^\alpha e_{HM}^{sym}}{\partial x^\alpha}\right|_{n=n_{sat},\delta=0}, \tag{1.40}$$

yielding the isoscalar parameters:

$$\begin{aligned} v_0^{is} &= E_{sat} - t_{sat}^{FG}(1+\kappa_{sat}), && (1.41)\\ v_1^{is} &= -t_{sat}^{FG}(2+5\kappa_{sat}), && (1.42)\\ v_2^{is} &= K_{sat} - 2t_{sat}^{FG}(-1+5\kappa_{sat}), && (1.43)\\ v_3^{is} &= Q_{sat} - 2t_{sat}^{FG}(4-5\kappa_{sat}), && (1.44)\\ v_4^{is} &= Z_{sat} - 8t_{sat}^{FG}(-7+5\kappa_{sat}), && (1.45) \end{aligned}$$

and isovector parameters:

$$\begin{aligned} v_0^{iv} &= E_{sym} - \frac{5}{9}t_{sat}^{FG}[1+(\kappa_{sat}+3\kappa_{sym})], && (1.46)\\ v_1^{iv} &= L_{sym} - \frac{5}{9}t_{sat}^{FG}[2+5(\kappa_{sat}+3\kappa_{sym})], && (1.47)\\ v_2^{iv} &= K_{sym} - \frac{10}{9}t_{sat}^{FG}[-1+5(\kappa_{sat}+3\kappa_{sym})], && (1.48)\\ v_3^{iv} &= Q_{sym} - \frac{10}{9}t_{sat}^{FG}[4-5(\kappa_{sat}+3\kappa_{sym})], && (1.49)\\ v_4^{iv} &= Z_{sym} - \frac{40}{9}t_{sat}^{FG}[-7+5(\kappa_{sat}+3\kappa_{sym})], && (1.50) \end{aligned}$$

Let us notice from Eq. (1.39) that the energy per particle does not converge to zero at zero density. This artifact, arising from the nature of the series expansion, can be fixed by introducing an exponential correction $u_\alpha^N(x)$ in the potential energy,

$$v_{MM}^N(n,\delta) = \sum_{\alpha\geq 0}^{N}(v_\alpha^{is}+\delta^2 v_\alpha^{iv})\frac{x^\alpha}{\alpha!}u_\alpha^N(x), \tag{1.51}$$

the expression of which is

$$u_\alpha^N(x) = 1-(-3x)^{N+1-\alpha}\exp(-b(1+3x)), \tag{1.52}$$

where we have introduced an extra low-density parameter $b$. It was shown in [Ant+19] that for most applications this parameter can be fixed to a constant, $b = 10\ln(2)$.

Let us now turn to the derivatives of the energy. The expression of the symmetry energy, Eq. (1.32), reads

$$e_{HM}^{sym}(n) = \frac{5}{9}t_{sat}^{FG}(1+3x)^{2/3}\left[1+(\kappa_{sat}+3\kappa_{sym})(1+3x)\right] + \sum_{\alpha\geq 0}^{N} v_\alpha^{iv}\frac{x^\alpha}{\alpha!}u_\alpha^N(x). \tag{1.53}$$

For the chemical potential, we have

$$\mu_{HM,q}(n,\delta) = e_{HM}^N + \frac{1+3x}{3}\left(\frac{\partial e_{HM}^N}{\partial x}\right)_\delta + (\tau_3-\delta)\left(\frac{\partial e_{HM}^N}{\partial \delta}\right)_x + m_q c^2, \tag{1.54}$$

The complete analytical expression of $\mu_{HM,q}$ is given in Appendix B. Finally, the pressure can be calculated through

$$P_{HM} = \sum_{q=n,p} n_q(\mu_{HM,q}(n,\delta)-m_q c^2) - n e_{HM}^N(n,\delta). \tag{1.55}$$

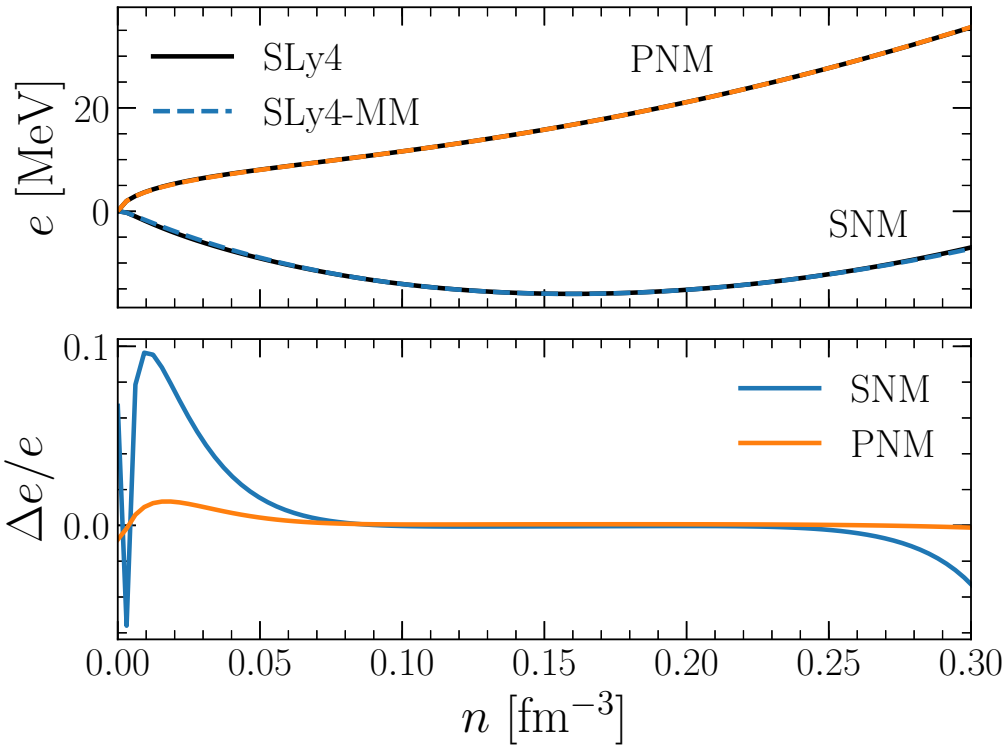



**Figure 1.4:** *Energy per nucleon as a function of density for symmetric nuclear matter, $\delta = 0$, and pure neutron matter, $\delta = 1$ (upper panel), and the associated relative error $\Delta e/e = (e_{MM} - e)/e$ (lower panel) for the SLy4 functional, with $N = 4$ for the metamodel. In the upper panel, black solid lines (dashed lines) correspond to the calculation with the exact functional (metamodel).*

There are two main advantages that come with the metamodeling technique. Firstly, It is flexible enough to reproduce the different existing energy functional of nuclear matter with very good accuracy up to $n \approx 2 - 3n_{sat}$, and even higher densities with a proper redefinition of the third and fourth order parameters [MHG18a]. Since very often the parameters of the model to be mimicked do not coincide with the empirical parameters, we derive the latter by calculating the derivatives of the energy per particle in nuclear matter at saturation density, following Eq. (1.40). In Fig. 1.4 is demonstrated the accuracy of the metamodeling technique for the SLy4 [Cha+98] functional with a Taylor expansion order $N = 4$. In the upper panel, the energy per nucleon is calculated using the metamodeling technique (dashed lines) and the exact functional (black solid lines). A tiny deviation is observed at low density for SNM, but overall a very good agreement is observed between the metamodel (labeled "SLy4-MM") and the exact functional (labeled "SLy4"). In the lower panel the relative error is represented for SNM and PNM. We can see that the error goes up to 10% for SNM at $n \approx 0.01$ fm$^{-3}$ and rapidly drops to 0% at $n \approx 0.07$ fm$^{-3}$. At $n \approx 2n_{sat}$, a deviation appears due the extrapolation far from the saturation point. The deviation at low density can be reduced by adjusting the parameter $b$ entering the low-density correction,

Eq. (1.52) [Ant+19]. However, this small deviation is not expected to cause any issue for the determination of the inner crust ground state. Indeed, the relative error for PNM is lower than 2% at most, and, in the inner crust, the matter inside nuclei is very neutron rich and the ambient nucleon gas is exclusively constituted of free neutrons. This ability of mimicking existing realistic functionals will allow us to easily compare predictions of astrophysical observables of different popular models. Another asset of the metamodeling technique is that no correlation is assumed *a priori* among the empirical parameters due to the nature of the series expansion. Therefore, all density dependences of the nuclear EoS can be explored. In addition, it allows us to vary each empirical parameter independently of the others to carry out complete statistical analysis using Bayesian inference.

#### 1.2.1.2 From homogeneous nuclear matter to finite nuclei in the CLD approximation

We now turn to the modeling of the energy of clusters present in the inner crust of cold neutron stars. We propose to extend the metamodeling of infinite nuclear matter to nuclei in order to take into account their surface properties, within the compressible liquid drop approximation, originally introduced in [BBP71]. This approach is expected to be less accurate than microscopic Hartree-Fock (HF) [NV73] or ETF [Ons+08] calculations since quantum effects are neglected, though it proved its quality in the past by giving surprisingly good results, see for example [BBP71; LS91; DH00; DH01]. In particular, it appears that most of the macroscopic observables related to neutron stars, such as masses and radii, are not very sensitive to the crust composition, thus a qualitative evaluation of it is sufficient in that case. The compressible liquid drop model (CLDM) comes with multiple advantages. It is very fast from the computational point of view since the energy does not require to be integrated all along the cell volume. For this reason, it is powerful for complete statistical analyses such as the one presented in the next chapter. It is also a model that is flexible, giving us the opportunity to account for different geometries for example, as we consider in 1.2.5. Last but not least, because of the artificial decomposition of the nuclear cluster as a bulk term, a surface term, and a Coulomb term, we are able to identify the contributions of the different terms. For all these reasons, the CLDM is considered as a suitable alternative to semiclassical ETF and microscopic HF treatments, that additionally does not suffer from technical complications such as the definition of boundary conditions [NS09].

In the CLD approximation, the energy of the cluster reads

$$E_{cl} = e_{HM}(n_0, I)A + E_{surf} + E_{Coul}, \tag{1.56}$$

where $E_{surf}$ represents the nuclear surface energy, and $E_{Coul}$ is the Coulomb energy, including the lattice correction and finite-size effects, written as follows in the WS approximation,

$$E_{Coul} = \frac{3}{5}\frac{e^2}{r_0^2}\eta_{Coul}(u)\frac{Z^2}{A^{1/3}} = \frac{3}{20}\frac{e^2}{r_0^2}\eta_{Coul}(u)A^{5/3}(1-I)^2, \tag{1.57}$$

with

$$\eta_{Coul}(u) = 1 - \frac{3}{2}u^{1/3} + \frac{1}{2}u, \tag{1.58}$$

a function of the volume fraction $u = n_e/n_{0,p}$, with $n_{0,p} = n_0(1-I)/2$ the average proton density inside cluster. Let us note that the factor $3/5 \times 3/2 = 9/10$ entering the lattice term can be replaced by the Mandelung constant for a body-centered cubic lattice, $C_M = 0.895929255682$ (see Table 2.4 of [HPY07]). The bulk term is taken from the metamodel, keeping the same empirical parameters as for the calculation of the neutron gas energy, thus insuring consistency between the crust and the core treatment. The bulk energy is evaluated at $n_0$, the average density inside the cluster, and $I$, its global asymmetry.

Let us now turn to the expression of the nuclear surface energy. Assuming that clusters are spherical, it is given by

$$E_{surf} = 4\pi r_0^2 A^{2/3}\sigma, \tag{1.59}$$

where $r_0 = (4\pi n_0/3)^{-1/3}$ is related to the cluster density $n_0$, and $\sigma$ is the nuclear surface tension. The simplest parametrization of the surface tension one could use is a constant, $\sigma \approx 1.03$ MeV/fm$^2$, as in the liquid drop model. However, clusters in the inner crust are expected to be very neutron rich and it appears evident that the surface tension of very asymmetric nuclei should be different to that of symmetric nuclei. In addition, it does not account for the interaction of the nuclear surface with the outside neutron gas, yielding $\sigma \to 0$ as $I \to 1$. This leads us to consider another parametrization for $\sigma$ which would depend on the asymmetry $I$ and consider the interaction with the gas. It should be mentioned that the exact value of $\sigma(I)$ is model dependent, and the uncertainty is particularly important for extreme isospin values encountered in the inner crust. Indeed, no experimental data exist on the surface energy of nuclei beyond the dripline, which is in-medium modified by the presence of the neutron gas [DHM00]. We use the expression originally proposed by Ravenhall *et al.* [RPL83] on the basis of TF calculations at extreme isospin ratios, and later employed in different works on neutron star crust and SN modeling within the CLD approximation [LS91; NGL12; LRP93]:

$$\sigma(I) = \sigma_0 \frac{2^{p+1} + b_s}{Y_p^{-p} + b_s + (1-Y_p)^{-p}}, \tag{1.60}$$

with $\boldsymbol{S} = \{\sigma_0, b_s, p\}$ the parameter space associated to the surface energy. The parameter $\sigma_0 = \sigma(I=0)$ represents the surface tension of symmetric nuclei, and $b_s$ and $p$ are the parameters that govern the isospin dependence of the surface tension. The proton fraction is related to the asymmetry inside the cluster via $Y_p = (1-I)/2$. Following [NGL12], we add a curvature term with the aim of having a better description of the nuclear surface and so of the composition of the inner crust in the ground state. For spherical clusters, the curvature energy reads

$$E_{curv} = 8\pi r_0 A^{1/3}\sigma_c, \tag{1.61}$$

where $\sigma_c$ is the curvature tension related to the surface tension $\sigma$, Eq. (1.60),

$$\sigma_c = \sigma \frac{\sigma_{0,c}}{\sigma_0}\alpha(\beta - Y_p), \tag{1.62}$$

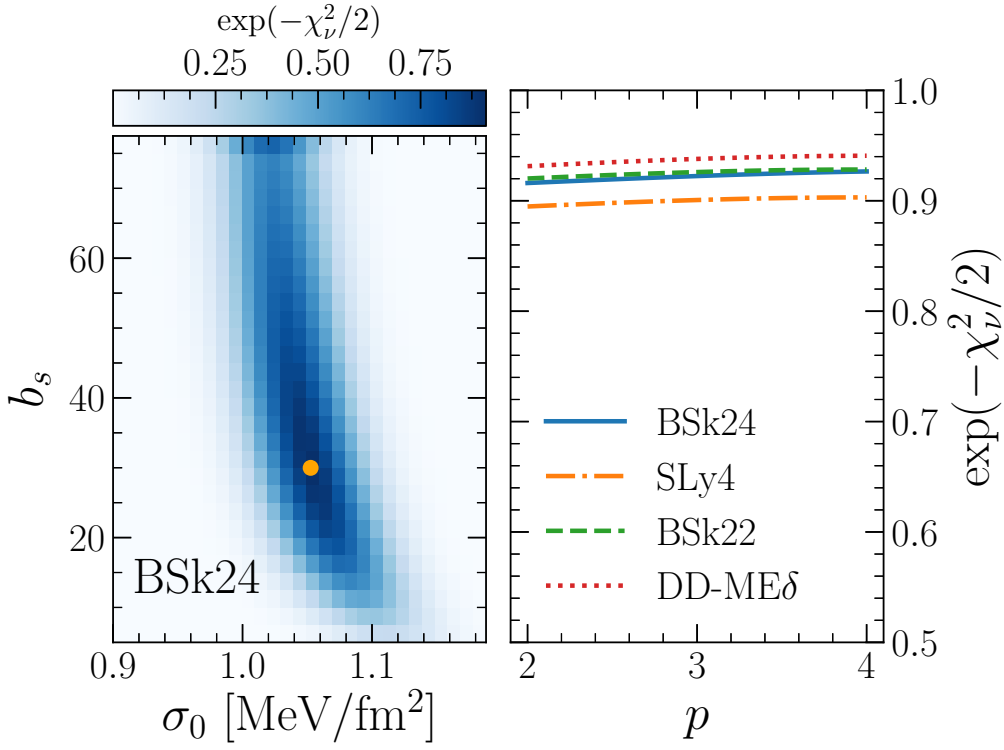



**Figure 1.5:** *Left: Goodness of fit (color scale) as described by the reduced $\chi^2$, in the space of the surface parameters $(\sigma_0, b_s)$ for the BSk24 CLDM with fixed value of the $p$ parameter, $p = 3$, for optimized curvature parameters $\sigma_{0c}$ and $\beta$. The orange point indicates the optimal value. Right: Weight $\exp(-\chi^2_\nu/2)$ as a function of the parameter $p$, calculated for the optimal value of $(\sigma_0, b_s, \sigma_{0c}, \beta)$, for the selected CLDM: BSk24, SLy4, BSk22, and DD-ME$\delta$.*

with $\alpha = 5.5$ as in [NGL12]. With the addition of the curvature energy comes two parameters added as extra dimensions to the surface parameter space, $\boldsymbol{S} = \{\sigma_0, b_s, \sigma_{0,c}, \beta, p\}$. For a given model of uniform matter, that is each given set of empirical parameters, the first four parameters can be fitted to experimental masses from the AME2016 [Hua+17] for a fixed value of the parameter $p$. The quality of reproduction of the experimental nuclear binding energy $E_{\mathrm{AME2016}}$ is measured by the reduced $\chi^2$, defined as

$$\chi^2_\nu = \frac{\chi^2}{\nu} = \frac{1}{\nu}\sum_i \left( \frac{E^{(i)}_{cl}/A^{(i)} - E^{(i)}_{\mathrm{AME2016}}/A^{(i)}}{\sigma^{(i)}} \right)^2 , \tag{1.63}$$

where $\nu$ is the number of degrees of freedom, and the denominator corresponds to the systematic theoretical error, 0.1 MeV/$A$, such as to have $\chi^2_{min} \approx 1$ over the parameter space sample [DNR14]. This point can be clearly understood by inspection of the left panel of Fig. 1.5, which shows the value of the weight function $\exp(-\chi^2_\nu/2)$, that is the goodness of fit, in the $(\sigma_0, b_s)$ plane, for the BSk24 CLDM with $p = 3$, and curvature

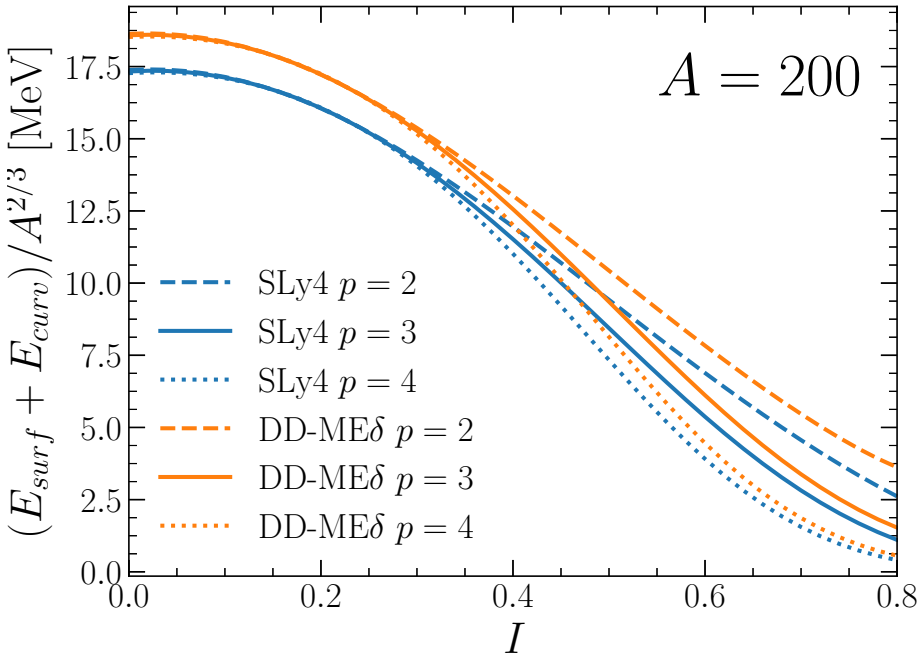



**Figure 1.6:** *Variation with cluster asymmetry $I$ of surface plus curvature energy per surface nucleon along the isobaric chain $A = 200$ for SLy4 [Cha+98] and DD-ME$\delta$ [Roc+11] CLDM at three selected values of parameter $p$: $p = 2$ (dashed lines), $p = 3$ (solid lines), and $p = 4$ (dotted lines).*

parameters already adjusted to experimental data. It is seen that the weight function is strongly peaked to the orange point, which indicates the optimal value for the parameters $\sigma_0$ and $b_s$. Conversely, we observe in the right panel of Fig. 1.5 that the error estimator $\chi^2_\nu$ is insensitive to the choice of the parameter $p$ in a range going from 2 to 4, for four representative functionals. This is understood from the fact that $p$ modifies the asymmetry dependence of the surface energy only for extreme values of $I$ where nuclear data are not available. This parameter is therefore not adjusted as the other parameters, in order to avoid poor extrapolations of $\sigma$. The value of $p$ is selected around $p = 3$, which is the value used in the popular Lattimer and Swesty EoS [LS91]. We show in Fig. 1.6 the surface plus curvature energy per surface nucleon as a function of the asymmetry inside the cluster for two popular models, SLy4 [Cha+98] and DD-ME$\delta$ [Roc+11], in the CLD approximation. Different values for the parameter $p$ are displayed in that figure. It is seen that $p$ determines the behavior of the surface tension for extreme isospin values, and cannot be accessed from experimental nuclear physics data. In addition, since the selected popular models contain parameters that are adjusted to the same data, we cannot consider their predictions (as for instance can be obtained by an ETF calculation in slab or spherical geometry in the WS cell) at high isospin as reliable. For these reasons, we will keep $p$ as a free parameter. In particular, from $I \approx 0.3$, we observe that a larger value of $p$ leads to larger surface energy at fixed asymmetry. The model dependence of the surface tension is also observed in that figure

and is particularly highlighted at low asymmetry where experimental measurements can still be performed.

Finally, we recall the final expression for the cluster binding energy in the CLD approximation,

$$\begin{aligned} E_{cl}(A, I, n_0, n_e) = \quad & e_{HM}(n_0, I)A \\ & +4\pi r_0^2 A^{2/3}\sigma(I) + 8\pi r_0 A^{1/3}\sigma_c(I) \\ & +\frac{3}{20}\frac{e^2}{{r_0}^2}\eta_{Coul}(I, n_0, n_e)A^{5/3}(1-I)^2. \end{aligned} \tag{1.64}$$

Let us notice that the energy does not depend on the neutron gas density via the surface term, as in [BBP71]. This dependence is in fact implicitly accounted for in the chosen parametrization of the surface tension, suggested from microscopic calculations in the WS cell [RPL83].

### 1.2.2 Variational formalism

The variational method for the calculation of the inner crust ground state with the CLDM was introduced in the pioneering work of BBP in their classical paper [BBP71]. Since then, huge progress has been made in constraining the NN effective interaction. For this reason, subsequent works using the same formalism with CLDM based on more realistic nuclear functionals followed. For instance we can mention the popular calculations of Douchin and Haensel (DH) [DH00; DHM00] with the SLy4 effective force [Cha+98]. Following those works, we use the same variational method as BBP, and we present it in the following.

Using the method of Lagrange multipliers, the ground state of the inner crust is obtained by minimizing the zero-temperature free energy density of the WS cell at fixed baryon density $n_B$ under the condition of charge neutrality, $n_e = n_p$. The minimization is carried out with respect to the set of variables $A$, $I$, $n_0$, $n_p$, and $n_g$. Let us notice that, in principle, one should minimize the Gibbs free energy at constant pressure, as for the outer crust. However, it would be very heavy from the computational point of view to do so in the regime of the inner crust, where nuclei are immersed in a gas of dripped neutrons. Fortunately, it is demonstrated that the error introduced by minimizing at constant baryon density instead of pressure is negligible [Pea+12]. The auxiliary function to be minimized is defined as

$$\begin{aligned} \mathcal{L}(A, I, n_0, n_p, n_g) &= \frac{E_{WS}}{V_{WS}} - \mu n_B \\ &= \frac{E_{cl}}{V_{WS}} + \varepsilon_e + \left(1 - \frac{A}{n_0 V_{WS}}\right)\varepsilon_g \\ &\quad +n_p \Delta m_{pn} c^2 - n_B(\mu - m_n c^2), \end{aligned} \tag{1.65}$$

with $\Delta m_{pn} = m_p - m_n$ the difference between the proton and neutron mass, and $\mu$ the Lagrange multiplier. The volume of the cell can be calculated as

$$V_{WS} = \frac{Z}{n_p} = \frac{A}{n_p}\frac{1-I}{2}, \tag{1.66}$$

and the baryon density is given by

$$\begin{aligned} n_B &= \frac{A_{WS}}{V_{WS}} \\ &= \frac{2n_p}{1-I}\left(1-\frac{n_g}{n_0}\right)+n_g. \end{aligned} \tag{1.67}$$

Replacing these quantities in Eq. (1.65), it results

$$\begin{aligned} \mathcal{L}(A,I,n_0,n_p,n_g) &= \frac{2n_p}{A(1-I)}E_{cl}+\varepsilon_e+\left(1-\frac{2n_p}{n_0(1-I)}\right)\varepsilon_g+n_p\Delta m_{pn}c^2 \\ &\quad -\frac{2n_p}{1-I}\left(1-\frac{n_g}{n_0}\right)(\mu-m_nc^2)-n_g(\mu-m_nc^2). \end{aligned} \tag{1.68}$$

Let us first minimize with respect to $A$:

$$\begin{aligned} \left.\frac{\partial\mathcal{L}}{\partial A}\right|_{I,n_0,n_p,n_g} &= 0 \\ \frac{2n_p}{A(1-I)}\frac{\partial E_{cl}}{\partial A}-\frac{2n_p}{A^2(1-I)}E_{cl} &= 0 \\ \frac{\partial E_{cl}}{\partial A}-\frac{E_{cl}}{A} &= 0, \end{aligned} \tag{1.69}$$

which is equivalent to

$$\frac{\partial(E_{cl}/A)}{\partial A}=0. \tag{1.70}$$

We can go trough this equation using the definition of the cluster energy, Eq. (1.64), yielding

$$\begin{aligned} -\frac{1}{3}\times 4\pi r_0^2\sigma A^{-4/3}-\frac{2}{3}\times 8\pi r_0\sigma_c A^{-5/3}+\frac{2}{3}\times\frac{3}{20}\frac{e^2}{r_0}\eta_{Coul}A^{-1/3}(1-I)^2 &= 0 \\ 4\pi r_0^2\sigma A^{2/3}+2\times 8\pi r_0\sigma_c A^{1/3}-2\times\frac{3}{20}\frac{e^2}{r_0}\eta_{Coul}A^{5/3}(1-I)^2 &= 0, \end{aligned}$$

or simply,

$$E_{surf}+2E_{curv}=2E_{Coul}. \tag{1.71}$$

This equation corresponds to the well-known Baym virial theorem with an additional curvature term with respect to the equation originally found in [BBP71]. It is interesting to notice that only the surface, the curvature, and the Coulomb energy are involved in this first equilibrium condition.

Minimizing with respect to the neutron gas density $n_g$, one obtains:

$$\begin{aligned} \left.\frac{\partial\mathcal{L}}{\partial n_g}\right|_{A,I,n_0,n_p} &= 0 \\ \left(1-\frac{2n_p}{n_0(1-I)}\right)\frac{\partial\varepsilon_g}{\partial n_g}+\frac{2n_p}{n_0(1-I)}(\mu-m_nc^2)-(\mu-m_nc^2) &= 0, \end{aligned} \tag{1.72}$$

giving us the expression of the Lagrange multiplier, which can be identified with the chemical potential of the gas, including the rest mass energy,

$$\mu = \frac{\partial \varepsilon_g}{\partial n_g} + m_n c^2 \equiv \mu_g. \tag{1.73}$$

We now turn to the minimization with respect to average cluster density $n_0$:

$$\begin{aligned} \left.\frac{\partial \mathcal{L}}{\partial n_0}\right|_{A,I,n_p,n_g} &= 0 \\ \frac{2n_p}{A(1-I)}\frac{\partial E_{cl}}{\partial n_0} + \frac{2n_p}{n_0^2(1-I)}\varepsilon_g - \frac{2n_p n_g}{n_0^2(1-I)}(\mu - m_n c^2) &= 0 \\ \frac{n_0^2}{A}\frac{\partial E_{cl}}{\partial n_0} - n_g(\mu - m_n c^2) + \varepsilon_g &= 0. \end{aligned} \tag{1.74}$$

Using well-known thermodynamical relations, we define $P_{cl} \equiv (n_0^2/A)(\partial E_{cl}/\partial n_0)$, and $P_g = n_g(\mu_g - m_n c^2) - \varepsilon_g$. Therefore, Eq. (1.74) simply results in

$$P_{cl} = P_g, \tag{1.75}$$

which can be interpreted as a pressure equilibrium condition between the cluster and the outside neutron gas. We can derive the expression of the cluster pressure from the CLD energy, Eq. (1.64), yielding

$$P_{cl} = P_{HM}(n_0, I) - \frac{2}{3}n_0\frac{E_{surf}}{A} - \frac{1}{3}n_0\frac{E_{curv}}{A} + n_0\frac{E_{coul}(u=0)}{A}\left(\frac{2}{3} + \frac{1}{2}u^{1/3} - \frac{1}{2}u\right). \tag{1.76}$$

The minimization with respect to the global asymmetry inside the cluster $I$ yields

$$\begin{aligned} \left.\frac{\partial \mathcal{L}}{\partial I}\right|_{A,n_0,n_p,n_g} &= 0 \\ \frac{2n_p}{(1-I)^2}\left(\frac{E_{cl}}{A} + \frac{1-I}{A}\frac{\partial E_{cl}}{\partial I} - \frac{\varepsilon_g}{n_0} - \left(1 - \frac{n_g}{n_0}\right)(\mu - m_n c^2)\right) &= 0 \\ \frac{E_{cl}}{A} + \frac{1-I}{A}\frac{\partial E_{cl}}{\partial I} - \frac{\varepsilon_g}{n_0} - \left(1 - \frac{n_g}{n_0}\right)(\mu - m_n c^2) &= 0, \end{aligned} \tag{1.77}$$

resulting in

$$\frac{E_{cl}}{A} + \frac{1-I}{A}\frac{\partial E_{cl}}{\partial I} + \frac{P_g}{n_0} = \mu - m_n c^2. \tag{1.78}$$

Due to the presence of the outside neutron gas, the neutron chemical potential of the cluster is modified with respect to the usual expression in the vacuum $\mu_n^{vac} = \partial E_{cl}/\partial N$. We define the neutron and proton chemical potential of the cluster as

$$\mu_p^{cl} = \left.\frac{\partial E_{cl}}{\partial Z}\right|_N + m_p c^2 \quad \text{and} \quad \mu_n^{cl} = \left.\frac{\partial E_{cl}}{\partial N}\right|_Z + \frac{P_g}{n_0} + m_n c^2, \tag{1.79}$$

where the derivatives are taken at constant $n_0$, $n_p$, and $n_g$. Consequently, we can work out Eq. (1.78) to find a chemical equilibrium condition between the neutrons of the cluster and those of the gas,

$$\mu_n^{cl} = \mu_g. \tag{1.80}$$

Finally, we minimize the auxiliary function, Eq. (1.65) with respect to the proton density $n_p$ inside the WS cell,

$$\begin{aligned} \left.\frac{\partial \mathcal{L}}{\partial n_p}\right|_{A,I,n_0,n_g} &= 0 \\ \frac{E_{cl}}{A} + \frac{n_p}{A}\frac{\partial E_{cl}}{\partial n_p} + \frac{1-I}{2}\left(\frac{\partial \varepsilon_e}{\partial n_p} + \Delta m_{pn}c^2\right) - \frac{\varepsilon_g}{n_0} - \left(1 - \frac{n_g}{n_0}\right)(\mu - m_n c^2) &= 0. \end{aligned} \tag{1.81}$$

By identifying common terms with Eq. (1.77), we recover the well-known beta equilibrium condition,

$$\frac{2}{A}\left(\frac{\partial E_{cl}}{\partial I} - \frac{n_p}{1-I}\frac{\partial E_{cl}}{\partial n_p}\right) - \Delta m_{pn}c^2 = \frac{\partial \varepsilon_e}{\partial n_p}, \tag{1.82}$$

or in terms of chemical potentials,

$$\mu_n^{cl} = \mu_p^{cl} + \mu_e + \Delta\mu, \tag{1.83}$$

where $\Delta\mu$ represents the modification due to the excluded-volume interaction with the neutron gas, and the electrostatic interaction between protons in the cluster and the background electrons. It is given by

$$\Delta\mu = \frac{P_g}{n_0} + \frac{2}{A(1-I)} n_p \frac{\partial E_{Coul}}{\partial n_p}. \tag{1.84}$$

One can remark that only the Coulomb energy enters in the derivative with respect to the proton density $n_p$. This derivative can be evaluated analytically from Eq. (1.57) as

$$\frac{\partial E_{Coul}}{\partial n_p} = \frac{3}{20}\frac{e^2}{r_0^2} A^{5/3}(1-I)\frac{1}{n_0}\left(1 - \left(\frac{2n_p}{n_0(1-I)}\right)^{-2/3}\right). \tag{1.85}$$

Finally, a possible set of mechanical and chemical equilibrium equations is

$$\frac{\partial (E_{cl}/A)}{\partial A} = 0, \tag{1.86}$$

$$\frac{n_0^2}{A}\frac{\partial E_{cl}}{\partial n_0} = P_g(n_g), \tag{1.87}$$

$$\frac{E_{cl}}{A} + \frac{1-I}{A}\frac{\partial E_{cl}}{\partial I} + \frac{P_g(n_g)}{n_0} = \mu_g(n_g) - m_n c^2, \tag{1.88}$$

$$\frac{2}{A}\left(\frac{\partial E_{cl}}{\partial I} - \frac{n_p}{1-I}\frac{\partial E_{cl}}{\partial n_p}\right) - \Delta m_{pn}c^2 = \mu_e(n_p), \tag{1.89}$$

or, equivalently Eqs. (1.71), (1.75), (1.80), and (1.83), respectively. This system of four coupled differential equations can be solved numerically, as explained in 1.2.3.1, in order to obtain the equilibrium composition and so the EoS in the free neutron regime. Let us mention that taking alternatives set of variables leads to the same equilibrium equations [HPY07; Viñ+17].

### 1.2.3 Results

We now turn to the results of the minimization. The building of the numerical code is presented first and the numerical results, such as the ground-state composition and EoS of the inner crust, afterwards. Some of the results presented in the following have been published in [CGM19a; CGM19b; Car+20].

#### 1.2.3.1 Numerical code

During the thesis, an open-source C library, NSEoS, has been built in relation to the physics of NS [Car17a]. Here we focus on the numerical methods used to solve the inner crust equilibrium equations in order to estimate the composition and EoS in the free neutron regime. Those methods can be found in the module `crust` of the library.

The ground state of the inner crust at baryon density $n_B$ is determined by solving numerically the system of four coupled differential equations, Eqs. (1.86), (1.87), (1.88), and (1.89). To do so, we use a root-finding algorithm, Broyden's method [Bro65], which is similar to the popular Newton's method. In Broyden's method, the 16 partial derivatives entering the 4×4 Jacobian matrix are replaced with finite differences. While the derivatives can be evaluated analytically from the CLD expressions with ease, using finite differences makes it easier to identify the effect of the different contributions entering the WS cell energy. This point will be covered in greater detail in Chapter 3. The Jacobian matrix is not computed at each iteration but is only evaluated at the first iteration then simply rank-one updated. In order to avoid an unreliable estimation of the equilibrium composition $\{A_{eq}, I_{eq}, n_{0,eq}, n_{p,eq}, n_{g,eq}\}$ due to the accumulation of errors, the maximum number of iterations is fixed to $N_{iter}^{max} = 1000$. In addition, the backstepping technique is employed to avoid nonphysical solutions, such as negative values for $A$ or $|I| > 1$, that could result in errors when reinjected in the equilibrium equations. For instance, if at a given iteration, a spurious value of $A$ is obtained, then we replace it by the previous value $A_{old}$ plus a smaller step $\Delta A' < \Delta A$, until we get a physical value. Finally, let us mention that as for Newton's method, Broyden's method requires an initial guess for the composition.

We proceed as follows. The calculation starts at the neutron drip density $n_{ND}$. A natural choice for the initial guess is to take the last solution for the ground state of the outer crust, with reasonable values $A_{guess} = 36$, $I_{guess} = 0.3$, $n_{0,guess} = 0.15$ fm$^{-3}$, and $n_{g,guess} = 10^{-6}$ fm$^{-3}$. Then, the proton density is calculated as

$$n_{p,guess} = (n_B - n_{g,guess}) \left(1 - \frac{n_{g,guess}}{n_{0,guess}}\right) \frac{1 - I_{guess}}{2}. \tag{1.90}$$

To continue, we make use of Broyden's method described previously to evaluate the equilibrium composition $A_{eq}$, $I_{eq}$, $n_{0,eq}$, and $n_{g,eq}$. The process is then repeated with $n_B$ increasing in steps of $\Delta n_B = 10^{-4}$ fm$^{-3}$. At each new value of $n_B$, the guess is updated to coincide with the last equilibrium composition, ensuring faster convergence of the algorithm. At a reasonable value of baryon density, $n_B = 10^{-3}$ fm$^{-3}$, we start to check whether it is beneficial or not to have a phase transition from clusterized matter to homogeneous matter. The calculation is stopped once the crust-core (CC) interface

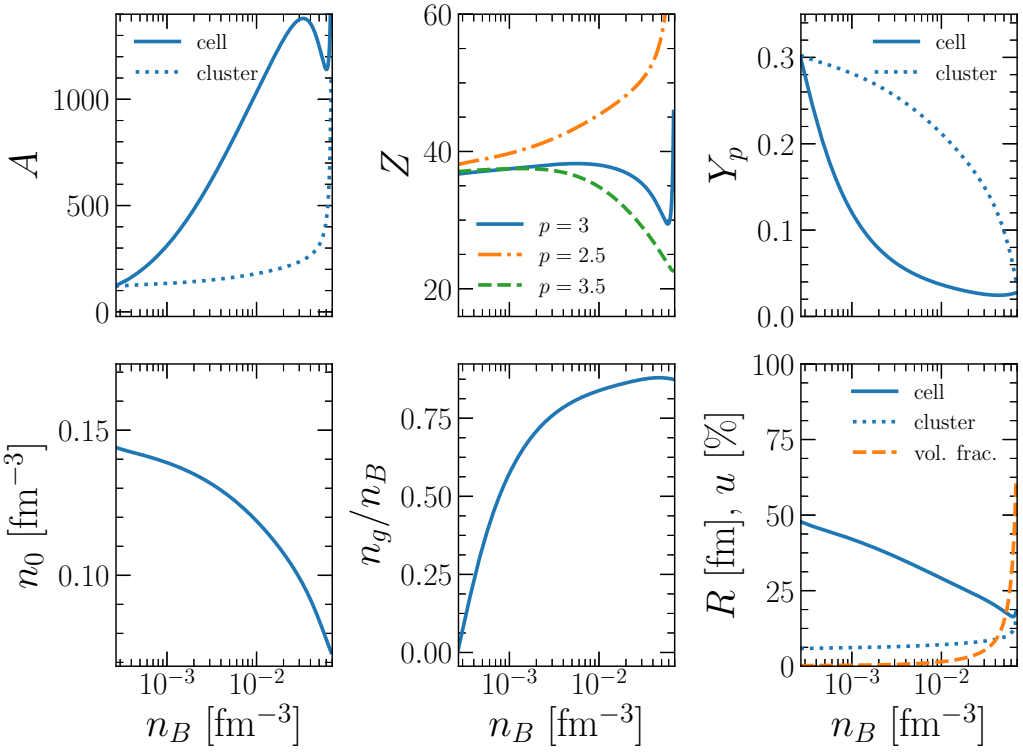



**Figure 1.7:** *Variation with baryon density $n_B$ of the equilibrium value of mass number $A$, atomic number $Z$, proton fraction $Y_p$, average cluster density $n_0$, neutron gas density to baryon density ratio $n_g/n_B$, radius $R$, and volume fraction $u$ in the inner crust, for BSk24 CLDM with $p = 3$. Solid (dotted) lines correspond to the results for the cell (cluster). In the upper-mid panel, three values of the parameter $p$ are selected: $p = 2.5$, $p = 3$, and $p = 3.5$.*

is reached, approximately for $n_B \approx n_{sat}/2$. The CC transition from the crust side is discussed in detail in 1.2.6.

#### 1.2.3.2 Equilibrium composition

Fig. 1.7 shows the evolution with baryon density $n_B$ of the equilibrium composition of the inner crust. The empirical parameters entering the bulk part of the CLDM energy correspond to the BSk24 effective force [GCP13], and the surface parameter $p$ is fixed to the value $p = 3$, which appears to be a reasonable value for Skyrme-type functionals, as we will discuss in 1.2.6.

It is found that the number of nucleons inside the cluster $A$ as well as inside the WS cell $A_{WS}$ monotonously increases with increasing density, going up to $\approx 700$ and $\approx 1500$, respectively, at high density. The number of free neutrons $N_g = A_{WS} - A$ can also be inferred. It is obviously equal to zero at the neutron drip density, since $A = A_{WS}$. The behavior of $A$ and $A_{WS}$ is in agreement with other CLD calculations, such as the one of BBP [BBP71] and that of DH [DH00]. The later study reports a

value of $A \approx 600$ at the CC interface, using the SLy4 functional, while BBP report a much higher value of $A = 7840$ (see their Table 1). Let us notice that the presence of such heavy spherical nuclei at the crust bottom raises the question of stability with respect to deformation and fission, as explained in [DH00]. In particular, nuclear fission, the approximate condition for which is $R_p/R_{WS} \gtrsim 1/2$ [BW39; PR95], $R_p$ being the proton radius, could occur at high density. In 1.2.5, we show that considering nonspherical geometries can stabilize the large clusters. It is important to stress that the composition, in particular $A$ and $Z$, is very sensitive to the isospin dependence of the surface tension at extreme isospin ratios.

The variation with baryon density of the equilibrium value of $Z$ is also represented in Fig. 1.7. We find $Z \approx 40$ all along the inner crust with $p = 3$, which is in a surprisingly good agreement with microscopic results. In particular, in the early work of Negele and Vautherin (NV) [NV73] is derived a set of nonlinear equations for the single particle wave functions of nucleons, using the density-matrix expansion for a realistic NN interaction. NV observed a predominance of $Z = 40$ at low density, and $Z = 50$ at high density. Subsequent works within the semiclassical ETF [Gor+05] and finite-temperature extended Thomas-Fermi plus Strutinsky integral (TETFSI) [Ons+08; Pea+18], as well as recent calculations using Gogny D1M* [Mon+20] also predict $Z = 40$ in the inner crust. As far as CLD calculations are concerned, DH find that the equilibrium value of $Z$ is almost constant in the vicinity of $\approx 40$ throughout the inner crust, whereas BBP find monotonically increasing values of $Z$. Once again, it should be stressed that $Z$ is very sensitive to the isospin dependence of the surface tension. In particular, it is observed by varying the parameter $p$ that governs the behavior of the surface tension at extreme isospin values. We can see that a lower surface tension, $p = 3.5$, favors smaller atomic number $Z$, and in general lighter clusters, unlike $p = 2.5$ that leads to heavier clusters. It is interesting to note that the influence of $p$ on the proton number is similar to that of the slope of the symmetry energy $L_{sym}$. In [OI07], it was shown that the charge number is larger for the EoS having smaller $L_{sym}$ (see their Fig. 3).

As in the outer crust, we find that the proton fraction inside the cell $Y_p$ continuously decreases in the free neutron regime, dropping from $\approx 0.3$ at the neutron drip point to $\approx 0.03$ at the edge of the crust. With increasing density, clusters also become more and more asymmetric, $I$ going up to $\approx 0.85$ in the bottom layers.

Clusters are found to be more and more dilute with increasing baryon density. At the neutron drip density, we get $n_0 \approx 0.145$ fm$^{-3}$, which is close to the saturation density of SNM of the BSk24 functional, $n_{sat} = 0.1578$ fm$^{-3}$. At the CC interface, the cluster density is as low as $n_0 \approx 0.07$ fm$^{-3}$, which is comparable to the neutron gas density, represented is the lower-mid panel. It is seen that the ratio $n_g/n_B$ rapidly reaches $\approx 75\%$ at $n_B = 2 \times 10^{-3}$ fm$^{-3}$ then stays approximately constant at higher densities.

The equilibrium radius of the spherical WS cell $R_{WS}$ and of the spherical cluster $R_{cl}$ are also displayed in Fig. 1.7. As DH, we observe that $R_{WS}$ monotonically decreases unlike $R_{cl}$ that slowly increases with increasing depth. Therefore, nuclei become closer and closer, eventually becoming close enough to touch each other at some point, creating a very large cluster, ultimately leading to homogeneous matter. We can also

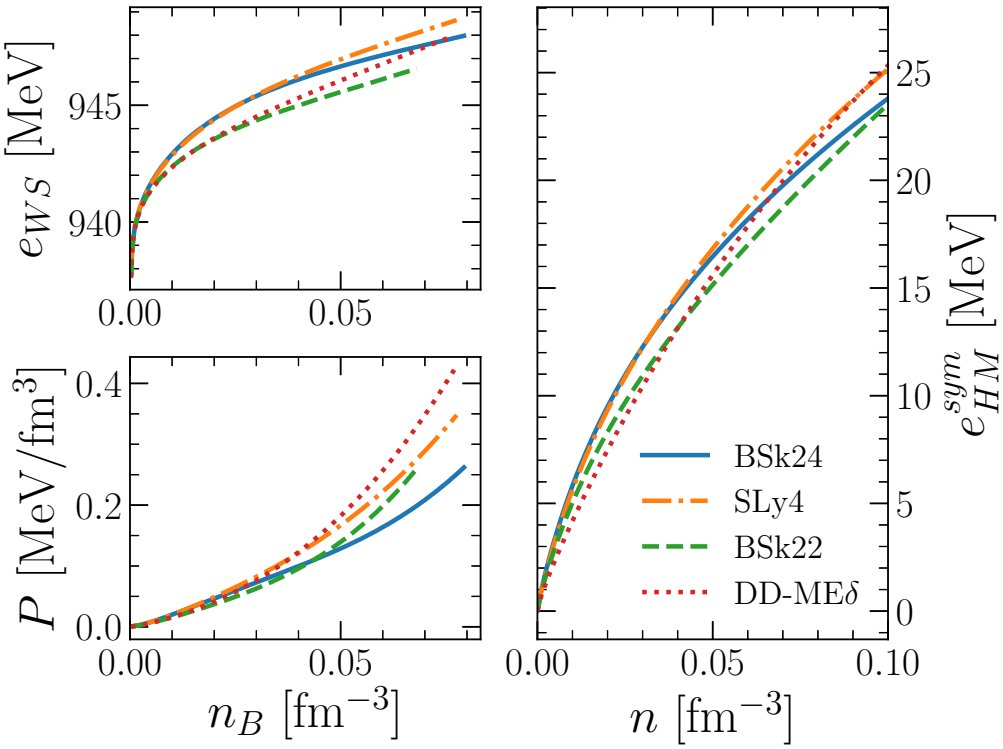



**Figure 1.8:** *Left: Equilibrium value of the energy per nucleon of the WS cell $e_{WS} = E_{WS}/A_{WS}$ (upper panel), and pressure $P$ (lower panel) as a function of the baryon density $n_B$ in the inner crust for four selected CLDM: BSk24, SLy4, BSk26, and DD-ME$\delta$. Right: Variation of symmetry energy $e^{sym}_{HM}$, Eq. (1.53), with density $n$, for the four models.*

understand this by calculating the volume fraction $u = (R_{cl}/R_{WS})^3 = 2n_p/(n_0(1-I))$ (orange dashed line). We find that the cluster fills up to 60% of the WS cell volume at the CC interface. This feature combined with the virial theorem, Eq. (1.71), outlines the fact that lattice and finite-size contributions to the Coulomb energy are crucial for the determination of the ground state of the inner crust.

#### 1.2.3.3 Equation of state

In Fig. 1.8, the equilibrium energy per nucleon of the WS cell $e_{WS} = E_{WS}/A_{WS}$ is plotted as a function of the baryon density $n_B$ for different CLDM, based on the relativistic model DD-ME$\delta$, and on three Skyrme-type interactions: SLy4, BSk22, and BSk24. It is observed that $e_{WS}$ depends on the nuclear model. In particular, it is known to be correlated with the symmetry energy, with higher symmetry leading to higher $e_{WS}$, at subnuclear densities [Pea+18]. This trend can be verified by looking at the right panel of the figure, that shows the symmetry energy, Eq. (1.53), as a function of density for the four models considered here.

Fig. 1.8 also shows the variation with the baryon density of pressure $P$, commonly

referred to as the EoS, in the inner crust. The total pressure, defined by the first law of thermodynamics as

$$P = n_B^2 \frac{de_{WS}}{dn_B}, \tag{1.91}$$

can be expressed as [BBP71]

$$P = P_g + P_e + P_L, \tag{1.92}$$

at the equilibrium composition, where $P_L$ is the lattice contribution to the total pressure. Using Eq. (1.92) rather than finite differences to estimate the derivative, Eq. (1.91), is more reliable and has the advantage to be faster from the computational point of view. In addition, it allows identifying the different contributions to the pressure. In the inner crust, the pressure is no longer dominated by the relativistic electron gas but by the ambient neutron gas [Car17b]. At subnuclear densities, we observe that the EoS is also correlated with the symmetry energy. In particular, the higher the empirical parameter $E_{sym}$, which is the symmetry energy at $n_{sat}$, the stiffer is the EoS. The value of $E_{sym}$ for each model is reported in Table 1.3.

### 1.2.4 Strutinsky shell corrections to the CLD energy

In the CLD approximation, shell effects, which are known since the pioneering work of BPS [BPS71] to be essential to correctly evaluate the outer-crust composition at zero temperature, are lost. In this same limit, microscopic calculations have shown that the neutron shell effects become vanishingly small beyond the neutron drip point [Cha06; Cha+07], but proton shell effects persist in the inner crust.

There are different ways to include shell corrections to the CLD energy. The simplest approach is to use an empirical formula, such as the one proposed by Myers and Swiatecki [MS66] which is accurate for reproducing masses of laboratory nuclei. However, a limitation of their method is that it requires *a priori* a list of magic numbers, which are obviously not known in the regime of the inner crust. Let us recall that NV found a persistence of $Z = 40$ while it is not considered as a magic number in ordinary nuclei. A more suitable alternative is to calculate shell corrections using the Strutinsky method [Ons+08]. Fortunately, Strutinsky shell corrections were calculated for modern BSk functionals, and are tabulated in [Pea+18] (see Supplementary data). We therefore add these corrections on top of the CLD energy for the corresponding models.

We now turn to the numerical method, proceeding as follows. The energy density is the quantity to be minimized at constant baryon density for a fixed number of protons inside the WS cell. We derive the system of equilibrium equations using the method of Lagrange multipliers, as in 1.2.2, yielding

$$\frac{\partial E_{cl}}{\partial A} - \frac{E_{cl}}{A} = \frac{1-I}{2}\left(\mu_e(n_p) + \frac{2np}{A(1-I)}\frac{\partial E_{cl}}{\partial n_p} - \frac{2}{A}\frac{\partial E_{cl}}{\partial I} + \Delta m_{pn}c^2\right), \tag{1.93}$$

$$\frac{\partial E_{cl}}{\partial A} + \frac{1-I}{A}\frac{\partial E_{cl}}{\partial I} + \frac{P_g(n_g)}{n_0} = \mu_g(n_g) - m_n c^2, \tag{1.94}$$

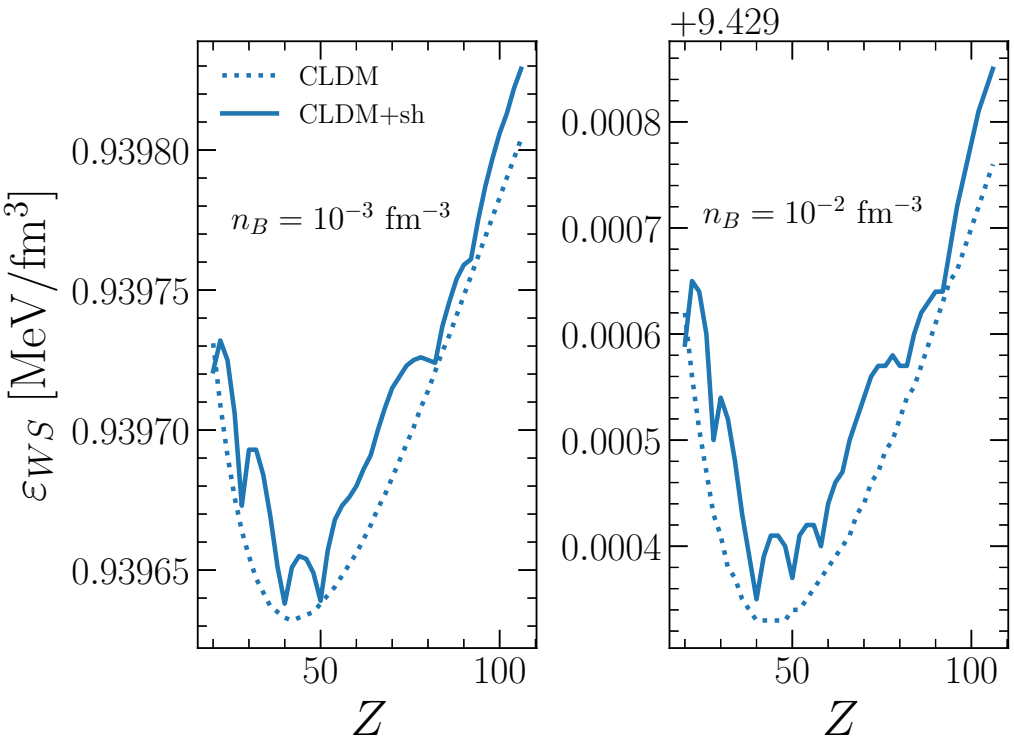



**Figure 1.9:** *WS cell energy density as a function of number of protons $Z$ at two different densities in the inner crust for BSk24 CLDM with (solid lines) and without (dotted lines) Strutinsky shell corrections on top of the CLD energy. In the right panel, the constant value* 9.429 MeV fm$^{-3}$ *is subtracted from the WS cell energy density.*

$$\frac{n_0^2}{A}\frac{\partial E_{cl}}{\partial n_0} = P_g(n_g). \tag{1.95}$$

Let us notice that beta equilibrium is not imposed anymore since $Z$ is fixed, causing a modification of Eq. (1.93) with respect to the virial theorem with curvature term, Eq. (1.86). For a given $n_B$, the minimization is carried out for each tabulated $Z$ using Broyden's method. The proton Strutinsky shell corrections are then added perturbatively to the CLD energy by interpolation among values of the table, which gives the shell energy per nucleon for a given $(n_B, Z)$. The WS energy density including shell corrections thus reads

$$\varepsilon_{WS}(n_B, Z) = \varepsilon_{WS}^{\mathrm{CLD}}(n_B, Z) + n_B \Delta e_{sh}(n_B, Z), \tag{1.96}$$

where $\varepsilon_{WS}^{\mathrm{CLD}}$ is the smooth part of the WS energy density at the equilibrium, and $\Delta e_{sh}$ is the interpolated shell energy per nucleon. The value of $Z$ that minimizes the energy density of matter is naturally defined as the equilibrium value.

Fig. 1.9 shows the variation of the WS energy density as a function of $Z$ at two selected values of baryon density $n_B$, for BSk24 CLDM. As expected, the pure CLD

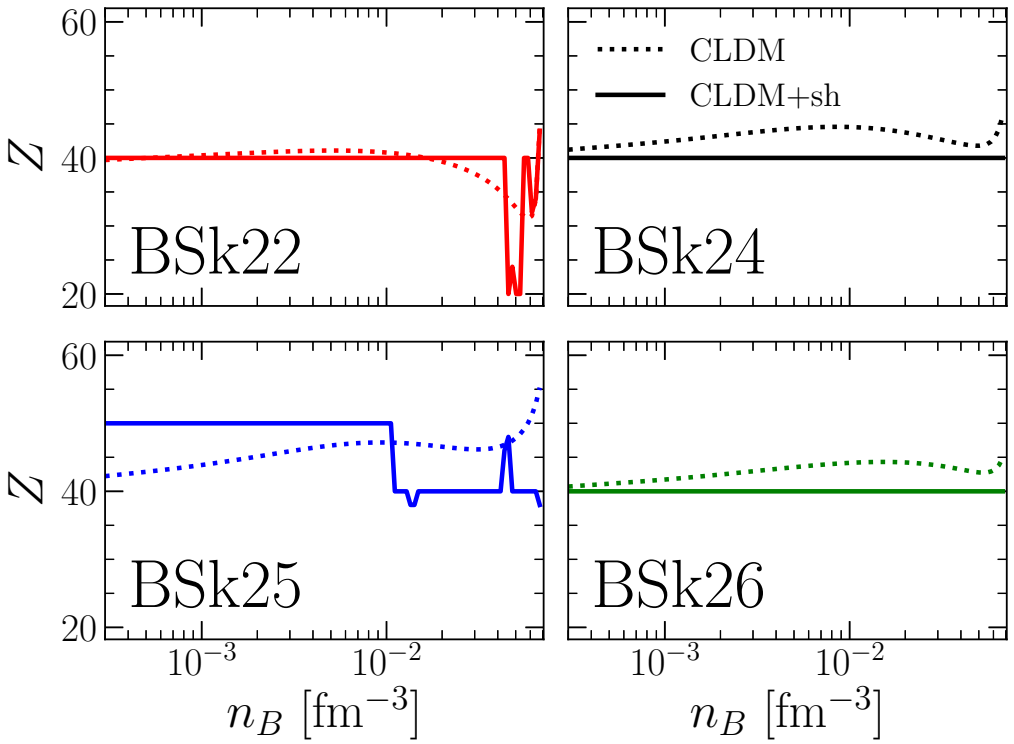



**Figure 1.10:** *Equilibrium value of $Z$ as a function of baryon density $n_B$ in the inner crust for BSk22, BSk24, BSk25, and BSk26 CLDM with (solid lines) and without (dotted lines) Strutinsky shell corrections on top of the CLD energy. Figure adapted from [Car+20].*

results, represented in dotted lines, are close to those including Strutinsky shell corrections, represented in solid lines, for closed-shell configurations, while remarkable differences exist for all other values of $Z$. This feature confirms the importance of a proper account of the shell structure. At $n_B = 10^{-3}$ fm$^{-3}$, a competition between $Z = 40$ and $Z = 50$ can be observed, with $Z = 40$ being slightly favored. However, it should be stressed that the difference in energy density is about $10^{-6}$ MeV/fm$^3$, which is expected to be lower than the precision reached by our modeling. It is observed that the shell closure $Z = 40$ is also favored over $Z = 50$ and $Z = 58$ at $n_B = 10^{-2}$ fm$^{-3}$.

Our results for the equilibrium value of $Z$ in the inner crust using BSk22, BSk24, BSk25, and BSk26 CLDM with (solid lines) and without (dotted lines) Strutinsky shell corrections can be seen in Fig. 1.10. It can be observed that magic numbers are recovered when shell corrections are added on top of the CLD energy. In particular, remarkable stability at $Z = 40$ is seen for BSk24 and BSk26, as well as $Z = 20$ and $Z = 40$ for BSk22, in a very good agreement with Fig. 12 of [Pea+18]. A small difference only appears for the BSk25 model, reflecting the limitations of the CLD approach. For this functional, after the plateau at $Z = 50$, also obtained with extended Thomas-Fermi plus Strutinsky integral (ETFSI) calculations of [Pea+18] for the same functional, the equilibrium number of protons drops to $Z = 40$ in our case, instead of

increasing as in [Pea+18]. However, we stress that the authors find a second minimum at $Z = 40$, and the energy difference between the two minima is of the order of $10^{-3}$ MeV [Pea+19].

Let us recall that surface and curvature parameters $\sigma_0$, $b_s$, $\sigma_{0c}$, and $\beta$ are so far fitted to experimental masses of nearly symmetric nuclei from the AME2016 [Hua+17] with a fixed value of the parameter $p$ that governs the behavior of the surface tension at extreme isospin values. Therefore the shell energy is implicitly accounted for in the surface tension by underestimating the value of $\sigma_0$, that is the surface tension of symmetric nuclei. This results in predicting slightly overbound nuclei with the CLD approach, but overall in a better description of spherical nuclei. However, we face an issue when adding Strutinsky shell corrections to the CLD energy, since we do not want to double-count the shell energy. To address this problem, we fit the surface and curvature parameters to the ETF results for each functional [Pea19], keeping the parameter $p$ fixed to the value $p = 3$ [Car+20], which gives an accurate reproduction of the CC transition points obtained in [Pea+19].

### 1.2.5 Nonspherical pasta phases

We have assumed so far that the inner crust only consists of spherical clusters. However, at high density just before the CC transition, nuclei are almost close enough to touch each other, and thus the lattice energy significantly reduces the Coulomb energy. Consequently, matter could in principle arrange itself into exotic structures, sometimes referred to as nuclear "pasta". In particular, from the density at which the volume fraction exceeds 1/2, it is expected that nuclei turn inside out, therefore forming neutron bubbles immersed in a proton-rich phase (the former cluster) [BBP71]. Furthermore, molecular dynamics simulations, in which a large number of interacting nucleons are let evolving in a very large box, predict the appearance of complex structures for $Y_p \approx 0.1$, which is comparable to the typical value in the bottom layers of the inner crust of neutron stars [Wat+03]. It should be stressed that these exotic phases of matter could constitute half of the crust mass [LRP93]. It is therefore straightforward to imagine that various astrophysical phenomena, such as the cooling process by neutrino emission, can be affected by their existence [WM11].

One of the virtues of the CLD approach is that different geometries for nuclear clusters can be considered in a simple way, allowing for the study of the pasta phases [RPL83; LS91; LRP93; NGL12]. Let us first recall the virial theorem with curvature term, here expressed in term of the surface, curvature, and Coulomb energy densities,

$$\varepsilon_{surf} + 2\varepsilon_{curv} = 2\varepsilon_{Coul}. \tag{1.97}$$

Following [RPL83; NGL12], the general expression for the surface energy density is

$$\varepsilon_{surf} = \frac{ud\sigma}{r}, \tag{1.98}$$

and that of the curvature energy density is

$$\varepsilon_{curv} = \frac{ud(d-1)\sigma_c}{r^2}, \tag{1.99}$$

where the surface tension $\sigma$ and curvature tension $\sigma_c$ are independent of the dimensionality, and therefore given by Eqs. (1.60) and (1.62), respectively. The Coulomb energy density reads

$$\varepsilon_{Coul} = 2\pi(eY_p n_0 r)^2 u \eta_{Coul,d}(u), \tag{1.100}$$

with $\eta_{Coul,2} = \frac{1}{4}\left[\ln\left(\frac{1}{u}\right) + u - 1\right]$ for $d = 2$, and $\eta_{Coul,d}(u) = \frac{1}{d+2}\left[\frac{2}{d-2}\left(1 - \frac{du^{1-2/d}}{2}\right) + u\right]$ otherwise. In the previous expressions, $r$ represents the radius (half-width in the case of planar geometry) of clusters or holes, $u$ the volume fraction occupied by the cluster (hole), $n_0$ the density of the dense phase, and $Y_p$ its associated proton fraction. The expression of the volume fraction is different depending on whether we have clusters or holes:

$$u = \begin{cases} (n_B - n_g)/(n_0 - n_g), & \text{for clusters} \\ (n_0 - n_B)/(n_0 - n_g), & \text{for holes} \end{cases} . \tag{1.101}$$

The parameter $d = \{3, 2, 1\}$ is related to the dimensionality, with $d = 3$ for spheres and bubbles, $d = 2$ for cylinders and tubes, and $d = 1$ for plates. In the former case, we naturally recover the expressions Eqs. (1.59), (1.61), and (1.57). Also, let us note that nuclei and bubble phases are identical as far as plates are concerned. Replacing these quantities in Eq. (1.97), we obtain an equation for the cluster (hole) radius/half-width,

$$4\pi(eY_p n_0)^2 \eta_{Coul,d}(u) r^4 - d\sigma r - 2d(d-1)\sigma_c = 0, \tag{1.102}$$

which has to be solved numerically. Let us notice that, neglecting the curvature term, the virial theorem reduces to $\varepsilon_{surf} = 2\varepsilon_{Coul}$, thus the expression of $r$ is analytical,

$$r = \left(\frac{d\sigma}{4\pi(eY_p n_0)^2 \eta_{Coul,d}(u)}\right)^{1/3} . \tag{1.103}$$

In order to find the most stable phase at a given baryon density, we proceed as follows. The composition is first calculated at a given $n_B$ in the spherical nuclei case ($d = 3$) following 1.2.2. Then, keeping the same composition, the radius/half-width $r$ is evaluated for the five different phases (spheres, cylinders, plates, tubes, and bubbles) by solving numerically Eq. (1.102). Finally, since the bulk and electron contributions to the WS cell are independent of the dimensionality, the equilibrium phase is the one that minimizes $\varepsilon_{surf} + \varepsilon_{curv} + \varepsilon_{Coul}$. Let us notice that this method has to be considered as an approximation since we do not consider the dimensionality dependence of the surface plus curvature energy in the minimization. This is similar to the so-called "coexisting phase method" employed in several works [Ava+08; Ava+10; Gra+17].

In the left panel of Fig. 1.11, we represent the WS energy density as a function of the baryon density for the five phases, using our CLDM to calculate the surface and curvature energy for the BSk24 functional. It is clearly seen that the spheres dominates up to $n_B \approx 0.05$ fm$^{-3}$, which is in good agreement with the semiclassical ETF results for this force [PCP20]. From this density, we find cylinders up to $n_B \approx 0.065$ fm$^{-3}$, before observing a transition to plates. Then, the differences in energy density become so small that the possible transition to another phase cannot be distinguished in the figure. However, one could expect the usual sequence, that is a transition to

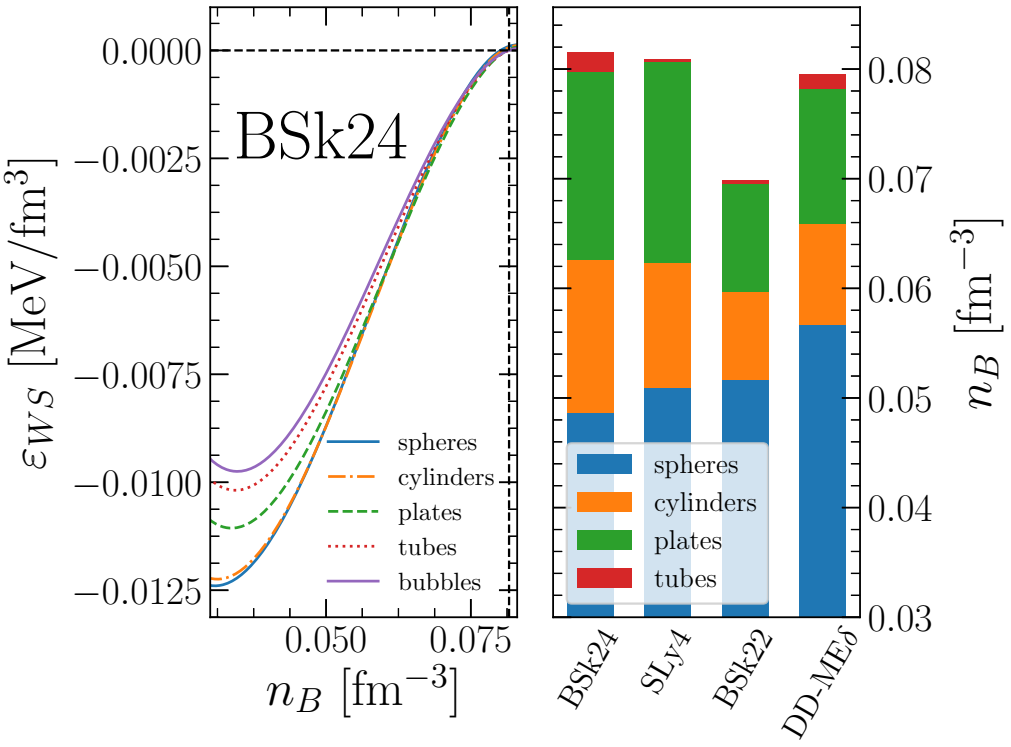



**Figure 1.11:** *Left panel: energy density of matter as a function of baryon density for the five phases, using BSk24 CLDM. The black dashed lines mark the CC transition point. Right panel: equilibrium phase as a function of baryon density for four selected CLDM: BSk24, SLy4, BSk22, and DD-ME$\delta$. For these calculations, the surface parameter $p$ is fixed to the value $p = 3$.*

tubes eventually followed by one to bubbles before the final transition to homogeneous matter [RPL83], here marked by the black dashed lines.

The right panel of Fig. 1.11 shows the equilibrium phase as a function of $n_B$ for four CLDM: BSk24, SLy4, BSk22, and DD-ME$\delta$. While model dependence is observed, it is interesting to notice that the sequence spheres → cylinders → plates → tubes is recovered for every model. Another shared feature is that the transition to homogeneous matter is found before the appearance of bubbles. Let us remark that, as in [MU15], we observe pasta phases for SLy4, whereas several previous CLD and TF calculations for this functional have predicted that the sphere is the most favorable shape at all densities up to the CC transition point [DH00; Viñ+17]. This contradiction can be understood by the fact that we are dealing with very tiny differences in energy density (all the shapes are very close), in a region where the matter is extremely neutron rich, thus where the nuclear surface tension is poorly constrained. In particular, we observed that varying the value of the surface parameter $p$ can affect the sequence of pasta phases.

### 1.2.6 Crust-core transition from the crust side

It is well known that a phase transition from a solid crust to a liquid core takes place at some $\approx 1$ km from the surface of the star, corresponding to subsaturation densities. A precise estimation of this transition point is necessary in order to evaluate the crust mass, thickness and moment of inertia, and so to understand phenomena involving NS, such as glitches, that are irregularities in the their rotational motion [Esp+11]. In that sense, a Bayesian analysis of the CC transition has been performed [CGM19a] and is presented in detail in Chapter 2.

The simplest approach for computing the phase transition is from the core side, in which the transition is defined as the density point where homogeneous NM at beta equilibrium becomes unstable with respect to density fluctuations. Two versions of this technique can be distinguished: the so-called thermodynamical [Kub04; Kub07; Gon+17] and dynamical [PRL95; Ant+19] methods. The former method consists in evaluating the thermodynamical spinodal, that is the instability point of NM with respect to the liquid-gas (LG) phase transition. The only necessary nuclear physics input for this method is the energy functional of homogeneous NM, which is well constrained through nuclear experiments and/or *ab initio* calculations in the vicinity of the nuclear saturation density $n_{sat}$. While it appears as a substantial advantage, it is known that the dynamics of the CC transition is very different from the LG one [DCG07; Duc+07; DMC08], thus applying this method results in an overestimation of the CC transition density and pressure. Indeed, the CC transition is expected to take place at approximately $\approx n_{sat}/2$, where the energy density of clusterized matter overcomes that of uniform NM [BBP71]. Since Coulomb, surface, and curvature terms, that are crucial for determining the equilibrium composition in the inner crust, vanish in homogeneous NM, they no not contribute to the determination of the LG thermodynamical spinodal. In the dynamical method, finite-size density fluctuations are added, thus it is expected to give a better estimation of the CC transition and pressure. The isovector gradient terms, needed in addition to the EoS, play a nonnegligible role for the determination of the dynamical spinodal, the location of which also depends on the many-body formalism adopted [DMC08].

While the dynamical method gives a better estimation of the CC transition point in comparison with the thermodynamical one, one should remark that the spinodal decomposition scenario is not compatible with the equilibrated crust in which matter is not uniform but composed of clusters immersed in a sea of electrons and neutrons. For this reason, the CC transition point is here computed from the crust side, by comparing the energy density of the two competing phases in beta equilibrium. The equation for the CC transition density $n_t$ is thus

$$\varepsilon_{WS}^{crust}(n_t) = \varepsilon_{npe}(n_t), \tag{1.104}$$

where $\varepsilon_{WS}^{crust}$ is the equilibrium energy density in the WS cell in the inner crust, and $\varepsilon_{npe}$ is the equilibrium energy density of matter in the outer core, which consists of homogeneous *npe* matter, studied in Section 1.3. The CC transition point is computed in the following for several nuclear models, using the metamodeling technique extended to finite nuclei in the CLD approximation, Eq. (1.64), to calculate the WS cell energy density in the inner crust, and keeping the same empirical matter for the description

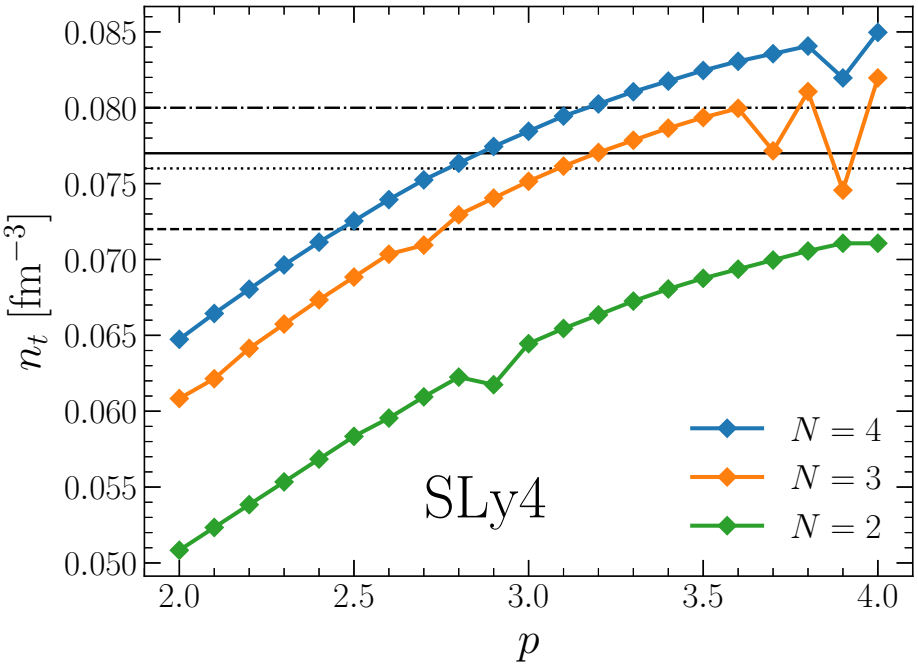



**Figure 1.12:** *Crust-core transition density as a function of the surface parameter $p$ with truncation order $N = 2$, $N = 3$, and $N = 4$, for SLy4 CLDM. The black horizontal bars represent different evaluations of $n_t$ for the SLy4 functional found in the literature: $n_t = 0.072$ fm$^{-3}$ [Viñ+17] (dashed line) and $n_t = 0.077$ fm$^{-3}$ [DH00] (solid line) in the CLDM approximation, $n_t = 0.076$ fm$^{-3}$ [Viñ+17] (dotted line) in the TF approximation, and $n_t = 0.080$ fm$^{-3}$ [Viñ+17] (dashdotted line) with the dynamical method.*

of uniform *npe* matter. One should stress the importance of having a unified EoS for the crust and the core [DH01] to estimate correctly the CC transition point. Indeed, it was shown that matching a crust and core EoS based on different nuclear models induce an uncertainty on the determination of the CC transition point, consequently inducing an uncertainty in the crustal observables, which can be as large as 30% for the crust thickness [For+16]. Let us mention that pasta phases are not considered here, since we have checked that their presence does not affect the estimation of the CC transition density and pressure.

In Fig. 1.12, we show the variation with surface parameter $p$ of $n_t$ for SLy4 CLDM. For each value of $p$, the surface and curvature parameters are fitted to experimental masses from the AME2016. The CC transition density is estimated for different values of the truncation order $N$ in the density development, Eq. (1.51). A convergence feature is observed from $N = 2$ to $N = 4$, almost achieved at $N = 3$. We can see that truncating at $N = 2$ leads to a substantial underestimation of about $\approx 20\%$ of the transition density. This observation highlights the importance of keeping the high-order parameters $Q_{sat}$ and $Q_{sym}$ ($N = 3$) as well as $Z_{sat}$ and $Z_{sym}$ ($N = 4$) in the Taylor expansion. A positive correlation is seen between the isovector surface

parameter $p$ and $n_t$: the higher the value of $p$ the higher the transition density. This can be understood from the fact that a low value of $p$ leads to a higher surface tension at extreme isospin values, thus it makes the cluster less bound and consequently the uniform *npe* matter becomes the favorable phase at lower density. The effect of varying the low-density parameter $b$ on $n_t$ is also evaluated in [CGM19a]. It is found that while it does not significantly affect the transition density in comparison with $N$ and $p$, it should be kept as an additional EoS parameter in any statistical analysis in order to make a quantitative prediction of the CC transition point. The introduction of the parameter $b$ in the parameter space is, in fact, an effective manner to account for the effect of orders $N > 4$, which are not explicitly included. For $p \approx 4$, the treatment of the surface tension at extreme isospin is marginal, resulting in numerical instabilities that can be observed in the figure.

Different estimations of the CC transition density for the SLy4 functional found in the literature are reported in Fig. 1.12 (black lines), with $n_t$ ranging from 0.072 fm$^{-3}$ [Viñ+17], in the CLD approximation, to 0.089 fm$^{-3}$ [Duc+11] (not represented in the figure), with the thermodynamical method. It is interesting to observe that the two different CLD calculations of the literature based on SLy4 functional, reported in the figure, give a different estimation of $n_t$, with 0.072 fm$^{-3}$ in [Viñ+17], and 0.077 fm$^{-3}$ in [DH00]. This stresses once again the importance of the treatment of the isovector surface tension for the determination of the CC transition point.

Fig. 1.13 shows our estimations of the transition density $n_t$ and pressure $P_t$ as a function of the slope of the symmetry energy $L_{sym}$ for a set of relativistic and nonrelativistic functionals, in comparison with the dynamical spinodal calculations of [Duc+11]. It is seen that the value $p = 3$ is in good agreement with the dynamical results for most of the models. For DD-ME2, the lower value needed for $p$ is supported by the TF calculations in [GPA12]. As in [Viñ+17], an anticorrelation is observed between $L_{sym}$ and $n_t$. Using a linear regression to model the relationship between $L_{sym}$ and our estimation of $n_t$ with $p = 3$, we find $n_t = -3.807 \times 10^{-4} L_{sym} + 0.098$ fm$^{-3}$, for a root mean square error of $3.094 \times 10^{-3}$ fm$^{-3}$. This linear equation for $n_t$ is in very good agreement with Eq. (17) of [Duc+11]. This downwards tendency with increasing values of $L_{sym}$ is not clearly observed for the transition pressure. We will see in Chapter 2 that the relation between those two quantities is more complicated than what is suggested by the selection of a limited number of models in Fig. 1.13. Indeed, a full statistical analysis reveals that the density and pressure at the transition point to homogeneous matter are correlated with the high-order empirical parameters, which blurs the effective correlation with $L_{sym}$.

## 1.3 Matter of the core

In the very bottom layers of the inner crust, clusters are so large and asymmetric that the CLD energy per nucleon, Eq. (1.64), becomes equal to that of infinite nuclear matter, marking the CC interface. While the composition and structure of the core close to the saturation density are well known, various scenarios have been proposed in the literature [Oer+17] concerning the relevant degrees of freedom above $2 - 3n_{sat}$.

This section deals with the matter of the core. In 1.3.1 we derive the system of

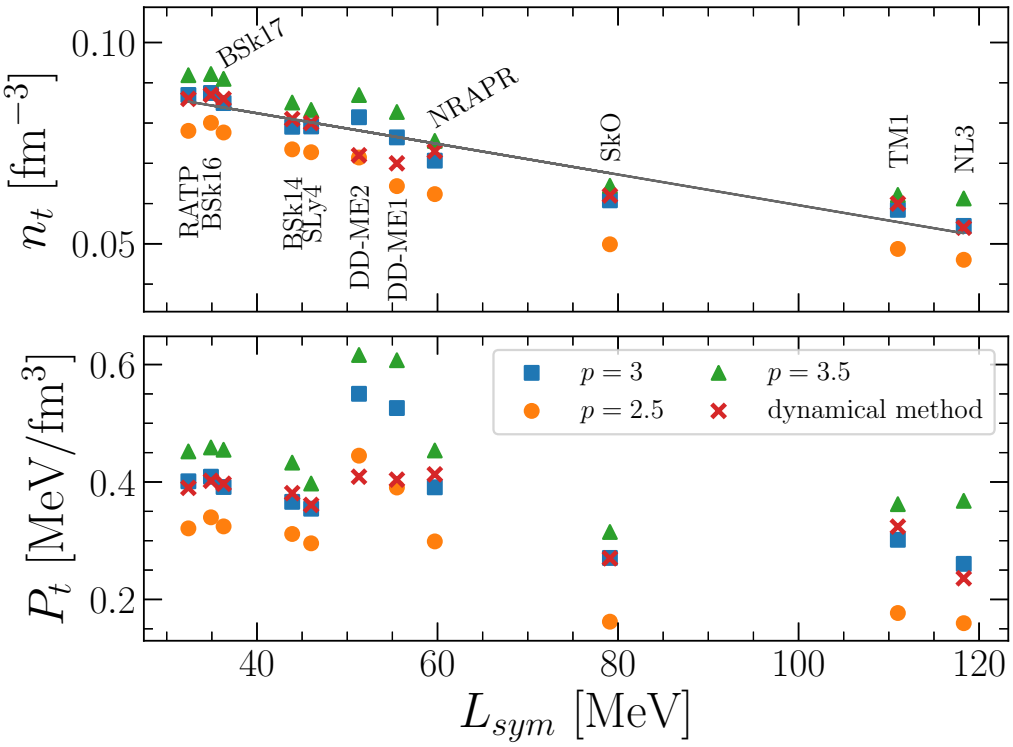



**Figure 1.13:** *Crust-core transition density $n_t$ (upper panel) and pressure $P_t$ (lower panel) as a function of $L_{sym}$ for several interactions. The crosses are the transition points calculated in [Duc+11] using the dynamical spinodal. The circles, squares, and triangles correspond respectively to our estimation of the transition points with $p = 2.5$, $p = 3$, and $p = 3.5$. The gray line is the linear regression curve fitted to the $p = 3$ results.*

variational equations for the ground state of the outer core. The model dependence of the composition and EoS is then explored. In particular, we focus on apparent correlations with the symmetry energy. The matter inside the inner core is finally discussed in 1.3.2.

### 1.3.1 Outer core: homogeneous *npeμ* matter

From the CC transition point, previously discussed in 1.2.6, up to $n_B \approx 2n_{sat}$, the matter of the core consists of a uniform plasma of neutrons, protons, electrons, and eventually muons, hereafter referred to as *npeμ* matter (or *npe* if muons are not present). This region of the star corresponds to the outer core. The energy density of *npeμ* matter reads

$$\varepsilon_{npe\mu}(n_B, \delta, n_e, n_\mu) = \varepsilon_{HM}(n_B, \delta) + \varepsilon_e(n_e) + \varepsilon_\mu(n_\mu) + n_B \frac{1-\delta}{2} \Delta m_{pn} c^2 + n_B m_n c^2, \tag{1.105}$$

with $\varepsilon_{HM} = ne_{HM}$ the energy density of nuclear matter given by the metamodel, Eq. (1.38). The expression of energy density of the relativistic muon gas $\varepsilon_\mu(n_\mu)$ is the same as that of the relativistic electron gas, and it is derived in Appendix A.

#### 1.3.1.1 Variational equations

Following 1.2.2, the system of equilibrium equations determining the composition and EoS of the outer core is obtained by minimizing the energy density of matter, Eq. (1.105), at constant baryon density under the condition of overall charge neutrality, which now reads

$$n_B \frac{1-\delta}{2} = n_e + n_\mu. \tag{1.106}$$

since muons may exist in this region of the star. Muons are present in the outer core if the electron chemical potential exceeds the muon rest-mass energy, that is $\mu_e \gtrsim m_\mu c^2$. As far as variational variables are concerned, a reasonable choice appears to be the asymmetry $\delta$ and the muon density $n_\mu$. Let us first minimize the energy density of matter with respect to $\delta$,

$$\begin{aligned} \left.\frac{\partial \varepsilon_{npe\mu}}{\partial \delta}\right|_{n_\mu} &= 0 \\ 2\frac{\partial e_{HM}}{\partial \delta} - \Delta m_{pn} c^2 - \mu_e &= 0. \end{aligned} \tag{1.107}$$

We can easily identify this equation with the well-known beta equilibrium condition. Indeed, using the definition of the neutron and proton chemical potentials, Eq. (1.54), we obtain

$$\mu_n = \mu_p + \mu_e. \tag{1.108}$$

We now turn to minimization with respect to the muon density,

$$\begin{aligned} \left.\frac{\partial \varepsilon_{npe\mu}}{\partial n_\mu}\right|_{\delta} &= 0 \\ \mu_\mu - \mu_e &= 0, \end{aligned} \tag{1.109}$$

where we have introduced the muon chemical potential $\mu_\mu = \partial \varepsilon_\mu / \partial n_\mu$. This equation corresponds to the chemical equilibrium between muons and electrons, and has to be satisfied if muons are present. Here, we consider that the core is transparent for neutrinos, which occurs as soon as the temperature falls below $10^9 - 10^{10}$ K [HPY07]. In this case we can put $\mu_{\nu_e} = \mu_{\bar{\nu}_e} = \mu_{\nu_\mu} = \mu_{\bar{\nu}_\mu} = 0$. These two equations, Eq. (1.108) and (1.109), express the equilibrium with respect to the weak interaction processes. Let us remark that each time we mention electrons and muons, we are always referring to their net number, that is particles minus antiparticles.

From the numerical point of view, we use Broyden's method to solve the beta equilibrium equation, Eq. (1.108), starting from the transition density $n_t$. The initial guess for the asymmetry $\delta_{guess}$ is taken to be the value of the global asymmetry inside the WS cell at the CC transition point, which is approximately $\approx 0.9$. At each new step of baryon density, the value of $\delta_{guess}$ is updated with the last equilibrium solution, and

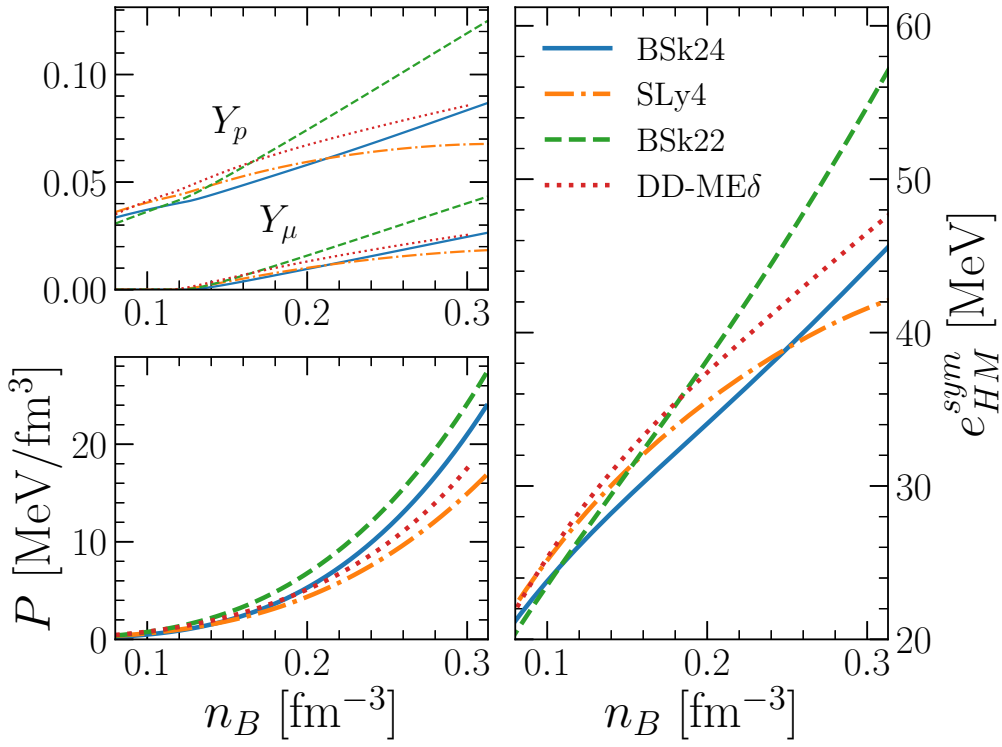



**Figure 1.14:** *Left: Proton fraction $Y_p$ and muon fraction $Y_\mu$ (upper panel), and pressure $P$ (lower panel) as a function of the baryon density $n_B$ in the outer core for four selected models: BSk24, SLy4, BSk22, and DD-ME$\delta$. Right: Variation with baryon density of the symmetry energy $e_{HM}^{sym}$, Eq. (1.53), for the four models.*

we check if $\mu_e \gtrsim m_\mu c^2$. In the case of *npe*$\mu$ being energetically favorable, Eq. (1.109) is added as a supplementary equation to be solved, setting the initial guess for the muon density to $n_{\mu,guess} = 10^{-5}$ fm$^{-3}$. The calculation is stopped when the baryon density reach $\approx 2n_{sat}$, from which the composition of matter becomes less certain.

#### 1.3.1.2 Equilibrium composition and equation of state

In Fig. 1.14, the proton fraction $Y_p = (1-\delta)/2$ and muon fraction $Y_\mu = n_\mu/n_B$ are plotted as a function of the baryon density for the four nuclear models BSk24, SLy4, BSk22, and DD-ME$\delta$, the empirical parameters of which are listed in Table 1.3. The variation $n_B$ of the electron fraction $Y_e$ can be deduced from the charge neutrality condition, Eq. (1.106). Surprisingly, it is observed that the proton fraction rises with $n_B$ in the outer core, while it monotonously decreases in the crust. A strong correlation between the proton fraction and the symmetry energy, represented in the right panel for the four models, is seen. One can relate the two quantities using the beta equilibrium condition. Indeed, we can easily go through Eq. (1.108) assuming a quadratic expansion for the NM energy per nucleon,

$$e_{HM}(n_B,\delta) \simeq e_{HM}(n_B,\delta=0) + \delta^2 e_{HM}^{sym}(n_B). \tag{1.110}$$

In that case, the beta equilibrium condition reads

$$4\delta e_{HM}^{sym}(n_B) - \Delta m_{pn}c^2 = \mu_e(n_e), \tag{1.111}$$

and we can thus express the equilibrium proton fraction as a function of the symmetry energy,

$$Y_p = \frac{1}{2} - \frac{\mu_e(n_e) + \Delta m_{pn}c^2}{8e_{HM}^{sym}(n_B)}. \tag{1.112}$$

From this equation it is clear that the higher the symmetry energy, the higher the proton fraction, which is the trend observed in the figure. The density from which muons are present is also shown in the upper left panel. It appears that we are dealing with *npe* matter up to $n_B \approx 0.12$ fm$^{-3}$, and it is seen that the threshold density for the appearance of muons, when $\mu_e \gtrsim m_\mu c^2$, is not very sensitive to the nuclear model.

Fig. 1.14 also shows the pressure as a function of the density (lower left panel). In the outer core, we can write the pressure as

$$P(n_B) = P_{HM}(n_B, \delta) + P_e(n_e) + P_\mu(n_\mu), \tag{1.113}$$

where $\delta$, $n_e$, and $n_\mu$ are the equilibrium values at $n_B$. The expression of the nuclear contribution $P_{HM}$ is given by Eq. (1.55). The electron and muon contributions to the total pressure, respectively $P_e$ and $P_\mu$, share the same expression, Eq. (1.11), which is that of a relativistic FG. A strong model dependence is observed for the pressure at suprasaturation densities, reflecting the large uncertainties associated to the isovector parameters beyond $E_{sym}$, as reported in the last column of Table 1.3.

### 1.3.2 Inner core

From the crust-core interface up to $n_B \approx 2n_{sat}$, it is commonly accepted that matter is exclusively composed of neutrons, protons, electrons, and muons. At higher densities however, the composition of matter becomes uncertain and different scenarios have been considered in the literature for the structure and composition of the inner core [Oer+17]. The presence of hyperons at suprasaturation densities has been considered in many studies, and its effect on the EoS and subsequently on NS observables has been evaluated [Bed+12; For+15]. In particular, the presence of hyperons softens the high-density EoS and thus lowers the maximum mass of neutron stars. As a consequence, many models fail to satisfy the NS mass constraint of $\approx 2M_\odot$ [Dem+10; Ant+13], leading to the so-called "hyperon puzzle" [ZH13]. Nevertheless, several existing hyperonic models can fulfill the constraint [Oer+15; CV16; FOP18]. In fact, the measurement of $\approx 2M_\odot$ NS also rules out several models that include a phase transition to quark matter or a boson condensate in the inner core, because the EoS is softened by the introduction of any additional degree of freedom without an interaction. Let us however mention that several EoS with a quark-hadron crossover at high density are stiff enough to support NS of masses greater thatn $2M_\odot$ [MHT13; Koj+15; Bay+19]. In particular, the recently proposed QHC19 EoS [Bay+19] allows a maximum mass of $2.35M_\odot$ and agrees with the constraints on NS properties inferred from the GW170817 event [Abb+18; Abb+19].

We propose here to extrapolate the $npe\mu$ matter at higher densities, in the inner core. The different studies that consider hyperons and satisfy the maximum mass constraint show that the hyperon-nucleon and hyperon-hyperon couplings must be such that, if hyperons exist, they are not abundant and can be neglected as a first approximation, at least in the EoS energetics (see [Oer+17] and references therein). Since the metamodeling does not make any assumption regarding the degrees of freedom, but only assumes that the functional is based on a Taylor expansion, we can consider that the technique can be safely extended at high density in the aim of calculating static properties, such as the EoS or the mass-radius relation. The only thing that could invalidate it would be the presence of a first-order phase transition, that is a discontinuity in the EoS. Thus, the only hypothesis that is made here is considering that there is no such transition. Actually, even a transition to quark matter could be smooth. Indeed, several works consider pasta phases in the hadron-quark phase transition, with the effect of washing out discontinuities [MTC09; YMT09; YMT11; Yas+14]. Finally, this is equivalent to a null hypothesis: since the metamodeling allows to control uncertainties, a disagreement with astrophysical observations would be the sign of new physics, indicating either the existence of a first-order phase transition or an alternative theory of gravity. Let us recall that the metamodeling technique gives an accurate reproduction of existing nuclear models up to $\approx 2-3n_{sat}$ (metamodeling ELFc in [MHG18a]), as we have verified in Fig. 1.4. A solution for achieving faster convergence at high density, the metamodeling ELFd, is proposed in [MHG18a]. It is based on a reevaluation of the high-order empirical parameters $Q_{sat}$, $Q_{sym}$, and $Z_{sat}$, $Z_{sym}$, by imposing a high-density point at which the energy per nucleon and the pressure are known for a given functional. This is encouraged by the fact that the impact of these parameters is very small in the vicinity of the saturation density. We will use this technique when we will want to reproduce existing hadronic models.

## 1.4 Unified metamodeling of the equation of state

As previously discussed, matching a crust and core based on different nuclear models can lead to large uncertainties associated with the CC transition density and pressure, which are the quantities for the determination of the crust observables. In particular, it was shown in [For+16] that it can lead to an error as large as $\approx 30\%$ for the crust thickness and $\approx 4\%$ for the radius. The main justification for working with nonunified EoS is that the core is responsible of most of the NS mass, thus one could simply match any crust EoS, for instance that of BPS in the outer crust [BPS71] plus that of BBP in the inner crust [BBP71], with its core EoS based on a different nuclear interaction. This is indeed sufficient if one is interested in observables such as the maximum mass. However, it obviously leaves a large freedom in the matching procedure. In addition, this amounts to consider that the crust segment is not model dependent, while we have clearly seen in 1.2.3.3 that the crust EoS is sensitive to the nuclear model, and is in particular correlated with the symmetry energy. It is therefore preferable to describe the crust and core in a unified manner.

Several unified EoS for cold nonaccreting NS have been proposed in the literature. For instance, the well-known DH EoS [DH01] is based on the Skyrme SLy4 effective

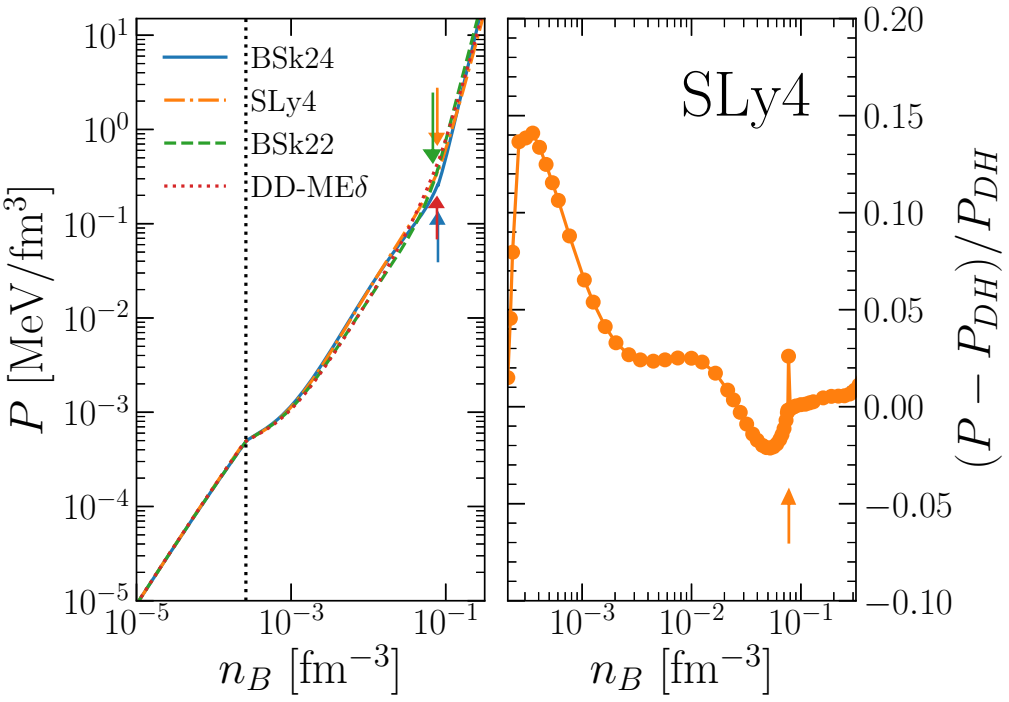



**Figure 1.15:** *Left: Pressure as a function of baryon density in the different regions of an NS for BSk24, SLy4, BSk22, and DD-MEδ. Crust and core are described in a unified manner, with the metamodeling technique. The black dotted line marks the onset of the inner crust, and arrows indicate the CC transition density for the different models. Right: Relative difference* $(P - P_{DH})/P_{DH}$ *with DH unified EoS for SLy4 [DH01] as a function of* $n_B$*. The arrow indicates our estimation of the CC transition density for SLy4.*

interaction [Cha+98]. In the inner crust, the authors use a version of the CLDM to calculate the energy of finite nuclei, the bulk term of which is given by the SLy4 functional in the infinite NM limit, which is also used to describe the outside neutron gas, and at high density to calculate the $npe\mu$ matter energetics in the core. Let us notice that the EoS of the outer-crust ground state is taken from [HP94] in this work. More recently, a series of unified EoS based on modern BSk functionals [GCP13] has been proposed [Pea+18]. In this work, the ground state of the outer crust is determined by application of the microscopic HFB method [Sam+02], and the ground state of the inner crust is calculated within the ETFSI approximation [Ons+08]. Also, a set of unified EoS built within a relativistic mean-field approach (RMF) was proposed in [For+16] and another one based on Skyrme functionals in [GR15].

One obvious reason explaining why crust and core matter are not consistently treated using the same microscopic interaction is that it is less trivial to evaluate the ground state of the inner crust in comparison to the ground state of matter in the core. Indeed, one can evaluate the inner-crust ground state within different many-body approaches, either using the CLDM, the semiclassical ETFSI method, or full

HF calculations. While the two last methods are expected to be more precise than the CLD approximation as far as the composition is concerned, they can become computationally heavy if one wants to compute the EoS for many nuclear models. In addition, these more microscopic methods can only be extended to finite temperature in the SNA, whereas the CLD approximation allows distributions of clusters, that exist at finite temperature, to be considered (see Chapter 3 of this thesis).

In view to provide a unified and thermodynamically consistent treatment of the crust and core of cold nonaccreting NS, we propose to compute the EoS within the metamodeling approach that we have presented throughout this chapter. For a given nuclear model, in other words a given set of empirical parameters $\boldsymbol{P_\alpha}$, we proceed as follows. The EoS in the outer crust is evaluated by application of the BPS method presented in 1.1.2, using the present day knowledge on experimental masses [Hua+17; Wel+17] supplemented by state-of-the-art microscopic HFB theoretical mass tables [GCP13] up to the neutron-drip point. The EoS in the inner crust is then calculated by solving the system of four differential equations, Eqs. (1.86), (1.87), (1.88), and (1.89). The metamodeling technique, discussed in 1.2.1.1, is used to calculate the neutron gas energy. The concept of metamodeling of homogeneous NM is extended to finite nuclei in the CLD approximation in order to evaluate the cluster energy, the bulk term of which is calculated with the same empirical parameters as the neutron gas. Finally, from the CC transition point, discussed in 1.2.6, the core EoS is computed by solving the two chemical equilibrium equations Eqs. (1.108) and (1.109). Again, the empirical parameters are the same as those used in the inner crust. Within such an approach, one can compute the unified EoS for any nuclear model. In addition, this method is not expensive from the computational point of view, which will allow us to make comprehensive statistical evaluations of the model uncertainties in Chapter 2.

The left panel of Fig. 1.15 shows the resulting unified EoS for the four nuclear models considered in this chapter: BSk24, SLy4, BSk22, and DD-ME$\delta$. The neutron-drip point is represented by the vertical dotted line, and arrows indicate the CC transition density for each model. The relative difference between the DH EoS [DH01] and our EoS for SLy4 is represented as a function of the baryon density in the right panel of Fig. 1.15. It is seen that the overall difference is smaller than 10% in the inner crust. The slight disagreement at low density comes from the fact that the onset of the inner crust is marked at $n_{ND} = 2.0905 \times 10^{-4}$ fm$^{-3}$ in the DH EoS (calculated in [HP94]), which is low in comparison with our estimation of the neutron drip density, $n_{ND} = 2.503 \times 10^{-4}$ fm$^{-3}$. Let us notice that the parametrization of the surface tension in both studies is different, therefore it might explain the difference between the two EoS at higher densities in the inner crust, in addition to the slight error introduced by the metamodel. In the core, we can observe that the relative difference is smaller that 1%.

## 1.5 Conclusions

In this chapter, we have first evaluated the ground state of the outer crust, which is obtained by the application of the BPS method, using recent experimental masses

[Hua+17; Wel+17] supplemented by state-of-the-art microscopic HFB theoretical mass tables. We have shown that the outer-crust composition and so the EoS are entirely determined by the present day knowledge on experimental masses up to $n_B \approx 3 \times 10^{-5}$ fm$^{-3}$. At higher densities, we have observed the persistence of $N = 82$ for each of the four mass models considered.

We have proposed a version of the CLDM based on the metamodeling technique [MHG18a; MHG18b]. We have seen that the metamodel offers the possibility to reproduce any functional of nuclear matter very precisely, with a unique functional form. The parametrization of surface tension was suggested from microscopic calculations in the free neutron regime [RPL83], and surface and curvature parameters are fitted to experimental masses. We have used the CLDM to calculate the ground state of the inner crust, which is obtained by minimizing the energy density of matter at constant baryon density under the condition of overall charge neutrality. We have therefore derived a system of four coupled differential equations, corresponding to chemical and mechanical equilibrium conditions, that we have solved numerically using Broyden's method [Bro65]. The ground-state composition of the inner crust for BSk24 empirical parameters was presented, and a very good agreement with more microscopic approaches was observed concerning the value of $Z \approx 40$. We have also seen that the proton fraction is continuously decreasing, as in the outer crust. The inner crust EoS was computed and a positive correlation with the empirical parameter $E_{sym}$ was revealed. We have shown that magic numbers, that vanish within the CLD approach, can be recovered by adding perturbatively Strutinsky shell corrections on top of the CLD energy. In this way, a very good agreement with ETFSI calculations was observed for recent BSk functionals [Pea+18]. With the CLDM, we have explored the possible presence of nonspherical pasta phases in the bottom layers of the inner crust, finding the sequence spheres $\rightarrow$ cylinders $\rightarrow$ plates $\rightarrow$ tubes for each of the four model considered: BSk24, SLy4, BSk22, and DD-ME$\delta$. We have shown that the transition point to homogeneous matter is very sensitive to the surface tension at extreme values of isospin, the behavior of which is governed by the isovector surface parameter $p$. Unfortunately, this parameter cannot be accessed from empirical nuclear physics data, which are limited to values around $I \lesssim 0.3$. We have seen that the CC transition density and pressure results of the literature for the dynamical spinodal [Duc+11] are globally nicely reproduced by our calculation from the crust with $p \approx 3$. We have also confirmed the correlation of the transition density $n_t$ with the empirical parameter $L_{sym}$ already observed in previous works.

We have derived the equilibrium equations characterizing the ground state of matter in the core, which consists of $npe\mu$ matter up to $n_B \approx 2n_{sat}$. The strong correlation between the symmetry energy and the proton fraction was explained. We have found that muons appear in the vicinity of $n_B \approx 0.12$ fm$^{-3}$ for each model. As in previous works [WFF88; DH01], we have extrapolated the $npe\mu$ model to higher densities, since the hyperon-hyperon and hyperon-nucleon interactions remain currently poorly constrained.

Finally, we have stressed that building unified EoS is essential to properly estimate crustal observables. In that sense we have proposed a metamodeling of the EoS of cold nonaccreting NS, where the crust and core are treated in a uniform manner, that

is with the same empirical parameters. Using the SLy4 empirical parameters, we have shown that the relative difference with the DH EoS is smaller than 10% in the inner crust and 1% in the core.

In Chapter 2, we will exploit the second advantage of the metamodeling technique, namely the fact that no artificial correlations are introduced *a priori* among the empirical parameters, to carry out complete statistical analyses that will allow us to settle the model dependence of the results.

# Chapter 2

# Bayesian inference of neutron star observables

This chapter deals with the determination of NS observables within a Bayesian framework.

Pulsars were identified to rotating NS which produce pulsed emission, soon after their chance discovery in 1967 by Jocelyn Bell [Hew+68]. Five decades later, we have now observed about 3000 of them, and numerous techniques have been developed to measure their characteristic observables. For instance, precise measurements of NS masses can be performed using the relativistic Shapiro delay effect [Dem+10; Cro+20], the ambitious NICER program is giving more and more constraining information on the NS radii [Bog+19a; Bog+19b; Mil+19; Raa+19; Ril+19], and the first detection of GW from the coalescence of two NS, the GW170817 event, has provided a constraint on the tidal deformability of NS [Abb+17; Abb+18; Abb+19]. All those observational data can be used to better constrain the nuclear EoS. Reciprocally, there has been a lot of efforts invested recently in the development of *ab initio* calculations, particularly based on the chiral EFT [DHS16] with the aim of providing new constraints on the low-density EoS, which can ultimately be translated into theoretical constraints on NS observables [CGM19a; CGM19b]. In this context, the Bayesian framework is particularly appealing for making realistic predictions for NS observables. It allows to update our prior beliefs on the EoS parameters with the constraints arising from the multiple sources mentioned above.

The plan of the chapter is as follows. In Section 2.1, global properties and crustal observables are calculated for several characteristic EoS by solving the equations of hydrostatic equilibrium in general relativity. The connection between the crust moment of inertia and the glitch phenomenon is explained. The EoS parameters are determined within a Bayesian framework in 2.2, given the present day constraints on nuclear physics, NS observables, and physical requirements. In particular, correlations among the empirical parameters are explored. General predictions for NS observables are proposed in 2.3, using the joint posterior distribution of EoS parameters. We confront our predictions with different constraints inferred from the GW170817 event. The CC transition density and pressure as well as the fractional crust moment of inertia are evaluated. The full crustal origin of Vela pulsar glitches is discussed. Finally,

conclusions are given in Section 2.4.

## Contents

**2.1 From the equation of state to neutron star observables . 59**
2.1.1 Masses and radii . . . . . 59
2.1.1.1 Mass-radius relation . . . . . 59
2.1.1.2 Crust thickness and mass . . . . . 62
2.1.2 Moment of inertia within the slow rotation approximation . 63
2.1.2.1 Total moment of inertia and fraction contained in the crust . . . . . 64
2.1.2.2 Connection to pulsar glitches . . . . . 66
2.1.3 Tidal deformability . . . . . 68
**2.2 Bayesian determination of the equation of state parameters 70**
2.2.1 Principle of Bayesian inference . . . . . 70
2.2.2 Prior distribution of equation of state parameters . . . . . 72
2.2.2.1 Flat prior compatible with empirical constraints . 72
2.2.2.2 Sensitivity analysis of the crust-core transition point 73
2.2.3 Determination of the likelihood function . . . . . 76
2.2.3.1 Constraints on nuclear physics observables . . . . 76
2.2.3.2 Physical requirements and constraints on neutron star observables . . . . . 78
2.2.4 Posterior distribution of equation of state parameters . . . 78
2.2.4.1 Marginalized one-parameter posterior distributions of empirical parameters . . . . . 79
2.2.4.2 Correlations among empirical parameters . . . . . 82
**2.3 General predictions for neutron star observables . . . . . 84**
2.3.1 Global properties: confrontation with popular models and the GW170817 event . . . . . 84
2.3.1.1 Equation of state . . . . . 85
2.3.1.2 Masses and radii . . . . . 86
2.3.1.3 Tidal deformability . . . . . 88
2.3.2 Bayesian analysis of the crust-core transition . . . . . 91
2.3.3 Pulsar glitches: answering the question "*Is the crust enough?*" 96
**2.4 Conclusions . . . . . 102**

## 2.1 From the equation of state to neutron star observables

The stellar EoS, the determination of which was studied thoroughly in Chapter 1, is the fundamental ingredient to build NS models. It enters into the basic equation for calculating macroscopic observables relevant to NS, the so-called Tolman-Oppenheimer-Volkoff (TOV) equation, which describes the hydrostatic equilibrium for a spherically symmetric nonrotating star in the framework of general relativity [Tol39; OV39].

This section deals with the estimation of NS observables for several popular EoS calculated within the metamodeling technique introduced in Chapter 1. In 2.1.1, we first solve the hydrostatic equilibrium equations so as to determine the mass-radius relation. The thickness and mass of the crust are also evaluated. The calculation of the NS moment of inertia in the slow rotation approximation is performed in 2.1.2. In particular, we show how the fractional crust moment of inertia is connected to the observation of pulsar glitches. In 2.1.3, we finally compute the tidal deformability, which describes how much the NS is deformed by tidal forces, arising, for instance, in the final approach phase of two merging NS.

### 2.1.1 Masses and radii

In the following, we turn to the theoretical prediction of NS masses and radii. The hydrostatic equilibrium equations in general relativity are first solved in order to represent the mass-radius relation for several popular EoS, which are then confronted to NS mass measurements. The estimation of the crustal thickness and mass is discussed later in 2.1.1.2.

#### 2.1.1.1 Mass-radius relation

Theoretically, the NS masses and radii correspond to the solution of the hydrostatic equilibrium equations, which are, in general relativity for spherical and nonrotating stars, given by [Tol39; OV39]

$$\frac{dP}{dr} = -\frac{G\rho m}{r^2}\left(1+\frac{P}{\rho c^2}\right)\left(1+\frac{4\pi P r^3}{mc^2}\right)\left(1-\frac{2Gm}{rc^2}\right)^{-1}, \tag{2.1}$$

$$\frac{dm}{dr} = 4\pi r^2 \rho, \tag{2.2}$$

$$\frac{d\Phi}{dr} = -\frac{1}{\rho c^2}\frac{dP}{dr}\left(1+\frac{P}{\rho c^2}\right)^{-1}, \tag{2.3}$$

where $G$ is the gravitational constant, $P$ the pressure, $\varepsilon = \rho c^2$ the total energy density, and $m(r)$ the is the gravitational mass inside the sphere of radius $r$, defined within the Schwarzschild metric $ds^2 = c^2 dt^2 e^{2\Phi} - e^{2\lambda} dr^2 - r^2(d\theta^2 + \sin^2\theta d\phi^2)$. The function $\Phi(r)$ corresponds to the gravitational potential in the Newtonian limit, and $\lambda(r)$ is related to the enclosed mass $m(r)$ through

$$e^{-\lambda} = \sqrt{1-\frac{2Gm}{rc^2}}. \tag{2.4}$$

| Parameter | Unit | $N$ | BSk14 | PKDD | TM1 |
|---|---|---|---|---|---|
| $E_{sat}$ | MeV | 0 | -15.85 | -16.27 | -16.26 |
| $n_{sat}$ | fm$^{-3}$ | 1 | 0.1586 | 0.1495 | 0.1450 |
| $K_{sat}$ | MeV | 2 | 239 | 261 | 281 |
| $Q_{sat}$ | MeV | 3 | -359 | -119 | -285 |
| $Z_{sat}$ | MeV | 4 | 1435 | 4213 | 2014 |
| $E_{sym}$ | MeV | 0 | 30.00 | 31.19 | 36.94 |
| $L_{sym}$ | MeV | 1 | 43.9 | 79.5 | 111.0 |
| $K_{sym}$ | MeV | 2 | -152 | -50 | 34 |
| $Q_{sym}$ | MeV | 3 | 389 | -28 | -67 |
| $Z_{sym}$ | MeV | 4 | -2191 | -1315 | -1546 |
| $m^*_{sat}/m$ | | | 0.80 | 0.65 | 0.71 |
| $\Delta m^*_{sat}/m$ | | | 0.03 | -0.08 | -0.09 |

**Table 2.1:** *Value of each of the empirical parameters, associated unit, and derivative order N for BSk14 [GSP07], PKDD [Lon+04], and TM1 [SKT95] functionals.*

Eq. (2.1) is called the TOV equation of hydrostatic equilibrium. The integration of Eq. (2.2) from $r = 0$ to the boundary $r = R$, $R$ being the NS radius, gives the total gravitational mass $M = m(R)$ of the star. Eq. (2.3) is a relativistic equation for the metric function $\Phi(r)$. This equation will be needed for the computation of the moment of inertia in 2.1.2. Here, we focus on solving Eqs. (2.1) and (2.2), which gives the profiles $P(r)$, $\rho(r)$, and $m(r)$ for a given EoS, $P(\rho_B)$, the determination of which was discussed in detail in Chapter 1.

In view of solving the hydrostatic equilibrium equations for a given tabulated EoS, one first has to choose an arbitrary value for the central mass density $\rho_c$ and interpolate the central pressure $P_c = P(\rho_{B,c})$, corresponding to $r = 0$, with the associated boundary condition $m(r = 0) = 0$. Then, using a Runge-Kutta method, we integrate up to $r = R$, defined as $P(r = R) = 0$ (our numerical condition is $P < 5 \times 10^{-4}$ MeV/fm$^3$, which is a sufficiently low value of the pressure to get convergent values for the total mass). At each new step of pressure, one has to interpolate the mass density $\rho$ in the table. In the end, for a given value of central mass density $\rho_c$, one obtains the profiles $P(r)$, $\rho(r)$, and $m(r)$, and therefore a value for the NS mass $M$ and radius $R$. The typical canonical value of the NS mass is $M = 1.4M_\odot$, with a corresponding radius $R = 10 - 14$ km [HPY07]. In fact, the central density inside a specific NS is not known, and is expected to range from $\approx 4.6 \times 10^{14}$ g/cm$^3$ to $\approx 4 \times 10^{15}$ g/cm$^3$. For this reason, we are rather interested in the mass-radius relation, which can be obtained by calculating $M$ and $R$, following the numerical method previously explained, for that range of central mass densities*.

The left panel of Fig. 2.1 shows the mass-radius relation for several popular EoS

*Let us recall that one has to redefine the high-order parameters $Q_{sat(sym)}$ and $Z_{sat(sym)}$ in order to reproduce existing functionals at densities greater than $2n_{sat}$ with the metamodeling technique. This corresponds to the ELFd technique introduced in [MHG18a], see 1.3.2.

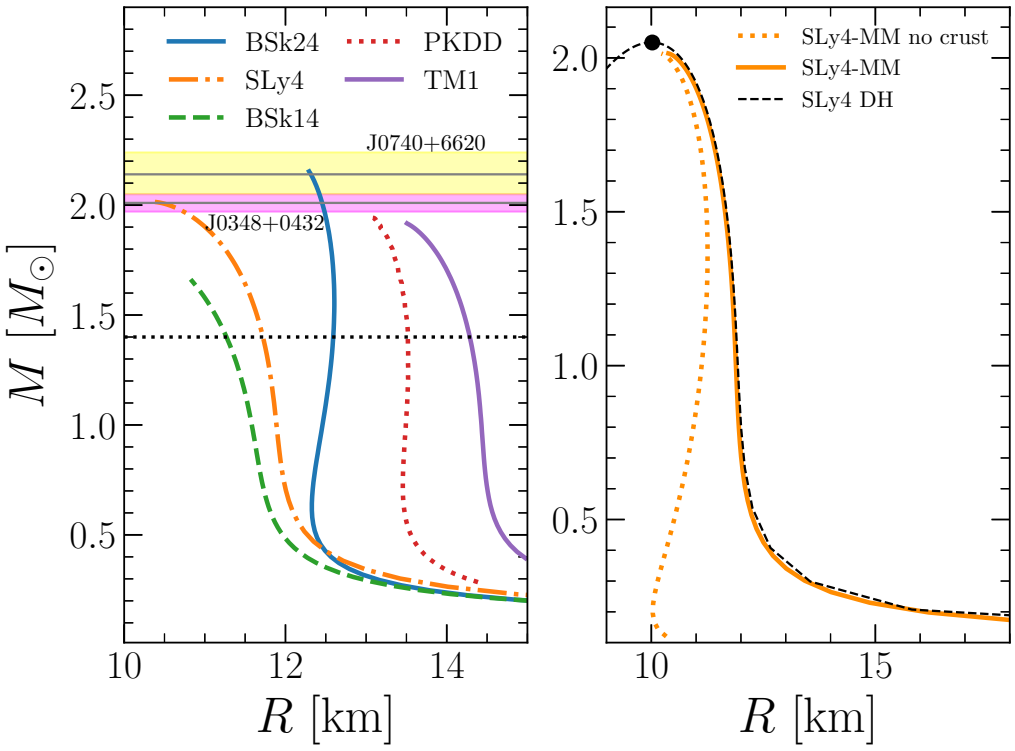



**Figure 2.1:** *Left: Mass-radius relation for several popular EoS calculated with the metamodeling technique. The black dotted line marks the NS canonical mass, that is* $1.4M_\odot$*. The magenta band represents the measured mass of PSR J0348+0432,* $(2.01 \pm 0.04)M_\odot$ *[Ant+13], and the yellow band that of PSR J0740+6620,* $2.14^{+0.10}_{-0.09}M_\odot$ *(68.3% credibility interval) [Cro+20]. Right: Mass-radius relation for the DH EoS for SLy4 functional (black dashed line), and the SLy4 EoS calculated with the metamodeling technique (solid orange line). The black circle indicates the maximum mass.*

based on Skyrme-type functionals BSk24, SLy4, and BSk14, and relativistic models PKDD and TM1, calculated within the metamodeling technique. A strong model dependence is observed, with radii of canonical NS ranging from $R_{1.4} = 11.5$ km for BSk14[†] to $R_{1.4} = 14.5$ km for TM1. More specifically, it is seen that a stiffer density dependence of the symmetry energy leads to larger radii. Indeed, a positive correlation between $R_{1.4}$ and $L_{sym}$ has been often highlighted in the literature [Ala+16; Ji+19; Hu+20]. However, to pin down which is the more influential parameter that determines the NS radius, a simple comparison between models is not enough, and a full statistical analysis is needed. Such analysis is presented in Section 2.3. The value of the empirical parameters associated to BSk14, TM1, and PKDD are reported in Table 2.1, whereas those of BSk24 and SLy4 can be found in Table 1.3. The bands correspond to the measured masses of two massive pulsars, which are traditionally

[†]The BSk14 parametrization is an old representative of the BSk functionals. More modern versions of the BSk family are employed elsewhere in this thesis. Even if it does not belong to the most up-to-date functionals, it gives a good illustration of the prediction of a very soft EoS.

used as viable constraints due to the limited model dependence of the determinations. The mass of PSR J0348+0432 was precisely estimated to $(2.01 \pm 0.04)M_\odot$ [Ant+13], and the very recent relativistic Shapiro delay measurements of PSR J0740+6620 led to $2.14^{0.10}_{-0.09}M_\odot$ (68.3% credibility interval) [Cro+20]. Naturally, if an EoS cannot allow such high masses, it should not be considered as reliable, in particular at high density, since the maximum mass is determined by the stellar core EoS. In particular, it is seen that the maximum mass corresponding to the BSk14 functional, $1.8M_\odot$, is lower than the measured mass of PSR J0348+0432. Also, while the SLy4 EoS satisfies this constraint, the maximum mass for this EoS, $2.05M_\odot$, is marginally compatible with the mass of PSR J0740+6620 at 68.3%. This outlines the fact that measuring the mass of pulsars is important, because it provides a strong constraint on the stellar matter EoS. Similarly, the NICER telescope is expected to provide, for years to come, a constraint on the NS radii with a precision of 5%. Ultimately, in the ideal case where one could accurately measure the mass and radius of one neutron star, it would be possible to determine the EoS by positioning the point in the $M - R$ diagram.

The mass-radius relation for the SLy4 EoS is represented in the right panel of Fig. 2.1. The solid orange line corresponds to $M(R)$ for the SLy4 EoS calculated within the metamodeling technique, and the dashed black line is the calculation for the same SLy4 functional from [DH01]. A perfect agreement is observed between the two curves, reflecting the small discrepancy between the EoS, already illustrated in Fig. 1.15. The dotted orange line shows the mass-radius relation for the SLy4 EoS without considering the clustering of matter at low density, that is assuming that the NS star interior consists of homogeneous $npe\mu$ matter at all densities. In that case, for a canonical NS, we find $R_{1.4} = 11.1$ km, which is almost 1 km lower with respect to the result with a crust EoS. Moreover, this difference is found to be larger with decreasing mass. This shows that the crust EoS is essential to properly predict NS radii [PCS20]. However, we can see that the NS maximum mass is entirely determined by the stellar core EoS. The black point marks the maximum mass for the SLy4 EoS, $M_{max} = 2.05M_\odot$. One can show that the branch left to the point is unstable, because from this point the mass decreases with increasing central density [Har+65].

#### 2.1.1.2 Crust thickness and mass

As explained in Chapter 1, a precise estimation of the CC transition point is required as far as crustal properties are concerned. In particular, the transition pressure $P_t$ is essential for the determination of the proper depth and mass of the crust, given respectively by $l_{crust} = R - R_{core}$ and $M_{crust} = M - M_{core}$, with $R_{core}$ ($M_{core}$) the radius (mass) of the stellar core. Indeed, in order to calculate the core radius and mass, which are involved in the calculation of the crustal observables, one has to integrate the hydrostatic equilibrium equations, Eqs. (2.1) and (2.2), from $r = 0$ to $r = R_{core}$, defined as $P(r = R_{core}) = P_t$.

Fig. 2.2 shows the variation with NS mass of crust thickness $l_{crust}$ and mass $M_{crust}$ for the same EoS as in Fig. 2.1. As explained in 1.3.2, for each functional, when we integrate the TOV equation, we redefine the high-order empirical parameters such to fasten the series convergence at high density. However, the transition pressure is calculated using the values of $Q_{sat(sym)}$ and $Z_{sat(sym)}$ derived from the Taylor expansion

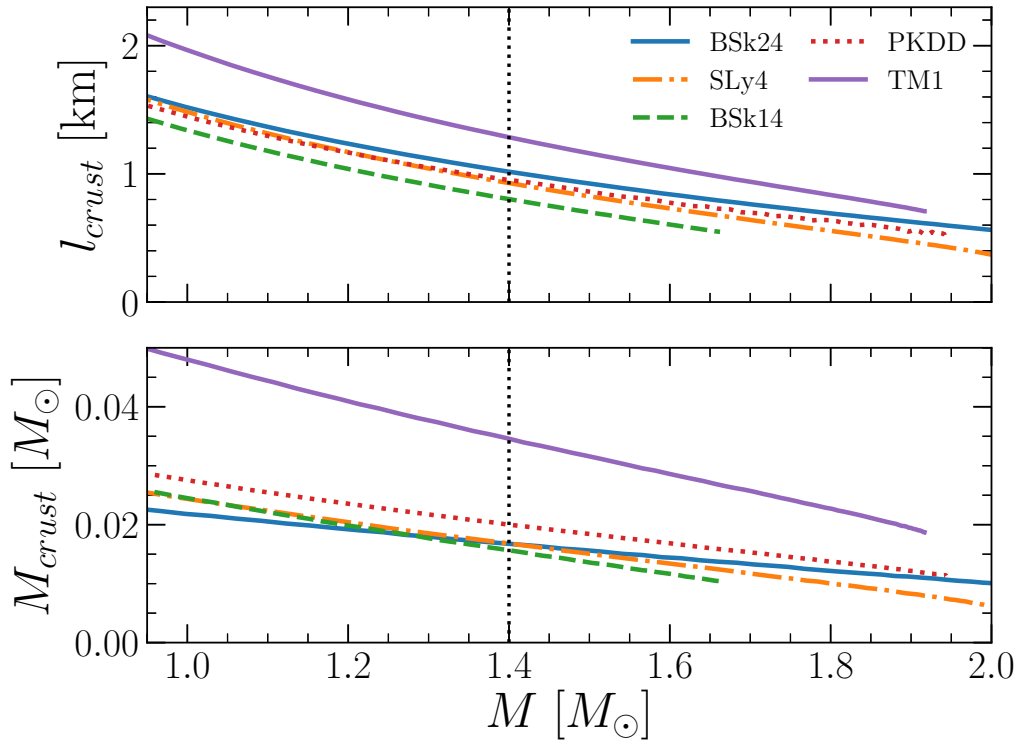



**Figure 2.2:** *Crust thickness $l_{crust}$ (upper panel) and mass $M_{crust}$ (lower panel) as a function of the NS mass $M$ for several popular EoS calculated within the metamodeling technique. The black dotted line marks the NS canonical mass, that is $1.4M_\odot$.*

at saturation. The reason is that, as shown in Fig. 1.12, the determination of CC transition point is sensitive to orders $N > 2$, and the Taylor expansion around saturation is reliable in the subsaturation regime. We find the interesting result that the crust is thicker for low-mass neutron stars, and that $M_{crust}$ drops continuously with increasing NS mass. At $M = 1.4M_\odot$ (black dotted line), we observe that the crust is $\approx 1$ km thick, and that the crust mass is approximately $0.02 - 0.04M_\odot$, which is $(1.5 - 3)\%$ of the total mass. Once again, a model dependence is observed. Nonetheless, the correlation of the crust thickness with the stiffness of the EoS is not clear. In Fig. 2.1, we have seen that the radius of the star is positively correlated with the stiffness of the density dependence of the symmetry energy. In fact, the same is true for the core radius, explaining why the correlations are less evident in the crust thickness $l_{crust} = R - R_{core}$.

### 2.1.2 Moment of inertia within the slow rotation approximation

We now turn to the calculation of the moment of inertia within the slow rotation approximation [Har67]. In fact, this approximation is not only applicable to slowly rotating pulsars but it is also reliable for most of them. Indeed, while many observed

pulsars show rapid rotation [SLL13], their structure is almost not altered by it since centrifugal forces are small in comparison to the gravity, $R^3\Omega^2/(GM) \ll 1$, $\Omega$ being the angular frequency. For instance, assuming canonical values $M = 1.4M_\odot$ and $R = 10$ km for the fastest-spinning pulsar known, PSR J1748-2446ad, at $\Omega = 716$ s$^{-1}$ [Hes+06], we find $R^3\Omega^2/(GM) \approx 0.0028$. However, there are limitations of the slow rotation approximation, namely the fact that it cannot accurately reproduce the mass-shedding limit, and that the definition of the gravitational mass and angular momentum are not accurate enough to robustly indicate an instability [Hae+16].

In the following, we first calculate the total moment of inertia and the fraction of it contained in the NS crust for several popular EoS. Then, we explain the connection between the fraction of crust moment of inertia and the glitch behavior exhibited by some pulsars [Esp+11].

#### 2.1.2.1 Total moment of inertia and fraction contained in the crust

In a slowly rotating NS, the total moment of inertia is given by [Har67]

$$I = \frac{8\pi}{3}\int_0^R dr r^4 \left(\rho + \frac{P}{c^2}\right)\frac{\bar{\omega}}{\Omega}e^{-\lambda-\Phi}. \tag{2.5}$$

We can see that the equation for the field, Eq. (2.3), has to be solved together with the TOV equation, Eqs. (2.1) and (2.2). In the above expression, we have introduced the rotational drag function $\bar{\omega}(r)$, which expresses the difference between the constant spin rate $\Omega$ and the local angular velocity of the initial frame $\omega(r)$, and satisfies

$$\frac{d}{dr}\left(r^4 j\frac{d\bar{\omega}}{dr}\right) = -4r^3\bar{\omega}\frac{dj}{dr}, \tag{2.6}$$

with $j = e^{-\Phi-\lambda}$. Eq. (2.6) satisfy the following boundary conditions at the surface and center of the NS, respectively:

$$\frac{1}{\Omega}\bar{\omega}(r = R) = 1 - \frac{2GI}{R^3c^2} \quad \text{and} \quad \left.\frac{d\bar{\omega}}{dr}\right|_{r=0} = 0. \tag{2.7}$$

One can translate Eq. (2.6) into a first-order differential equation by introducing $w = (1/\Omega)d\ln\bar{\omega}/d\ln r$, yielding

$$\frac{dw}{dr} = \frac{4\pi G}{c^2}\frac{(P+\rho c^2)(4+w)r^2}{rc^2 - 2Gm} - \frac{w}{r}(3+w), \tag{2.8}$$

with the boundary condition $w(r = 0) = 0$. This equation is solved together with Eqs. (2.1) and (2.2) instead of Eq. (2.3) in order to calculate the total moment of inertia, which can be rewritten more simply as a function of the function $w$ as

$$I = \frac{c^2}{G}\frac{w(R)R^3}{6 + 2w(R)}. \tag{2.9}$$

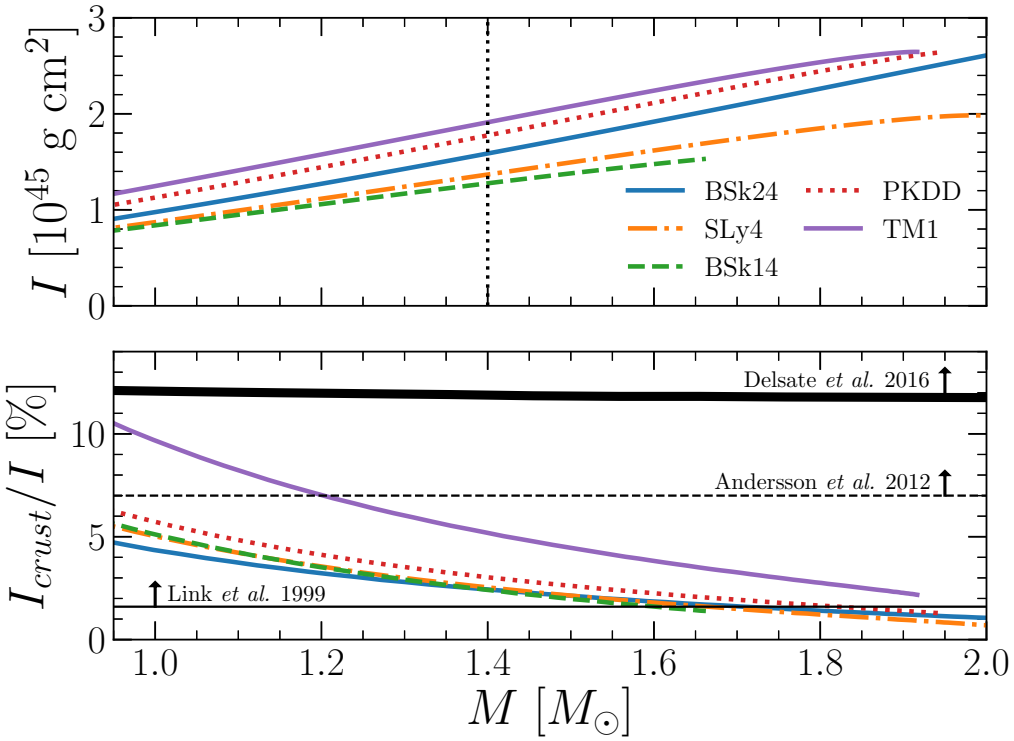



**Figure 2.3:** *Moment of inertia $I$ (upper panel) and fraction of crust moment of inertia $I_{crust}/I$ (lower panel) as a function of the NS mass $M$ for several popular EoS calculated within the metamodeling technique. In the upper panel, the black dotted line marks the NS canonical mass, that is $1.4M_\odot$. In the lower panel, the minimum values needed to justify Vela glitches with (Delsate et al. [Del+16] and Andersson et al. [And+12]) and without (Link et al. [LEL99]) crustal entrainment are represented.*

The fractional crust moment of inertia can also be calculated as [LHS19]

$$\begin{aligned} \frac{I_{crust}}{I} &= 1 - \frac{I_{core}}{I} \\ &= 1 - \left(\frac{R_{core}}{R}\right)^3 \frac{w(R_{core})}{w(R)} \exp\left[-\int_{R_{core}}^{R} \frac{w(r)}{r} dr\right], \end{aligned} \tag{2.10}$$

where we have introduced the moment of inertia of the core $I_{core}$, defined by the integration of Eq. (2.5) up to the core radius $R = R_{core}$.

The total moment of inertia is plotted as a function of the NS mass in the upper panel of Fig. 2.3 for EoS based on Skyrme-type functionals BSk24, SLy4, and BSk14, and relativistic models PKDD and TM1. For $M = 1.4M_\odot$, it is found that $I$ ranges from $\approx 1.2 \times 10^{45}$ g cm$^2$ for the soft BSk14 EoS to $\approx 2 \times 10^{45}$ g cm$^2$ for the very stiff TM1 EoS. This shows the strong dependence on the EoS, that appears to be even larger for high-mass NS.

The lower panel of Fig. 2.3 shows the variation with NS mass of $I_{crust}/I$ for the same EoS. It is seen that the more massive an NS is, the less moment of inertia it

stores in its crust, which follows the trends observed in Fig. 2.2. This is expected from the sensitivity of crustal properties to the CC transition pressure. Given the selected EoS, the value of $I_{crust}/I$ at $M = 1.4M_\odot$ ranges from $\approx 2\%$ for BSk14 to $\approx 5\%$ for TM1, showing once again the important dependence on the EoS. The studies on crust properties requires a unified modeling, such as the one introduced in Chapter 1. Nonetheless, there have been propositions to obtain crust properties from the mere knownlege of the EoS of homogeneous matter and the density and pressure at the CC transition point [ZFH17], though we have tested those methods and found that they are imprecise for $M \lesssim 1.2M_\odot$.

#### 2.1.2.2 Connection to pulsar glitches

As discussed in the introduction, sudden spin-ups of radio pulsars, called glitches, are thought to be produced by angular momentum transfer from the superfluid component of the stellar interior to the solid crust.

For a given glitcher, three quantities are usually measured: its spin frequency $\Omega$, its average spin-down rate $\dot{\Omega}$, and its glitch activity parameter $\mathcal{A}$, defined as

$$\mathcal{A} = \frac{1}{t}\sum_{i=1}^{N}\frac{\Delta\Omega_i}{\Omega}, \tag{2.11}$$

where $\sum_i \Delta\Omega_i/\Omega$ represents the cumulative spin-up rate over the $N$ glitches occurring during a time $t$.

It was demonstrated in [LEL99] that the ratio of the moment of inertia associated to the neutron superfluid which drives the glitches $I_{sf}$ to the moment of inertia of the solid crust – plus any portion of the star strongly coupled to it – $I_c$ must satisfy

$$\frac{I_{sf}}{I_c} \geq \frac{\Omega}{|\dot{\Omega}|}\mathcal{A} \equiv \mathcal{G}, \tag{2.12}$$

where we have introduced the coupling parameter $\mathcal{G}$. In view of relating the observational constraint $\mathcal{G}$ to the fractional moment of inertia $I_{crust}/I$ to ultimately set a constraint on the stellar EoS, we assume that the angular momentum reservoir is confined to the neutron superfluid coexisting with the crystal lattice of the inner crust. This is justified by the fact that the pairing gap in PNM vanishes at suprasaturation densities [CLS06]. In that case, we have $I_c = I - I_{res} \simeq I$ ($I_{res}$ being the moment of inertia of the reservoir) and $I_{crust} \simeq I_{sf}$, yielding [LEL99]

$$\frac{I_{sf}}{I_c} \simeq \frac{I_{crust}}{I} \geq \mathcal{G}. \tag{2.13}$$

In reality, the neutron superfluid is strongly coupled to the solid crust due to nondissipative entrainment effects [Cha13], limiting the amount of angular momentum that can be transferred during a glitch event. The importance of the entrainment coupling is related to the neutron effective mass $m_n^*$ in the inner crust, which is proportional to the ratio of unbound neutrons to those that are not entrained, $m_n^* \equiv m_n n_g/n_g^c$.

Taking into account the entrainment effects, the previous constraint, Eq. (2.13), then becomes [CCH05; And+12]

$$\frac{I_{crust}}{I} \geq \mathcal{G}\frac{\langle m_n^* \rangle}{m_n}, \tag{2.14}$$

with $\langle m_n^* \rangle$ the average neutron effective mass[‡]. It should be stressed that systematic calculations of $m_n^*$ throughout the NS crust are very costly from the computational point of view. To get an order of magnitude of the effect, following [And+12; PFH14], we adopt the value $\langle m_n^* \rangle / m_n = 4.3$, which is inferred from the results of [Cha12] obtained with the BSk14 functional. Naturally, one recover the expression without crustal entrainment in the case of $\langle m_n^* \rangle = m_n$. We should stress that the importance of the effect of crustal entrainment, that is the value of the average neutron effective mass throughout the solid crust, is currently under debate [MU16; WP17].

The Vela pulsar (PSR B0833-45) is one of the most active glitchers known, with glitches occurring four times per decade on average. Since the beginning of its monitoring, almost 50 years ago, it has exhibited 20 glitches in total [Jod], allowing for a precise estimation of the corresponding coupling parameter, $\mathcal{G}_{\rm Vela} = (1.62 \pm 0.03) \times 10^{-2}$ [Ho+15]. This can be translated into a constraint for the fraction of crust moment of inertia,

$$\left(\frac{I_{crust}}{I}\right)_{\rm Vela} \geq (1.62 \pm 0.03) \times 10^{-2} \frac{\langle m_n^* \rangle}{m_n} \approx 0.07. \tag{2.15}$$

In other words, in the standard picture where the angular momentum reservoir is exclusively confined to the neutron superfluid permeating the inner crust, the crust must store more than 7% (with entrainment effects included) of the total moment of inertia in order to justify the large glitches occurring in the Vela pulsar.

The Vela constraints on $I_{crust}/I$ are displayed in the lower panel of Fig. 2.3. Neglecting entrainment effects [LEL99], it is seen that the constraint is easily satisfied. For BSk14 EoS, which is the softest EoS here, it leads to $\approx 1.6 M_\odot$ for the maximum mass of Vela. Now including crustal entrainment with $\langle m_n^* \rangle / m_n = 4.3$ [And+12], it is not clear, due to dependence on the EoS, whether the superfluid neutron in the crust can carry enough angular momentum to explain Vela glitches. For the three nonrelativistic Skyrme-based EoS that we consider, we see that the constraint is unlikely to be satisfied, because it would require Vela mass to be very low, $M_{\rm Vela} \lesssim 0.9 M_\odot$. While theoretically possible [HPY07], such low-mass NS have never been observed to this day. On the other hand, it is observed that very stiff EoS such as TM1 can be consistent with the constraint [PFH14]. Finally, given the constraint on the fractional moment of inertia calculated with the present largest estimation of crustal entrainment [Del+16] (black thick line), we find that the inferred mass of Vela is at most $\approx 0.85 M_\odot$ for the stiff TM1 EoS and $\approx 0.65 M_\odot$ for the soft EoS based on Skyrme functionals. Clearly

[‡]It is important to stress that this effective mass differs from the definition Eq. (1.35), which corresponds to the $k$-mass $m_k$ arising from the spatial nonlocality of the mean field. For transport properties, which correspond to a dynamical phenomemon, the full nonlocality of the interaction in space and time must be considered, leading to the definition of the $\omega$-mass, $\omega$ being the frequency. In this context, the effective mass reads $m^* = m_k m_\omega / m$, where $m_\omega = 1 - \partial U(k,\omega)/\partial\omega$ is the $\omega$-mass. In the latter expression, $U(k,\omega)$ corresponds to the momentum and frequency dependent average potential.

the question "*Is the crust enough?*" deserves further investigations. In that sense, it will be addressed in 2.3.3 in the context of a complete statistical analysis [CGM19b].

### 2.1.3 Tidal deformability

Theoretically, for the gravitational signal observed before merger, the tidal deformability is the part which is sensitive to the EoS. In that sense, GW observations can ultimately provide new constraints on the EoS. In particular, the first detection of GW from the coalescence of two NS, the GW170817 event, has yielded important constraints for the tidal deformability of NS [Abb+18].

Let us consider a static, spherically symmetric NS, placed in a static external quadrupolar tidal field $\mathcal{E}_{tid}$. The induced quadrupole moment of this star is given by

$$Q_{tid} = -\lambda \mathcal{E}_{tid}, \tag{2.16}$$

where $\lambda$ is the tidal deformability, which is related to the so-called tidal Love number $k_2$ by

$$\lambda = \frac{2}{3} k_2 \left( \frac{Rc^2}{G} \right)^5 . \tag{2.17}$$

Let us also define the dimensionless tidal deformability,

$$\Lambda = \frac{\lambda}{M^5} = \frac{2}{3} k_2 \beta^{-5}, \tag{2.18}$$

where we have introduced the compactness of the star $\beta = GM/(Rc^2)$. Similarly to the moment of inertia in the slow rotation approximation, $k_2$ can be obtained from the solution of the following first-order differential equation [Hin+10],

$$\begin{aligned} \frac{dy}{dr} &= -\frac{y^2}{r} - \frac{y-6}{r-2Gm/c^2} \\ &\quad -\frac{4\pi G}{c^2} r^2 \frac{(5-y)\rho + (9+y)P/c^2 + (P+\rho c^2)/c_s^2}{r-2Gm/c^2} \\ &\quad +\frac{1}{r}\left[ \frac{2G}{c^2} \frac{(m+4\pi p r^3/c^2)}{r-2Gm/c^2} \right]^2 , \end{aligned} \tag{2.19}$$

where we have introduced the speed of sound $c_s = \sqrt{\partial P/\partial \rho}$. The function $y = y(r)$ must satisfy the boundary condition $y(r=0) = 2$. Eq. (2.19) together with the hydrostatic equilibrium equations, Eqs. (2.1) and (2.2), are solved simultaneously. The tidal Love number reads

$$k_2 = \frac{8}{5} \beta^5 (1-2\beta)^2 [2 - y(R) + 2\beta(y(R)-1)]/a, \tag{2.20}$$

with

$$\begin{aligned} a &= 6\beta[2 - y(R) + \beta(5y(R)-8)] \\ &\quad +4\beta^3[13 - 11y(R) + \beta(3y(R)-2) + 2\beta^2(1+y(R))] \\ &\quad +3(1-2\beta)^2[2 - y(R) + 2\beta(y(R)-1)]\ln(1-2\beta). \end{aligned} \tag{2.21}$$

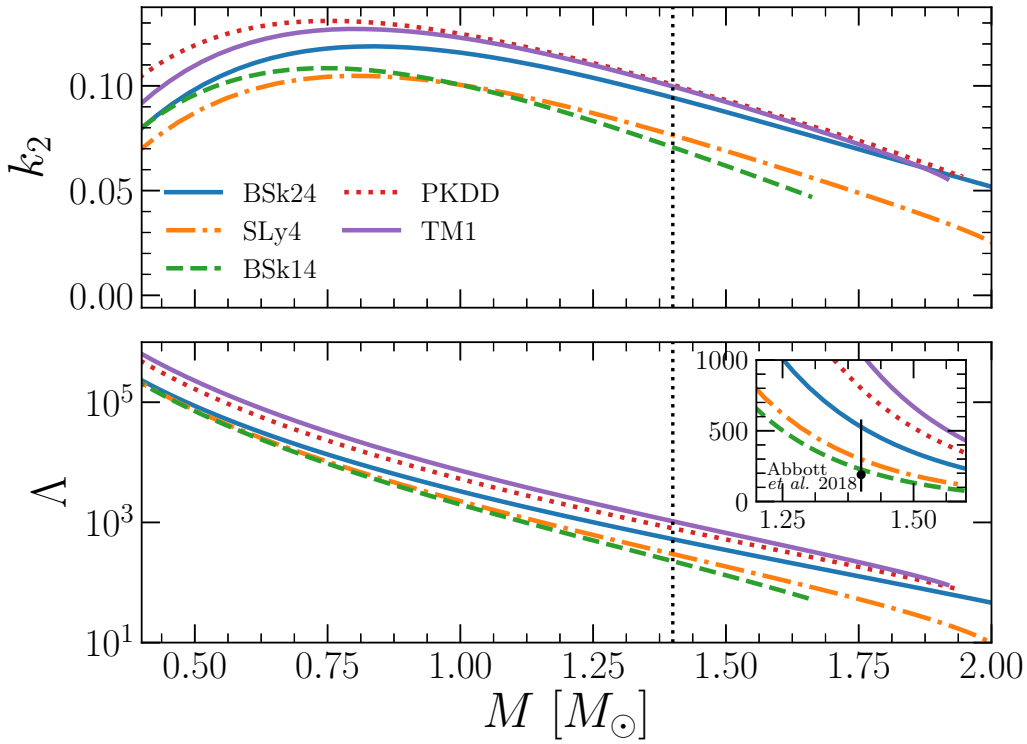



**Figure 2.4:** *Tidal Love number $k_2$ (upper panel) and dimensionless tidal deformability $\Lambda$ (lower panel) as a function of the NS mass $M$ for several popular EoS calculated within the metamodeling technique. The black dotted line marks the NS canonical mass, that is $1.4M_\odot$. In the inset of the lower panel, the value $\Lambda_{1.4} = 190^{+390}_{-120}$ (at 90% level) inferred from GW170817 event is represented [Abb+18].*

Fig. 2.4 shows the variation with NS mass of $k_2$ for the several popular EoS that we consider in this chapter. The tidal Love number measures how easily the bulk of the matter in an NS is deformed. In the case of the mass being concentrated at the center of the star, the tidal deformation is small, and so is $k_2$. In agreement with [Hin+10], we find that $k_2$ lies in the range $\approx 0.05 - 0.15$. The relative difference between the present EoS is of the order of $\approx 35\%$ for $M = 1.4M_\odot$, showing once again the notable dependence on the EoS. In particular, it has been shown very recently that $k_2$ is sensitive to $L_{sym}$ but not to $E_{sym}$ [PCS19; PCS20]. Let us also point out that the tidal Love number is very sensitive to the description of the crustal component of the EoS [PF19].

The dimensionless tidal deformability is plotted as a function of $M$ in the lower panel of Fig. 2.4. In the mass range considered, it is seen that the more massive the NS is, the less it gets deformed when orbiting another massive compact object. In the inset, we show the value of the dimensionless tidal deformability for a $1.4M_\odot$ NS inferred from the GW170817 event, $\Lambda_{1.4} = 190^{+390}_{-120}$ at the 90% level. We can observe that the EoS which predict the largest tidal effects, PKDD and TM1, are unlikely. One can notice the tension between the evidence of a rather soft EoS, typically satisfied

by nonrelativistic Skyrme-type functionals, which predict small tidal deformations, and the need of a rather stiff EoS, typically obtained in the framework of relativistic models, to explain the glitch phenomenon as well as the most massive NS.

## 2.2 Bayesian determination of the equation of state parameters

In recent years, there has been a lot of efforts invested in the development of the chiral EFT [DHS16] with the aim of providing new constraints on the low-density EoS. As we have already discussed, the maximum observed mass of NS [Ant+13; Cro+20] establishes a stringent constraint on the EoS. Furthermore, and for the same reason, future observations of GW signatures associated to binary NS mergers with LIGO and Virgo, and radius measurements from observatories such as NICER and Chandra will be beneficial. Bayesian inference is a statistical method which allows to account both for the present day knowledge on nuclear physics and NS observables for predicting the stellar matter EoS.

This section deals with the Bayesian determination of the EoS parameters. The general formalism of Bayesian inference is recalled and its application for constraining the EoS is explained in 2.2.1. In 2.2.2, we give the prior distribution of EoS parameters and a sensitivity analysis of the CC transition point is carried out afterwards. The likelihood function, based on constraints on nuclear physics observables, constraints on NS observables, and physical requirements, is constructed in 2.2.3. Finally, we present the posterior distribution of empirical parameters in 2.2.4. A particular attention is paid to the correlations among parameters.

### 2.2.1 Principle of Bayesian inference

The core of Bayesian inference is based on Bayes' theorem, which provides an expression for the conditional probability (or posterior probability) of a set of values for an ensemble of random variables $A$ given a second set $B$,

$$P(A|B) = \frac{P(B|A)P(A)}{P(B)}. \tag{2.22}$$

In this equation, $P(B|A)$ is the conditional probability of $B$ given $A$, $P(A)$ is the prior probability of $A$, and $P(B)$ that of $B$. The key point of the method is to realize that random variables are not limited to observational data, but they can comprise unknown parameters entering a theoretical modeling (the EoS parameters in our case). In this model form of Bayes' theorem, one replaces $B$ by data, $A$ with a parameter set $\boldsymbol{X}$, and $P$ with probability density functions (PDF) $p$, resulting in [SS06]

$$p(\boldsymbol{X}|\text{data}) = \frac{p(\text{data}|\boldsymbol{X})p(\boldsymbol{X})}{p(\text{data})}. \tag{2.23}$$

The denominator acts as a normalization constant which makes sure that the posterior distribution $p(\boldsymbol{X}|\text{data})$ is a true probability distribution, by ensuring that the sum of

the distribution is equal to 1. It is given by

$$p(\text{data}) = \int p(\text{data}|\boldsymbol{X})p(\boldsymbol{X})d\boldsymbol{X}. \tag{2.24}$$

The model-based formulation of Bayes' theorem, Eq. (2.23), is therefore often written as

$$p(\boldsymbol{X}|\text{data}) \propto p(\text{data}|\boldsymbol{X})p(\boldsymbol{X}). \tag{2.25}$$

The marginal one- and two-parameter posterior distributions can be extracted from the posterior distribution. They are defined respectively as

$$p(X_j|\text{data}) = \left\{\prod_{i\neq j}\int dX_i\right\} p(\boldsymbol{X}|\text{data}), \tag{2.26}$$

$$p(X_j, X_k|\text{data}) = \left\{\prod_{i\neq j,k}\int dX_i\right\} p(\boldsymbol{X}|\text{data}). \tag{2.27}$$

Let us describe the different components of Bayesian inference. The prior distribution $p(\boldsymbol{X})$ represents our knowledge or bias on the model parameters, prior to the measurement noted "data". It can thus be more or less informative. $p(\text{data}|\boldsymbol{X})$ is the likelihood of observing the data given the model parameters $\boldsymbol{X}$. It is determined from the data comparison between the model and the measurement via an error estimator. In that sense, the link between the data and the model parameters is encoded in the likelihood distribution. Multiplying the prior by the likelihood function, one obtains the unnormalized joint posterior PDF, which corresponds to the conditional distribution of model parameters $\boldsymbol{X}$ given the data. Let us notice that the prior distribution obviously affects the posterior distribution, implying that it has to be handled with care, and the choice of the prior is the most delicate part of the method.

Bayesian inference is an appealing statistical method in the sense that it allows to calculate the joint posterior distribution of model parameters using prior beliefs updated with the likelihood. In the context of NS physics, and from the nuclear physicist point of view, it allows for instance to update our knowledge on the nuclear EoS by taking into consideration the data arising from various astrophysical observations, that are for example the NS mass inferred from Shapiro delay or the tidal deformability from GW measurements. Conversely, one can account for nuclear physics constraints in the prediction of macroscopic observables related to NS. In our case, we first generate a large number of EoS, each of them being defined by a set of parameters $\boldsymbol{X}$, to numerically sample the prior parameter distribution. Then, we filter those EoS through constraints, which arise from physical requirements, astrophysical observations, and *ab initio* calculations of SNM and PNM. This gives us the joint posterior distribution of model parameters, from which we can finally calculate the posterior EoS and make general predictions for NS observables. Those predictions are presented in Section 2.3.

Let us describe the parameter set $\boldsymbol{X}$. Our calculation of the stellar EoS is based on the metamodeling of nuclear matter energy [MHG18a] introduced in 1.2.1.1. The empirical parameters $E_{sat}$, $n_{sat}$, $K_{sat}$, $Q_{sat}$, $Z_{sat}$, $E_{sym}$, $L_{sym}$, $K_{sym}$, $Q_{sym}$, and $Z_{sym}$ – which we recall are given by the successive derivatives of the NM energy at saturation density in isoscalar and isovector sectors – therefore enter into the parameter set.

The parameter $b$ is also added in order to explore different functional behaviors close to the $n \to 0$ limit. This is motivated by the fact that the behavior of Skyrme-type functionals is not correct at extremely low densities [GLY17]. The parameter $b$, together with the isoscalar effective mass $m^*_{sat}/m$ and isospin splitting $\Delta m^*_{sat}/m$, completes the parameter space, associated to the description of bulk matter. In the solid crust, the metamodeling technique is supplemented by a surface plus curvature term in order to describe the surface properties of finite nuclei. Thus, one could consider adding the surface and curvature parameters, respectively $\sigma_0$, $b_s$, $p$, and $\sigma_{0c}$, $\beta$, as extra parameters to $\boldsymbol{X}$. However, we have seen in Fig. 1.5 that the $\chi^2$ function, which evaluates the goodness of the fit of those parameters to experimental nuclear masses given BSk24 empirical parameters and $p = 3$, is strongly peaked on a given set $\boldsymbol{S} = \boldsymbol{S_{opt}}$. This feature is generic and not limited to BSk24, and we therefore choose to not include the surface and curvature parameters in $\boldsymbol{X}$ but to take the set $\boldsymbol{S_{opt}}$ that minimizes $\chi^2$, as explained in 1.2.1.2. It is important to stress that, even if we keep only the optimized values for the surface and curvature parameters for each parameter set, a large parameter space is explored for the surface energy because of the large variation of the bulk properties and the physical correlation between surface and bulk due to the fit to experimental data. We consider two choices for the value of the parameter $p$, which determines the behavior of the surface tension for extreme isospin values for a given set of empirical parameters. Either it is fixed to the educated value $p = 3$, or the range $p = \{2.5, 3, 3.5\}$ is explored. The latter option is considered for the determination of observables that are sensitive to the CC transition point, which we have seen is strongly correlated to the isovector properties of the surface tension.

## 2.2.2 Prior distribution of equation of state parameters

We now discuss the prior distribution of empirical parameters. We first give insights concerning the selected intervals for the prior. A sensitivity analysis of the CC transition point is performed afterwards.

### 2.2.2.1 Flat prior compatible with empirical constraints

The prior distribution of $\boldsymbol{X}$ is given by an uncorrelated ansatz and an uniform distribution of each parameter within the interval specified in Table 2.2,

$$p(\boldsymbol{X}) = \prod_{i=1}^{2(N+1)+3} \mathcal{U}(X_i^{min}, X_i^{max}; X_i), \tag{2.28}$$

where the parameter $X_i$ is uniformly distributed from $X_i^{min}$ to $X_i^{max}$. The use of a flat prior means that all possible values of $\boldsymbol{X}$ inside the intervals are equally likely *a priori*.

The range of variation for the model parameters reflects the degree of uncertainty on the EoS parameters, as measured by their variation in the functionals which reproduce successfully low energy nuclear physics data [MHG18a]. We can distinguish three groups of empirical parameters, depending on how well they are experimentally constrained. The first group consists of the low-order isoscalar parameters $E_{sat}$, $n_{sat}$, $K_{sat}$,

| Parameter | Unit | $N$ | Min | Max |
|---|---|---|---|---|
| $E_{sat}$ | MeV | 0 | -17 | -15 |
| $n_{sat}$ | $\mathrm{fm}^{-3}$ | 1 | 0.15 | 0.17 |
| $K_{sat}$ | MeV | 2 | 190 | 270 |
| $Q_{sat}$ | MeV | 3 | -1000 | 1000 |
| $Z_{sat}$ | MeV | 4 | -3000 | 3000 |
| $E_{sym}$ | MeV | 0 | 26 | 38 |
| $L_{sym}$ | MeV | 1 | 10 | 80 |
| $K_{sym}$ | MeV | 2 | -400 | 200 |
| $Q_{sym}$ | MeV | 3 | -2000 | 2000 |
| $Z_{sym}$ | MeV | 4 | -5000 | 5000 |
| $m^*_{sat}/m$ | | | 0.6 | 0.8 |
| $\Delta m^*_{sat}/m$ | | | 0.0 | 0.2 |
| $b$ | | | 1 | 10 |

**Table 2.2:** *Minimum value and maximum value of each of the parameters of parameter set* $\boldsymbol{X}$*. The associated unit and derivative order* $N$ *are also reported.*

the symmetry energy at saturation density $E_{sym}$, as well as the effective mass $m^*_{sat}$ and isospin splitting $\Delta m^*_{sat}/m$. These parameters are rather well determined by nuclear experiments, with associated relative uncertainties lower than 15%. The second group consists of the parameters that are still poorly determined by nuclear experiments. The uncertainties on the isoscalar skewness $Q_{sat}$, the slope of the symmetry energy $L_{sym}$, and the isovector incompressibility $K_{sym}$ are very large, yet one can expect a better accuracy to be reached in the near future. In particular, the determination of $L_{sym}$ is an highly topical issue nowadays [Li+14]. Finally, the last group concerns the parameters which are inaccessible to nuclear experiments to the present day, that is the isovector skewness $Q_{sym}$ as well as the parameters of order $N = 4$, $Z_{sat}$ and $Z_{sym}$. As a consequence, we explore very large ranges for these parameters. The choice of the interval for the low-density parameter, $b = [1, 10]$, is discussed thoroughly in [Ant+19]. In this paper, we have investigated the influence of the uncertainties of the EoS parameters on the CC transtion point, calculated using the dynamical method with the ETF approach for the surface contribution. We have considered a Bayesian framework with the same prior distribution of empirical parameters and likelihood function as in this thesis, and we have found that $K_{sym}$ and $Q_{sym}$ have the most significant correlations with the transition density and pressure.

#### 2.2.2.2 Sensitivity analysis of the crust-core transition point[§]

Let us recall that one of the advantages of the metamodeling approach is that all the EoS model parameters, that is the empirical parameters, are *a priori* uncorrelated. It is therefore possible to vary each one of them independently of the others, which

[§]Partial results of the presented work have been published in Eur. Phys. J. A (2019) **55**: 188.

is not feasible using specific functional behaviors such as Skyrme, Gogny, or the different versions of RMF, as discussed in detail in [MHG18a; MG19]. Indeed, common functionals describing infinite NM have a smaller number of parameters compared to the metamodel, which creates *a priori* correlations that are not fully controlled. If we take the example of Skyrme forces, the density dependence of SNM is controlled by only three parameters, which are fixed to reproduce the coordinates of the saturation point: $n_{sat}$, $E_{sat}$, and $K_{sat}$. Thus, the isoscalar skewness $Q_{sat}$ is correlated with the three other parameters, and it turns out that this correlation is not the same, for instance, in Skyrme, Gogny, or in RMF functionals [MG19]. A similar argument applies to the symmetry energy: when the density dependence of the symmetry energy is governed by a single parameter as for example often assumed in heavy ion transport models, an isosoft behavior at suprasaturation density is necessarily associated to an isostiff behavior at subsaturation density, while more complicated behaviors are possible [MG19]. The independent variation of the different empirical parameters allows a simple determination of the most influential parameters impacting a given observable under study.

Such a sensitivity analysis is presented in Fig. 2.5 for the CC transition density $n_t$ and transition pressure $P_t$. The reference metamodel used in the sensitivity analysis can have an influence. For this reason, the sensitivity analysis varying one by one the EoS parameters is performed around two different reference parameter sets $\boldsymbol{X_{ref}}$, namely the parameter set corresponding to the BSk24 functional (solid blue lines), and the one corresponding to the BSk22 functional (dashed orange lines)[¶]. For both sets of parameter, we fix $p = 3$ as well as $b = 10\ln(2)$.

The range of variation for each of the EoS parameters corresponds to the intervals for the prior distribution $p(\boldsymbol{X})$ specified in Table 2.2. Let us however notice that some sets produce nonviable EoS, for which a solution for the CC transition point cannot be found. This occurs in particular when varying the value of the isovector incompressiblity parameter $K_{sym}$ with BSk24 as reference parameter set. Indeed, we find an extremely soft behavior for the symmetry energy for the minimum value $K_{sym}^{min} = -400$ MeV. In that very situation, we increase the minimum value of the parameter to $K_{sym}^{min} \approx -300$ MeV so as to find a solution for $n_t$ and $P_t$.

The symbols in Fig. 2.5 give the transition density and pressure domain obtained when the EoS parameters are one by one varied around the reference model, within the interval of Table 2.2. More specifically, circles and squares are respectively associated to the minimum value and maximum value of each parameter. Since the uncertainty on the different parameters is not the same, the relative distance between circles and squares is a qualitative measurement of the propagation of the uncertainty on the transition point brought by each parameter. We can see that the sensitivity of each parameter depends on the value of the other parameters, that is on the chosen reference set $\boldsymbol{X_{ref}}$. Still, universal trends clearly emerge. We can see that the CC phase transition, at variance with the standard liquid-gas of SNM, is almost insensitive to isoscalar parameters. In particular, the influence of the isoscalar parameters in the transition pressure is almost negligible, and only the third derivative term $Q_{sat}$ is influential on $n_t$. This underlines the importance of the energetics of the neutron gas

[¶]Other choices can be found in [CGM19a], leading to same qualitative results.

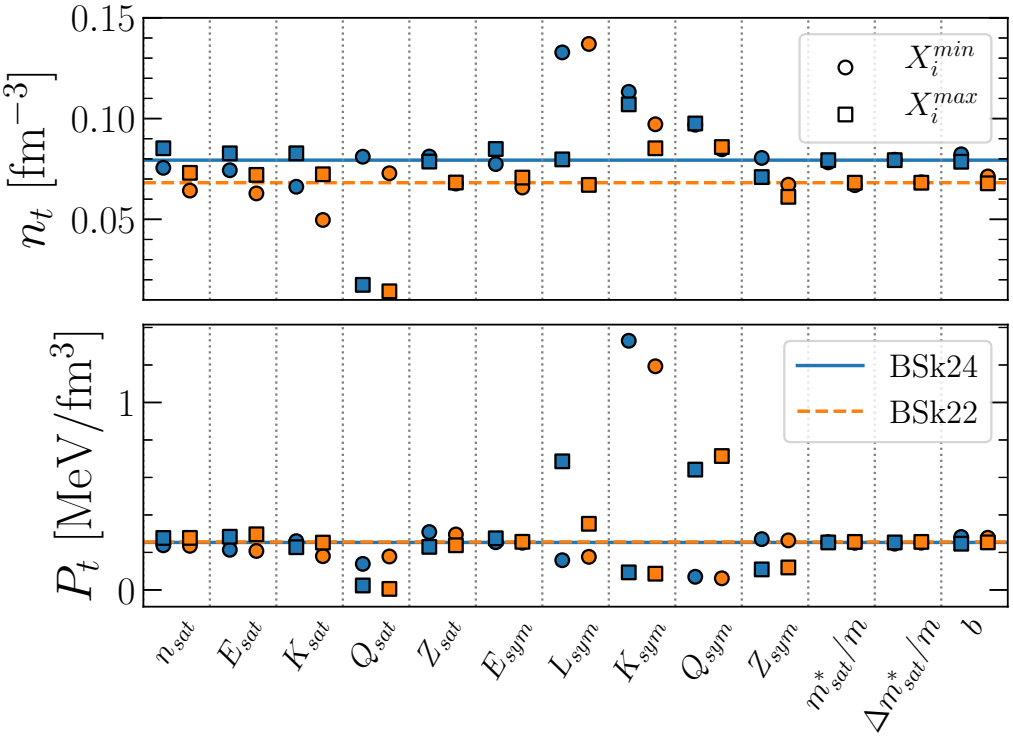



**Figure 2.5:** *Sensitivity analysis of the transition density $n_t$ (upper panel) and transition pressure $P_t$ (lower panel) with respect to EoS parameters. $p = 3$ is fixed and two different reference point are chosen: BSk24 parameters (solid blue lines) and BSk22 parameters (orange dashed lines). For each parameter, the symbols on left (blue) correspond to BSk24 and those on right (orange) to BSk22. The parameters are varied one by one around the two different reference sets of parameters. Circles and squares are respectively associated to the minimum value $X_i^{min}$ and maximum value $X_i^{max}$ of the parameter, which are listed in Table 2.2.*

on the transition point. Concerning the isovector sector, we can see that $L_{sym}$ is the most important parameter as far as the transition density is concerned. This result is in agreement with previous findings by many authors [Duc+11] and was already anticipated in 1.2.6. The symmetry energy at saturation $E_{sym}$ and the effective mass splitting $\Delta m^*_{sat}/m$ do not play any role in the transition. This can be understood from the fact that the symmetry energy at saturation is already relatively well constrained, and that the effective mass enters the kinetic energy, thus at equilibrium variations of $\Delta m^*_{sat}/m$ are compensated by variations of the density derivatives. The transition density and pressure show also a great sensitivity to the isovector incompressibility parameter $K_{sym}$. This can explain why the transition pressure exhibits an irregular behavior when plotted as a function of $L_{sym}$ (see Fig. 1.13): the different functionals considered in the literature have very different values of $K_{sym}$, which blurs the correlation with $L_{sym}$. This effect is also amplified by the fact that, depending on the reference point, the dependence of $P_t$ with $L_{sym}$ is not monotonic. Finally, we can notice that

the influence of the fully unknown high-order derivatives $Q_{sym}$ and $Z_{sym}$, though less important than the one of $L_{sym}$, is not negligible and comparable to the one of the isovector surface energy parameter $p$ that can be inferred from Fig. 1.13. We have checked that similar conclusions can be drawn if the sensitivity analysis is performed using the definition of the transition point from the dynamical spinodal [Ant+19].

### 2.2.3 Determination of the likelihood function

The likelihood function corresponds to the probability of observing the data given the model parameters $\boldsymbol{X}$. In the context of our analysis, it is defined as

$$p(\text{data}|\boldsymbol{X}) = w_{LD}(\boldsymbol{X}) \times w_{HD}(\boldsymbol{X}) \times p_{\text{AME2016}}(\boldsymbol{X}). \tag{2.29}$$

In this expression, $w_{LD}$ and $w_{HD}$ are strict filters that concentrate on constraining the low-density EoS and high density EoS, respectively. Both filters are given by sharp $\delta$ functions that output 1 if the constraint is satisfied, and 0 otherwise. Constraints on nuclear physics observables, yielding the filter $w_{LD}$ and the probability $p_{\text{AME2016}}$ are presented in 2.2.3.1. In 2.2.3.2, we present the constraints corresponding to the filter $w_{HD}$, which are associated to general physical requirements and measurements of NS observables.

#### 2.2.3.1 Constraints on nuclear physics observables

Let us concentrate first on the strict filter $w_{LD}$, hereafter referred to as low-density (LD) filter. It is introduced to verify whether the metamodel associated to a set of parameters $\boldsymbol{X}$ is compatible with the recent chiral EFT calculations for SNM and PNM by Drischler *et al.* [DHS16]. The authors have calculated the energy per particle for several values of isospin at low density within the many-body perturbation theory, based on a set of seven different Hamiltonians with chiral NN and three-nucleon interactions.

The resulting predicted bands for energy per nucleon as well as pressure of SNM and PNM are shown in Fig. 2.6 (pink bands), together with the predictions of the popular BSk24 (solid blue lines) and DD-ME$\delta$ (green dashed lines) functionals. The fact that the seven different Hamiltonians lead to different predictions shows that the *ab initio* calculation is associated to a PDF exactly like an experimental measurement. For this reason, in principle one should not apply a strict filter but rather a likelihood one based on the PDF. The PDF being unknown, this is however practically not feasible, and this is why we employ a strict filter. The pressure band is calculated by taking the density derivative of the energy per nucleon for the seven Hamiltonians, thus only few density dependencies of the pressure are explored. In other terms, because of the uncertainty propagation taking the derivative, the width of the pressure band does not correspond to the same likelihood than the width of the energy band. Assuming that the energy band corresponds to a $k$-$\sigma$ surface (with $k$ unknown), we expect that if we would calculate the same $k$-$\sigma$ pressure surface from the energy PDF, it would be larger than the band of Fig. 2.6. This can explain why even realistic models such as BSk24 are not compatible with the theoretical band for the pressure of PNM above

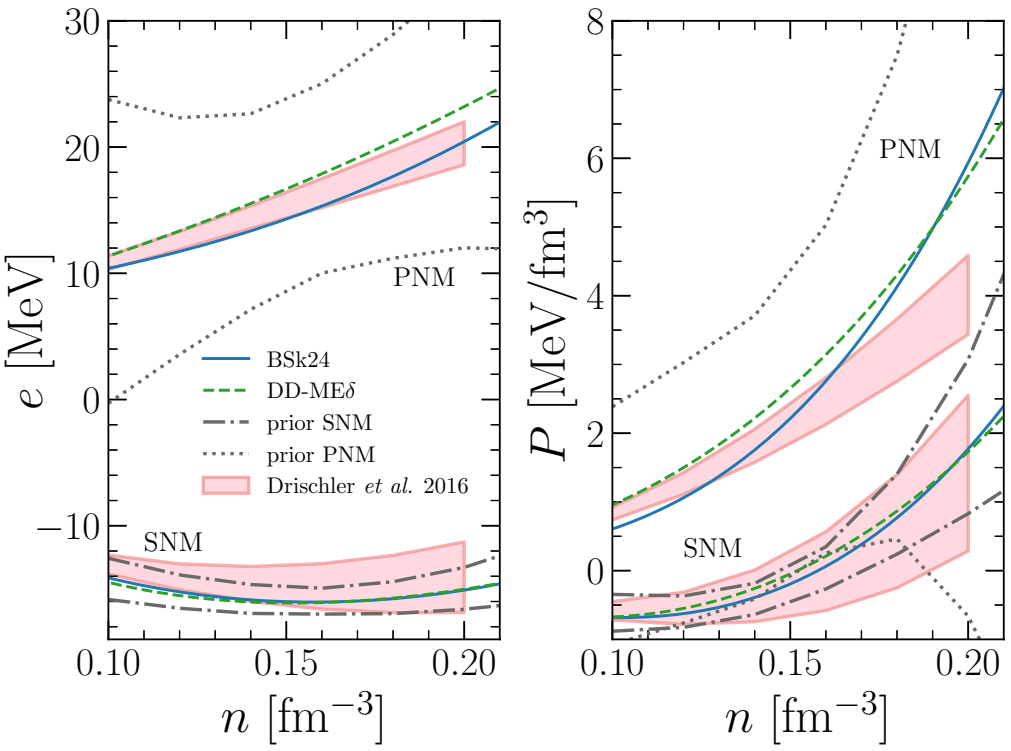



**Figure 2.6:** *Energy per nucleon (left panel) and pressure (right panel) as a function of density for both SNM and PNM from chiral ETF calculations of [DHS16] (pink bands). The predictions of BSk24 and DD-MEδ functionals are represented in solid blue lines and dashed green lines, respectively. The gray lines give the minimum and maximum values of the prior distribution.*

$\approx n_{sat}$. It is therefore debatable whether we should add the chiral EFT bands for pressure of NM in our list of constraints defining our pass-band filters $w_{LD}$. In the following, we will not consider this particular constraint by default, yet we will still investigate how it affects the posterior distribution EoS in 2.3. In the context of the pass-band filter $w_{LD}$, the chiral ETF predicted bands are widened by 5% in order to account for other existing *ab initio* calculations in an effective manner. In addition, we will not apply the filter in the low-density region $n < 0.10$ fm$^{-3}$ because the width of the band becomes extremely small, causing numerical issues.

The minimum and maximum values of the prior distribution are also represented in Fig. 2.6 (gray lines). Let us notice that one can infer the posterior band graphically by the comparison with the chiral ETF bands. Interestingly, the inferred posterior band of the prior energy per nucleon and pressure of SNM around saturation density is narrower than the one corresponding to the *ab initio* calculation. The reason is that low energy nuclear physics experiments provide strong empirical constraints for SNM [MHG18a], which have been embedded effectively in the intervals for the empirical parameters of the prior distribution in Table 2.2. The same is not true for the PNM case. Indeed, the present day knowledge on the empirical parameters of the

isovector sector is insufficient. For this reason, we can see that the corresponding *ab initio* bands are very thin in comparison to the prior distribution.

We now turn to the calculation of the probability $p_{\mathrm{AME2016}}$, which describes the ability of the CLDM defined from a parameter set $\boldsymbol{X}$, to fit the measured nuclear masses of the AME2016 [Hua+17]. The goodness of fit is evaluated by the reduced $\chi^2$, Eq. 1.63. We can define the associated likelihood probability as

$$p_{\mathrm{AME2016}}(\boldsymbol{X}) = \exp\left[-\frac{1}{2}\chi^2_\nu(\boldsymbol{X})\right]. \tag{2.30}$$

#### 2.2.3.2 Physical requirements and constraints on neutron star observables

The filter $w_{HD}$, hereafter referred to as high density (HD) filter, is applied subsequently to the LD filter $w_{LD}$. It imposes general physical constraints to the global density behavior of the functional, as follows:

- the causality condition, $c_s/c < 1$,
- the thermodynamic stability of the EoS, $dP/d\rho > 0$,
- the maximum observed NS mass, $M_{max}(\boldsymbol{X}) \geq M^{obs}_{max}$,
- the positiveness of the symmetry energy at all densities,

where $M_{max}(\boldsymbol{X})$ is the maximum mass supported by the EoS calculated for a parameter set $\boldsymbol{X}$, and $M^{obs}_{max}$ is the maximum observed NS mass. By default we choose $M^{obs}_{max} = 1.97M_\odot$, which corresponds to a $1\sigma$ conservative estimate, based on the observation of PSR J0348+0432 [Ant+13]. Let us however notice that it does not correspond to the mass of the heaviest NS observed to the present day [Cro+20]. The reason is that the observation of PSR J0740+6620 with $M = 2.14^{+0.10}_{-0.09}M_\odot$ is very recent and it was not yet published at the time of this study. Since this measurement is affected by nonnegligible error bars, an implementation of this extra constraint should be done using a likelihood filter as in Eq. (2.30).

The possibility of a negative symmetry energy at high density was sometimes mentioned in the literature [Li17; WFF88]. However, extremely soft functionals are generally incompatible with the maximum mass constraint, and relaxing the condition of the positiveness of the symmetry energy does not alter our results.

Finally, let us notice that we do not include the constraint on the tidal deformability inferred from the GW170817 event [Abb+17] in the $w_{HD}$ filter, the reason being that we are interested in confronting our results with the observations of LIGO and Virgo.

### 2.2.4 Posterior distribution of equation of state parameters

We now turn to the description of the joint posterior distribution of equation of state parameters. The effect of the different filters on marginalized one-parameter probabilities both for isoscalar and isovector parameters is analyzed in 2.2.4.1. Correlations among empirical parameters are extracted from the Bayesian analysis in 2.2.4.2.

#### 2.2.4.1 Marginalized one-parameter posterior distributions of empirical parameters

The marginal one-parameter probabilities can be evaluated from the joint posterior distribution $p(\boldsymbol{X}|\text{data})$ using Eq. (2.26). The generated PDF for isoscalar and isovector empirical parameters of orders $N \leq 3$ are shown in Fig. 2.7 and 2.8, respectively. The effect of the different filters on the one-parameter PDF can be seen. We find that the likelihood probability $p_{\text{AME2016}}$, originating from the mass fit, has a negligible impact on the distributions. This can be understood from the fact that the prior distribution of empirical parameters already contains information provided by nuclear experiments. Hence, in all cases, the probability $p_{\text{AME2016}}$ is accounted for in the evaluation of the PDF. The isovector surface tension parameter $p$ is fixed to be $p = 3$ for this study, but the results presented in the following are unmodified if $p$ is allowed to vary. The reason is that $p$ is decoupled by construction from the homogeneous EoS parameters, and it additionally does not play any role in the mass fit, see Fig. 1.5, meaning that it is also independent of the other surface parameters. Five combinations of filters are considered:

- the LD only without the constraint on pressure (solid blue lines),
- the LD filter only with the constraint on pressure (dashdotted blue lines),
- the HD filter only with $M_{max}^{obs} = 1.97 M_\odot$ [Ant+13] (solid orange lines),
- the HD filter only with $M_{max}^{obs} = 2.05 M_\odot$ [Ant+13] (dashdotted orange lines),
- both LD and HD filters with the constraint on pressure, for $M_{max}^{obs} = 1.97 M_\odot$ (solid green lines).

By comparing the LD predictions in Fig. 2.7, it is seen that adding the pressure bands, predicted by chiral EFT [DHS16], as a constraint has a negligible effect on the posterior distributions of isoscalar empirical parameters. Since empirical information is available in SNM and included in our prior distribution, we observe that applying the LD filter does not impose strong constraints on the one-parameter PDF in the isoscalar sector. Still, we can notice that low values of $E_{sat}$ and $n_{sat}$ are disfavored by the passage through the chiral EFT predicted bands shown in Fig. 2.6. Conversely, it is clear from Fig. 2.8 that applying LD constraints on the energy per nucleon has a enormous effect on the marginalized posterior distributions of the low-order isovector empirical parameters $E_{sym}$ and $L_{sym}$, shown in the two upper panels. The effect on the posterior PDF of $L_{sym}$ is even larger if we impose the sets to be compatible with the chiral EFT predicted bands for pressure of SNM and PNM. It also allows very tight determination of isovector incompressibility $K_{sym}$, its distribution being peaked at $K_{sym} \approx -200$ MeV, while it is rather flat without the constraint on pressure. Overall, we see that the posterior probabilities for these parameters are narrower than those without the additional constraints on pressure. These observations can be easily understood considering the expression for the pressure of PNM in the vicinity of the saturation density $n_{sat}$,

$$P_{PNM}(n) = P_{HM}(n, \delta = 1) \simeq \frac{1}{3} n_{sat} (1 + 3x)^2 (K_{sat} x + L_{sym} + K_{sym} x), \tag{2.31}$$

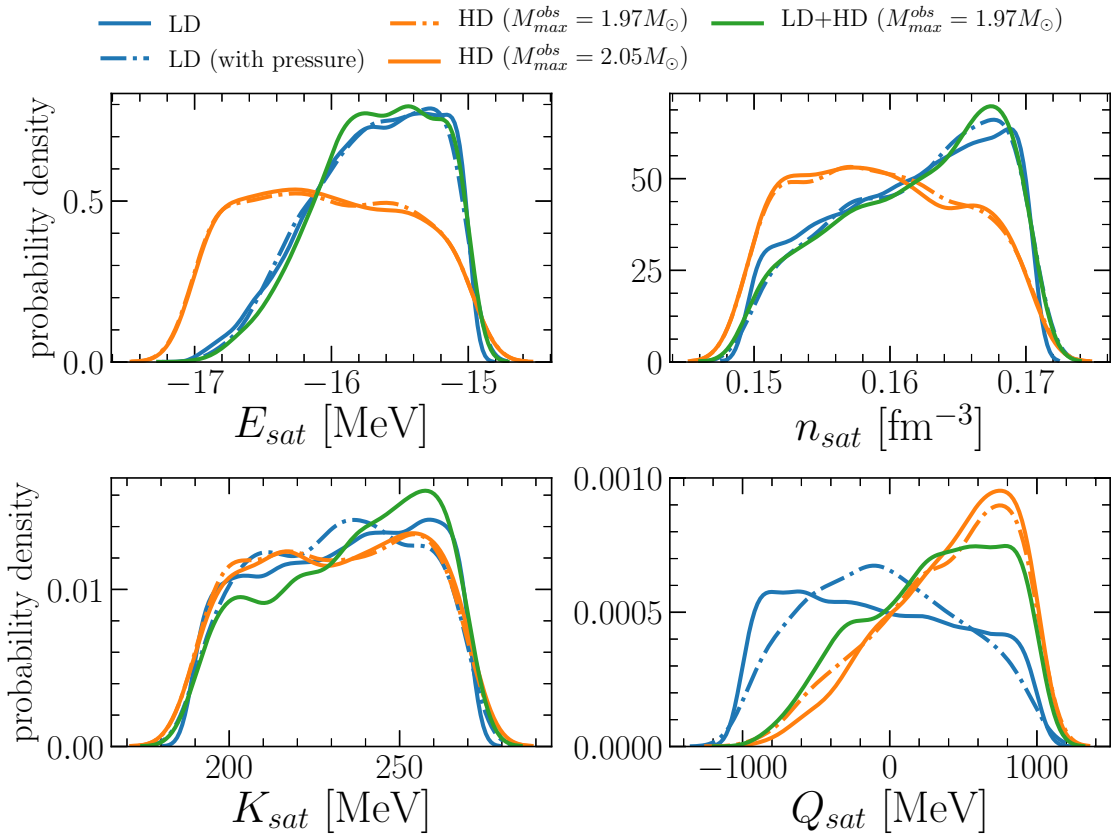



**Figure 2.7:** *Marginalized posteriors for $E_{sat}$, $n_{sat}$, $K_{sat}$, and $Q_{sat}$ for the sets passing through the LD filter without (solid blue lines) and with (dashdotted blue lines) the constraint on pressure, HD filter with $M^{obs}_{max} = 1.97M_\odot$ [Ant+13] (solid orange lines) and with $M^{obs}_{max} = 2.05M_\odot$ [Cro+20] (dashdotted orange lines), and both filters without the constraint on pressure, for $M^{obs}_{max} = 1.97M_\odot$ (solid green lines). In all cases, the likelihood probability $p_{AME2016}$ is accounted for and $p = 3$ is fixed.*

which gives $P_{PNM}(n = n_{sat}) = n_{sat}L_{sym}/3$ at the saturation point. The posterior distributions of $Q_{sat}$ and $Q_{sym}$ are only very slightly affected by the LD constraints. The same is true for parameters of order $N = 4$, $Z_{sat}$ and $Z_{sym}$, which are not shown in the figures. The reason is that the high-order parameters contribute to the EoS at suprasaturation densities, where predictions of chiral EFT are not yet fully trustable.

The one-parameter PDF for the sets passing through the HD pass-band filter $w_{HD}$ are represented in orange lines. Overall, we find that the effect of varying the value $M^{obs}_{max}$, so as to be compatible with the two considered observations of heavy NS [Ant+13; Cro+20], is very small. This also implies that treating this constraint with a likelihood filter, as it would be more correct from the viewpoint of Bayesian inference, would not change our results. In the isoscalar sector, we can see the distributions of the low-order parameters $E_{sat}$, $n_{sat}$ and $K_{sat}$ are not affected by the passage through the $w_{HD}$ filter. On the other hand, it has an important effect on the PDF of $Q_{sat}$, with large values being favored. In the isovector sector, the HD filter has a signif-

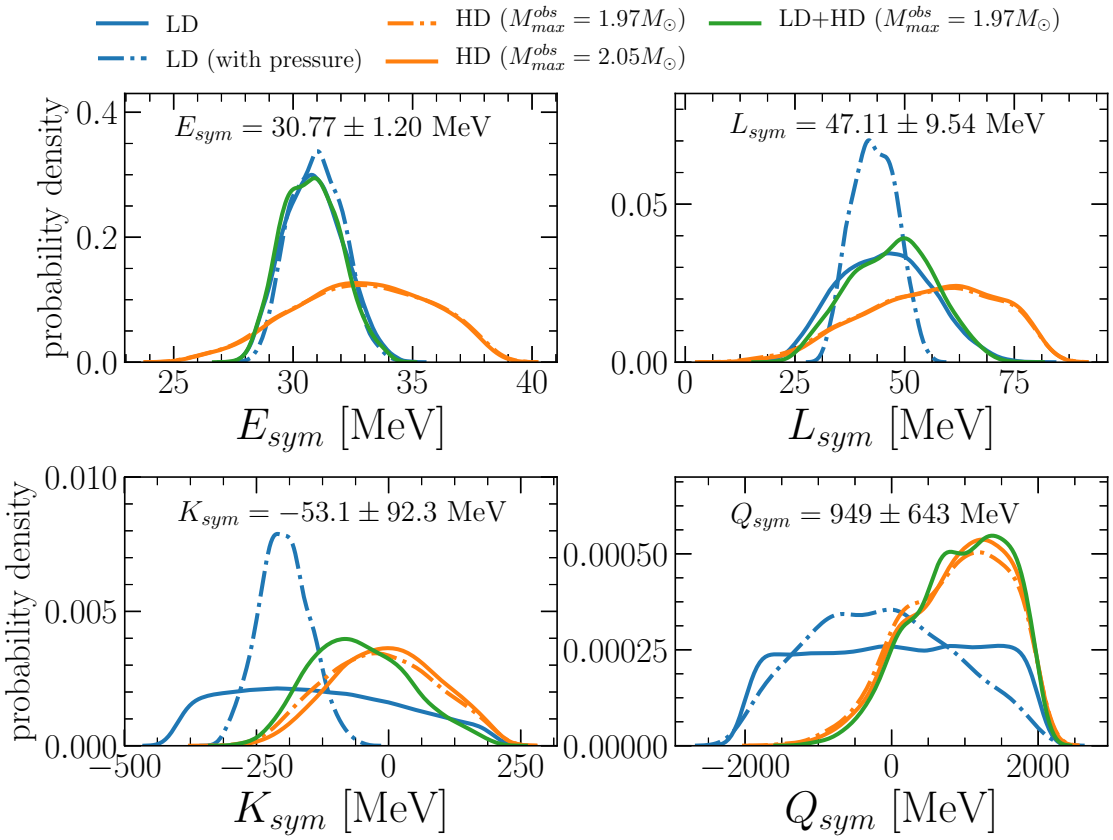



**Figure 2.8:** *Marginalized posteriors for $E_{sym}$, $L_{sym}$, $K_{sym}$, and $Q_{sym}$ for the sets passing through the LD filter without (solid blue lines) and with (dashdotted blue lines) the constraint on pressure, HD filter with $M^{obs}_{max} = 1.97M_\odot$ [Ant+13] (solid orange lines) and with $M^{obs}_{max} = 2.05M_\odot$ [Cro+20] (dashdotted orange lines), and both filters without the constraint on pressure, for $M^{obs}_{max} = 1.97M_\odot$ (solid green lines). The resulting mean value and uncertainty, corresponding to the latter option, are shown for each parameter. In all cases, the likelihood probability $p_{AME2016}$ is accounted for and $p = 3$ is fixed.*

icant impact on the PDF of $E_{sym}$, $L_{sym}$ and $K_{sym}$, yet less effective than that of the LD filter, except for $K_{sym}$. Concerning the isovector skewness parameter $Q_{sym}$, which we recall is not affected by the LD filter, we find negative values to be very unlikely. Overall, we can see that HD constraints favor stiff EoS with respect to the LD predictions. The reason is obviously that stiff EoS better verify the maximum mass constraint. The generated one-parameter PDF associated to the sets passing through the combination of both LD and HD filters without the constraint on pressure, for $M^{obs}_{max} = 1.97M_\odot$, are plotted in solid green lines. The mean value and standard deviation application of LD and HD constraints are given for each of the isovector parameters. Let us notice that the marginalized posteriors for the effective mass $m^*_{sat}/m$ and the isospin splitting $\Delta m^*_{sat}/m$ are not displayed here, because the associated posteriors distributions are very close the prior distributions. The same is true for the low-density parameter $b$.

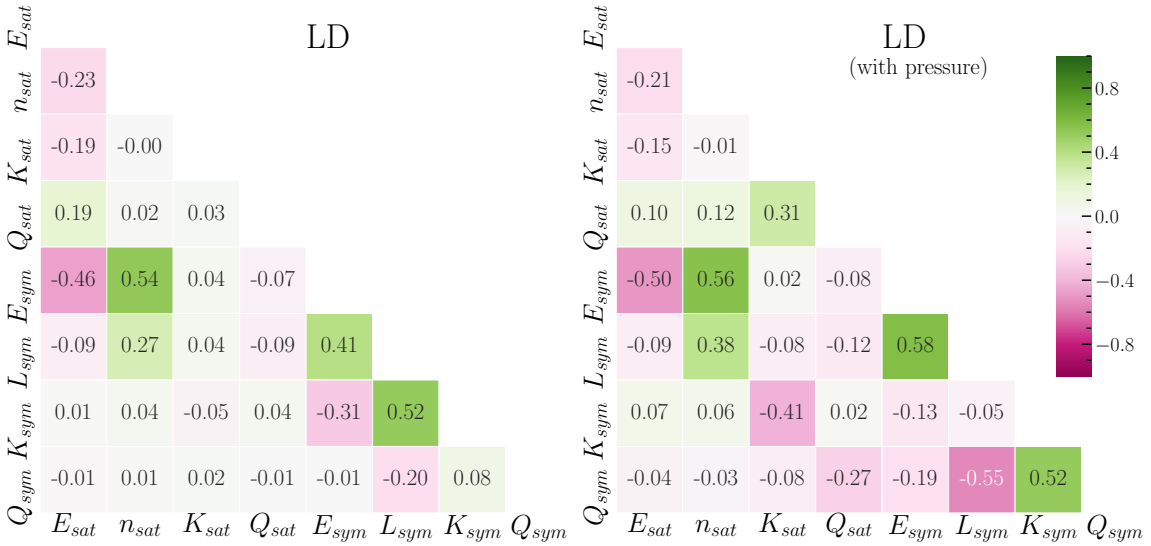



**Figure 2.9:** *Correlation matrix for the empirical parameters of orders $N \leq 3$ for the sets passing through the LD filter without (left) and with (right) the constraint on pressure. The likelihood probability $p_{AME2016}$ is accounted for and $p = 3$ is fixed.*

The latter point can be understood from the fact that none of the filters concern the $n \to 0$ limit.

#### 2.2.4.2 Correlations among empirical parameters

We now turn to explore the correlations between empirical parameters, as obtained by applying the different conditions. As in 2.2.4.1, $p = 3$ is fixed, and the likelihood probability $p_{\mathrm{AME2016}}$ is accounted for in all cases. Given a pair of parameters $(X_i, X_j)$, the Pearson correlation coefficient is calculated as

$$r_{ij} = \frac{\mathrm{cov}(X_i, X_j)}{\sigma_{X_i}\sigma_{X_j}}, \tag{2.32}$$

where $\mathrm{cov}(X_i, X_j)$ is the covariance and $\sigma_{X_i}$ ($\sigma_{X_j}$) is the standard deviation of the parameter $X_i$ ($X_j$).

In Fig. 2.9, we find that many correlations appear due to the LD constraints. The left panel of the figure shows the correlation matrix for the empirical parameters of orders $N \leq 3$ for the sets passing through the LD filter without applying the constraint on pressure arising from chiral EFT. We find an anticorrelation between $E_{sat}$ and $E_{sym}$, and a positive correlation between $E_{sym}$ and $n_{sat}$. More interesting correlations among the different isovector parameters are induced by the constraint of reproducing the *ab initio* EFT calculations. Indeed, we recover the correlation between $E_{sym}$ and $L_{sym}$, which has been already observed by many authors using different models [LH19; Kor+12; DL14; TCV08; CGS14]. We also observe a strong correlation between $L_{sym}$ and $K_{sym}$ and find that $E_{sym}$ is slightly anticorrelated to $K_{sym}$.

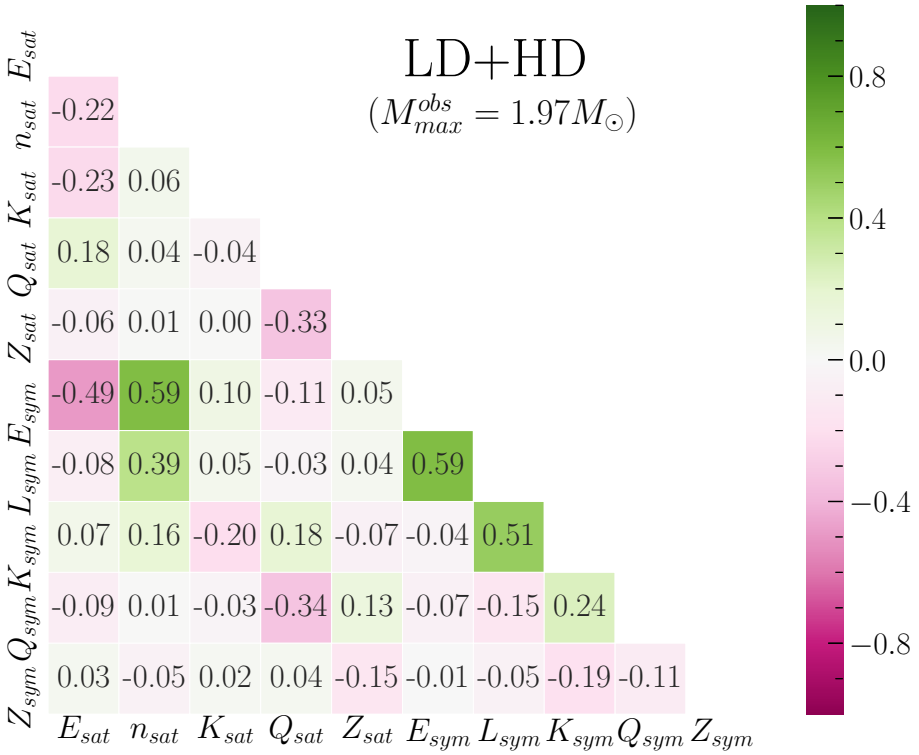



**Figure 2.10:** *Correlation matrix for the empirical parameters of orders $N \leq 4$ for the sets passing through both LD and HD filters without the constraint on pressure, for $M^{obs}_{max} = 1.97M_\odot$ [Ant+13]. The likelihood probability $p_{AME2016}$ is accounted for and $p = 3$ is fixed.*

The correlation matrix calculated from the joint posterior distributions of parameters for the sets passing through chiral EFT predicted bands both for energy per nucleon and pressure of NM is displayed in right panel of Fig. 2.9. Several differences with respect to the matrix in the left panel can be noticed. Among the isovector parameters, it is seen that the previously found correlation between the slope of the symmetry energy $L_{sym}$ and the isovector incompressibility $K_{sym}$ disappears in favor of a strong correlation between $K_{sym}$ and the isovector skewness $Q_{sym}$, and an anticorrelation between $L_{sym}$ and $Q_{sym}$. We also observe that the isoscalar parameters $K_{sat}$ and $Q_{sat}$ are weakly correlated with the corresponding isovector ones $K_{sym}$ and $Q_{sym}$. These nontrivial correlations can only be revealed within the metamodeling strategy, because in usual functionals, such as Skyrme ones, the high-order parameters are *a priori* strongly correlated from the functional form.

In both cases studied in Fig. 2.9, the fourth order parameters $Z_{sat}$ and $Z_{sym}$ do not show any correlation with any other parameter, showing their negligible influence on the density relatively close to saturation implied in the LD filter. Similarly, the isoscalar effective mass and effective mass splitting are also essentially uncorrelated with the others. The reason is that variations of these parameters, which play a crucial role in the structure of finite nuclei, are fully compensated by variations of the

density derivatives as long as only the total energetics, that is kinetic plus potential, is involved [Cha+17].

Fig. 2.10 shows the correlation matrix for the empirical parameters of orders $N \leq 4$ for the sets passing through both LD and HD filters without the constraint on pressure, for $M_{max}^{obs} = 1.97 M_\odot$ [Ant+13]. One can identify the correlations induced by the application of HD filter by comparison with the left panel of Fig. 2.9. Doing so, we infer that the $w_{HD}$ pass-band filter does not induce any correlation among the empirical parameters, with the exception of $Q_{sat}$ being now slightly anticorrelated to $Q_{sym}$ and $Z_{sat}$. This can be understood from the fact that the maximum mass constraint is essentially sensitive to the global stiffness of the EoS, and given the large uncertainties on the high-order parameters, a stiff EoS can be obtained with many different combinations of $K_{sym}$, $Q_{sym}$, $Q_{sat}$, $Z_{sym}$, and $Z_{sat}$, indicating a certain reduncancy in our parameter space with this limited set of constraints.

## 2.3 General predictions for neutron star observables

This section deals with general predictions for NS observables, based on the Bayesian analysis performed in Section 2.2. The marginalized posterior for the observable $\mathcal{O}$,

$$p(\mathcal{O}|\text{data}) = \left\{ \prod_{i=1}^{2(N+1)+3} \int dX_i \right\} \mathcal{O}(\boldsymbol{X}) p(\boldsymbol{X}|\text{data}), \tag{2.33}$$

can be extracted from the joint posterior distribution of empirical parameters $p(\boldsymbol{X}|\text{data})$, where $\mathcal{O}(\boldsymbol{X})$ is the value of the observable $\mathcal{O}$ as obtained with the parameter set $\boldsymbol{X}$. Our predictions for global properties of the NS are presented and confronted with popular models as well as with the GW170817 event in 2.3.1. The Bayesian determination of the CC transition density and pressure is carried out in 2.3.2. Finally, in 2.3.3, we calculate the fraction of crust moment of inertia for the joint posterior distribution of parameters in order to investigate whether *the crust is enough* to explain pulsar glitches in the standard picture presented in 2.1.2.2. Some of the results presented in the following have been published [CGM19a; CGM19b].

### 2.3.1 Global properties: confrontation with popular models and the GW170817 event

A large number of EoS models, based for instance on Skyrme functionals or relativistic mean-field models, have been proposed in the literature over the years. Astrophysical observations can provide strong constraints on the nuclear EoS and therefore allow discriminating between the different models. For instance, we have seen from 2.1.1 that the observations of massive pulsars require from the EoS to support $M_{max} \gtrsim 2M_\odot$ [Dem+10; Ant+13; Cro+20]. The recent GW170817 event, which is the first detection of GW from a binary NS coalescence, has provided a constraint on the NS tidal deformability [Abb+17; Abb+18; Abb+19].

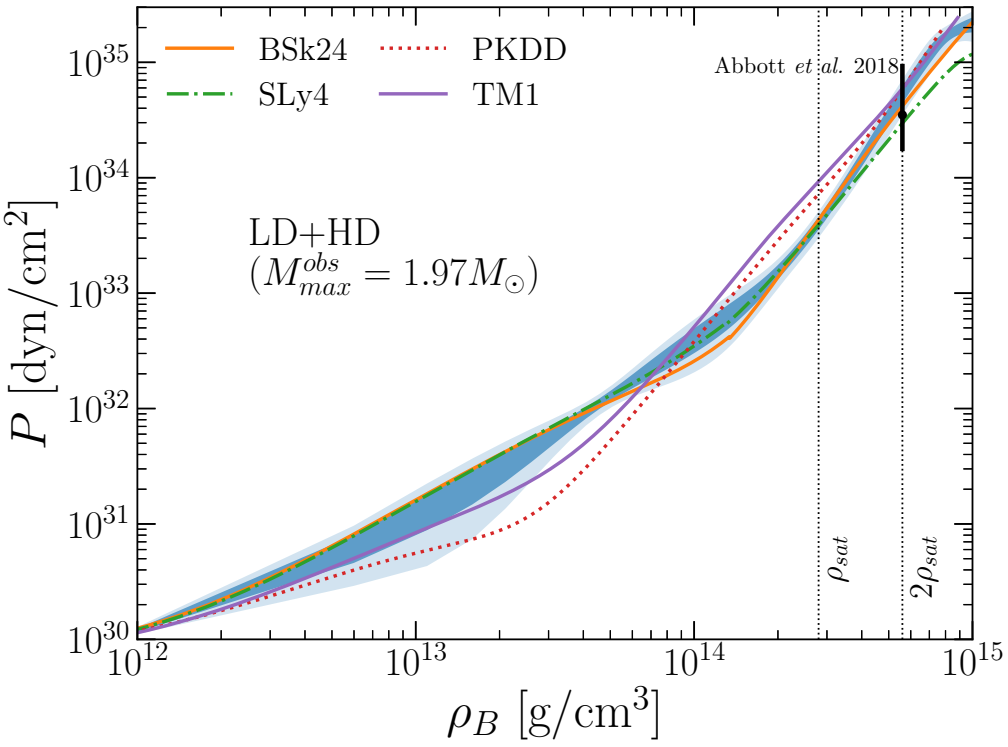



**Figure 2.11:** *Marginalized posterior for the pressure $P$ as a function of the baryon mass density $\rho_B$ of the NS interior for the sets passing through both LD and HD filters without the constraint on pressure, for $M_{max}^{obs} = 1.97 M_\odot$ [Ant+13]. The likelihood probability $p_{AME2016}$ is accounted for and $p = 3$ is fixed. The blue dark and light shaded regions show the $1\sigma$ and $2\sigma$ confidence intervals, respectively. The BSk24 (solid orange line), SLy4 (dashdotted green line), PKDD (dotted red line), and TM1 (solid purple line) unified EoS calculated within the metamodeling technique with $p = 3$ are represented. The constraint on $P_{2\rho_{sat}}$ inferred from GW170817 [Abb+18] is given.*

In the following, we calculate global properties of NS from the LD+HD joint posterior distribution of parameters and confront our results with popular EoS models as well as with the GW170817 constraints provided by the LIGO and Virgo collaborations.

#### 2.3.1.1 Equation of state

The $1\sigma$ and $2\sigma$ confidence regions for the posterior unified EoS, obtained from the sets passing through both LD and HD constraints, are shown in Fig. 2.11 along with four popular EoS calculated within the metamodeling technique, namely BSk24 (solid orange line), SLy4 (dashdotted green line), PKDD (dotted red line), and TM1 (solid purple line) EoS. We can see that only the EoS based on BSk24 functional is compatible, at $2\sigma$, with the final LD+HD prediction in the whole density domain considered in the figure. It is observed that the SLy4 EoS deviates below the $2\sigma$ band at suprasatu-

ration densities. The two EoS based on functionals issued from relativistic mean-field theory, namely PKDD and TM1, do not meet the final LD+HD predictions. The reason is that the *ab initio* calculations considered for our LD filter [DHS16] tend to favor soft EoS, typically based on Skyrme functionals, as we can see in Fig. 2.8. Indeed, we find $E_{sym} = 30.77 \pm 1.20$ MeV and $L_{sym} = 47.11 \pm 9.54$ MeV for the low-order isovector parameters for the LD+HD prediction, which is very close to the LD one for these parameters. The two relativistic functionals considered here, the empirical parameters of which are reported in Table 2.1, exhibit a very stiff behavior at saturation.

The recent constraint, provided by the observation of GW170817, on the pressure at twice nuclear saturation density, $P_{2\rho_{sat}} = 3.5^{+2.7}_{-1.7} \times 10^{34}$ dyn/cm$^2$ at the 90% level [Abb+18], is also shown in Fig. 2.11. We can see that this result is in very good agreement with our analysis. Let us notice that our predicted $2\sigma$ band at $2\rho_{sat}$ is very thin in comparison with the constraint arising from GW170817. This is because the *ab initio* calculations, not considered as a filter in [Abb+18], impose stringent constraints on the low-density EoS. The very tight determination of the EoS at $2\rho_{sat}$ comes from the fact that we have applied the LD constraint up to 0.20 fm$^{-3}$. If we only trust the *ab initio* calculations up to $\rho_{sat}$, because of the uncertainties on the three-body interactions that are still under debate [TMR19], the prediction remains good, but the band is larger and compatible with the SLy4 EoS.

#### 2.3.1.2 Masses and radii

In Fig. 2.12, we plot the 68%, 95% and 99% confidence regions for the mass-radius relation obtained from the Bayesian modeling of the EoS for the LD+HD prediction, using the marginalization principle, Eq. (2.33). The mass-radius relationship for the same popular EoS as in Fig. 2.11, namely the Skyrme-based BSk24 and SLy4 EoS, and relativistic PKDD and TM1 EoS, are represented. As we can see, only the BSk24 result (solid orange line) is compatible with our prediction at 95% credible level in the whole mass domain considered. The two relativistic models predict large radii compared to our prediction. Given the results presented in this figure and in Fig. 2.11, we therefore find that all known models considered would have been rejected by the filters except BSk24, which satisfy both LD and HD constraints.

Let us now confront our prediction for the radius of a canonical NS, $R_{1.4} = 12.88^{+0.53}_{-0.65}$ km (90% credible interval), with different constraints found in the literature. De *et al.* have performed a Bayesian parameter estimation for the tidal deformabilities and radii of NS from the observation of GW170817 within the approximation $R_1 = R_2$, $R_1$ being the radius of the heavier star and $R_2$ that of the lighter star, that is assuming an identical value for the radius of binary components. The authors found $R_{1.4} = 10.7^{+2.1}_{-1.6}$ km (90% credible interval) [De+18], which is in a very close agreement with the estimation of the LIGO/Virgo collaborations when they use EoS-insensitive relations, $R_{1.4} \approx R_1 = 10.7^{+2.1}_{-1.5}$ km (90% credible interval) [Abb+18]. Using a parametrized EoS and imposing the constraint on the maximum mass $M^{obs}_{max} = 1.97 M_\odot$, LIGO and Virgo collaborations further constrain $R_{1.4} \approx R_1 = 11.9^{+1.4}_{-1.4}$ km (90% credible interval). In all analyses, a uniform prior was used on the component masses. We find that our estimation of the canonical radius $R_{1.4}$ is compatible with these three analyses, even though we can notice that our value for the median is larger, and the

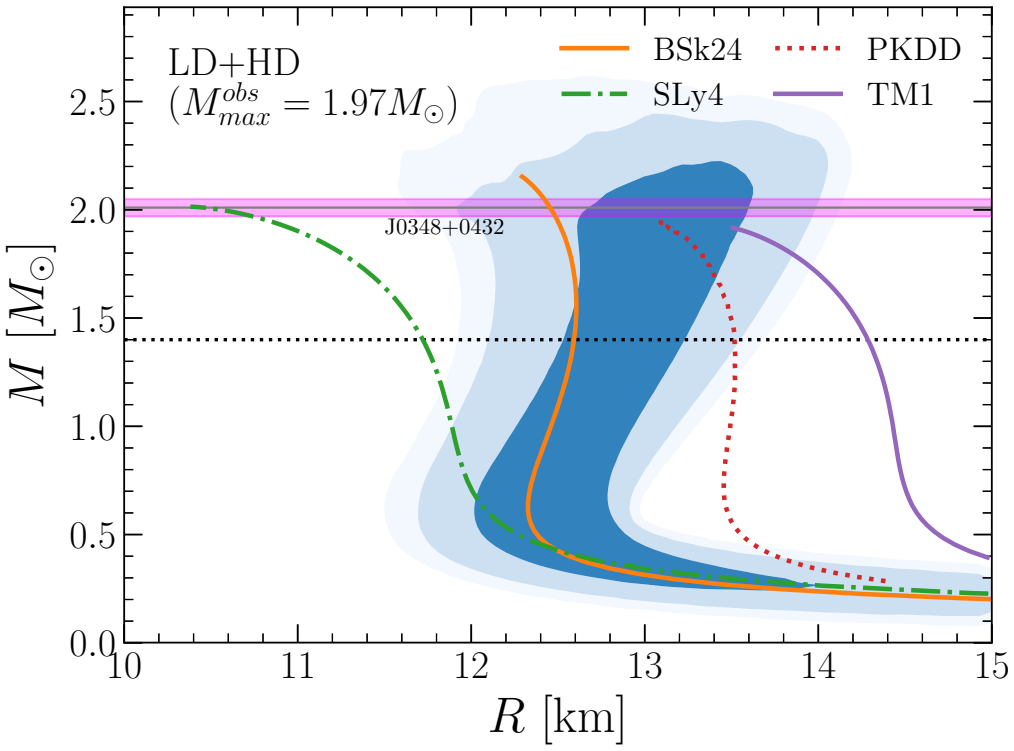



**Figure 2.12:** *Marginalized posterior for the NS mass $M$ as a function of the radius $R$ for the sets passing through both LD and HD filters without the constraint on pressure, for $M^{obs}_{max} = 1.97M_\odot$ [Ant+13] (magenta band). The likelihood probability $p_{AME2016}$ is accounted for and $p = 3$ is fixed. The blue shaded regions show the 68%, 95% and 99% confidence intervals. The mass-radius relation for the same popular EoS as in Fig. 2.11 are represented.*

90% confidence interval is tighter. This outlines the importance of the LD filter in our calculation, which ensure that our posterior is compatible with chiral EFT predicted bands for the energy per nucleon of SNM and PNM. Moreover, our prior distribution of EoS parameters contains information arising from nuclear experiments. This feature, and the fact that, for each set of empirical parameters, we fix the surface and curvature parameters to the optimized values, explain why the likelihood probability $p_{\rm AME2016}$ has a negligible impact on the distribution. In [De+18; Abb+18], constraints on nuclear physics observables were not considered.

In Fig. 2.1, we have observed that the study of five characteristic EoS models suggests a possible correlation between the radius of the star $R$ and the slope of the symmetry energy $L_{sym}$. This correlation has been highlighted recently in several studies, using EoS based either on Skyrme forces or relativistic mean-field models [Ala+16; Ji+19; Hu+20]. Surprisingly, for the LD prediction, we find that $R_{1.4}$ is especially correlated with the isovector incompressibility $K_{sym}$, $r(K_{sym}, R_{1.4}) = 0.69$ rather than with the $L_{sym}$, $r(L_{sym}, R_{1.4}) = 0.33$. As previously discussed in 2.2.2.2, the functional forms of Skyrme forces or relativistic models generally induce artificial correlations

between some of the empirical parameters, with the effect of altering true correlations. The metamodeling technique prevents this problem because no *a priori* correlation exists among the empirical parameters, so the true correlation are brought by the passage through LD and HD filters. For instance, correlations in the isovector sector between $E_{sym}$ and $L_{sym}$, and between $K_{sym}$ and $3E_{sym} - L_{sym}$, have been shown in [Mon+17; MG19] using a larger set of characteristic EoS models.

#### 2.3.1.3 Tidal deformability

The tidal effects arising from a binary NS coalescence are encoded in the GW signal through the binary tidal deformability,

$$\tilde{\Lambda} = \frac{16}{13}\frac{(m_1 + 12m_2)m_1^4\Lambda_1 + (m_2 + 12m_1)m_2^4\Lambda_2}{(m_1 + m_2)^{1/5}}, \tag{2.34}$$

where $\Lambda_{1,2}$ are the individual NS tidal deformabilities, and $m_{1,2}$ the component masses satisfying the inequality $m_1 \geq m_2$. The binary tidal deformability is essentially correlated with the so-called chirp mass,

$$\mathcal{M} = \frac{(m_1 m_2)^{3/5}}{(m_1 + m_2)^{1/5}}. \tag{2.35}$$

For the specific case of GW170817, this quantity has been well constrained to $\mathcal{M}_{\rm GW170817} = 1.186^{+0.001}_{-0.001} M_\odot$ [Abb+19]. The probability distributions for the component masses $m_1$ and $m_2$ are obtained from $\mathcal{M}_{\rm GW170817}$ and the mass ratio $m_2/m_1$ (see Fig. 4 of [Abb+17]). The black dashed lines in Fig. 2.13 show the 50% and 90% confidence intervals as obtained by the LIGO and Virgo collaborations for the low-spin prior ($|\chi| < 0.05$, $\chi$ being the dimensionless spin), which is consistent with binary NS systems [Abb+19].

We show in Fig. 2.13 the 50% and 90% confidence regions corresponding to the joint probability distribution for $\Lambda_1$ and $\Lambda_2$ that we obtain for the sets passing through both LD and HD filters for the chirp mass $\mathcal{M}_{\rm GW170817}$. The mass of the components have been sampled according to their respective individual probability distributions given in [Abb+17], and the same EoS have been used to calculate the individual tidal deformabilities. The part under the diagonal corresponds to the unphysical region $\Lambda_2 > \Lambda_1$ since the convention $m_1 \geq m_2$ has been taken. It is seen that our LD+HD prediction meets the results of the LIGO/Virgo collaborations at 90% confidence level, but we find that our posterior favors slightly larger values of $\Lambda_{1,2}$, that can be obtained with stiffer EoS, associated to less compact NS. This tension arises due to the inclusion of nuclear-physics constraints in our calculation. The only hypothesis of the metamodel is that the EoS can be written as a Taylor series, which excludes the eventuality of a first-order phase transition, notably to quark-gluon plasma. Hence, a discrepancy between our posterior and that of the LIGO and Virgo collaborations would be a smoking gun for the existence of quarks in the core of NS. Indeed, a possible explanation could be that one of the stars has undergone a phase transition and the other not, leading to two different EoS for the two stars. We do not observe such evidence in our results, thus the hypothesis of a purely nucleonic EoS cannot be excluded. Increasing the

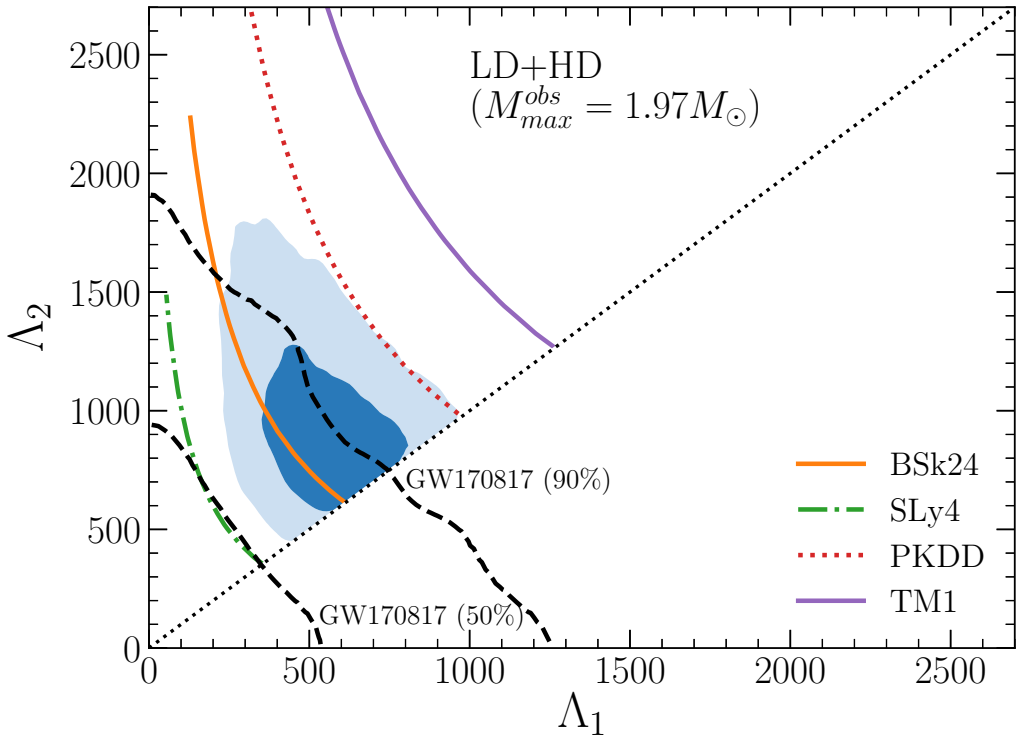



**Figure 2.13:** *Marginalized posterior for $\Lambda_1$ (more massive component) and $\Lambda_2$ (less massive component) for the sets passing through both LD and HD filters without the constraint on pressure, for $M_{max}^{obs} = 1.97M_\odot$. The value of the chirp mass corresponds to the specific case of GW170817, $\mathcal{M} = 1.186^{+0.001}_{-0.001}M_\odot$ [Abb+19], and the individual probability distributions for $m_1$ and $m_2$ are taken from [Abb+17]. Dark (light) shaded regions represents the 50% (90%) confidence interval with our Bayesian estimation with $p = 3$. The black dashed lines show the 50% and 90% confidence regions as obtained by LIGO/Virgo collaborations for the low-spin prior [Abb+18]. The $\Lambda_1 - \Lambda_2$ relation is also represented for the same popular EoS as in Fig. 2.11. The diagonal dotted line marks the $\Lambda_1 = \Lambda_2$ boundary.*

number of binary NS GW signals will help to conclude on the strength of the tension. The dimensionless tidal deformabilities are also calculated for the same four popular EoS as in Figs. 2.11 and 2.12. We observe that the soft SLy4 and BSk24 EoS are in a rather good agreement with the analysis of the LIGO and Virgo collaborations, whereas the relativistic models PKDD and TM1 seems very unlikely. Among the four popular EoS, only the one based on BSk24 functional is compatible with the LD+HD prediction.

The marginalized posterior distribution that we obtain for the dimensionless tidal deformability of a $1.4M_\odot$ NS is shown in Fig. 2.14, along with the prediction of characteristic EoS based on Skyrme and relativistic models. The 90% confidence interval corresponding to the LD+HD prediction is $\Lambda_{1.4} = 634^{+204}_{-190}$. It meets the results of the LIGO/Virgo collaborations for GW170817, $\Lambda_{1.4} = 190^{+390}_{-120}$, the 90% confidence interval

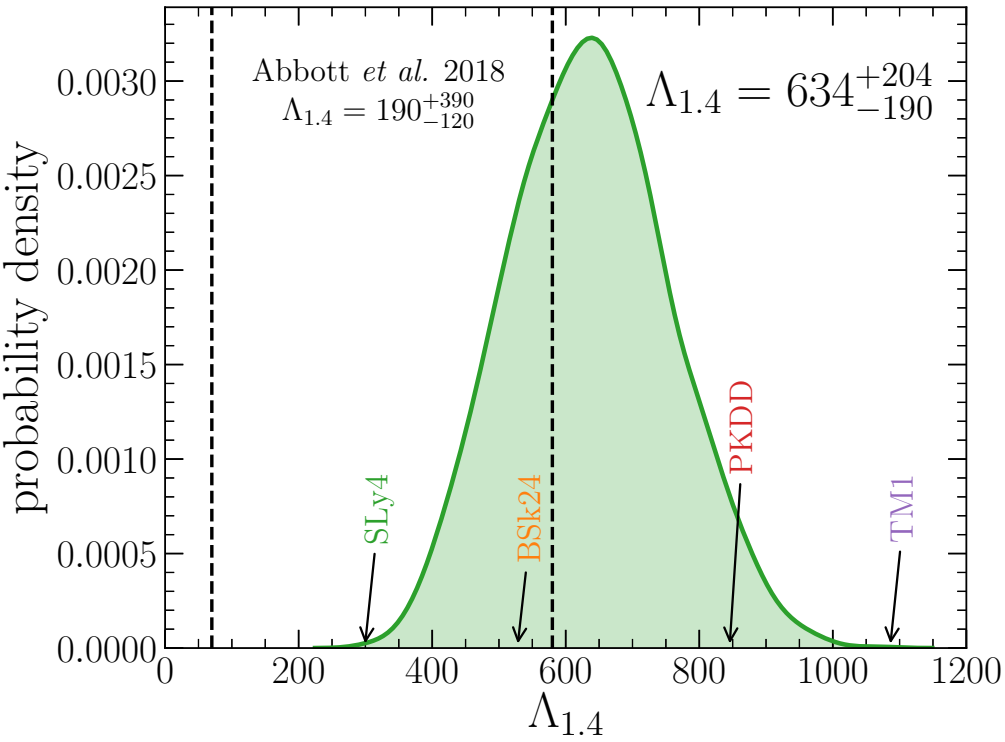



**Figure 2.14:** *Marginalized posterior probability distribution for the dimensionless tidal deformability of a $1.4M_\odot$ NS, calculated for the sets passing through both LD and HD filters without the constraint on pressure, for $M_{max}^{obs} = 1.97M_\odot$. The resulting 90% credible interval is indicated in the top right corner. The arrows give the value of $\Lambda_{1.4}$ for four characteristic EoS: BSk24, SLy4, PKDD, and TM1. The vertical dashed lines delimit the 90% confidence interval associated to the constraint of the LIGO/Virgo collaborations for GW170817, $\Lambda_{1.4} = 190^{+390}_{-120}$ [Abb+18].*

of which is given by the vertical dashed lines in the figure. However, we find that the probability for $\Lambda_{1.4} < 300$ is negligible. The shift of the median with respect to that inferred from GW170817 event outlines the importance of the LD filter in our calculation. Indeed, it is known that $\Lambda_{1.4}$ is strongly correlated to the NS radius $R_{1.4}$, we find a Pearson correlation coefficient of $r(R_{1.4}, \Lambda_{1.4}) = 0.98$, and we have seen that the radius of a $1.4M_\odot$ NS is correlated with the isovector incompressibility parameter $K_{sym}$. Hence, we observe that $K_{sym}$ and $\Lambda_{1.4}$ are correlated, with $r(K_{sym}, \Lambda_{1.4}) = 0.66$. We have seen in Fig. 2.8 that the isovector empirical parameters are strongly constrained by the *ab initio* calculations of NM, particularly when the constraint on pressure is accounted for in the LD pass-band filter. More specifically, we find that the isovector incompressibility is tightly determined in that case, with a distribution being peaked at $K_{sym} \approx -200$ MeV, therefore favoring soft EoS and in consequence smaller values of the tidal parameter $\Lambda_{1.4}$.

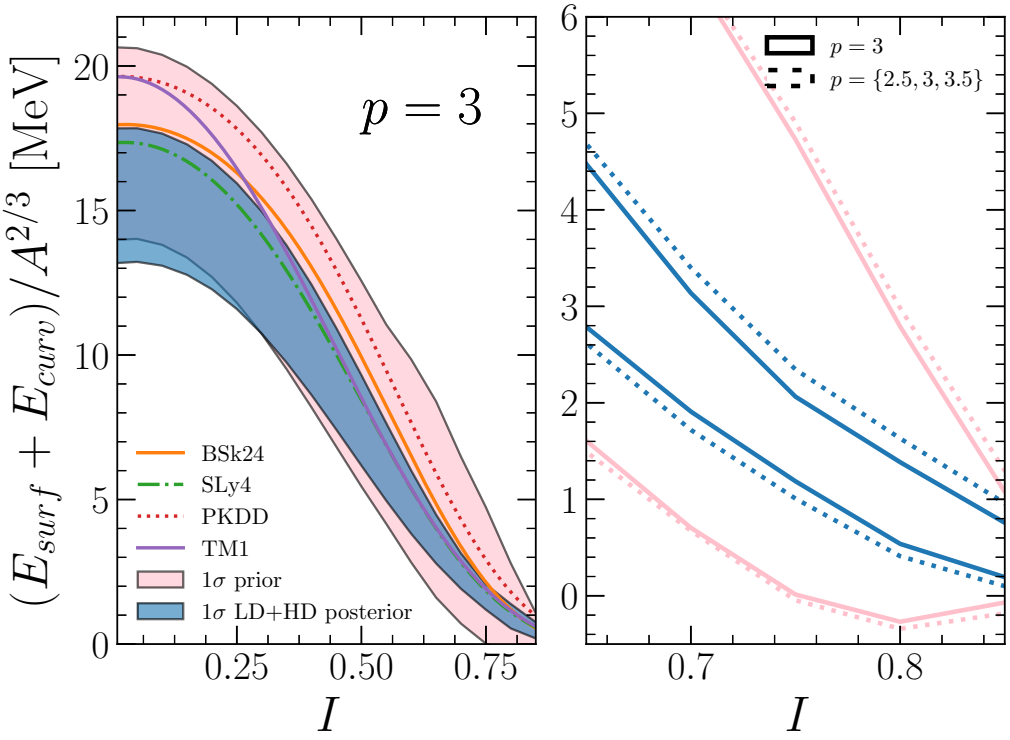



**Figure 2.15:** *Left:* $1\sigma$ *prior (pink band) and LD+HD posterior distribution (blue band) for the surface plus curvature energy per surface nucleon, defined by Eqs. (1.59)-(1.62), as a function of the isospin asymmetry long the isobaric chain* $A = 200$ *for* $p = 3$. *The results for four characteristic EoS are also given. Right:* $1\sigma$ *prior and LD+HD posterior for* $(E_{surf} + E_{curv})/A^{2/3}$ *at high isospin for* $p = 3$ *(solid lines) and* $p = \{2.5, 3, 3.5\}$ *(dotted lines).*

### 2.3.2 Bayesian analysis of the crust-core transition

The computation of the crustal observables with the hydrostatic equilibrium equations requires the knowledge of the CC transition pressure $P_t$ in addition to the EoS. In the following, we make quantitative predictions on the density and pressure at the CC transition point from the joint posterior distribution, and examine in detail the influence of the different EoS parameters, as well as the effectiveness of the different filters entering the likelihood probability, Eq. (2.29).

Following the strategy introduced in 1.2.6, we calculate the CC transition properties from the crust, the description of which demands an explicit modeling of clusterized matter, thus the introduction of a surface (and eventually curvature) term in the energetics. This is done within the classical CLD approximation, using Eqs. (1.59)-(1.62). For a given set of empirical parameters, we expect that the theoretical determination of the CC transition point is sensitive to the surface energy at high isospin, which is essentially governed by the isovector surface parameter $p$, see Fig. 1.12. Unfortunately, experimental data are unavailable above $I = (N - Z)/A \gtrsim 0.3$, which approximately

corresponds to the neutron drip line in the laboratory.

The prior and LD+HD posterior distribution for the surface plus curvature energy per surface nucleon are displayed in the left panel of Fig. 2.15 as a function of isospin asymmetry for the $p = 3$ case, along the isobaric chain $A = 200$. To obtain the prior distribution, we calculate the surface plus curvature energy for the uncorrelated prior distribution of empirical parameters given in Table 2.2. Since, for a given set of empirical parameters sampled according to the uniform distribution, we only keep the set of surface and curvature parameters that minimizes the reduces $\chi^2$ defined in Eq. (1.63), the prior distribution already takes into account the present knowledge on experimental masses. The variation with $I$ of $(E_{surf} + E_{nuc})/A^{2/3}$ is also shown for four popular models. All of them are compatible with the $1\sigma$ band for the prior distribution. It is seen that the LD+HD distribution predicts a lower surface energy for nearly symmetric nuclei with respect to the prior distribution and the selected popular functionals. This is not surprising because we know that the surface parameter $\sigma_0 = \sigma(I = 0)$ is strongly anticorrelated with the energy per nucleon of SNM at saturation $E_{sat}$ [CGM19a], for which large values are favored by the LD filter, see Fig. 2.7. Above the neutron drip line, $I \gtrsim 0.35$, we can see that the filters defining our likelihood probability allow a tight determination of the surface energy in comparison to the prior distribution. This translates into smaller uncertainties for the CC transition density and pressure.

The effect of allowing a distribution for the parameter $p$ on the prior and LD+HD posterior distributions can be seen in the right panel of Fig. 2.15. In spite of the simple discrete ansatz $p = \{2.5, 3, 3.5\}$, we observe a continuous and smooth distribution of the surface tension. The reason is that the variation of the surface tension $\sigma$ with $p$ is continuous and smooth, and that the other surface parameters, which are fixed by the fit to experimental masses, have a continuous distribution. The effect of allowing a distribution for the parameter $p$ does not modify the behavior of the surface energy in the vicinity of $I = 0$. However, above the drip line and particularly in the high isospin region, we can clearly observe that the uncertainties associated to the discrete ansatz are larger than those associated to $p = 3$ case. Let us notice that this effect is much more important in [CGM19a]. This can be understood from the fact that, in the latter study, curvature terms were not accounted for, and that the surface parameters were fitted to the spherical magic and semimagic nuclei $^{40,48}$Ca, $^{48,58}$Ni, $^{88}$Sr, $^{90}$Zr, $^{114,132}$Sn, and $^{208}$Pb, while the surface and curvature parameters are here fitted to the 2498 experimental masses of the AME2016 [Hua+17].

The correlation coefficients between the EoS parameters and the density and pressure at the CC transition point are calculated and reported in Fig. 2.16 for different joint distributions of parameters. For the prior distribution, which corresponds to the consideration of nuclear experimental constraints included as fully uncorrelated parameters sets, we observe that the most influential empirical parameters on $n_t$ and $P_t$ are the high-order parameters $Q_{sat}$ and $Q_{sym}$. We also recover a small anticorrelation between the transition density and the $L_{sym}$ parameter, as anticipated in 1.2.6. The transition density directly depends on the energy of beta-equilibrated matter. The transition pressure being linked to the first derivative of the energy density, it is not surprising to observe that $P_t$ is rather slightly anticorrelated with $K_{sym}$. Since this

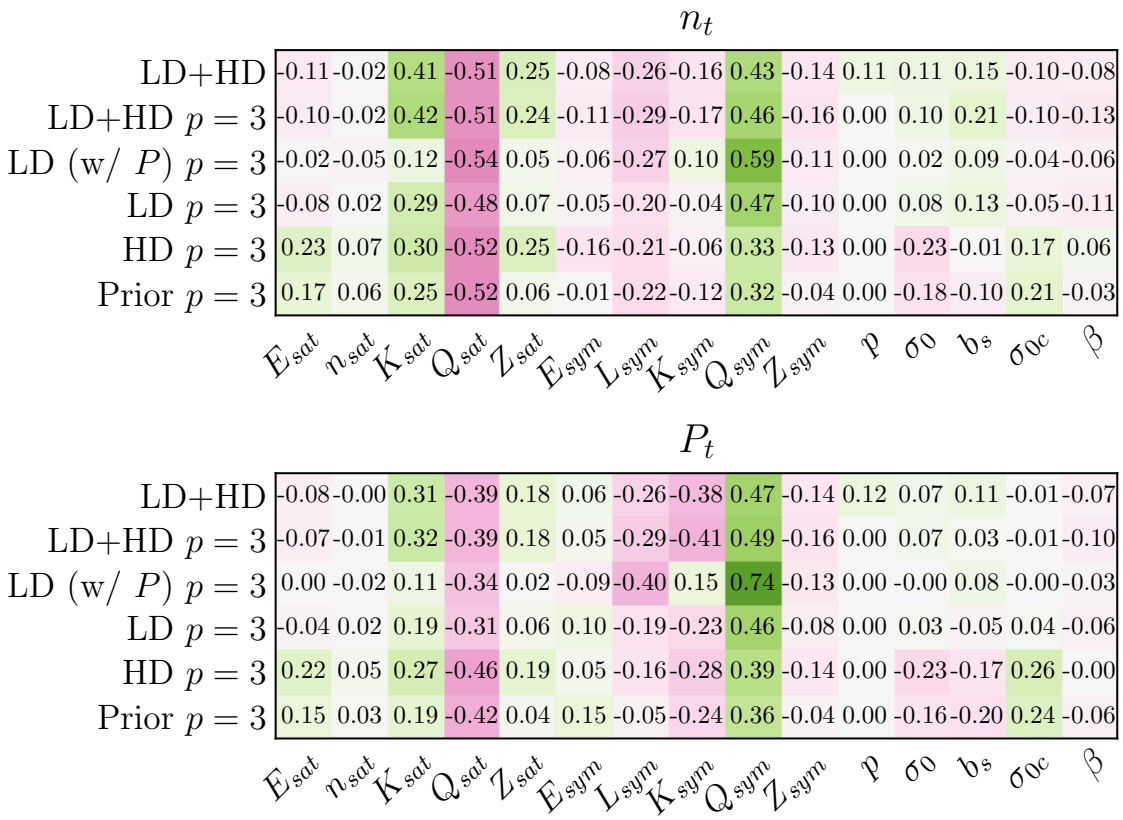



**Figure 2.16:** *Correlation of the CC transition density $n_t$ (upper panel) and pressure $P_t$ (lower panel) with the empirical, surface, and curvature parameters for different distributions: prior, HD, LD, LD with pressure filter, and LD+HD joint posterior distributions for $p = 3$, and LD+HD joint posterior distribution for the discrete ansatz $p = \{2.5, 3, 3.5\}$.*

parameter widely varies in existing functionals, this can explain why the present predictions of the transition pressure are so largely scattered, see Fig. 1.13. The HD filter does not impose further correlations between the transition quantities and the EoS, apart from tiny correlations with the isoscalar kurtosis $Z_{sat}$. We can see that the LD filter slightly reinforces the correlation of transition density and pressure with the isovector skewness $Q_{sym}$. If the pressure filter, which allows a tight determination of the low-order isovector parameters, is also considered, the correlations with $Q_{sym}$ are even stronger, $r(Q_{sym}, n_t) = 0.59$ and $r(Q_{sym}, P_t) = 0.74$. In addition, the anticorrelation between $L_{sym}$ and $P_t$ emerges, with $r(L_{sym}, P_t) = -0.40$. For our final LD+HD prediction with $p = 3$, we find that $n_t$ is correlated with $K_{sat}$ and $Q_{sym}$, and anticorrelated with $Q_{sat}$. A slight correlation with $L_{sym}$ can also be seen. Concerning the transition pressure $P_t$, correlations with the isovector empirical parameters $L_{sym}$, $K_{sym}$ and $Q_{sym}$ are observed, as well as with $K_{sat}$ and $Q_{sat}$ in the isoscalar sector. It is seen that correlations of the transition quantities with the surface and curvature parameters are negligible in this study, even if the isovector surface parameter $p$ is

| | This thesis | | [CGM19a] | |
|---|---|---|---|---|
| Distribution | $n_t$ (fm$^{-3}$) | $P_t$ (MeV/fm$^3$) | $n_t$ (fm$^{-3}$) | $P_t$ (MeV/fm$^3$) |
| Prior | $0.062^{+0.028}_{-0.036}$ | $0.225^{+0.379}_{-0.167}$ | $0.078 \pm 0.040$ | $0.342 \pm 0.426$ |
| HD | $0.059^{+0.023}_{-0.029}$ | $0.190^{+0.232}_{-0.120}$ | $0.076 \pm 0.032$ | $0.394 \pm 0.327$ |
| LD | $0.073^{+0.025}_{-0.032}$ | $0.281^{+0.478}_{-0.179}$ | | |
| LD (w/ $P$) | $0.068^{+0.021}_{-0.021}$ | $0.263^{+0.302}_{-0.149}$ | $0.074 \pm 0.011$ | $0.307 \pm 0.167$ |
| LD+HD | $0.074^{+0.019}_{-0.033}$ | $0.277^{+0.276}_{-0.168}$ | | |
| LD (w/ $P$)+HD | $0.083^{+0.016}_{-0.045}$ | $0.463^{+0.262}_{-0.338}$ | $0.077 \pm 0.010$ | $0.389 \pm 0.111$ |

**Table 2.3:** 68% *confidence intervals for the CC transition density $n_t$ and pressure $P_t$ for different distributions: prior, HD, LD with and without the pressure filter, and LD+HD with and without the pressure filter. In all cases, $p = 3$ is fixed. The right two columns give the average value and standard deviation $\sigma$ of $n_t$ and $P_t$ calculated in [CGM19a].*

allowed to vary (lines "LD+HD"). This observation contrasts with some of the results of [CGM19a], in which important correlations between the transition quantities and the surface parameters were revealed. Once again, this is because the surface energy is better controlled in the present calculation, as permitted by the introduction of curvature terms, supplemented by the fact that a larger pool of nuclear masses is used for the fit of surface and curvature parameters. We can say that the fact that important differences are observed with respect to our published results, when the surface parameters are more strongly constrained, is a confirmation of the main conclusion of our paper [CGM19a], namely that a control on the surface energy is mandatory to correctly predict the transition properties.

The joint distribution for $n_t$ and $P_t$ as well as the corresponding marginalized one-parameter probability distributions are shown in Fig. 2.17 for different filters. In the first five panels, the dashed lines delimit the 50% and 90% confidence regions, and the different symbols give the CC transition point as obtained with the popular models BSk24, SLy4, PKDD and TM1. In all cases and in agreement with [CGM19a], we find that $n_t$ and $P_t$ are strongly correlated. The Pearson correlation coefficient is as high as $r = 0.92$ when using the LD filter with the constraint on pressure. We can observe in a graphical way that the LD and HD constraints lead to compatible predictions for the CC transition point. It is clearly seen that the most constraining filter for both $n_t$ and $P_t$ is the LD filter which account for the constraint on pressure ("LD (with pressure)"), ensuring the compatibility of the empirical parameters with the chiral ETF predicted bands for energy per nucleon and pressure of SNM and PNM [DHS16]. From the corresponding joint distribution, we obtain $n_t = 0.068^{+0.021}_{-0.021}$ fm$^{-3}$ and $P_t = 0.263^{+0.302}_{-0.149}$ MeV/fm$^3$ at the $1\sigma$ confidence level. The passage through the HD filter has a significant impact on the distribution of $P_t$. We find that the resulting CC transition points, for three of the four popular models considered in this study, meet our final LD+HD prediction at the 50% confidence level.

The 68% confidence intervals for the transition density and pressure for each of the

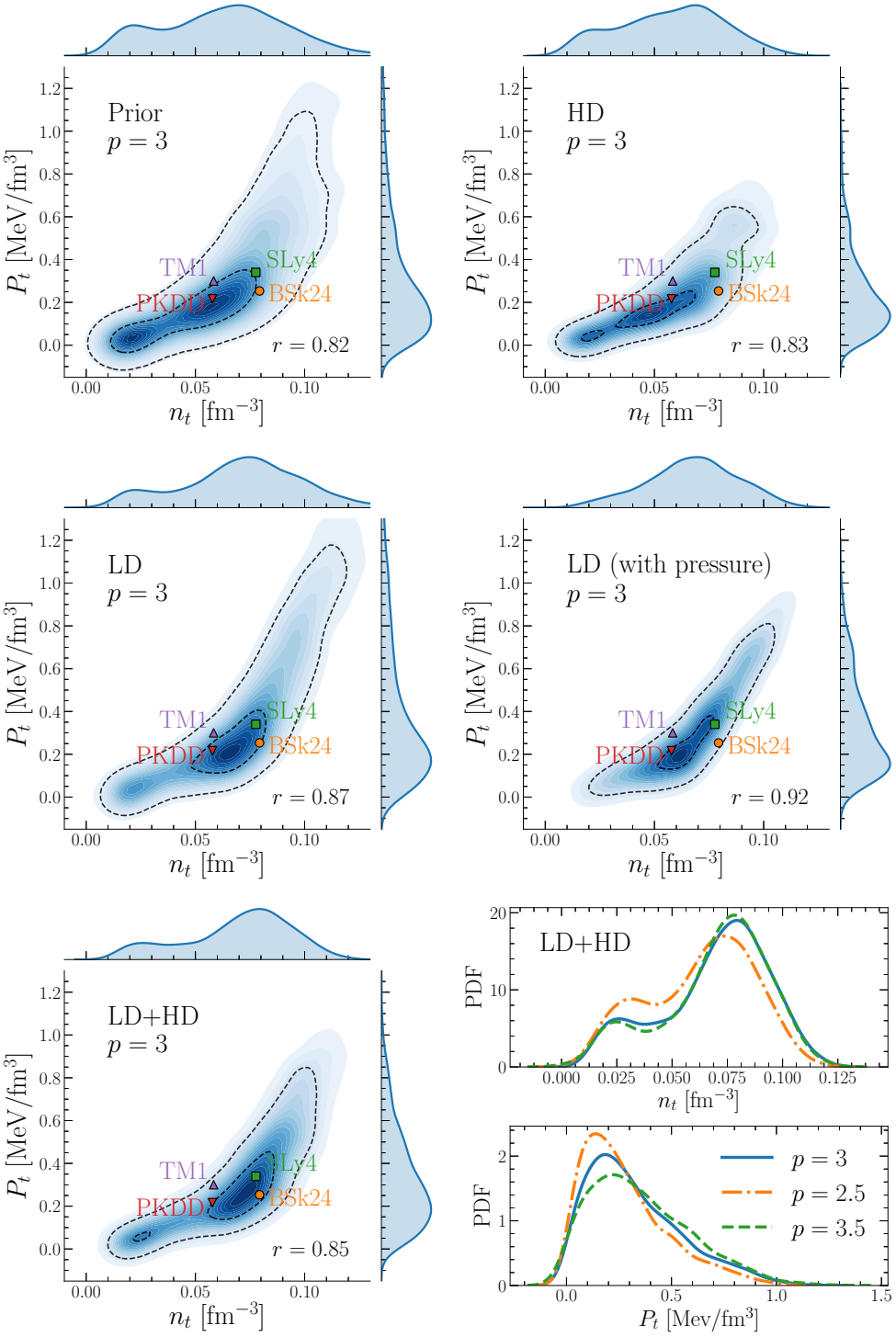



**Figure 2.17:** *Marginalized probabilities for the transition density $n_t$ and pressure $P_t$ for different distributions. In the first five panels, the dashed lines delimit the 50% and 90% confidence regions. For each distribution, the Pearson correlation coefficient $r(n_t, P_t)$ is given. The results for four characteristic EoS are also shown.*

considered distributions as well as for LD+HD with the pressure filter are reported in Table 2.3. For each filter, our predictions for $n_t$ and $P_t$ are compatible with our published results reported in the right two columns [CGM19a], though not identical due to a different treatment of the surface energy. Indeed, a limited pool of nine magic and semimagic nuclei were used to fit the surface parameters in [CGM19a], whereas the surface and curvature parameters are fitted to all experimental masses from AME2016 (2498 nuclei) in the present study. Both options have limitations. On the one hand, fitting all presently measured masses and considering a curvature term allows a better reproduction of experimental masses and a tighter determination of the surface parameters. On the other hand, we fit a spherical model to nonspherical nuclei and we thus take the risk to incorporate deformation energy components in the surface energy. The fact that changing the fitting protocol of the surface and curvature parameters alters sensitively the predictions of the transition density and pressure means that the surface energy is a key quantity (together with the high-order empirical parameters that are strongly constrained by the pressure filter), and that further investigations are desirable. In particular, a fit of the experimental masses with a deformation degree of freedom and shell effects, and an improved control of the uncertainty on pressure are advisable. Let us remark that in [CGM19a], we limited us to the calculation of the standard deviation for $n_t$ and $P_t$. However, in the present study, and especially for the LD+HD prediction, we observe that the 68% credible interval for $n_t$ and $P_t$ deviates from the standard deviation ($\sigma_{n_t} = 0.024$ fm$^{-3}$ and $\sigma_{P_t} = 0.224$ MeV/fm$^3$) because of the non-Gaussianity of the distributions arising from the tension between LD and HD constraints observed in Fig. 2.17.

The effect of varying $p$ on the marginalized one-parameter distributions for $n_t$ and $P_t$ is displayed in the last panel of Fig. 2.17, for the LD+HD prediction. Overall, only minor differences are observed between the $p = 2.5$, $p = 3$ and $p = 3.5$ cases. We can see that the difference between the $p = 3$ and $p = 3.5$ cases is even smaller than that between $p = 2.5$ and $p = 3$ as far as the transition density was concerned, as it was expected from Fig. 1.12. In [CGM19a], we suggested that extra data on neutron rich nuclei are needed to pin down the value of $p$, and consequently the transition point. The present study suggests that an accurate reproduction of the whole pool of presently measured masses might be sufficient to compensate the uncertainty led by the poorly constrained $p$ parameter.

### 2.3.3 Pulsar glitches: answering the question "*Is the crust enough?*"

For a given EoS, the determination of the fractional crust moment of inertia, using Eq. (2.10), and more generally of any crustal observable, is possible if the location of the transition point to homogeneous matter is known. As discussed in 2.1.2.2, the NS crustal moment of inertia is related to the theoretical description of the glitch phenomenon, which consists of the sudden spin-up of the rotational frequency of an NS. In the standard interpretation, a pulsar glitch is observed as the consequence of the angular momentum transfer from the neutron superfluid permeating the inner crust to the solid crust [AI75]. For a specific pulsar for which the coupling parameter

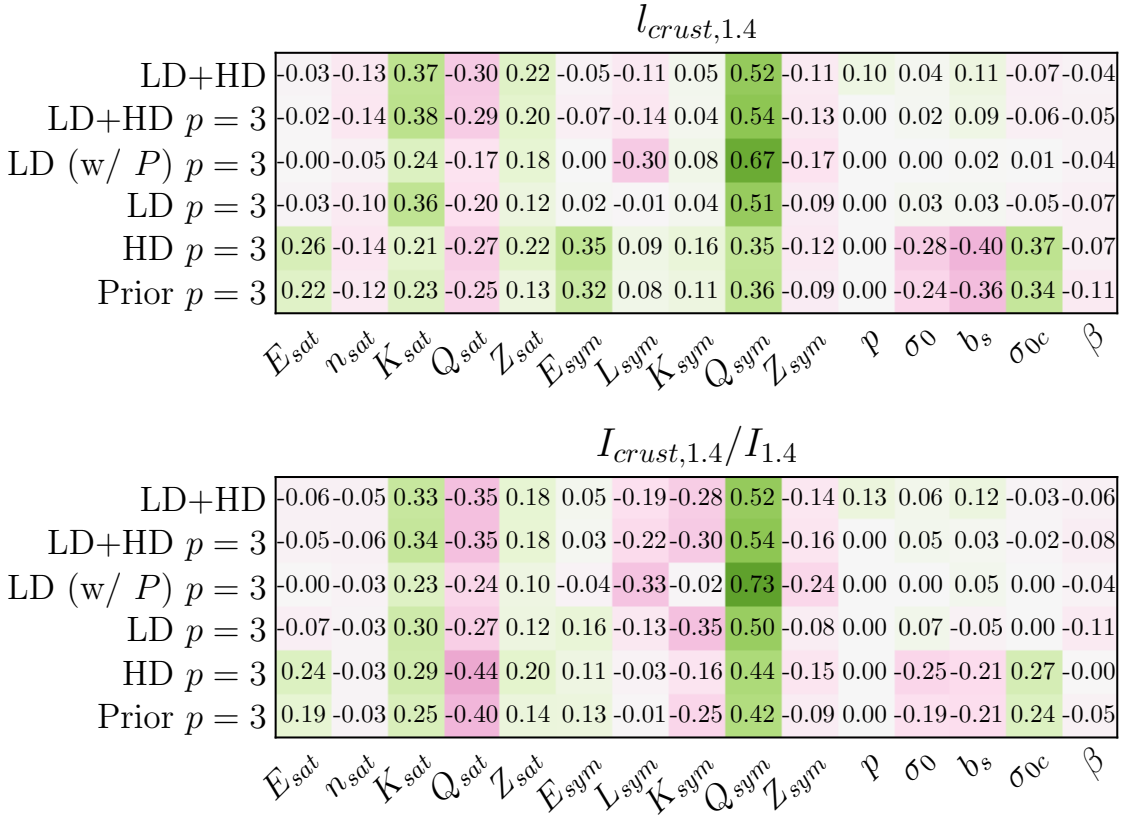



**Figure 2.18:** *Correlation of the crust thickness $l_{crust,1.4}$ (upper panel) and fractional crust moment of inertia $I_{crust,1.4}/I_{1.4}$ (lower panel) of a $1.4M_\odot$ NS with the empirical, surface, and curvature parameters for different distributions: prior, HD, LD, LD with pressure filter, and LD+HD joint posterior distributions for $p = 3$, and LD+HD joint posterior distribution for the drscrete ansatz $p = \{2.5, 3, 3.5\}$.*

$\mathcal{G}$ has been measured, and depending of the importance of the crustal entrainment effect [Cha13], the crust must therefore be sufficiently thick to store enough angular momentum. Naturally, it yields the question "*Is the crust enough?*", for which the answer is known to be very sensitive to the EoS [And+12; PFH14] and, most important to the CC transition density and pressure [CGM19b]. In the following, the crustal origin of pulsar glitches is discussed for the specific case of Vela, using the LD+HD joint posterior distribution of EoS parameters.

The correlation coefficients between the EoS parameters and the crust thickness and fractional crust moment of inertia of a $1.4M_\odot$ NS are displayed in Fig. 2.18 for different joint distributions of parameters. In agreement with our published results [CGM19b], we find that $l_{crust,1.4}$ and $I_{crust,1.4}/I_{1.4}$ are strongly correlated with the isovector skewness $Q_{sym}$. A small correlation is also obtained between the fractional crust moment of inertia and the isovector incompressibility $K_{sym}$. Therefore, the conclusion drawn in [CGM19b], that higher precision in the experimental determination of $K_{sym}$ and $Q_{sym}$ in the low density EFT theoretical predictions is required to reduce the un-

| | This thesis | | [CGM19b] | |
|---|---|---|---|---|
| Distribution | $l_{crust,1.4}$ (km) | $I_{crust,1.4}/I_{1.4}$ (%) | $l_{crust,1.4}$ (km) | $I_{crust,1.4}/I_{1.4}$ (%) |
| Prior | $1.06^{+0.25}_{-0.33}$ | $2.33^{+3.37}_{-1.69}$ | $1.13 \pm 0.29$ | $3.40 \pm 3.34$ |
| HD | $1.10^{+0.21}_{-0.24}$ | $2.20^{+2.32}_{-1.35}$ | $1.17 \pm 0.29$ | $4.39 \pm 3.26$ |
| LD | $1.08^{+0.19}_{-0.27}$ | $3.06^{+3.65}_{-2.08}$ | | |
| LD (w/ $P$) | $0.98^{+0.21}_{-0.20}$ | $2.99^{+2.65}_{-1.87}$ | $0.95 \pm 0.11$ | $3.54 \pm 1.33$ |
| LD+HD | $1.11^{+0.14}_{-0.21}$ | $2.89^{+2.51}_{-1.68}$ | | |
| LD (w/ $P$)+HD | $1.10^{+0.15}_{-0.25}$ | $4.16^{+2.20}_{-2.90}$ | $1.03 \pm 0.10$ | $4.50 \pm 1.25$ |

**Table 2.4:** 68% *confidence intervals for the crust thickness and fractional crust moment of inertia of a* $1.4M_\odot$ *NS for different distributions: prior, HD, LD with and without the pressure filter, and LD+HD with and without the pressure filter. In all cases,* $p = 3$ *is fixed. The right two columns give the average value and standard deviation* $\sigma$ *of* $l_{crust,1.4}$ *and* $I_{crust,1.4}/I_{1.4}$ *calculated in [CGM19b].*

certainties on crustal observables, clearly holds despite the different fitting protocol employed in the present study. Interestingly, as observed in Fig. 2.16 for the CC transition density and pressure, we can see that the correlations with the surface and curvature parameters that we observed in [CGM19b] disappear when a refined control of the surface energy is considered. Indeed, in the present study we consider a curvature term, and we fit the surface parameters to the 2498 experimental masses of the AME2016, while they were fitted to the experimental masses of only 9 spherical nuclei in [CGM19b].

The 68% confidence intervals for the crust thickness and fractional crust moment of inertia of a $1.4M_\odot$ NS are reported in Table 2.4. As for the transition density and pressure, we can see that the present predictions and our published results [CGM19b], reported in the right two columns, are compatible within error bars, but again are not identical due to a different treatment for the surface energy. Combined with the HD filter, the incorporation of the pressure filter into the likelihood probability has the effect of strongly increasing the value of $I_{crust,1.4}/I_{1.4}$. This can be observed by comparing the results presented in the bottom two rows.

The strong correlation between the crust thickness and the fraction of crust moment of inertia for $M = 1.4M_\odot$ is seen in Fig. 2.19. It means that the thicker the crust is, the more angular momentum is confined to the neutron superfluid coexisting with the crystal lattice of the inner crust. As expected from previous studies [PFH14; CGM19b], we observe large correlations between the crustal observables and the transition quantities, notably $r(P_t, I_{crust,1.4}/I_{1.4}) = 0.98$. Among the four popular models considered, only the prediction of the BSk24 EoS (orange circle) meets our distribution. The results for SLy4 (green square), PKDD (red triangle) and TM1 (purple triangle) EoS are only marginally compatible with the LD+HD prediction at the 90% confidence level (dashed lines). We can see that a crustal origin for the glitches, if the Vela pulsar has the canonical $1.4M_\odot$ mass, appears marginal but still cannot be excluded at the 90% level, even if entrainment is accounted for (horizontal dashed

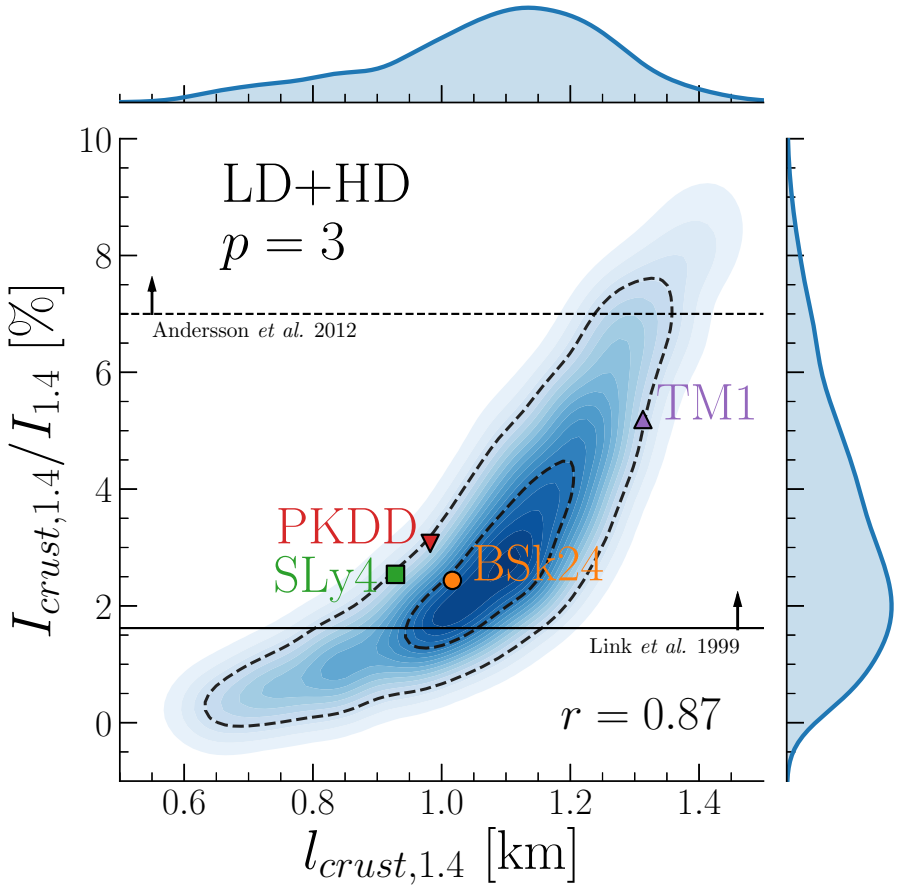



**Figure 2.19:** *Marginalized probabilities for the crust thickness $l_{crust,1.4}$ and fraction of crust moment of inertia $I_{crust,1.4}/I_{1.4}$ for a $1.4M_\odot$ NS, using the LD+HD distribution. The dashed lines delimit the 50% and 90% confidence regions. The Pearson correlation coefficient $r$ is given. The symbols show the prediction of four characteristic EoS models. The minimum values needed to justify Vela glitches with (Andersson et al. [And+12]) and without (Link et al. [LEL99]) crustal entrainment are represented.*

line).

From pulsar timing techniques, it is possible to infer the coupling parameter $\mathcal{G}$ of a given pulsar. This parameter is related to the fraction of crust moment of inertia via Eq. (2.14). In the specific case of the Vela pulsar (PSR B0833-45), the coupling parameter is very well constrained thanks to its long-term monitoring, $\mathcal{G}_{\rm Vela} = (1.62 \pm 0.03) \times 10^{-2}$ [Ho+15]. Fig. 2.20 displays the marginalized posterior distributions for the mass and radius of Vela for two estimations of crustal entrainment, using our LD+HD distribution. Let us recall that the importance of the crustal entrainment effect is encoded in the neutron effective mass. Here, we consider $\langle m_n^* \rangle / m_n = 1$, that is no entrainment [LEL99], and $\langle m_n^* \rangle / m_n = 4.3$, which is an estimation of crustal entrainment [And+12]. In this calculation, we assume that the observed glitches correspond to the maximum amplitude that can be sustained by the crust reservoir,

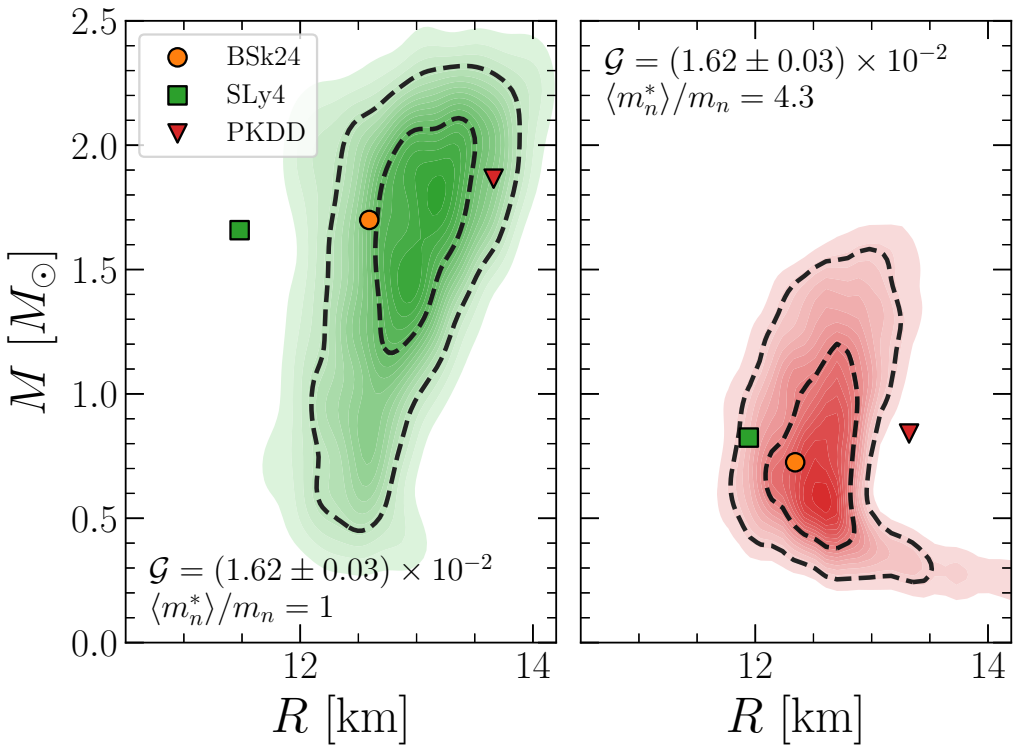



**Figure 2.20:** *Marginalized posterior for the NS mass $M$ and radius $R$ of Vela, $\mathcal{G} = (1.62 \pm 0.03) \times 10^{-2}$, without ($\langle m_n^* \rangle / m_n = 1$ [LEL99], left panel) and with an estimation of crustal entrainment ($\langle m_n^* \rangle / m_n = 4.3$ [And+12], right panel), using the LD+HD filter for $p = 3$. Dashed lines represent the 50% and 90% confidence intervals, and symbols show the prediction of characteristic EoS models.*

which means that we impose the equality

$$\frac{I_{crust}}{I} = \mathcal{G}_{\text{Vela}} \frac{\langle m_n^* \rangle}{m_n}. \tag{2.36}$$

Since the fractional moment of inertia is a decreasing function of the pulsar mass, see lower panel of Fig. 2.3, this means that the masses predicted in Fig. 2.20 should be considered as upper limits of the mass. Hence, the marginalized two-parameter distribution for Vela mass and radius is computed as

$$p(M, R|\text{data}) = \sum_{\boldsymbol{X}} \delta(M(\boldsymbol{X}) - M)\delta(R(\boldsymbol{X}) - R)p(\boldsymbol{X}|\text{data}), \tag{2.37}$$

where $M(\boldsymbol{X})$ and $R(\boldsymbol{X})$ are the mass and radius obtained with the parameter set $\boldsymbol{X}$ when the central density is such that the corresponding fractional moment of inertia verifies Eq. (2.36). The resulting distribution for Vela mass and radius without entrainment (left panel) is compatible with the uncertainties reported in Table 2 of [Ho+15]. Evidently, the uncertainties are larger in our work since we consider a distribution of models, while three specific EoS (BSk20, BSk21, and APR) were used in [Ho+15]. In

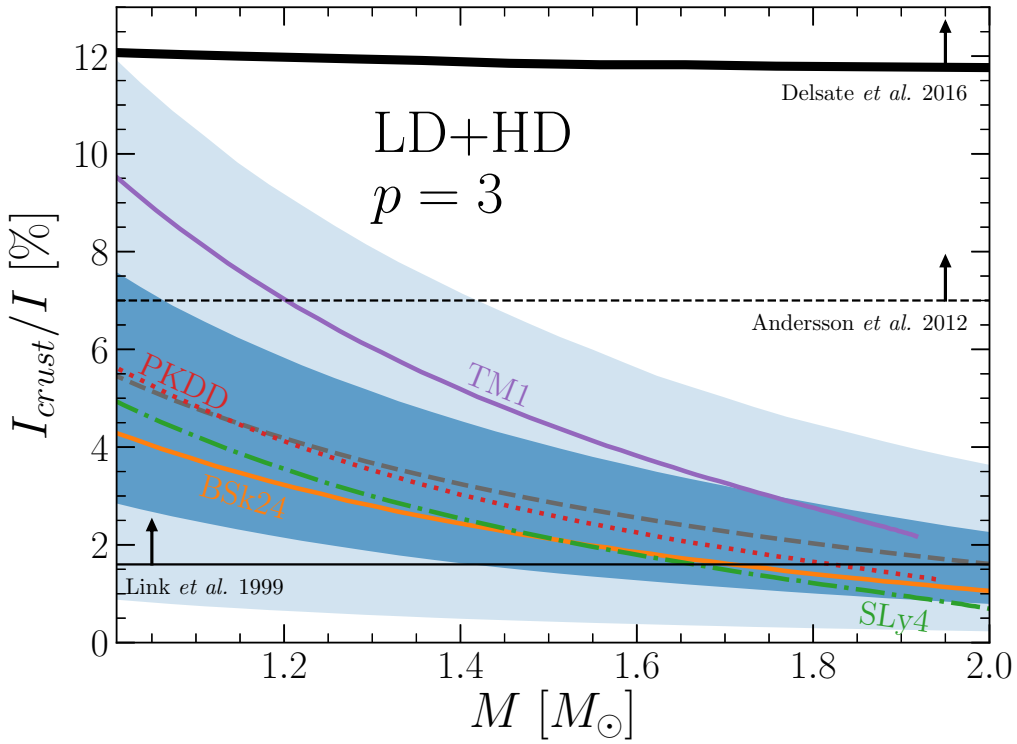



**Figure 2.21:** *Marginalized posterior for the fraction of crust moment of inertia $I_{crust}/I$ as a function of the NS mass $M$, using the LD+HD distribution. The blue dark and light shaded regions show the 50% and 90% confidence intervals, respectively. The gray dashed line represents the average value. The results for four characteristic EoS models are given. The minimum values needed to justify Vela glitches with (Delsate et al. [Del+16] and Andersson et al. [And+12]) and without (Link et al. [LEL99]) crustal entrainment are represented.*

the same spirit, we show the prediction of BSk24, SLy4, and PKDD EoS. Considering the specific treatment of the entrainment effect with $\langle m_n^* \rangle / m_n = 4.3$ (right panel), the predicted Vela mass is significantly lower than that inferred in the case where entrainment is neglected, with $M_{\rm Vela} = 0.79^{+0.41}_{-0.33} M_\odot$ at the $1\sigma$ confidence level. This shows that a proper treatment of crustal entrainment is more important than the EoS uncertainty and the experimental uncertainty on the glitch amplitude. Let us notice that an innovative method was recently proposed to determine the mass using observations of the maximum observed glitches: providing the pinning and effective mass density profiles as well as the EoS of stellar matter, the maximum glitch size only depends on the NS mass, $\Delta\Omega_{max} = \Delta\Omega_{max}(M)$ [Piz+17].

Fig. 2.21 shows the average value of the fractional crust moment of inertia $I_{crust}/I$ and the 50% and 90% regions as a function of the NS mass for the LD+HD posterior distribution. It should be stressed that the uncertainty on $I_{crust}/I$ is smaller in [CGM19b] because this quantity is correlated with the isovector empirical parameters $K_{sym}$ and $Q_{sym}$, which are strongly constrained by the filter on pressure, see

Fig. 2.8, not accounted for in the present calculation. The black lines represent the minimum values to justify the large glitches exhibited by Vela with [Del+16; And+12] and without [LEL99] accounting for the entrainment effect. As expected from [LEL99], we find that the amount of angular momentum stored in the crust is sufficient to explain pulsar glitches if the entrainment effect is neglected. Given the intermediate estimation of crustal entrainment [And+12] ($\langle m_n^* \rangle / m_n = 4.3$), we infer that the mass of Vela must be lower than $\approx 1.4 M_\odot$ to meet the LD+HD prediction at the 90% level. This can also be seen in Fig. 2.19. Finally, it is clearly observed that the largest estimation of the crustal entrainment effect [Del+16] is incompatible with the present nuclear physics knowledge if we keep the standard picture where a full crustal origin is assumed [AI75]. Indeed, it yields $M_{\rm Vela} \lesssim 1 M_\odot$, yet such low-mass NS have never been observed to this day. The same conclusion was drawn in our published paper [CGM19b], where a different protocol for the fit of the surface energy was employed, and a more stringent filter including the chiral EFT pressure estimation was included. The fact that the conclusion does not change fully neglecting the EFT results on pressure confirms the robustness of the prediction.

## 2.4 Conclusions

In this chapter, we have first introduced the basic equations of hydrostatic equilibrium in general relativity, for spherical nonrotating stars. We have solved these equations for different popular EoS in order to obtain the relationship between the mass and radius of the star. In the same spirit, we have computed the moment of inertia as well as the tidal deformability within the slow rotation approximation, which is expected to be valid for most pulsars. The determination of the CC transition density and pressure, discussed thoroughly in Chapter 1, allows the calculation of crustal observables. We have thus computed the crust thickness and fraction of crust moment of inertia. We have explained in detail the connection between the latter observable and the glitch phenomenon in the standard picture, that is where a glitch is observed as the consequence of the transfer of angular momentum from the neutron superfluid in the inner crust to the rest of the star [AI75]. A major issue exhibited in Section 2.1 is the sensitivity of the results on the EoS, and more specifically on the isovector empirical parameters. We have shown that not every EoS successfully passes the maximum mass constraint of $M_{max} \gtrsim 2 M_\odot$ [Dem+10; Ant+13; Cro+20] favoring a stiff EoS. Moreover, a full crustal origin for the glitch phenomenon can only be accepted with very stiff EoS, given the present estimations of crustal entrainment [And+12; PFH14]. Conversely, the recent constraint on the tidal deformability parameter $\Lambda_{1.4}$ inferred from GW170817 [Abb+18] tends to favor soft EoS.

We have recalled the principle of Bayesian inference before performing the Bayesian determination of the EoS parameters, using the metamodeling technique [MHG18a]. We have used a uniform prior distribution for the parameters, given empirical constraints. The results and analyses presented in this chapter follow closely, but are not identical to our published results [CGM19a; CGM19b]. Indeed, a Bayesian analysis crucially depends both on the prior and on the choice of the filters. In the present work, we have varied both the prior distribution of surface parameters, adopting a different

protocol from the one of [CGM19a; CGM19b] and introducing curvature terms which were neglected in the previous study, and the filters, exploring the specific effect of including or not the EFT predictions of the pressure of SNM and PNM. The different results are compatible within error bars, but different correlations are observed. These differences are discussed, and have allowed us to better understand the effect of the different conditions. A sensitivity analysis on the CC transition point has revealed that the isovector parameters are the most important for the precise determination of $n_t$ and $P_t$. We have calculated the likelihood function using constraints on nuclear physics observables (LD constraints), namely the experimental masses [Hua+17] and chiral EFT calculations on SNM and PNM [DHS16], and on NS observables as well as physical requirements (HD constraints). The posterior distribution of empirical parameters was analyzed. We have observed that the LD filter is very effective in constraining the isovector parameters, particularly if the impose the compatibility with the chiral ETF predicted bands for pressure. We have shown that only the constraints arising from nuclear physics impose correlations among the empirical parameters. In the isovector sector, the correlation between $E_{sym}$ and $L_{sym}$ is recovered, and we find that $L_{sym}$ is correlated with $K_{sym}$. We have found new interesting correlations when imposing pressure filter: $r(L_{sym}, Q_{sym}) = -0.55$ and $r(K_{sym}, Q_{sym}) = 0.52$.

Finally, we have made general predictions for the static properties and crustal observables of NS, using the LD+HD joint posterior distribution of parameters calculated in Section 2.2. Overall, we have found that our predictions for the NS observables are in a rather good agreement with the constraints on the EoS, radius, and tidal deformability, inferred from the GW170817 event [De+18; Abb+18]. We have obtained $R_{1.4} = 12.88^{+0.53}_{-0.65}$ km and $\Lambda_{1.4} = 634^{+204}_{-190}$ at the 90% level. We have shown that the transition density and pressure are correlated with the isovector parameters, and particularly with the skewness parameter $Q_{sym}$. Within the present experimental and theoretical uncertainty on those parameters, we have estimated the transition density and pressure respectively as $n_t = 0.068^{+0.021}_{-0.021}$ fm$^{-3}$ and $P_t = 0.263^{+0.302}_{-0.149}$ MeV/fm$^3$, at the $1\sigma$ confidence level. In contrast with our previous work [CGM19a], with the present protocol we do not observe a strong influence of the surface parameters on the CC transition quantities. This can be explained by a refined control of the surface energy in the present work. We have observed that the thicker the crust is, the more angular momentum is confined to the neutron superfluid coexisting with the crystal lattice in the inner crust. The large uncertainty on the transition pressure is reflected on the fraction of crust moment of inertia. Indeed, for a $1.4M_\odot$ NS, we have obtained $I_{crust,1.4}/I_{1.4} = 2.89^{+2.51}_{-1.68}\%$, at the $1\sigma$ confidence level. The joint distribution for Vela mass and radius was computed for two different estimations of the crustal entrainment effect. It has confirmed that a control on crustal entrainment is the key phenomenon to associate the glitch phenomenon to crustal physics, even if the uncertainty on the EoS blurs the results. We have observed the variation with NS mass of the fraction of crust moment and inertia and concluded that a full crustal origin is excluded if we consider the present largest estimation of crustal entrainment [Del+16].

# Chapter 3

# Crystallization of the crust of protoneutron stars

It is widely accepted that NS are born hot in SN explosions, after their presupernova progenitors exhaust nuclear fuel in their cores. During the subsequent neutrino-transparent stage that takes place approximately one minute after the explosion, the PNS begins to cool down by neutrino emission and by heat diffusion from the internal layers to the surface, leading in later times to the thermal emission of photons. In the cooling process, the composition and properties of the crust are thought to be fixed at the finite temperature where nuclear reactions fall out of equilibrium. A lower estimate for this temperature is given by the crystallization temperature, which can be as high as $\approx 9 \times 10^9$ K in the crust, potentially leading to sizable differences with respect to the simplifying cold catalyzed matter (CCM) hypothesis.

NSE approaches have been developed to account for the full distribution of nuclei at finite temperature [EH80; HS10; RAG14; GR15], in contrast with the SNA, or one-component plasma (OCP) approximation, which considers a unique configuration for a given thermodynamic condition. NSE approaches, also referred to as multicomponent plasma (MCP) approaches, allow properly calculating the so-called impurity parameter entering cooling simulations, generally taken as free parameter directly fitted to cooling data. Another quantity of interest that can be evaluated in an MCP approach is the fraction of odd-mass and odd-charge nuclei in the outer crust. Their presence at low temperature might be the sign of ferromagnetic phase transitions, which could alter the relativistic electron gas. The importance of these effects depends partly on the spin of odd nuclei.

As in the zero-temperature limit, results in the inner-crust regime at finite temperature are model dependent, and a nuclear free energy functional is required. Given its simplicity and because it is not expensive from the computational point of view, the CLD approach is very appealing, and has been already used in the past [GR15; Gra+18]. However, within this approach, the problem of the temperature dependence of shell corrections needs to be addressed in order to make realistic predictions for the crystallization temperature and associated composition in the inner crust.

This chapter is organized as follows. In Section 3.1, we introduce the model of the crust at finite temperature. The OCP approximation and MCP treatment are

presented, and the expression of the nuclear free energy employed in the free neutron regime is given. Results relevant for the outer crust and inner crust of NS at finite temperature and particularly at crystallization are then shown in Sections 3.2 and 3.3, respectively. Finally, conclusions are given in Section 3.4. Most of the results presented in this chapter have been published in [Fan+20; Car+20; CFG20].

## Contents

**3.1 Model of the crust at finite temperature . . . . . 107**
3.1.1 One-component Coulomb plasma approximation . . . . . 107
3.1.1.1 OCP in a liquid phase . . . . . 108
3.1.1.2 OCP in a solid phase . . . . . 109
3.1.1.3 Crystallization of a OCP . . . . . 110
3.1.2 Multicomponent Coulomb plasma in a liquid phase . . . . . 112
3.1.2.1 Nuclear statistical equilibrium . . . . . 112
3.1.2.2 Evaluation of the chemical potentials . . . . . 114
3.1.2.3 Evaluation of the rearrangement term . . . . . 115
3.1.3 Nuclear free energy functional in the free neutron regime . 116
3.1.3.1 Thermodynamics of nuclear matter . . . . . 117
3.1.3.2 Energetics of clusters at finite temperature in the CLD approximation . . . . . 120
**3.2 Study of the outer crust at crystallization . . . . . 120**
3.2.1 Crystallization temperature . . . . . 122
3.2.2 Equilibrium composition . . . . . 122
3.2.3 Impurity parameter . . . . . 126
3.2.4 Abundancies of odd nuclei . . . . . 126
**3.3 Study of the inner crust at crystallization . . . . . 129**
3.3.1 Influence of shell effects in the OCP approximation . . . . . 130
3.3.1.1 Temperature dependence of shell corrections . . . 130
3.3.1.2 Equilibrium composition of the OCP at crystallization for modern BSk functionals . . . . . 133
3.3.2 MCP results . . . . . 136
3.3.2.1 Equilibrium composition of the MCP . . . . . 137
3.3.2.2 Impurity parameter . . . . . 139
**3.4 Conclusions . . . . . 140**

## 3.1 Model of the crust at finite temperature

This section deals with the modeling of the crust at finite temperature. Since the possible contribution of a free proton gas is expected to be small at the temperatures considered, we neglect it. This working hypothesis is *a posteriori* confirmed by the calculation of the proton fugacity, $z_p = \exp[(\mu_p - m_p c^2)/(k_B T)]$. The existence of nonspherical pasta phases expected in the deeper layers of the inner crust ($n_B \gtrsim 0.05$ fm$^{-3}$ [PCP20]) is difficult to account for within the MCP approach [BMG20], and it is not considered in this study.

We review the OCP in 3.1.1. We give the expressions of the ideal and interacting contributions to the ion free energy in solid and liquid phases, and discuss the thermodynamic condition for crystallization. The nuclear statistical equilibrium is implemented perturbatively in the MCP approach in 3.1.2. The derivation of the rearrangement term, required to guarantee thermodynamic consistency, is carried out. In 3.1.3, we present the free energy functional used in the free neutron regime.

### 3.1.1 One-component Coulomb plasma approximation

At zero temperature, WS cells are supposed to be identical, thus the OCP (single-nucleus) approximation [BH80], which considers a unique fully ionized ion species $(A, Z)$ for a given thermodynamic condition of pressure and temperature $(P, T)$, is exact. Let us recall that the equilibrium composition is determined by minimizing the Gibbs free energy per nucleon at fixed pressure [BPS71] (or equivalently the free energy density at fixed baryon density [LS91; GR15; Car+20]). At finite temperature in the OCP approximation, the expected distribution of nuclei is replaced by the equilibrium nucleus obtained from the minimization of the relevant thermodynamic potential. The physical properties of the OCP are fully characterized by the dimensionless Coulomb coupling parameter,

$$\Gamma = \frac{Ze^2}{a_N k_B T}, \tag{3.1}$$

where $a_N = (4\pi n_N/3)^{-1/3}$ is the ion-sphere radius, $n_N = 1/V_{WS}$ being the ion density. More precisely, $\Gamma$ allows quantifying the nonideality of the system, that is the importance of the many-body interactions in the OCP. The higher $\Gamma$, the lower the temperature, the more coupled are the ions. The crystallization of the OCP into a lattice is observed at $T = T_m$, corresponding to $\Gamma = \Gamma_m \approx 175$.

The total free energy per ion in the crust – which coincides with the WS cell free energy in the OCP approximation – is given by

$$F = F_i + F_g + F_e, \tag{3.2}$$

where $F_i$ is the ion free energy in the e-cluster representation, see 1.2.1, $F_g$ is the neutron gas free energy, and $F_e$ is the electron gas free energy, given by [HPY07]

$$\mathcal{F}_e = \frac{F_e}{V_{WS}} = \varepsilon_e - \frac{P_r}{6} t_r^2 x_r \gamma_r, \tag{3.3}$$

with $t_r = T/(m_e c^2)$. The expressions of the energy density $\varepsilon_e$, relativistic unit of the electron pressure $P_r$, relativity parameter $x_r$, and $\gamma_r$ are given in 1.1.1.2. It should be

stressed that Eq. (3.3) is obtained by employing a Sommerfeld expansion in the limit $t_r \ll \gamma_r - 1$. Let us notice that in the regime of the outer crust, neutrons are still bound to the nuclei, thus $F_g = 0$ MeV, and consequently $F_i$ coincides with the ion free energy in the r-cluster representation. The ion free energy reads

$$F_i = M_i c^2 + F_i^{\rm id} + F_i^{\rm int}, \tag{3.4}$$

where $M_i$ represents the ion mass in the e-cluster representation, which is given at zero temperature by Eq. (1.29). At finite temperature, we only keep the finite-size contribution entering the Coulomb energy (third term in Eq. (1.58)), expressing the extra Coulomb interaction with respect to the nucleus in the vacuum due to the electrostatic effect of the homogeneous electron background. The temperature-independent static lattice energy only enters the Coulomb interaction term corresponding to a solid OCP. The modeling of $M_i$ at finite temperature as well as of the neutron gas free energy $F_g$ is presented in detail in 3.1.3. In Eq. (3.4), $F_i^{\rm id}$ represents the ideal contribution to the ion free energy, that is the noninteracting part, and $F_i^{\rm int}$ the interacting part.

#### 3.1.1.1 OCP in a liquid phase

Above the crystallization temperature, $T > T_m$, the OCP is in a liquid phase. In the Coulomb liquid, each ion can move freely within the volume of the WS cell in which it is confined. This translational center-of-mass motion is accounted for in the noninteracting part of the ion free energy, which therefore reads [HPY07]

$$F_i^{\rm id} = k_B T \left[ \ln\left( \frac{n_N \lambda^3}{g_s} \right) - 1 \right], \tag{3.5}$$

where $g_s$ is the spin degeneracy, which we take $g_s = 1$ for nuclei whose ground-state angular momentum is unknown, and $\lambda$ is the de Broglie wavelength of the component given by

$$\lambda = \sqrt{\frac{2\pi(\hbar c)^2}{M_i c^2 k_B T}}. \tag{3.6}$$

The interacting part of the ion free energy can be decomposed as [Fan+20]

$$F_i^{\rm int} = F_{ii,\rm liq} + F_{ie,\rm liq}^{\rm pol} \tag{3.7}$$

Analytical formulae have been derived for these two terms in [PC00]. In the present study, we find that the importance of the correction associated to electron polarization effects, $F_{ie,\rm liq}^{\rm pol}$ (Eq. (19) of [PC00]), is very small in the density and temperature regime of interest, and is therefore neglected. The only significant effect of the latter correction is to change drastically the composition around $P \approx 1.25 \times 10^{-4}$ MeV/fm$^3$, leading to a change of the crystallization temperature of $40 - 50\%$ [Fan+20]. This change in the composition is observed due to shell effects that we will neglect in our CLD approach, thus within the CLD approximation electron polarization effects are negligible. For the excess free energy of the Coulomb liquid, we employ the parametrization proposed

in [PC00]:

$$\begin{aligned}\frac{F_{ii,\mathrm{liq}}}{k_BT} &= A_1\left[\sqrt{\Gamma(A_2+\Gamma)}-A_2\ln\left(\sqrt{\Gamma/A_2}+\sqrt{1+\frac{\Gamma}{A_2}}\right)\right]\\ &\quad +2A_3\left(\sqrt{\Gamma}-\arctan\sqrt{\Gamma}\right)+B_1\left[\Gamma-B_2\ln\left(1+\frac{\Gamma}{B_1}\right)\right]\\ &\quad +\frac{B_3}{2}\ln\left(1+\frac{\Gamma^2}{B_4}\right),\end{aligned} \tag{3.8}$$

with $A_1 = -0.9070$, $A_2 = 0.62954$, $A_3 = -\sqrt{3}/2 - A_1/\sqrt{A_2}$, $B_1 = 4.56\times10^{-3}$, $B_2 = 211.6$, $B_3 = -10^{-4}$, and $B_4 = 4.62\times10^{-3}$. Let us notice that the latter parametrization solely depends on the Coulomb coupling parameter $\Gamma$, Eq. (3.1), and that $F_{ii,\mathrm{liq}}$ vanishes at high temperature.

#### 3.1.1.2 OCP in a solid phase

Once the crystallization temperature $T_m$ is reached, we assume that the OCP crystallizes into a perfect body-centered cubic lattice [CF16], as in the zero temperature case studied in Chapter 1. In the solid OCP, ions are able to oscillate near their equilibrium positions. Hence, the ideal part of the ion free energy accounting for the translational motion in the liquid OCP, $F_i^{\mathrm{id}}$, is replaced by the zero-point motion energy, $E_{zp}$, Eq. (1.3). The ion free energy in the e-cluster representation is therefore rewritten as

$$F_{i,\mathrm{sol}} = M_ic^2 + E_{zp} + F_{ii,\mathrm{sol}} + F_{ie,\mathrm{sol}}^{\mathrm{pol}}, \tag{3.9}$$

where $F_{ie,\mathrm{sol}}^{\mathrm{pol}}$ corresponds to the polarization correction in the solid phase [PC00], which is neglected here, and $F_{ii,\mathrm{sol}}$ is the Coulomb interaction term that can be decomposed as

$$F_{ii,\mathrm{sol}} = E_L + F_{\mathrm{th}} + F_{\mathrm{ah}} - k_BT\ln(g_s). \tag{3.10}$$

In the latter expression, $E_L$ represents the temperature-independent static lattice term, given by Eq. (1.5). The last term in Eq. (3.10) is the spin entropy. As previously, we fix $g_s = 1$ for nuclei whose spin degeneracy is unknown, yet the inclusion of this term has no effect on the determination of the crystallization temperature because it is the same for both liquid and solid OCP.

The thermal contribution due to the ion vibrations around their equilibrium position in the harmonic approximation and the anharmonic correction have been analytically fitted by Baiko *et al.* [BPY01] and Potekhin & Chabrier [PC10], respectively. The expression employed for the thermal contribution reads [BPY01]

$$\frac{F_{\mathrm{th}}}{k_BT} = \sum_{n=1}^{3}\ln\left(1-\mathrm{e}^{-\alpha_n\theta}\right) - \frac{A(\theta)}{B(\theta)}, \tag{3.11}$$

where $\theta \equiv \hbar\omega_p/(k_BT)$, $\omega_p$ being the ion plasma frequency, Eq. (1.4), and

$$A(\theta) = \sum_{n=0}^{8} a_n\theta^n, \tag{3.12}$$

$$B(\theta) = \sum_{n=0}^{7} b_n \theta^n + \alpha_6 a_6 \theta^9 + \alpha_8 a_8 \theta^{11}, \tag{3.13}$$

with $\alpha_n$, $a_n$, and $b_n$ numerical constants (see Table II in [BPY01]). The analytical expression of the anharmonic correction used in our study is [PC10]

$$F_{\rm ah} = F_{\rm ah}^{(0)} \mathrm{e}^{-c_1\theta^2} - k_B T d_1 \frac{\theta^2}{\Gamma}, \tag{3.14}$$

where

$$F_{\rm ah}^{(0)} = k_B T \sum_{n\geq 1} \frac{f_n}{n\Gamma^n}, \tag{3.15}$$

with $c_1$, $d_1$, and $f_n$ numerical constants. One should stress that Eq. (3.14) is modified with respect to that proposed by Farouki & Hamaguchi, $F_{\rm ah}^{(0)}$, based on numerical simulations of the solid OCP for $170 \leq \Gamma \leq 2000$ [FH93], so as to reproduce the zero-temperature and classical limits.

#### 3.1.1.3 Crystallization of a OCP

As in previous works [Fan+20; Car+20; CFG20], we compute the crystallization temperature within the OCP approximation, which is simple and not costly from the numerical point of view. We expect it to be a reasonable approximation because, as we will show later in this chapter, the average free energy of the MCP is very close to the one of the OCP in the temperature domain of this study.

The condition of crystallization of a OCP with associated composition $\boldsymbol{\theta} = \{A, Z, n_g\}$ and baryon density $n_B$ is defined as

$$\mathcal{F}_{\rm liq}(\boldsymbol{\theta}, T_m) = \mathcal{F}_{\rm sol}(\boldsymbol{\theta}, T_m), \tag{3.16}$$

where $\mathcal{F}_{\rm liq}$ and $\mathcal{F}_{\rm sol}$ are the WS cell free energy density in the liquid and solid phase, respectively. The latter equation is equivalent to

$$F_i^{\rm id} + F_{ii,\rm liq} = E_{zp} + F_{ii,\rm sol}, \tag{3.17}$$

which shows that the Coulomb coupling parameter at melting temperature $\Gamma_m$ does not depend on leading mass terms, but is fully determined by the corrections that step in at finite temperature. Furthermore, those corrections are small in the vicinity of the the crystallization temperature, making it difficult to estimate $\Gamma_m$ with precision. Still, several works estimate the Coulomb parameter to a constant $\Gamma_m \approx 175$ [Hor69; HPY07]. The crystallization temperature of a OCP at a given baryon density $n_B$ can then be approximated by inverting Eq. (3.1), yielding

$$T_m \simeq \frac{(Ze)^2}{k_B a_N \Gamma_m}\ \mathrm{K}, \tag{3.18}$$

assuming the composition to be the same as in CCM. We proceed as in [Fan+20] in order to precisely calculate the crystallization temperature. At each value of the baryon

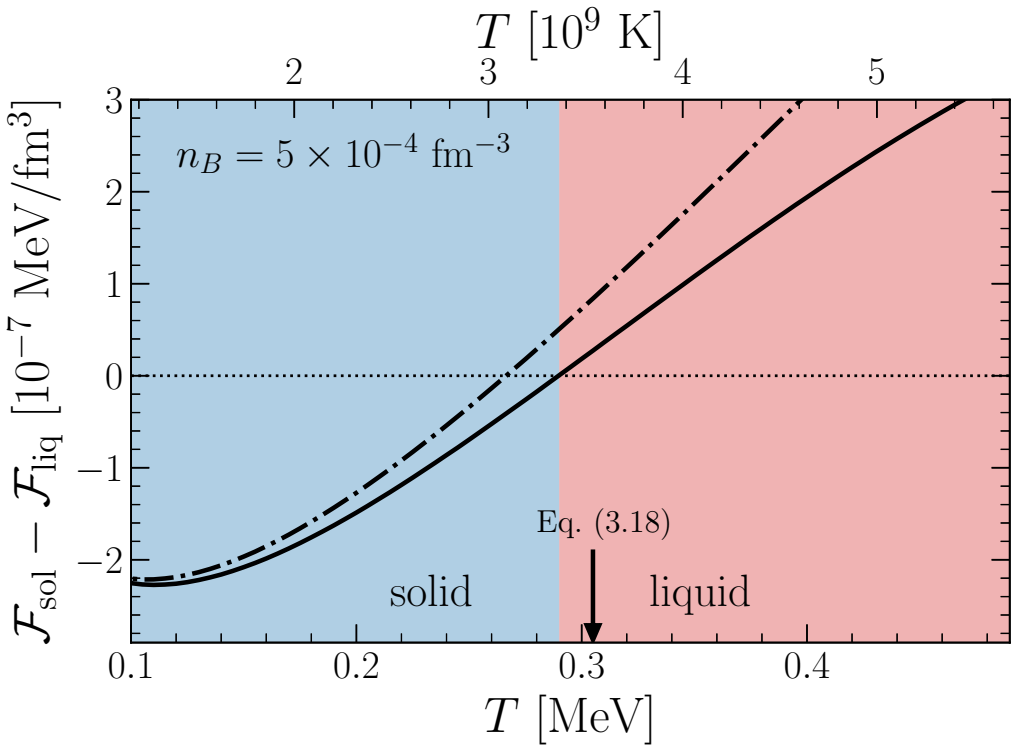



**Figure 3.1:** *Variation with temperature $T$ of the free energy density difference between liquid and solid phases $\mathcal{F}_{sol}-\mathcal{F}_{liq}$ for the optimal composition $\boldsymbol{\theta}_{liq}$ at $n_B = 5\times10^{-4}$ fm$^{-3}$ (free neutron regime) with (solid line) and without (dashdotted line) the anharmonic contribution, Eq. (3.14), to the free energy in the solid phase, using BSk24 CLDM. The crystallization temperature obtained from Eq. (3.18) is also indicated.*

density $n_B$ and temperature $T$, the equilibrium composition is computed following the procedure detailed in Chapter 1. Specifically, we solve the coupled differential equations, Eqs. (1.86)-(1.89), using the expressions of $F_i^{\rm id}$ and $F_i^{\rm int}$ of the liquid phase, yielding the optimal liquid composition $\boldsymbol{\theta}_{\rm liq}$ and the associated WS cell free energy density $\mathcal{F}_{\rm liq}$. Then, for the same composition $\boldsymbol{\theta}_{\rm liq}$, we calculate the free energy density assuming a solid phase $\mathcal{F}_{\rm sol}(\boldsymbol{\theta}_{\rm liq})$. The lowest temperature for which $\mathcal{F}_{\rm liq} \geq \mathcal{F}_{\rm sol}$ is identified as the crystallization temperature $T_m$ corresponding to the baryon density under study. The first guess for $T_m$ is obtained from the application of Eq. (3.18).

Fig. 3.1 shows the variation with temperature of the free energy difference $\mathcal{F}_{\rm sol}-\mathcal{F}_{\rm liq}$ at a given baryon density $n_B = 5\times10^{-4}$ for the BSk24 CLDM based on the metamodeling technique. The intersect of the solid line and zero marks the crystallization temperature, $T_m = 0.29$ MeV, which is equivalent to $T_m = (1.16\times10^{10})\times(0.29) = 3.36\times10^9$ K. We can observe that the crystallization temperature is significantly lower if the anharmonic contribution to the free energy of the solid OCP is neglected (dashdotted line). This stresses the importance of the small thermal corrections in the calculation. It is also seen that the effect of the anharmonic contribution becomes bigger with increasing temperature, and vanishes in case of strong coupling, that is in the zero-

temperature limit. We will show in Section 3.2 that the simple expression Eq. (3.18) gives a fairly good estimation of the crystallization temperature.

### 3.1.2 Multicomponent Coulomb plasma in a liquid phase

The OCP approximation is expected to be reliable at the temperatures typically encountered at low density in the crystallized crust, yet the very principle of statistical mechanics tells us that at finite temperature different configurations of the WS cell are realized for a same total density. In the following, the nuclear distribution is included in an MCP approach at equilibrium, as in [Fan+20; CFG20]. A particular attention is paid to the evaluation of the chemical potentials, as well as of the rearrangement term, which is required to ensure thermodynamic consistency.

#### 3.1.2.1 Nuclear statistical equilibrium

The NS crust at a given depth in the star is supposed to contain different ion species characterized by their mass and charge number $(A^{(j)}, Z^{(j)})$, associated to different WS cells of volume $V_{WS}^{(j)}$, such that $p_j$ is the frequency of occurrence (or probability) of the component $(j)$, with $\sum_j p_j = 1$. Thermodynamic quantities are defined in terms of the ion densities of the different species $n_N^{(j)}$, which are related to the probabilities $p_j$ through

$$n_N^{(j)} = \frac{p_j}{\langle V_{WS} \rangle}. \tag{3.19}$$

where the average WS cell volume has been introduced,

$$\langle V_{WS} \rangle = \sum_j p_j V_{WS}^{(j)}, \tag{3.20}$$

the notation $\langle\rangle$ indicating ensemble averages. The different configurations $(A^{(j)}, Z^{(j)})$ are associated with different different baryon densities $n_B^{(j)}$, such that the total baryon density is

$$n_B = \sum_j p_j n_B^{(j)}. \tag{3.21}$$

Conversely, they share the same total pressure $P$ imposed by the hydrostatic equilibrium and the same background densities of electrons, $n_e^{(j)} = n_e$, and of free neutrons, $n_g^{(j)} = n_g$. It is assumed that the charge neutrality is assured at the level of each cell, implying that the proton density is the same in each cell, $n_p^{(j)} = n_p$, and equal to the electron density,

$$n_e = n_p = \sum_j n_N^{(j)} Z^{(j)} = \frac{Z^{(j)}}{V_{WS}^{(j)}}. \tag{3.22}$$

The free energy density of the MCP is given by

$$\mathcal{F} = \sum_j n_N^{(j)} F^{(j)}, \tag{3.23}$$

where $F^{(j)}$ is the free energy per ion of a single component $(j)$ defined in Eq. (3.2). The probabilities $p_j$ and ion densities $n_N^{(j)}$ are calculated such as to maximize the

thermodynamic potential in the canonical ensemble. Because of the chosen free energy decomposition, we can observe that the free neutron and electron contributions to the free energy density, respectively $\mathcal{F}_g$ and $\mathcal{F}_e$, do not depend on $n_N^{(j)}$,

$$\mathcal{F}\left(\left\{n_N^{(j)}\right\}\right) = \mathcal{F}_i\left(\left\{n_N^{(j)}\right\}\right) + \mathcal{F}_g + \mathcal{F}_e, \tag{3.24}$$

with

$$\mathcal{F}_i = \sum_j n_N^{(j)} F_i^{(j)}. \tag{3.25}$$

This means that the variation can be performed on the ion part only, yielding

$$\begin{aligned} d\mathcal{F}_i &= \sum_j \left( F_i^{(j)} + n_N^{(j)} \frac{\partial F_i^{(j)}}{\partial n_N^{(j)}} \right) dn_N^{(j)} \\ &= \sum_j \left( F_i^{(j)} + k_B T + n_N^{(j)} \frac{\partial F_i^{(j),\mathrm{int}}}{\partial n_N^{(j)}} \right) dn_N^{(j)} \\ &= \sum_j \left( \Omega_i^{(j)} + k_B T \ln n_N^{(j)} \right) dn_N^{(j)}, \end{aligned} \tag{3.26}$$

where the single-ion canonical potential has been introduced,

$$\Omega_i^{(j)} = M_i c^2 + k_B T \ln \frac{(\lambda^{(j)})}{g_s^{(j)}} + F_i^{(j),\mathrm{int}} + n_N^{(j)} \frac{\partial F_i^{(j),\mathrm{int}}}{\partial n_N^{(j)}}. \tag{3.27}$$

A deviation to the linear-mixing rule (the hypothesis of uncorrelated WS cells) is observed in Eq. (3.27) due to the translational degree of freedom in the liquid phase [GR15], because within the MCP approach the center-of-mass position of each ion is not confined to the single cell volume $V_{WS}^{(j)}$ but can freely explore the whole volume. As a consequence, the average composition of the MCP does not coincide with the OCP optimal configuration in general.

In Eq. (3.26), the variations $dn_N^{(j)}$ are not independent because of the normalization of probabilities, and the baryon number and charge conservation laws:

$$\frac{1}{\langle V_{WS} \rangle} = \sum_j n_N^{(j)}, \tag{3.28}$$

$$n_B - n_g = \sum_j n_N^{(j)} A^{(j)} \left( 1 - \frac{n_g}{n_0^{(j)}} \right), \tag{3.29}$$

$$n_p = \sum_j n_N^{(j)} Z^{(j)}. \tag{3.30}$$

We can identify the mass number associated to component $(j)$ in e-cluster representation $A_e^{(j)}$ in the right hand side of Eq. (3.29). Let us recall that in the regime of the outer crust, $n_g = 0$ fm$^{-3}$ thus $A_e^{(j)} = A^{(j)}$. The average density of the ion $(j)$ $n_0^{(j)}$ is obtained by solving numerically the equation corresponding to the pressure equilibrium between the ion and the gas (see 1.2.2 for the derivation),

$$\frac{n_0^{(j)}}{A^{(j)}} \frac{\partial F_i^{(j)}}{\partial n_0^{(j)}} = P_g, \tag{3.31}$$

$P_g$ being the pressure of the neutron gas, whose expression is given in Eq. (1.55). As in [Gra+18], the neutron gas density is taken to be the OCP solution, $n_g = n_g^{\mathrm{OCP}}$. The constraints Eqs. (3.28)-(3.30) are taken into account by introducing the Lagrange multipliers $\alpha$, $\mu_n$, and $\mu_p$, leading to the following equations for the equilibrium densities $n_N^{(j)}$:

$$\sum_j \left(\Omega_i^{(j)} + k_B T \ln n_N^{(j)} - \alpha\right) dn_N^{(j)} - \mu_n \sum_j N_e^{(j)} dn_N^{(j)} - \mu_p \sum_j Z^{(j)} dn_N^{(j)} = 0 \tag{3.32}$$

with $N_e^{(j)} = A_e^{(j)} - Z^{(j)}$. Considering independent variations, the solutions are given by

$$p_j = \mathcal{A} \exp\left(-\frac{\tilde{\Omega}_i^{(j)}}{k_B T}\right), \tag{3.33}$$

with the normalization constant

$$\mathcal{A} = \exp\left(\frac{\alpha}{k_B T}\right) = \sum_j \exp\left(-\frac{\tilde{\Omega}_i^{(j)}}{k_B T}\right). \tag{3.34}$$

The single-ion grand-canonical potential reads

$$\tilde{\Omega}_i^{(j)} = \Omega_i^{(j)} - \mu_n N_e^{(j)} - \mu_p Z^{(j)}, \tag{3.35}$$

where $\mu_n$ and $\mu_p$ physically correspond to the neutron and proton chemical potentials, respectively. Let us note that the rest-mass energies are included in the chemical potentials since they are contained in the ion free energy. The calculation of the grand-canonical potential $\tilde{\Omega}_i^{(j)}$, entering the definition of the probabilities $p_j$, requires the evaluation of the chemical potentials $\mu_n$ and $\mu_p$, as well as of the rearrangement term

$$\mathcal{R}^{(j)} = n_N^{(j)} \frac{\partial F_i^{(j),\mathrm{int}}}{\partial n_N^{(j)}}, \tag{3.36}$$

which are discussed thoroughly in 3.1.2.2 and 3.1.2.3, respectively.

#### 3.1.2.2 Evaluation of the chemical potentials

For a given thermodynamic condition of pressure $P$ and temperature $T$, the expression of the chemical potentials $\mu_n$ and $\mu_p$ can be derived from the well-known thermodynamic relation $\mathcal{F}+P = \mu_n n_n + \mu_p n_p + \mu_e n_e$ together with the beta equilibrium condition $\mu_n = \mu_p + \mu_e$,

$$\mu_n = \frac{\mathcal{F} + P}{n_B} \quad \text{and} \quad \mu_p = \mu_n - \frac{\mathcal{F}_e + P_e}{n_p}, \tag{3.37}$$

where the electron chemical potential and pressure, respectively $\mu_e$ and $P_e$ have been introduced. The determination of the equilibrium probabilities $p_j$ within the complete NSE formalism therefore requires to solve a complex nonlinear system of coupled equations, which is obviously numerically costly. The implementation of the complete NSE was carried out in different studies in recent years (see for example [Oer+17; FF18]),

but in those studies simplified nuclear functionals were adopted, baryon density was imposed instead of the pressure, and the rearrangement term was neglected.

We choose here to implement the NSE perturbatively, as proposed in [Gra+18]. The motivation for this option comes from the fact that the difference between the chemical potentials in the OCP and MCP treatment were found to be very small in [GR15]. Moreover, in the recent work of Fantina *et al.*, a very fast convergence of the chemical potentials is observed, along with a reduction of the computational time and an increase of the numerical precision [Fan+20]. We start by solving the OCP variational equations in order to get the equilibrium composition, which gives a first guess for the chemical potentials, $\mu_n^{\mathrm{OCP}}$ and $\mu_p^{\mathrm{OCP}}$, via Eq. (3.37). The probabilities $p_j$ can then be evaluated using Eq. (3.33), and an improved estimation of the chemical potentials $\mu_n$ and $\mu_p$ is calculated via

$$\mu_n = \frac{\sum_j n_N^{(j)} F^{(j)}}{\sum_j n_N^{(j)} A_e^{(j)} + n_g} + \frac{P}{n_B} \quad \text{and} \quad y_p \mu_e = \frac{\sum_j n_N^{(j)} F_e^{(j)}}{\sum_j n_N^{(j)} A_e^{(j)} + n_g} + \frac{P_e}{n_B}, \tag{3.38}$$

where the average proton fraction of the mixture $y_p = \langle Z \rangle / (n_B \langle V_{WS} \rangle)$ has been introduced, with $\langle Z \rangle = \sum_j p_j Z^{(j)}$. The problem is thus solved by iteration until the convergence of the chemical potentials is observed. The convergence criterion is reasonably set to be $\Delta\mu_n < 10^{-9}$ MeV between iterations. We find that the number of iterations required to achieve convergence never exceeds 3. The reason is that the OCP result for $\mu_n$ and $\mu_p$ is already very close to the actual solutions for all pressures and temperatures explored in this work, thus confirming the results of [GR15]. Therefore, while we do solve the self-consistent problem by iterations in the regime of the outer crust to calculate the chemical potentials, the OCP estimation is safely kept in the free neutron regime so as to drastically reduce the computational cost. Indeed, in doing so the MCP calculation becomes equivalent to the much simpler OCP one.

#### 3.1.2.3 Evaluation of the rearrangement term

At a given thermodynamic condition $(P, T)$, the rearrangement term entering Eq. (3.27) requires to be evaluated if one wants to compute the ion abundancies through Eq. (3.33). As already discussed in [Gra+18; Fan+20], the rearrangement term arises from the self-consistency induced by the Coulomb part of the ion free energy. This stems from the fact that, due to the strong incompressibility of the electrons, the condition of charge neutrality has been imposed at the level of each cell, see Eq. (3.22), in contrast with the baryon density $n_B$ that can fluctuate from cell to cell, see Eq. (3.29). In consequence, any component of the free energy density that depends on the local cell proton density $n_p^{(j)} = n_p$ leads to a dependence on the local density $n_N^{(j)}$ through Eq. (3.22). With our prescription for the WS cell free energy, this is only the case for the interacting part $F_i^{(j),\mathrm{int}}$. We can therefore rewrite the rearrangement term of

component $(j)$ as

$$\begin{aligned}\mathcal{R}^{(j)} &= n_N^{(j)} \left.\frac{\partial F_i^{(j),\mathrm{int}}}{\partial n_N^{(j)}}\right|_{\{n_N^{(j)}\}_{i\neq j}} = n_N^{(j)} \frac{\partial F_i^{(j),\mathrm{int}}}{\partial n_p}\frac{\partial n_p}{\partial n_N^{(j)}} \\ &= n_N^{(j)} Z^{(j)} \frac{\partial F_i^{(j),\mathrm{int}}}{\partial n_p}. \end{aligned} \tag{3.39}$$

The complication of the self-consistent resolution of Eq. (3.33) can be avoided by imposing the most probable ion in the MCP mixture to coincide with the OCP result, if nonlinear mixing terms are omitted [Gra+18]. This approximation for the rearrangement term is justified by the principle of ensemble equivalence in the thermodynamic limit [GR15].

The maximum probability corresponds to the minimum of the single-ion grand-canonical potential $\tilde{\Omega}_i$. We therefore minimize the single-ion grand-canonical potential with respect to $A$, $I = 1-2Z/A$, and $n_0$ ($n_p$ and $n_g$ are fixed at a given thermodynamic condition), yielding the following nonlinear system of coupled equations:

$$\frac{n_0^2}{A}\left(\frac{\partial F_i}{\partial n_0} + \frac{\partial \mathcal{R}}{\partial n_0}\right) = P_g \tag{3.40}$$

$$\frac{2}{A}\left(\frac{\partial F_i}{\partial I} + \frac{\partial \mathcal{R}}{\partial I}\right) = \mu_n - \mu_p \tag{3.41}$$

$$\frac{\partial F_i}{\partial A} + \frac{\partial \mathcal{R}}{\partial A} + \frac{1-I}{A}\left(\frac{\partial F_i}{\partial I} + \frac{\partial \mathcal{R}}{\partial I}\right) = \mu_n - \frac{P_g}{n_0}, \tag{3.42}$$

where the partial derivatives are calculated at the values corresponding to the equilibrium OCP solution, with nonlinear mixing terms being excluded. The comparison of Eqs. (3.40)-(3.42) with Eqs. (1.87)-(1.89) indicates that $\mathcal{R}^{(j)}$ should not depend on $n_0^{(j)}$, meaning that $R^{(j)} = R^{(j)}(A^{(j)}, Z^{(j)})$. In addition, the rearrangement term should verify the following equation at the OCP solution:

$$\frac{1-I}{A}\frac{\partial \mathcal{R}}{\partial I} = -\frac{\partial \mathcal{R}}{\partial A}, \tag{3.43}$$

which is satisfied if $R^{(j)}$ linearly depends on $Z^{(j)} = A^{(j)}(1-I^{(j)})/2$. Our final expression for the rearrangement term is therefore

$$\mathcal{R}^{(j)} \simeq Z^{(j)} \left\langle \langle n_N^{(j)} \rangle \frac{\partial F_i^{(j),\mathrm{int}}}{\partial n_p} \right\rangle_j = \frac{Z^{(j)}}{V_{WS}^{\mathrm{OCP}}} \left.\frac{\partial F_i^{\mathrm{int}}}{\partial n_p}\right|_{\mathrm{OCP}}, \tag{3.44}$$

where $V_{WS}^{\mathrm{OCP}}$ is the equilibrium OCP cell volume, and the derivative is evaluated numerically at the OCP solution.

### 3.1.3 Nuclear free energy functional in the free neutron regime

As previously discussed in Chapter 1, in the regime of the outer crust we use the present day knowledge on experimental masses of neutron rich nuclei [Hua+17; Wel+17], combined with state-of-the-art microscopic HFB theoretical mass tables [GCP13]. In principle, at finite temperature an entropy term should be added to the mass table leading

to a temperature dependent degeneracy replacing the ground state spin degeneracy $g_s$. However, the crystallization temperature is so low in the outer crust that we make the approximation that the nuclei are in their ground state. The ion mass $M_i$ in the outer crust is therefore simply calculated using Eq. (1.6).

In the regime of the inner crust, $n_B \gtrsim 2.6 \times 10^{-4}$ fm$^{-3}$, we have seen that the ions are immersed in a neutron gas, whose free energy density $\mathcal{F}_g$ enters the expression of the ion mass in the e-cluster representation,

$$M_i^{(j)}c^2 = (A^{(j)} - Z^{(j)})m_n c^2 + Z^{(j)}m_p c^2 + F_{cl}^{(j)} - \frac{A^{(j)}}{n_0^{(j)}}(\mathcal{F}_g + n_g m_n c^2), \tag{3.45}$$

where $F_{cl}^{(j)}$ represents the nuclear free energy, including the contribution of the resonant and continuum excited states. In the range of densities corresponding to the free neutron regime, the clusters are by definition above the drip line, so that experimental data are not available. As a consequence, the modeling of $F_{cl}^{(j)}$ is required.

In the following, we first recall the simple case of free FG before deriving the expressions required to describe to the ambient neutron gas at finite temperature. We then give the expressions of the different quantities entering the expression of the smooth part of the nuclear free energy functional $F_{cl}^{(j)}$. The temperature dependence of shell corrections and its effect on the crystallization temperature is investigated in 3.3.1.

#### 3.1.3.1 Thermodynamics of nuclear matter

Let us first consider a collection of noninteracting fermions. In the grand-canonical ensemble, it obeys Fermi-Dirac statistics and the average number of fermions occupying a single-particle state $i$ is given by the Fermi-Dirac distribution,

$$\langle n_i \rangle = \left[1 + \exp\left(\frac{e_i - \mu}{k_B T}\right)\right]^{-1}, \tag{3.46}$$

where $e_i$ is the energy of the single-particle state $i$, and $\mu$ is the total chemical potential. At the thermodynamic limit, the sum over states $i$ is replaced by an integral over the energy, thus the Fermi-Dirac function that describe the occupation rate of state of given energy $e$ is introduced,

$$f_{\mathrm{FD}}(e, T, \mu) = \left[1 + \exp\left(\frac{e - \mu}{k_B T}\right)\right]^{-1}. \tag{3.47}$$

When replacing the sum by an integral, one needs to introduce the density of energy states $\rho(e)$. For a spinless free particle of energy $e = \hbar^2 k^2/(2m)$, the density of states is given by $\rho(\vec{k}) = \frac{V}{(2\pi)^3}$, with $k$ the wave vector and $V$ the volume. Using the relation $\rho(\vec{k})d^3k = \rho(e)de$, one obtains

$$\rho(e) = g\frac{V}{4\pi^2}\left(\frac{2m}{\hbar^2}\right)^{3/2}\sqrt{e}, \tag{3.48}$$

where the spin degeneracy $g = 2s + 1$ (for fermions, $s = 1/2$) has been introduced, and $m$ is the mass of a particle. At the thermodynamic limit, that is if we consider a

huge number of particles at a given temperature $T$ so that a large number of states are occupied, all ensembles are equivalent. This means that we can use the expressions of the grand-canonical ensemble to calculate for instance the exact number of particles and the energy, respectively

$$N = \sum_i \langle n_i \rangle \simeq \int_0^\infty \rho(e) f_{\rm FD}(e) de \quad \text{and} \quad E \simeq \int_0^\infty e\rho(e) f_{\rm FD}(e) de. \tag{3.49}$$

At zero temperature, states are populated up to the Fermi energy $\mu(T=0) = e_F$. Indeed, $f_{\rm FD} = 1$ for $e < \mu$, otherwise $f_{\rm FD} = 0$, which allows us to rewrite Eq. (3.49) as

$$N(T=0) = \int_0^{e_F} de\rho(e), \tag{3.50}$$

yielding the expression of the Fermi energy,

$$e_F = \frac{\hbar^2}{2m}\left(3\pi^2 \frac{N(T=0)}{V}\right)^{2/3} = \frac{\hbar^2 k_F^2}{2m}, \tag{3.51}$$

with $k_F = (3\pi^2 N(T=0)/V)^{1/3}$ the Fermi wave vector. At $T = 0$ K, the free energy is simply equivalent to the energy:

$$F(T=0) = E(T=0) = \int_0^{e_F} e\rho(e) de = \frac{3}{5} N e_F. \tag{3.52}$$

At nonzero temperature, the calculation of thermodynamic properties of a free FG generally requires the numerical evaluation of Fermi integrals,

$$F_\nu(u) = \frac{1}{\Gamma(\nu+1)} \int_0^\infty \frac{t^\nu}{1+\exp(t-u)} dt, \tag{3.53}$$

where $\Gamma(\nu) = (\nu-1)!$ is the gamma function. It is however useful to apply Sommerfeld development in the limit $T \ll e_F$ – which is satisfied in the range of temperatures explored in our work – in order to derive analytical formulas. In that case, we can obtain the expression of the chemical potential from $N = \int_0^\infty \rho(e) f_{\rm FD}(e) de$, assuming that $\mu = e_F(1 + \alpha T^2)$. By identifying terms scaling as $T^2$, we get

$$\mu = e_F \left[1 - \frac{\pi^2}{12}\left(\frac{T}{e_F}\right)^2\right]. \tag{3.54}$$

We can proceed in the same manner to calculate the energy at finite temperature and the entropy, respectively

$$E = \frac{3}{5} N e_F \left[1 + \frac{5\pi^2}{12}\left(\frac{T}{e_F}\right)^2\right] \quad \text{and} \quad S = \frac{\pi^2}{2} N \frac{T}{e_F}, \tag{3.55}$$

which finally gives, using the thermodynamic relation $F = E - TS$, the expression of the free energy of a nonrelativistic free FG,

$$F = \frac{3}{5} N e_F \left[1 - \frac{5\pi^2}{12}\left(\frac{T}{e_F}\right)^2\right]. \tag{3.56}$$

In the framework of the finite temperature self-consistent mean-field approximation, it is possible to show that those results can still be used in the case of a huge number of interacting fermions in a infinite volume at a finite density, that is for infinite nuclear matter [Vau96]. The energy density $\mathcal{H} = \mathcal{K} + \mathcal{V}$ for this idealized system can be derived from an effective functional, and is often decomposed into a kinetic term and a contribution due to the nuclear interactions, respectively $\mathcal{K}$ and $\mathcal{V}$, which both in infinite homogeneous nuclear matter only depend on local densities $n_q$. As discussed in 1.2.1.1, the Landau effective mass $m_q^*$ of species $q$ is usually introduced to regroup in a single term of kinetic energy the momentum dependence of the mean field,

$$\frac{\hbar^2 k_q^2}{2m_q^*} = \frac{\hbar^2 k_q^2}{2m_q} + U_{\text{eff}}(k_q). \tag{3.57}$$

In the grand-canonical ensemble, the occupation rate of state of given energy $e_q$ for interacting fermions reads

$$f_q(e_q + U_q, T, \mu_q) = \left[1 + \exp\left(\frac{e_q + U_q - \mu_q}{k_B T}\right)\right]^{-1}, \tag{3.58}$$

where $e_q + U_q = \hbar^2 k_q^2/(2m_q^*) + U_q$ is the single-particle energy of species $q$, $U_q = \partial\mathcal{H}/\partial n_q$ being the local mean field potential, which is given in the metamodel by ($q = n, p$)

$$\begin{aligned} U_q &= v_{MM}(n,\delta) + \frac{1+3x}{3}\left(\frac{\partial v_{MM}}{\partial x}\right)_\delta + (\tau_3 - \delta)\left(\frac{\partial v_{MM}}{\partial \delta}\right)_x \\ &\quad + (1+3x)\sum_{l=n,p}\frac{3}{5}\frac{1+\tau_{3,l}\delta}{2}e_{F,l}\left[1 - \frac{5\pi^2}{12}\left(\frac{T}{e_{F,l}}\right)^2\right] \\ &\quad \times \frac{m_l^*}{m}\left[\kappa_{sat} + \tau_{3,l}\kappa_{sym}\left(\delta + \frac{\tau_3 - \delta}{1+3x}\right)\right], \end{aligned} \tag{3.59}$$

with $\tau_{3,l} = 1$ ($\tau_{3,l} = -1$) for $l = n$ ($l = p$). The expressions of the potential energy $v_{MM}$ and effective masses are given in 1.2.1.1. The simple case of free FG is recovered by introducing the effective chemical potential $\tilde{\mu}_q = \mu_q - U_q$, yielding the free energy per particle of nuclear matter,

$$f_{HM}(n,\delta,T) = \sum_{q=n,p}\frac{3}{5}\frac{1+\tau_3\delta}{2}e_{F,q}\left[1 - \frac{5\pi^2}{12}\left(\frac{T}{e_{F,q}}\right)^2\right] + v_{MM}(n,\delta), \tag{3.60}$$

which enters the expression of the neutron gas free energy, $\mathcal{F}_g = n_g f_{HM}(n_g, 1, T)$. It is important to stress that the Fermi energy $e_F, q$ contains the effective mass in the above equation, contrary to Eq. (3.51). Let us note that the chemical potential does not include the rest mass energy in the above expressions. We can remark the well-known fact that in the mean-field approximation the temperature affects only the occupation of the single-particle levels, and not the value of the single-particle energies. As a consequence, if the density is homogeneous, $n_q = cst$, the potential part of the free energy is temperature independent, and the same expressions as in Chapter 1 are obtained. An effect of the functional on the finite temperature properties however is expected, because the interaction enters the kinetic part via the effective mass.

#### 3.1.3.2 Energetics of clusters at finite temperature in the CLD approximation

Within the CLD approximation, the nuclear free energy $F_{cl}$ at temperature $T$ of a cluster of mass number $A$, isospin asymmetry $I$, and average density $n_0$, can be decomposed into a bulk, surface and Coulomb part as

$$F_{cl}^{(CLD)} = A f_{HM}(n_0, I, T) + F_{surf} + F_{curv} + F_{Coul}, \tag{3.61}$$

where $f_{HM}(n_0, I, T)$ represents the free energy per baryon of bulk nuclear matter, which is calculated using Eq. (3.60). The expressions used for the surface and curvature free energy are given in Eqs. (1.59) and (1.61) respectively, with the exception of the surface tension, Eq. (1.60) whose expression is modified with respect to the zero temperature case in order to effectively account for the excitation of surface modes:

$$\sigma(I, T) = \sigma(I, T = 0) h(T), \tag{3.62}$$

with $h(T > T_c) = 0$ and $h(T \leq T_c) = [1 - (T/T_c)^2]^2$ (see Eq. (2.31) of [LS91]). However, because the critical temperature $T_c$ is of the order of $T_c \approx 1.75 \times 10^{11}$ K and the crystallization temperature is lower than $10^{10}$ K in the inner crust [HPY07], $h \approx 1$ and the excitation of surface modes can be neglected. Assuming spherical clusters, we write the Coulomb energy as

$$F_{Coul} = \frac{3}{5} \frac{e^2}{r_0^2} \frac{Z^2}{A^{1/3}}. \tag{3.63}$$

We limit ourselves to the empirical parameters associated to four different functionals of the BSk family taken from [GCP13]: BSk22, BSk24, BSk25, and BSk26. We choose these models because they all provide excellent fits to the AME2016 [Hua+17], are compatible both with *ab initio* and NS mass constraints, and explore a relatively large domain in the symmetry energy parameters (consistent with existing experimental constraints), which constitute the most important part of the EoS uncertainty [Pea+14; Pea+18]. Moreover, for each functional, surface and curvature parameters can be fitted to the ETF results [Pea+19], and the corresponding Strutinsky shell corrections, which are tabulated in [Pea+18], can be added on top of the CLD free energy, see 1.2.4 and 3.3.1. Another motivation is that full mass tables obtained by deformed HFB calculations have been published for these models [Xu +13] and can therefore be used in the regime of the outer crust as a complement to experimental masses [Fan+20]. However, some different models, not considered in [Fan+20], are also considered in order to appreciate the model dependence of the results. A full Bayesian study at finite temperature is left for future work.

## 3.2 Study of the outer crust at crystallization

In this section, we present the results for the outer crust at finite temperature, and more specifically at crystallization. Unless explicitly stated, all thermal corrections

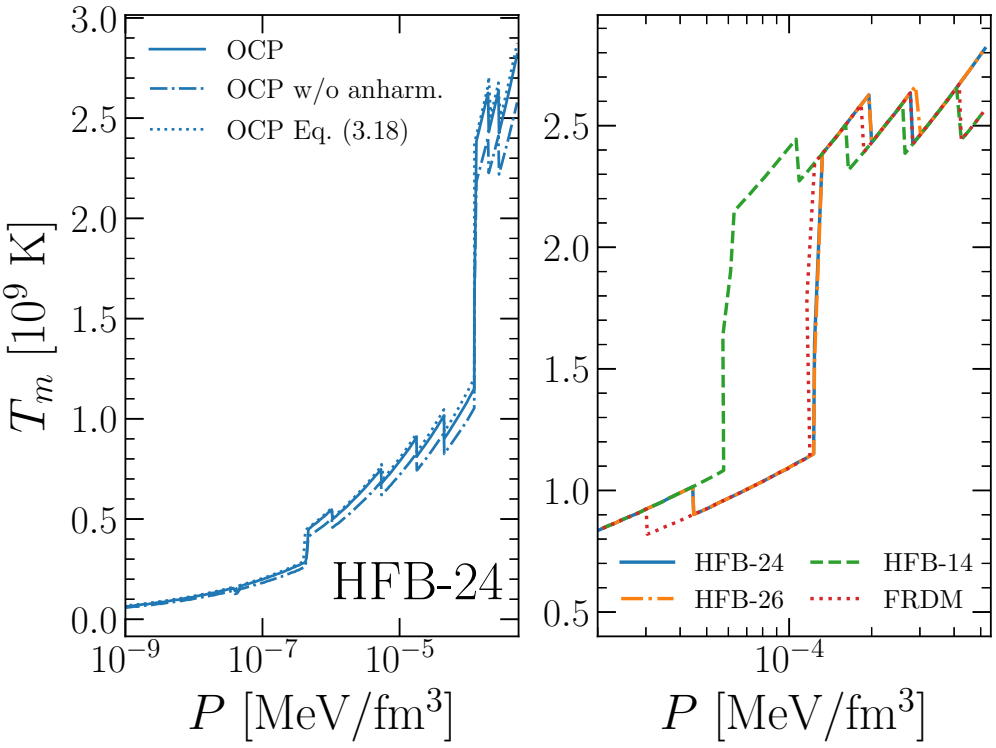



**Figure 3.2:** *Crystallization temperature $T_m$ as a function of pressure $P$ for the OCP in the outer crust. The left panel shows $T_m$ for the OCP with all corrections included (solid line), without taking into account the anharmonic contribution (dashdotted line), and the result obtained from Eq. (3.18) (dotted line). Experimental data are supplemented with masses from the microscopic HFB-24 theoretical mass table [GCP13]. The right panel shows $T_m$ in the bottom layers of the outer crust for four selected models: HFB-24 (solid blue line), HFB-26 [GCP13] (dashdotted orange line), HFB-14 [GSP07] (dashed green line), and FRDM [Mol+95] (dotted red line).*

introduced in Section 3.1 are included in the ion free energy. We made use of experimental masses from AME2016 [Hua+17] when available, apart from the mass excesses of $^{77-79}$Cu which are better constrained in [Wel+17]. The calculations are performed independently of those of Fantina *et al.* [Fan+20], observing a perfect agreement between the two studies shows that the numerical code of this work is under control.

The crystallization temperature of a OCP is calculated throughout the outer crust in 3.2.1. In 3.2.2, the equilibrium composition of the MCP at crystallization is presented, and deviations from the ground-state composition are investigated. The variation with pressure of the impurity parameter is analyzed in 3.2.3. Finally, the fraction of odd nuclei present in the outer crust at crystallization is computed in 3.2.4.

### 3.2.1 Crystallization temperature

The left panel of Fig. 3.2 shows the crystallization temperature as a function of the pressure in the outer crust, as obtained in the OCP approximation, Eq. (3.16). Experimental masses are supplemented with the microscopic HFB-24 theoretical mass table [GCP13]. It is seen that the crystallization temperature is overall an increasing function of the pressure in the outer crust, and ranges from approximately $5 \times 10^7$ K (4 keV) at very low pressure to $2.8 \times 10^9$ K (240 keV) close to the neutron-drip point. As one could have expected from the quadratic dependence on $Z$ observed in Eq. (3.18), we can see that the effect of shell structure on the crystallization temperature is very important. Indeed, each change in the equilibrium OCP composition results in an abrupt change in $T_m$, that is clearly noticeable in Fig. 3.2. In particular, the fact that the curve of the crystallization temperature is very steep in the vicinity of $P = 1.2 \times 10^{-4}$ MeV/fm$^3$, with $T_m$ rapidly increasing from $1.2 \times 10^9$ K to $2.4 \times 10^9$ K, can be attributed to the transition from $N = 50$ to $N = 82$, observed in Fig. 1.1. The importance of the anharmonic contribution to the ion free energy of a solid OCP, already investigated in Fig. 3.1, can be appreciated in the left panel of Fig. 3.2 by comparing the solid and dashdotted blue lines. We recover the result of [Fan+20] that the crystallization temperature is quite sensitive to the anharmonic contribution. We find that not accounting for this thermal correction induces an error on $T_m$ of the order of 10% in the range of pressure corresponding to the outer crust. The dotted blue line shows the result of the approximation Eq. (3.18). It is seen that one can obtain a very good estimation of the crystallization temperature for all pressures in the outer crust by using this approximation, which indicates that the crystallized composition (at $T = T_m$) is very similar to that at $T = 0$ K. This is discussed in detail in 3.2.2. The fact that Eq. (3.18) systematically but only slightly overestimates the crystallization temperature justifies its use for getting a first estimate so as to reduce the computational time.

The model dependence of the crystallization temperature of a OCP is illustrated in the right panel of Fig. 3.2, where $T_m$ is represented as a function of $P$ for four different models that supplement experimental data: HFB-24, HFB-26 [GCP13], HFB-14 [GSP07], and FRDM [Mol+95]. As for the equilibrium composition of CCM, see Fig. 1.1, the crystallization temperature becomes sensitive to the model from $P \approx 3 \times 10^{-5}$ MeV/fm$^3$, due to nuclei being so neutron rich that experimental masses are not available. We can see that the results are very close for HFB-24, HFB-26, and FRDM, even if these models considerably differ in their mass prediction, and HFB-24 and HFB-26 correspond to very different EoS. This finding shows once again the importance of the small thermal corrections in the calculation, which determine in first approximation the crystallization temperature independently of the mass model.

### 3.2.2 Equilibrium composition

The crystallization temperature in the outer crust does not exceed $\approx 0.25$ MeV, which is very low from the nuclear physics point of view. Hence, one can ask whether the composition at crystallization is different to that of CCM, presented in Section 1.1. Fig. 3.3 shows the equilibrium composition of a OCP as a function of the baryon

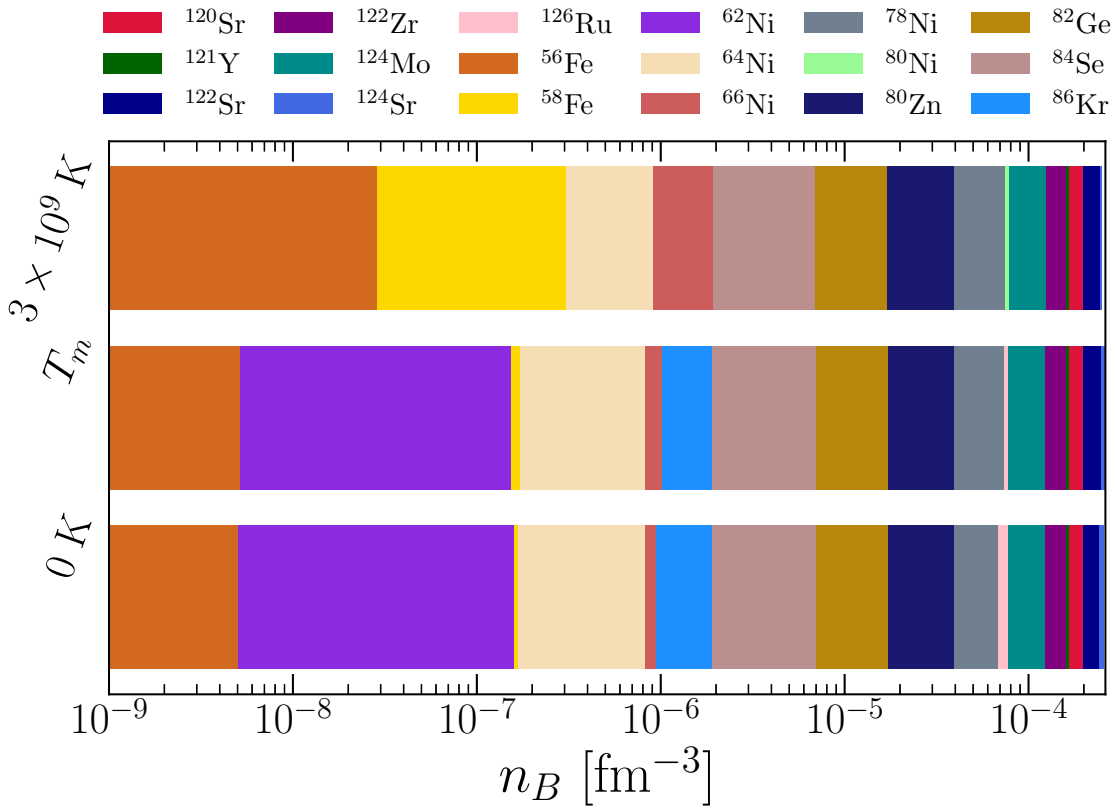



**Figure 3.3:** *Equilibrium composition of a OCP as a function of baryon density $n_B$ in the outer crust at $T = 0$ K, $T = T_m$, and $T = 3 \times 10^9$ K. Experimental data are supplemented with masses from the microscopic HFB-24 theoretical mass table [GCP13].*

density $n_B$ in the regime of the outer crust for two different temperatures: $T = 0$ K (CCM) and $T = 3 \times 10^9$ K, and at crystallization, $T = T_m$. We make use of the microscopic HFB-24 theoretical mass table to complement the experimental data. Let us notice that for all densities encountered in the outer crust, nonlinear mixing effects are so small that the equilibrium nucleus obtained within OCP approximation coincides with the most probable ion in the MCP mixture. We find that the difference between $T = 0$ K and $T = T_m$ is very small and hardly visible in the figure. The exact same sequence of layers is observed in the two cases, only the transition densities being slightly different. This shows that the CCM hypothesis gives an accurate description of the composition of the outer crust at crystallization. Significant deviations with respect to the results at $T = 0$ K and $T = T_m$ are observed at $T = 3 \times 10^9$ K, which is above the crystallization temperature in the outer crust. In particular, the layers of $^{62}$Ni and $^{86}$Kr are not recovered, and $^{80}$Ni is favored over $^{126}$Ru around $n_B \approx 8 \times 10^{-5}$ fm$^{-3}$. These results could have some implications in NS cooling simulations, where the approximation is often made that the composition at finite temperature is the same as at zero temperature [For+10]. A possible relevance to the physics of (cold) NS cannot be excluded either, since the ion distribution could be frozen at some

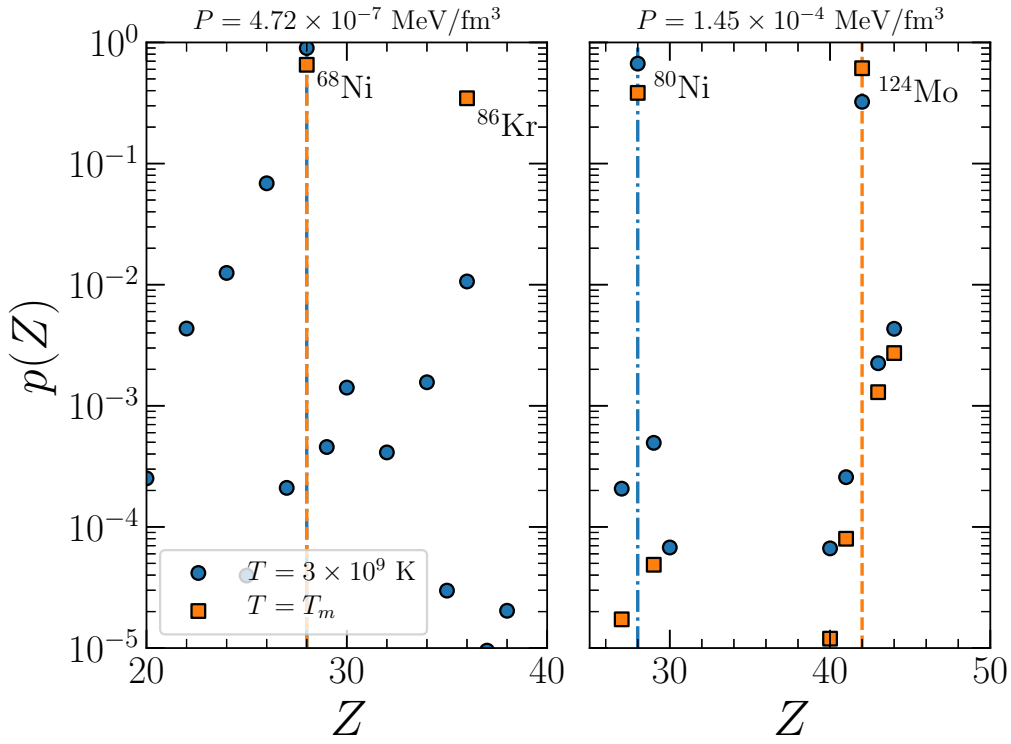



**Figure 3.4:** *Normalized probability distribution $p(Z)$ for $P = 4.72 \times 10^{-7}$ MeV fm$^{-3}$ (left panel) and $P = 1.45 \times 10^{-4}$ MeV fm$^{-3}$ (right panel), at $T = 3 \times 10^9$ K (blue circles) and $T = T_m$ (orange squares). The blue dashdotted and orange dashed vertical lines indicate the OCP solution at $T = 3 \times 10^9$ K and $T = T_m$, respectively. Experimental data are supplemented with masses from the microscopic HFB-24 theoretical mass table [GCP13]. Figure inspired from [Fan+20].*

temperature $T_f > T_m$ considering the present uncertainties on timescales relative to NS cooling [Gor+11]. This point deserves further investigations.

The normalized probability distribution $p(Z)$ of the MCP mixture is represented in Fig. 3.4 for different thermodynamic conditions relevant for the regime of the outer crust: $P = 4.72 \times 10^{-7}$ MeV/fm$^3$ (left panel) and $P = 1.45 \times 10^{-4}$ MeV/fm$^3$ (right panel). For both selected values of pressure, we plot the distribution for $T = 3 \times 10^9$ K (blue circles) and for the crystallization temperature $T = T_m$ calculated within the OCP approximation (orange squares). For each selected thermodynamic condition, it is observed that the most probable $Z$ in the MCP mixture coincides with the OCP solution represented by a vertical line. At low pressure, the crystallization temperature is small and consequently only very few configurations occur. This can be seen in the left panel of the figure, $P = 4.72 \times 10^{-7}$ MeV/fm$^3$, where only $Z = 28$ ($p(^{66}\text{Ni}) = 0.65$) and $Z = 36$ ($p(^{86}\text{Kr}) = 0.35$) are associated to nonnegligible probabilities. This contrasts with the distribution calculated at $T = 3 \times 10^9$ K for the same value of pressure, for which a large number of configurations are found with $p(Z) > 10^{-5}$. Still, at this temperature the distribution is strongly peaked at $Z = 28$, while for

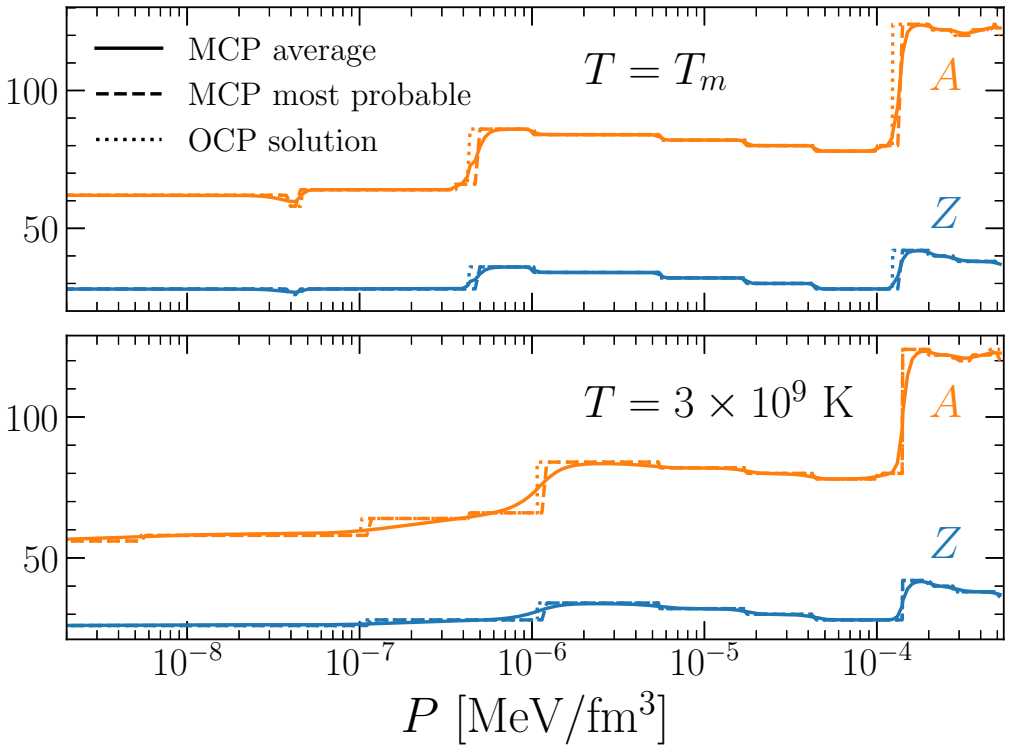



**Figure 3.5:** *Average (solid lines) and most probable values (dashed lines) of the charge number $Z$ (blue lines) and mass number $A$ (orange lines) in the MCP mixture as a function of pressure in the regime of the outer crust at $T = T_m$ (upper panel) and $T = 3\times10^9$ K (lower panel). The OCP solution is represented in dotted lines. Experimental data are supplemented with masses from the microscopic HFB-24 theoretical mass table [GCP13]. Figure inspired from [Fan+20].*

$T = T_m$ the distribution is bimodal. In the right panel of Fig. 3.4, a bimodal behavior is also clearly exhibited around $Z = 28$ and $Z = 42$, respectively corresponding to $^{80}$Ni and $^{124}$Mo, in the vicinity of $P = 1.45 \times 10^{-4}$ MeV/fm$^3$, where the curve of the crystallization temperature becomes very steep, see Fig. 3.2. While $^{124}$Mo is favored over $^{80}$Ni at high temperature, it turns out that the most probable nucleus changes to $^{80}$Ni as the temperature is decreased, and ultimately corresponds to the most probable nucleus at the crystallization temperature. The same feature is observed for the OCP solution.

Fig. 3.5 shows the equilibrium composition of the MCP as a function of pressure in the regime of the outer crust at the crystallization temperature (upper panel) and at $T = 3\times10^9$ K (lower panel). At $T = T_m$, it is seen that the average equilibrium values $\langle Z\rangle$ and $\langle A\rangle$ (solid blue and orange lines, respectively) coincides almost perfectly with the OCP solution (dotted blue and orange lines), apart in the vicinity of $P = 4.5\times10^{-7}$ MeV/fm$^3$ and $P = 1.5\times10^{-4}$ MeV/fm$^3$, where the distribution $p(Z)$ exhibits a bimodal character, as observed in Fig. 3.4. This results in the softening of the shell effects, which is even more striking at $T = 3\times10^9$ K. Those deviations from the OCP approximation

are reflected in the Coulomb coupling parameter, which exhibits spikes and can be as high as $\approx 330$ at the crystallization temperature, see Fig. 4 of [Fan+20].

### 3.2.3 Impurity parameter

Once the abundancies of the different ions are computed via Eq. (3.33), the so-called impurity parameter of the solid crust, which represents the variance of the ionic charge distribution, can be evaluated. It is defined as [Mei+18]

$$Q_{\rm imp} = \sum_j p(Z^{(j)})(Z^{(j)} - \langle Z \rangle)^2, \tag{3.64}$$

where $p(Z^{(j)})$ represents the normalized probability distribution (integrated over all $N^{(j)}$) of the atomic number $Z^{(j)}$. This parameter allows quantifying the presence of amorphous and heterogeneous phases in the solid crust, which is expected to reduce its electrical conductivity. For this reason, the impurity factor is expected to play an important role in the magneto-thermal evolution of the star (see the discussion in Sect. 7 in [Mei+18] for a review). For instance, $Q_{\rm imp}$ is directly related to impurity scattering, which alters the cooling of the crust. In NS cooling simulations, the impurity factor is however generally taken as a free parameter directly fitted to cooling data.

In Fig. 3.6, the impurity parameter $Q_{\rm imp}$ is plotted as a function of the pressure in the regime of the outer crust. As previously, we make use of the microscopic HFB-24 theoretical mass table [GCP13] to complement the present day experimental information on nuclear masses [Hua+17; Wel+17]. We recall that, considering the present uncertainties on timescales relative to NS cooling [Gor+11], the ion distribution could be frozen at some temperature higher than $T_m$. For this reason, we consider three different temperatures at which the composition could potentially freeze: $T_f = T_m$ (solid blue line), $T_f = 1 \times 10^9$ K (dashdotted orange line), and $T_f = 3 \times 10^9$ K (dashed green line). For a given pressure, it is seen that the impurity factor tends to be larger as the temperature is increased. Low values of $Q_{\rm imp}$ indicate that the distribution $p(Z)$, see Fig. 3.4, is strongly peaked on one particular nucleus. In that case, the OCP approximation is reliable. This is for instance seen at low pressure for $T_f = T_m$. Conversely, the impurity parameter can reach values as high as $\approx 50$ around $P = 1.5 \times 10^{-4}$ MeV/fm$^3$ where the charge distribution exhibits a multimodal character. Strong oscillations of $Q_{\rm imp}$ are observed due to shell structure effects, suggesting that the outer crust is constituted of an alternation of highly resistive and highly conductive layers. This was originally observed by Fantina *et al.* [Fan+20], and we have checked that this conclusion is not sensitive to the model, as far as state-of-the-art theoretical mass tables are used to complement experimental data.

### 3.2.4 Abundancies of odd nuclei

In the original calculation of the outer-crust ground state at zero temperature, the possibility of having odd-mass or odd-charge nuclei was not envisaged due to nuclear pairing [BPS71]. However, using the HFB-24 mass model, a thin layer of odd-mass

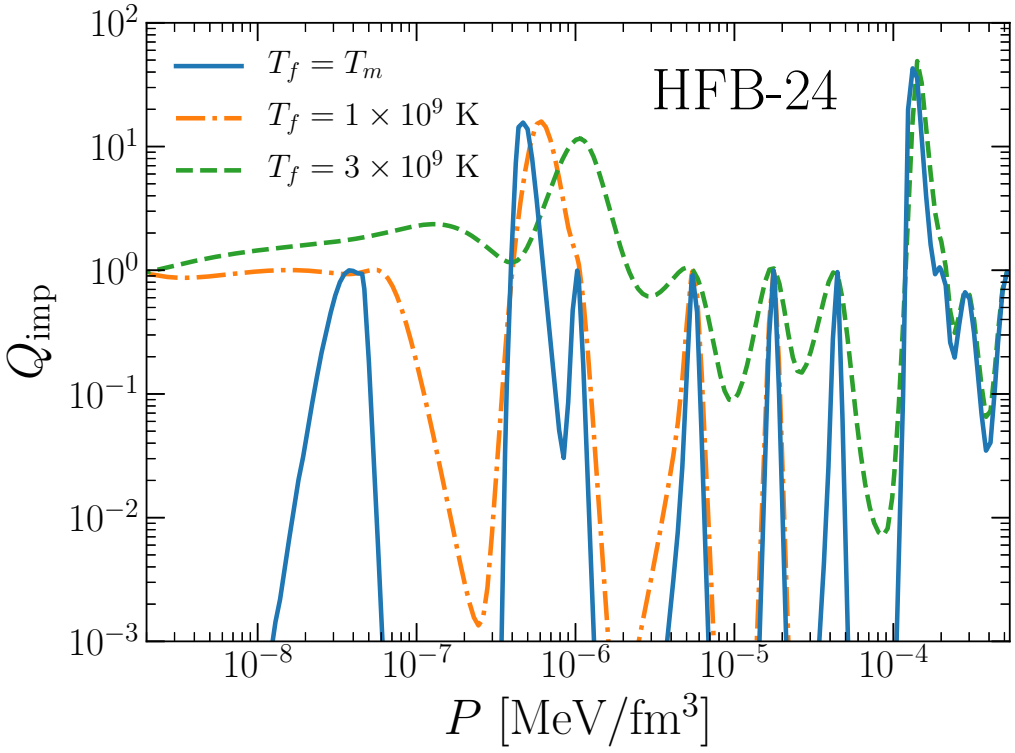



**Figure 3.6:** *Variation with pressure $P$ of the impurity parameter $Q_{imp}$, Eq. (3.64), in the regime of the outer crust for three selected temperatures at which the composition is assumed to be frozen: $T_f = T_m$ (solid blue line), $T_f = 1 \times 10^9$ K (dashdotted orange line), and $T_f = 3 \times 10^9$ K (dashed green line). Experimental data are supplemented with masses from the microscopic HFB-24 theoretical mass table [GCP13]. Figure inspired from [Fan+20].*

$^{121}$Y is observed at high pressure in the outer crust, see Table 1.1. One can therefore expect the MCP mixture to be composed of several odd nuclei at finite temperature. The presence of unpaired nucleons in the outer crust could lead to ferromagnetic phase transitions at low temperature, which in return could generate a magnetic field and alter the existing one, and so affect the electron gas. The importance of those effects depends on the spin and global abundancy of odd nuclei. Related quantities of interest are the fraction $\mathcal{N}_{\rm odd}/\mathcal{N}$ and baryonic mass fraction $M_{B,{\rm odd}}/M_B$ of odd nuclei in the outer crust, which can be evaluated once the abundancies of odd-$A$ and odd-$Z$ nuclei are computed for all pressures in the outer crust.

The fraction of odd-$A$ and odd-$Z$ nuclides in a given thermodynamic condition $(P, T)$ is obtained from the probabilities $p_j$ through

$$y_{\rm odd} = \frac{\sum_j p_j \delta_{\rm odd}}{\sum_j p_j} = \sum_j p_j \delta_{\rm odd}, \tag{3.65}$$

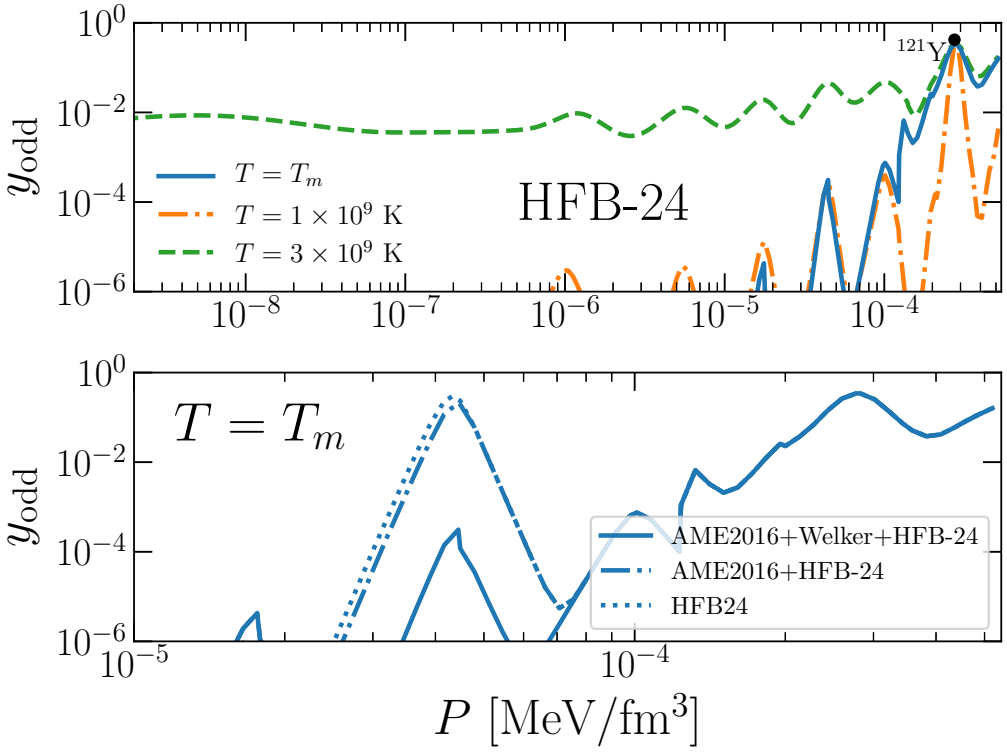



**Figure 3.7:** *Upper panel: Variation with pressure $P$ of the fraction of odd-$A$ and odd-$Z$ nuclei $y_{odd}$, Eq. (3.65), in the regime of the outer crust for three selected temperatures: $T = T_m$ (solid blue line), $T = 1 \times 10^9$ K (dashdotted orange line), and $T = 3 \times 10^9$ K (dashed green line). Experimental data are supplemented with masses from the microscopic HFB-24 theoretical mass table [GCP13]. Lower panel: $y_{odd}$ as a function of $P$ in the deepest layers of the outer crust at the crystallization temperature, using three different mass tables: AME2016+Welker+HFB-24 (solid line), AME2016+HFB-24 (dashdotted line), and HFB-24 (dotted line).*

with

$$\delta_{\rm odd} = \begin{cases} 1, & \text{if } A^{(j)} \text{ or } Z^{(j)} \text{ odd} \\ 0, & \text{if } A^{(j)} \text{ and } Z^{(j)} \text{ even} \end{cases} . \tag{3.66}$$

The upper panel of Fig. 3.7 shows the variation with pressure of $y_{\rm odd}$ in the regime of the outer crust at the crystallization temperature, (solid blue line), $T = 1 \times 10^9$ K (dashdotted orange line), and $T = 3 \times 10^9$ K (dashed green line). The HFB-24 mass table is used to complement the available experimental masses. We can see that more odd-mass and odd-charge nuclei are present in the outer crust as the temperature is increased, because the influence of pairing decreases with temperature. The fraction of odd-nuclei at crystallization is negligible, except in the deepest layers of the outer crust where oscillations of $y_{\rm odd}$ are observed. In particular, a remarkable peak, $y_{\rm odd} = 0.42$, can be seen around $P = 2.75 \times 10^{-4}$ MeV/fm$^3$, the most probable nucleus being $^{121}$Y.

The influence of the mass table on the fraction of odd nuclei present in the bottom

| $T$ ($10^9$ K) | $\mathcal{N}_{\rm odd}/\mathcal{N}$ (%) | $M_{B,{\rm odd}}/M_B$ (%) |
|---|---|---|
| $T_m$ | 2.05 | 2.40 |
| 1.0 | 2.30 | 2.65 |
| 2.0 | 4.70 | 5.35 |

**Table 3.1:** *Value of the fraction of odd nuclei $\mathcal{N}_{odd}/\mathcal{N}$ and baryon mass fraction of odd nuclei $M_{B,odd}/M_B$ in the outer crust for three selected temperatures. Experimental data are supplemented with masses from the microscopic HFB-24 theoretical mass table [GCP13].*

layers of the outer crust at crystallization is investigated in the lower panel of Fig. 3.7. It is observed that $y_{\rm odd}$ is very sensitive to the mass excesses of copper isotopes $^{77-79}$Cu in the vicinity of $P = 5 \times 10^{-5}$ MeV/fm$^3$, and ranges from $\approx 4 \times 10^{-4}$ (with mass excesses taken from [Wel+17]) to $\approx 0.35$ (with HFB-24 mass excesses). Such difference highlights the fact that measuring masses of odd nuclei is important.

The fraction of odd nuclei contained in the outer crust is computed as

$$\frac{\mathcal{N}_{\rm odd}}{\mathcal{N}} = \frac{\int_{R=R'}^{\infty} d\mathcal{N}_{\rm odd}(r)}{\int_{R=R'}^{\infty} d\mathcal{N}(r)}, \tag{3.67}$$

where $R'$ is the radial coordinate at the bottom of the outer crust, and therefore depends on the imposed central density $\rho_c$. The number of (odd) nuclei contained in the elementary volume $dV(r) = 4\pi r^2 dr$ is given by $d\mathcal{N}(r) = dV(r)n(r)$ ($d\mathcal{N}_{\rm odd} = dV(r)n_{\rm odd}(r)$), with $n(r) = 1/\langle V_{WS}\rangle$ ($n_{\rm odd} = \sum_j p_j \delta_{\rm odd}/\langle V_{WS}\rangle$). Similarly, the baryon mass fraction of odd nuclei is defined as

$$\frac{M_{B,{\rm odd}}}{M_B} = \frac{\int_{R=R'}^{\infty} dm_{\rm odd}(r)}{\int_{R=R'}^{\infty} dm(r)}. \tag{3.68}$$

The baryon mass of (odd) nuclei in the elementary volume $dV$ is given by $dm(r) = dV(r)\rho_B(r)$ ($dm_{\rm odd} = dV(r)\rho_{B,{\rm odd}}$), with the baryon mass density $\rho_B \propto \sum_j p_j F_i^{(j)}/\langle V_{WS}\rangle$ ($\rho_{B,{\rm odd}} \propto \sum_j p_j \delta_{\rm odd} F_i^{(j)}/\langle V_{WS}\rangle$). We report our estimation of the fraction and baryon mass fraction of odd-$A$ and odd-$Z$ nuclei in the outer crust at crystallization, $T = 1 \times 10^9$ K, and $T = 2 \times 10^9$ K in Table 3.1. At the crystallization temperature, we find that odd nuclei constitute 2.05% of species in the outer crust and contribute 2.40% of the outer-crust baryonic mass.

## 3.3 Study of the inner crust at crystallization

While slightly softened with respect to CCM, shell effects in the outer crust at crystallization are still very important and are clearly reflected on the impurity parameter $Q_{\rm imp}$, see Fig. 3.6. Since the crystallization temperature increases with increasing depth, one can wonder whether the shell corrections can be neglected in the free neutron regime. The composition of the inner crust is strongly model dependent due to

the presence of an external neutron gas, thus the problem of the model dependence of the impurity factor naturally arises.

In this section, we present the results for the inner crust at finite temperature, and more specifically at crystallization, using the CLD approach developed in Chapter 1 with parameters optimized on four different microscopic models, namely BSk22, BSk24, BSk25, and BSk26, introduced in [GCP13]. As in Section 3.2, all thermal corrections introduced in Section 3.1 are included in the ion free energy, unless explicitly specified. The highest average baryon density considered in this section is $n_B = 0.04$ fm$^{-3}$. Above this value, the presence of nonspherical pasta phases, see 1.2.5, is expected at finite temperature. The influence of shell effects at the crystallization temperature is settled within the OCP approximation in 3.3.1. In 3.3.2, the equilibrium composition of the MCP mixture is presented, and the importance of the rearrangement term is investigated. Finally, the EoS dependence of the impurity parameter is explored.

## 3.3.1 Influence of shell effects in the OCP approximation

In 1.2.4, we have proposed a strategy to add perturbatively proton shell corrections to the CLD energy in the free neutron regime. Let us recall that neutron shell effects become vanishingly small beyond the neutron-drip point [Cha06; Cha+07]. Strutinsky proton shell corrections have been tabulated in the inner crust at zero temperature for four recent functionals of the BSk family, namely BSk22, BSk24, BSk25, and BSk26 [Pea+18]. In the following, we introduce an empirical temperature-dependent factor to the zero-temperature shell corrections in the CLD free energy, before studying the influence of shell effects and exploring the model dependence of the inner-crust properties at the crystallization temperature.

### 3.3.1.1 Temperature dependence of shell corrections

The total free energy per ion including shell corrections in the crust reads

$$F(n_B, Z, T) = F^{\mathrm{CLD}}(n_B, Z, T) + E_{sh}(n_B, Z) - TS_{sp}(n_B, Z, T), \tag{3.69}$$

where $E_{sh}$ is the interpolated Strutinsky shell energy at $T = 0$ K (see 1.2.4), and $S_{sp}$ the entropy responsible of the softening of shell effects at finite temperature. In the zero temperature limit, we want to recover $F(T = 0) = E^{\mathrm{CLD}}(T = 0) + E_{sh}$, whereas at high temperature shell effects should vanish, $F \to F^{\mathrm{CLD}}$, yielding

$$\lim_{T\to\infty} TS_{sp}(n_B, Z, T) = E_{sh}(n_B, Z). \tag{3.70}$$

As a ansatz, we take

$$F = F^{\mathrm{CLD}} + E_{sh}(n_B, Z)\xi(T), \tag{3.71}$$

the temperature-dependent factor being given by

$$\xi(T) = \left(1 - \frac{2}{\pi}\arctan(\lambda T)\right). \tag{3.72}$$

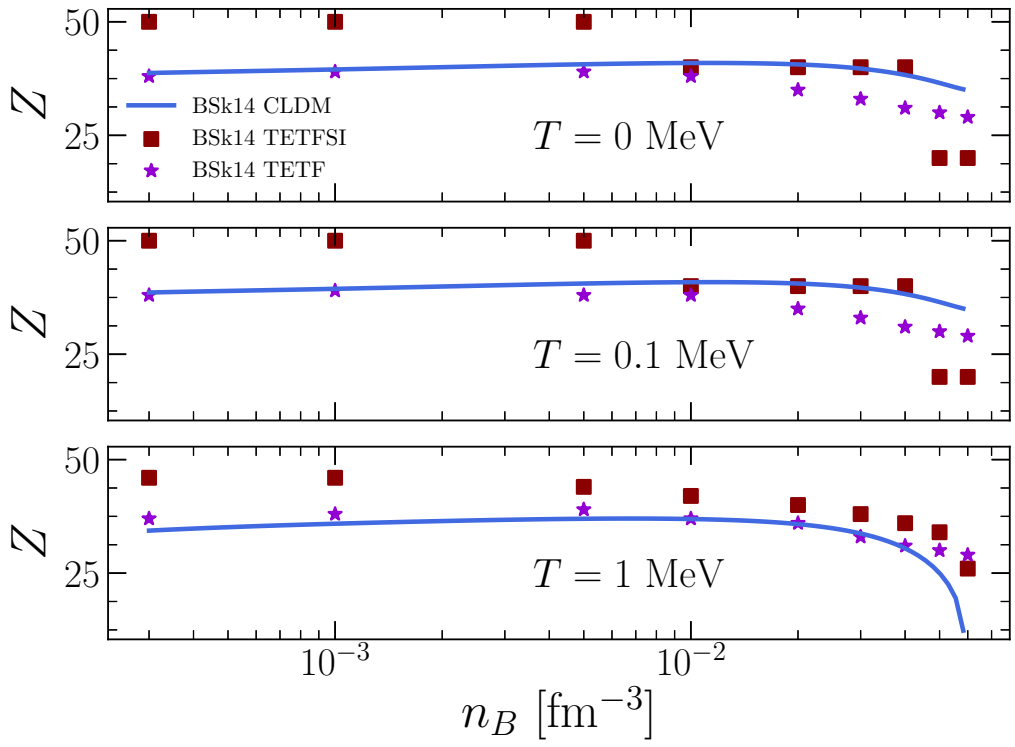



**Figure 3.8:** *Equilibrium value of proton number $Z$ as a function of baryon density $n_B$ in the inner crust for the BSk14 functional for different temperatures: $T = 0$ MeV (upper panel), $T = 0.1$ MeV (middle panel), and $T = 1$ MeV (lower panel). Solid lines correspond to the CLD model calculations without shell effects, and square (star) symbols correspond to the TETFSI (TETF) results from [Ons+08]. Figure adapted from [Car+20].*

The coefficient $\lambda$ can thus be determined by two parameters, $T_0$ and $\xi_0 = \xi(T_0)$, such that

$$\lambda = \frac{1}{T_0} \tan\left(\frac{\pi}{2}(1 - \xi_0)\right). \tag{3.73}$$

This is obviously a very rough treatment of the temperature dependence of shell effects, but we will show in 3.3.1.2 that the difference in the results obtained with or without this temperature dependence is smaller than the uncertainty due to our imperfect knowledge of the CLD part of the nuclear functional.

A reasonable choice consists in adjusting $T_0$, corresponding to the temperature at which shell effects are wiped out, and $\xi_0$, which governs the drop of $\xi$ with temperature, so as to reproduce the TETFSI results of Onsi *et al.* for the equilibrium value of $Z$ in the inner crust using the BSk14 functional [Ons+08] (see their Tables III and IV), represented in Fig. 3.8, along with the results obtained with our CLD modeling for the same interaction. As expected, it is seen that shell effects decrease as temperature is increased, and that the discontinuous behavior of $Z$ persists until $T \approx 1$ MeV $\approx 1.2 \times 10^{10}$ K, when the TETFSI results follow the same smooth trend as the TETF

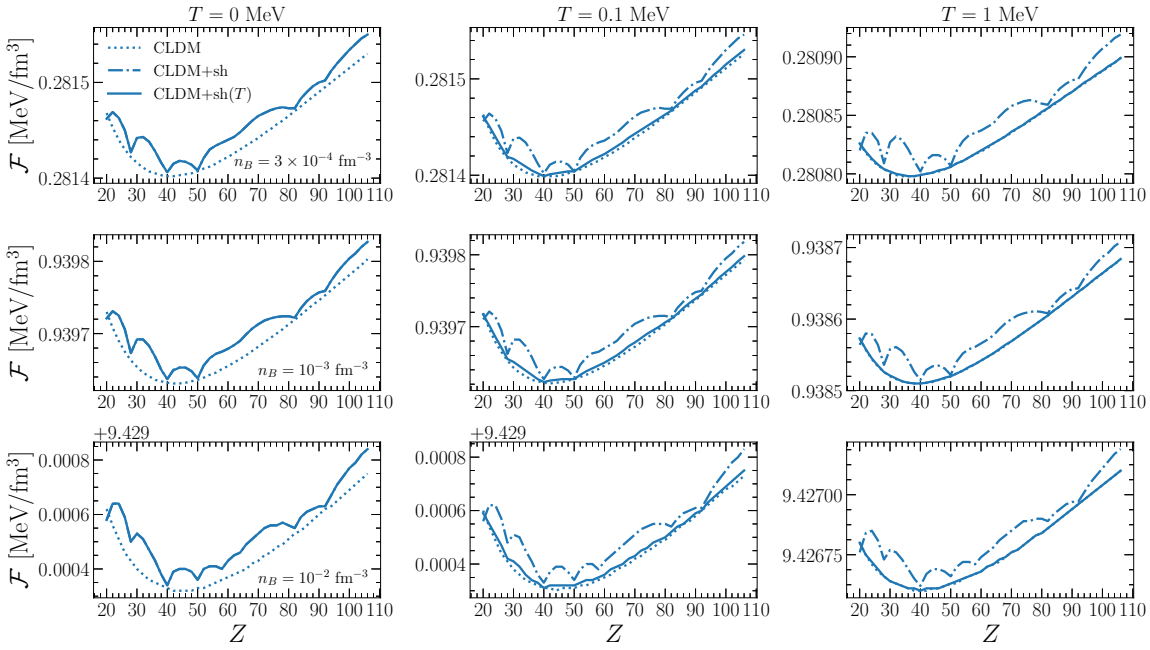



**Figure 3.9:** *Free energy density as a function of the proton number $Z$ for BSk24 CLDM for temperatures $T = 0$ MeV (left panels), $T = 0.1$ MeV (central panels), and $T = 1$ MeV (right panels), and baryon densities $n_B = 3 \times 10^{-4}$ fm$^{-3}$ (upper panels), $n_B = 10^{-3}$ fm$^{-3}$ (middle panels), and $n_B = 10^{-2}$ fm$^{-3}$ (lower panels). In each panel, dashdotted (solid) lines correspond to the calculations including temperature-independent (temperature-dependent) shell corrections, and dotted lines represent the results without shell effects. Figure adapted from [Car+20].*

and CLDM predictions. Based on these considerations, we fix the two parameters to $T_0 = 1$ MeV and $\xi_0 = 0.02$. An excellent agreement is observed between the CLDM and TETF results – for which proton shell corrections are also neglected – at relatively high temperature. Let us remark that higher values of $Z$ are obtained in the CLD calculations than in the TETF ones at low temperature and high density, which shows the limit of the CLD approach.

Fig. 3.9 shows the WS cell free energy density as a function of the proton number $Z$ for different conditions of density and temperature in the free neutron regime, for BSk24 CLDM with and without temperature-independent (temperature-dependent) shell corrections. The right panels show the results at zero temperature, which have been already discussed in in Fig. 1.9. The free energy density with temperature-dependent and zero-temperature shell corrections perfectly coincide since $\xi = 1$ for $T = 0$ MeV. We can clearly see that shell corrections are softened by the temperature-dependent factor at finite temperature (central and right panels). At the intermediate value $T = 0.1$ MeV, we can appreciate the large difference between the free energy density with zero-temperature Strutinsky shell corrections and that including temperature-dependent shell corrections through the factor $\xi(T)$. Let us recall that this difference is sensitive to the value of $\xi_0$. We recover the expected behavior

that nonsmooth effects are fully wiped out at $T = 1$ MeV, corresponding to $\xi = 0$. In that case, the pure CLD prediction is therefore equivalent to that accounting for temperature-dependent shell corrections.

#### 3.3.1.2 Equilibrium composition of the OCP at crystallization for modern BSk functionals

In the free neutron regime, the model dependence arises from the lack of experimental and theoretical constraints for very neutron rich nuclei and nuclear matter. This concerns the bulk properties, that is the nuclear EoS of asymmetric matter, but also surface properties, more specifically the surface tension of extremely neutron rich nuclei. In Fig. 3.10, we investigate the relative weight of the bulk and surface properties in determining the uncertainties in the crystallization temperature of a OCP (upper panel) and the corresponding equilibrium value of the ion atomic number $Z$ (lower panel). These inner-crust properties are calculated for BSk22, BSk24, and BSk25 functionals within the CLD approximation, up to $n_B = 0.04$ fm$^{-3}$. Dashdotted lines correspond to the calculations in which surface and curvature parameters are fitted to experimental masses of 9 spherical and semimagic nuclei only, namely $^{40,48}$Ca, $^{48,58}$Ni, $^{88}$Sr, $^{90}$Zr, $^{114,132}$Sn, and $^{208}$Pb, while solid lines show the predictions with surface properties being fitted to the associated ETF calculations performed up to the respective neutron-drip lines [Pea19] (default option). Let us notice that in both cases, the isovector surface parameter is fixed to the value $p = 3$, which ensures a good reproduction of the CC transition density and pressure for each considered BSk functional [Car+20]. The resulting predictions then differ solely in their bulk properties, and the width of the gray bands can therefore be interpreted as an estimate of the uncertainty on $T_m$ and $Z$ arising from our incomplete knowledge of the nuclear EoS of asymmetric matter. In the upper panel, it is observed that higher values of the OCP ion atomic number $Z$ are obtained when surface tension of neutron-rich nuclei is adjusted on the microscopic ETF results, and of course this difference reflects on the crystallization temperature of the OCP (lower panel), which roughly scales as $Z^{5/3}$ according to the approximation Eq. (3.18). One should stress that the bulk parameters of the considered BSk functionals were precisely fitted to the properties of finite nuclei and *ab initio* neutron-matter calculations [GCP13]. The residual uncertainty in the nuclear EoS is not negligible, but its consequence is less important than the uncertainties on the surface energy for neutron-rich nuclei close to neutron drip. The latter can then be considered as the key physical quantity determining the crust composition and crystallization temperature. Given the present CLD calculations, we find that the crystallization temperature of a OCP in the inner crust ranges from $\approx 3 \times 10^9$ K at the neutron-drip point to $\approx 9 \times 10^9$ K at high density close to the CC transition point. The different functionals lead to predictions that progressively diverge with increasing depth, the crystallization temperature differing by up to 40% at the highest density considered. The anticorrelation between the symmetry energy and the crystallization temperature is clearly observed in the regime of the inner crust: the higher the symmetry energy at saturation, the lower the crystallization temperature, with $E_{sym} = 32$ MeV, $E_{sym} = 30$ MeV, and $E_{sym} = 29$ MeV for BSk22, BSk24, and BSk25, respectively. The same is true for the equilibrium value of $Z$, which is as in CCM $\approx 40$ all along the inner crust when surface

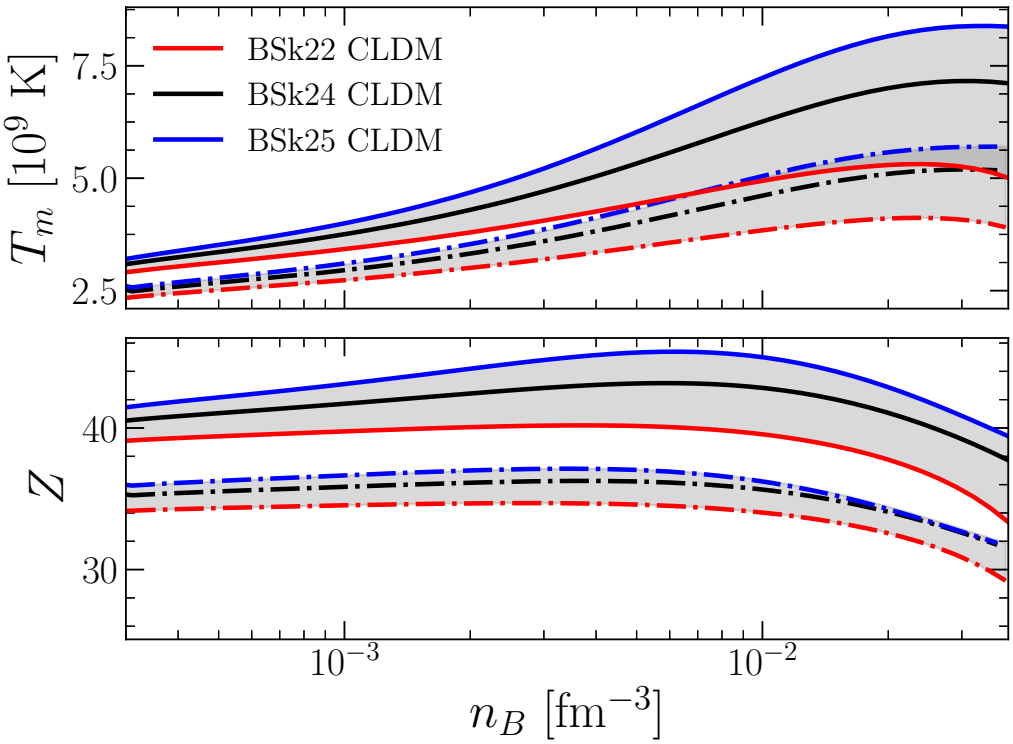



**Figure 3.10:** *Crystallization temperature $T_m$ (upper panel) and equilibrium value of $Z$ (lower panel) as a function of baryon density $n_B$ in the inner crust for BSk22, BSk24, and BSk25 CLDM with surface and curvature parameters fitted to spherical nuclei (dashdotted lines), or to associated ETF calculations (solid lines). Gray bands represent extrema. Figure adapted from [Car+20].*

properties are optimized on microscopic ETF calculations.

In Fig. 3.11, we show the results obtained for the same CLDM, with temperature-independent (temperature-dependent) shell corrections as dashdotted (solid) lines. The gray bands corresponding to the pure CLD results with surface parameters optimized on ETF calculations are reported in both panels. It is seen that, apart from BSk25 under the extreme and quite unrealistic hypothesis that shell effects are not affected by temperature, all calculations including shell corrections fit in the CLD bands. Given our estimation of the parameters entering the temperature-dependent factor, $T_0 = 1$ MeV and $\xi_0 = 0.02$, we find that the discontinuous behavior of the equilibrium value of ion atomic number $Z$ is entirely smoothed out at the crystallization temperature in the inner crust. For these reasons, the simple CLD modeling, in which nonsmooth effects are neglected, could be sufficient to study the inner-crust properties at crystallization. Within the MCP approach, neglecting proton shell corrections in the free neutron regime will have the positive impact of drastically reducing the computational time.

Fig. 3.12 shows the proton fraction of the OCP at the equilibrium as a function of the temperature for four different baryon densities in the regime of the inner crust. For

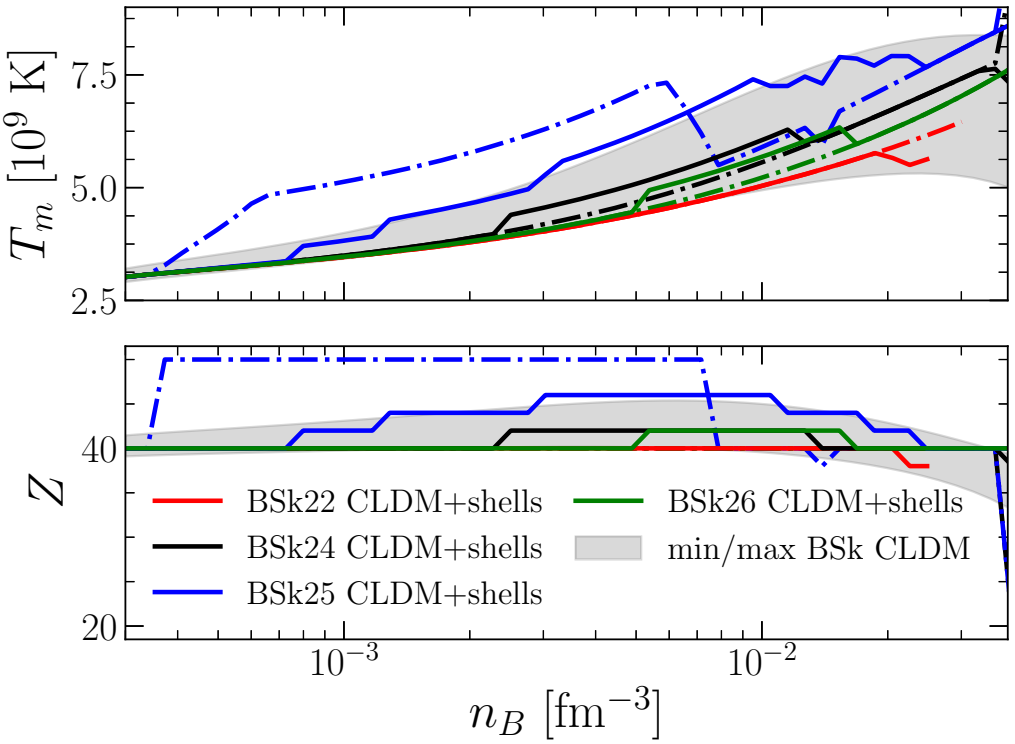



**Figure 3.11:** *Crystallization temperature $T_m$ (upper panel) and equilibrium value of $Z$ (lower panel) as a function of baryon density $n_B$ in the inner crust. The gray bands correspond to extrema for the BSk22, BSk24, and BSk25 CLDM with surface parameters fitted to associated ETF calculations. Solid (dashdotted) lines represent the calculations for BSk22, BSk24, BSk25, and BSk26 CLDM with temperature-dependent (temperature-independent) shell corrections. Figure adapted from [Car+20].*

each value of $n_B$, the equilibrium proton fraction $y_p$ is calculated for BSk22, BSk24, BSk25, and BSk26 CLDM including temperature-dependent shell corrections for $T$ up to $1.2 \times 10^{10}$ K, and a band is plotted to indicate the minima and maxima. It is clearly seen that the band becomes thicker as we go deeper in the star, showing that the model dependence of $y_p$ is more important at high density. The band associated to $n_B = 3 \times 10^{-4}$ fm$^{-3}$, which is very close to the neutron-drip point, is quite thin, reflecting the fact that the determination of the beta equilibrium is insensitive to the nuclear model employed at low density. The fact that $y_p$ drops with temperature can be explained from the beta equilibrium equation $\mu_n - \mu_p = \mu_e$. Indeed, the electron chemical potential increases with temperature, yielding an increasing difference between the neutron and proton chemical potentials, and therefore a decreasing proton fraction. While the CCM hypothesis appears to be well-founded in the inner-crust bottom layers, deviations at low density are observed with respect to the results at the crystallization temperature, which is indicated for each BSk functional. As previously discussed, the composition of the crust could be frozen at some temperature $T_f > T_m$ depending on the typical timescale of the weak interaction relative to the cooling dynamics. In

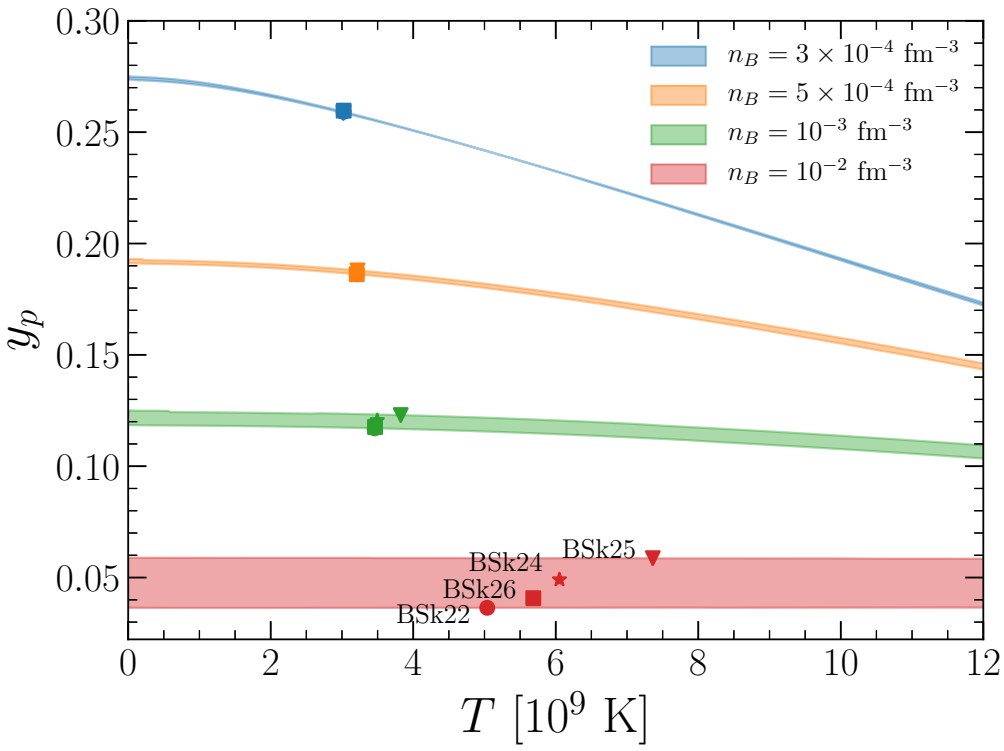



**Figure 3.12:** *Variation with temperature of the equilibrium proton fraction of the OCP for different values of the baryon density:* $n_B = 3 \times 10^{-4}$ fm$^{-3}$ *(blue band),* $n_B = 5 \times 10^{-4}$ fm$^{-3}$ *(orange band),* $n_B = 10^{-3}$ fm$^{-3}$ *(green band), and* $n_B = 10^{-2}$ fm$^{-3}$ *(red band). Each of the bands represents extrema of pure CLD calculations for the four BSk functionals including temperature-dependent shell corrections with* $T_0 = 1$ MeV *and* $\xi_0 = 0.02$*. Circles, stars, triangles, and squares indicate the crystallization temperature for BSk22, BSk24, BSk25, and BSk26, respectively. Figure adapted from [Car+20].*

that case, and independently of the nuclear model, the equilibrium proton fraction as obtained within the CCM hypothesis would be overestimated, and as a consequence the latter hypothesis would be challenged.

### 3.3.2 MCP results

We now turn to present the results obtained within the MCP approach introduced in 3.1.2. The equilibrium composition of the MCP and the impurity parameter are computed in the inner crust at the crystallization temperature and, for comparison, at $T = 1 \times 10^{10}$ K, at which the MCP is in a liquid phase. From 3.3.1, we have seen that the nonsmooth effects vanish in the inner crust at the crystallization temperature. Therefore, all the results that we present in the following are based on pure CLD calculations for BSk functionals, that is without including proton shell corrections. The surface and curvature parameters are fitted to the corresponding ETF calculations.

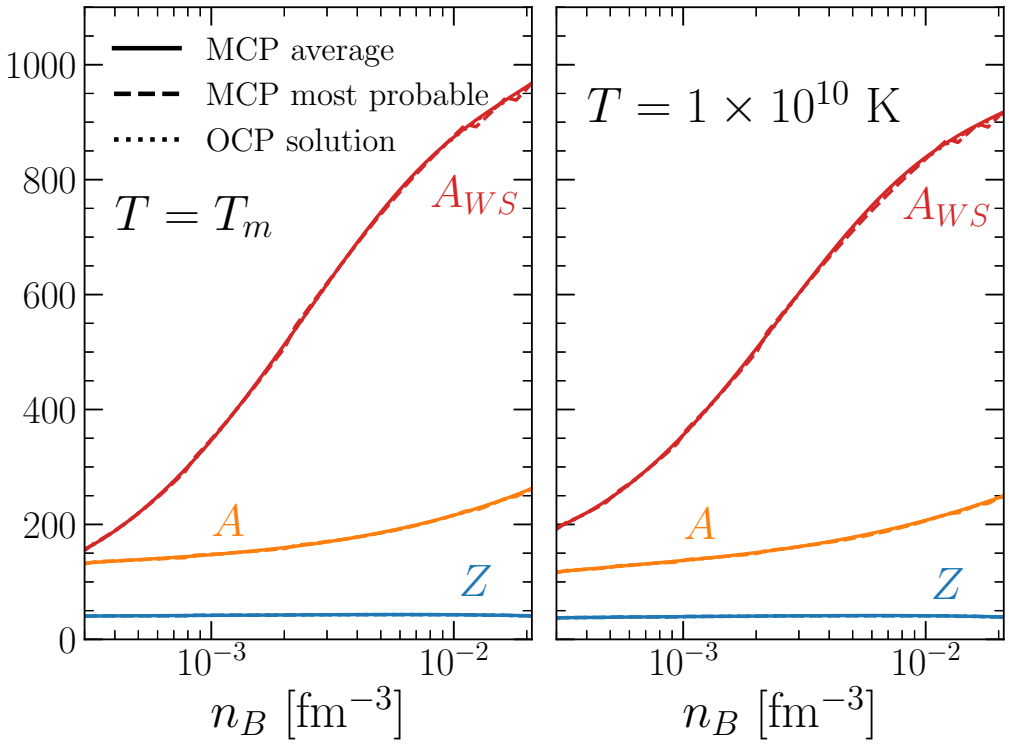



**Figure 3.13:** *Average (solid lines) and most probable values (dashed lines) of the charge number $Z$ (blue lines), cluster mass number $A$ (orange lines), and total mass number $A_{WS}$ (red lines) in the MCP mixture as a function of the average baryon density in the regime of the inner crust at $T = T_m$ (left panel) and $T = 1 \times 10^{10}$ K (right panel). The OCP solution is represented in dotted lines. Figure adapted from [CFG20].*

#### 3.3.2.1 Equilibrium composition of the MCP

The average (solid lines) and most probable value (dashed lines) of the proton number $Z$, cluster mass number $A$, and WS cell mass number $A_{WS}$ in the MCP mixture are plotted as a function of the average baryon density in the free neutron regime at crystallization (left panel) and at a higher temperature $T = 1 \times 10^{10}$ K (right panel) for the BSk24 CLDM. It is observed that the MCP results are extremely close to the OCP ones, which are represented as dotted lines. This shows that, as in the regime of the outer crust [Fan+20], deviations with respect to the linear mixing rule are very small. By comparing the results displayed in the two panels, we can see that the cluster mass and total mass increase as the temperature is decreased. As in the zero-temperature limit, see Fig. 1.7, the average value of the ion atomic number stays almost constant in the inner crust, $\langle Z \rangle \approx 40$.

The left panels in Fig. 3.14 shows the normalized probability distribution $p(Z)$ for $T = T_m$ (orange squares) and $T = 1 \times 10^{10}$ K (blue circles), and for two selected values of the average baryon density in the inner-crust regime: $n_B = 5 \times 10^{-4}$ fm$^{-3}$ (top

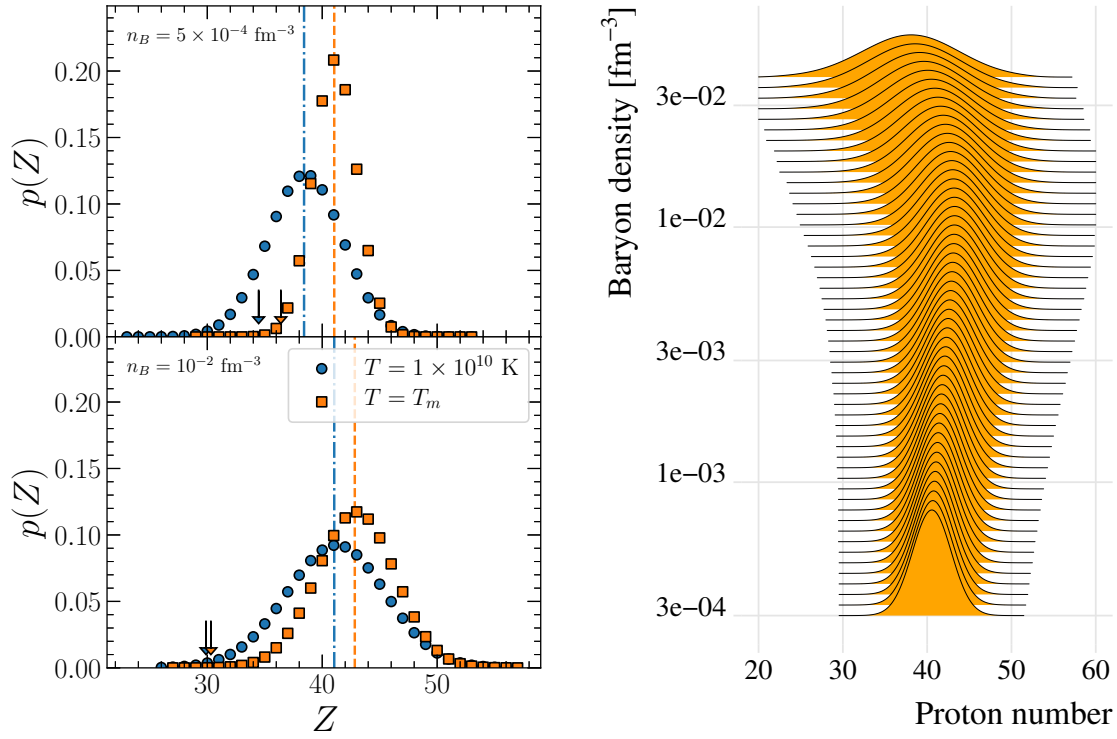



**Figure 3.14:** *Left: Normalized probability distribution $p(Z)$ for $n_B = 5 \times 10^{-4}$ fm$^{-3}$ (upper panel) and $n_B = 10^{-2}$ fm$^{-3}$ (lower panel), at $T = 1 \times 10^{10}$ K (blue circles) and $T = T_m$ (orange squares) for BSk24 CLDM. The blue dashdotted and orange dashed vertical lines correspond to the respective OCP solutions, and arrows indicate the value of $\langle Z \rangle$ without considering the rearrangement term. Right: $p(Z)$ with increasing baryon density $n_B$ in the inner crust at crystallization for BSk24 CLDM. Figure adapted from [CFG20].*

panel) and $n_B = 10^{-2}$ fm$^{-3}$ (bottom panel). The BSk24 CLDM is used. Once again, the fact that the peaks of the distributions, that is the most probable $Z$, coincides with the OCP solutions, represented by the vertical lines, shows that nonlinear mixing effects are negligible and thus that the linear mixing rule is a good approximation. The importance of the rearrangement term, Eq. (3.44) can be appreciated by comparing, for each thermodynamic condition, the most probable value of the ion atomic number with the average value obtained if the rearrangement term is not included in the calculation, indicated by the corresponding arrow. Without including the rearrangement term, we observe a systematic and significant shift toward lower $Z$, showing that it is needed in order to ensure thermodynamic consistency. We can see that this effect becomes more important as we go deeper in the inner crust. We stress that this term is not included in any of the NSE models which are presently available for astrophysical simulations. We can notice that, as expected, $p(Z)$ gets flatter as density and temperature are increased, thus making the OCP approximation less reliable. This is better demonstrated in the right panel of Fig. 3.14, which shows the variation with average baryon density of the

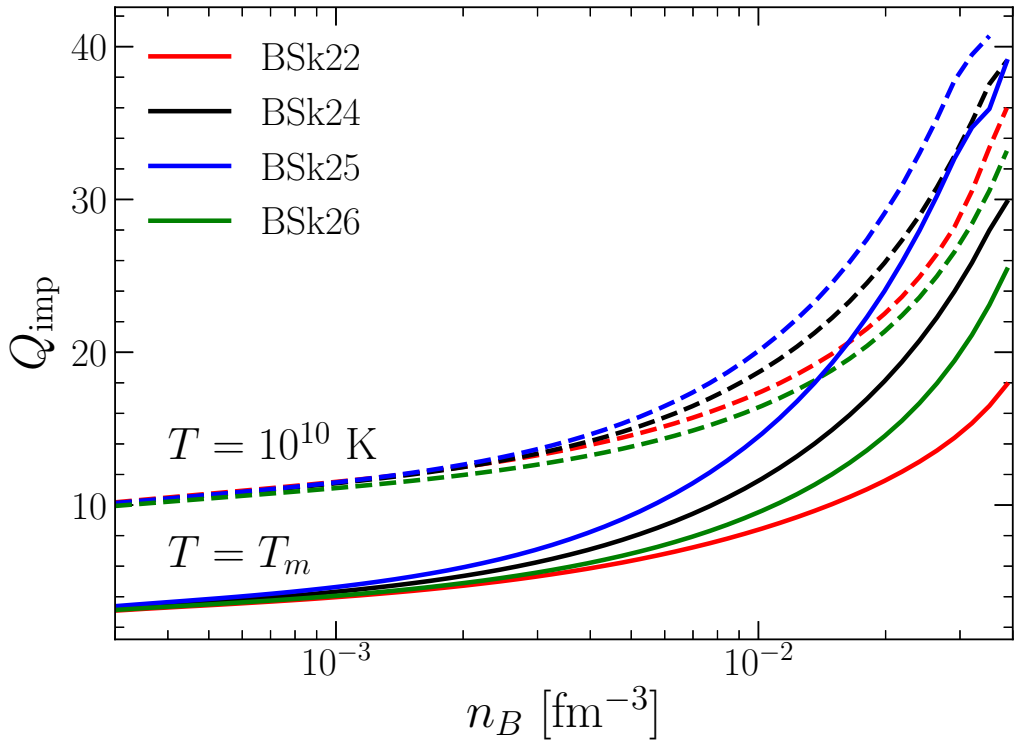



**Figure 3.15:** *Variation with average baryon density $n_B$ of the impurity parameter $Q_{imp}$ in the regime of the inner crust for two selected temperatures: $T = T_m$ (solid lines) and $T = 1 \times 10^{10}$ K (dashed lines), based on BSk22 (red lines), BSk24 (black lines), BSk25 (blue lines), and BSk26 (green lines) CLD calculations. Figure published in [CFG20].*

normalized probability distribution $p(Z)$ in the inner crust at crystallization. It is seen that the distribution is peaked around 40 throughout the inner crust. At high density close to the CC transition, the range of $Z$ of the distribution varies from $\approx 20$ up to $\approx 50$.

#### 3.3.2.2 Impurity parameter

In the inner crust, we have to address the problem of model dependence in order to make a quantitative prediction of the impurity parameter $Q_{\rm imp}$. Apart from the modeling of finite temperature shell effects discussed thoroughly in 3.3.1, the main source of uncertainty of the calculation comes from the choice of the nuclear functional. We show, in Fig. 3.15, the impurity parameter, Eq. (3.64), as a function of the average baryon density in the inner crust, at the crystallization temperature $T_m$ (solid lines), for the four considered BSk CLD models. Considering that the chosen models are believed to cover the main uncertainty on the nuclear EoS at subsaturation density [Pea+18], we can take the spread of $Q_{\rm imp}$ values as obtained by the four calculations, as a reasonable estimation of the uncertainty on the impurity parameter.

Since this latter represents the variance of the charge distribution, low values of $Q_{\rm imp}$ indicate that the distribution is quite peaked and thus that the OCP approach is a good approximation, as it can also be seen from Figs. 3.13 and 3.14. In particular, the monotonic increase of the impurity parameter with baryon density is in aggreement with the right panel of Fig. 3.14, which clearly show the growth of the width of the ion atomic number distribution with increasing density. While at lower densities all the models predict similar values of the impurity parameter, $Q_{\rm imp} \lesssim 5$, at higher densities the spread among the models becomes larger, with the functional associated to the larger symmetry energy at saturation density $E_{sym}$ having the larger $Q_{\rm imp}$, leading to a relative difference of $\approx 55\%$ at $n_B = 0.04$ fm$^{-3}$. Let us recall that the obtained values of the impurity parameter represent a lower limit. Indeed, larger values are expected in the presence of nonspherical geometries and/or fast cooling dynamics. For this reason, we also represent the impurity parameter for $T = 1 \times 10^{10}$ K (dashed lines). At this value of temperature, the same trend is observed, although the hierarchy of the models is not preserved.

## 3.4 Conclusions

In this chapter, we have considered the modeling of the crust at finite temperature. The OCP approximation, in which the expected distribution of nuclei is replaced by a single nucleus obtained from the minimization of the thermodynamic potential at a given thermodynamic condition, has been reviewed. We have given the expressions of the thermal corrections entering the ion free energy, namely the translational center-of-mass motion term in the liquid phase, the zero-point quantum vibrations term in the solid phase, and the Coulomb interaction contribution which differs according to the phase of matter. We have discussed the definition of the transition from liquid to solid, and we have then included the nuclear distribution in an MCP approach at the equilibrium. Within this treatment, nonlinear mixing effects arise due to the fact that the center-of-mass position of each ion is not confined to the single WS cell volume but can freely explore the whole volume. This is well known in the plasma literature under the term of "mixing entropy". The neutron and proton chemical potentials in the MCP mixture were found to be very close to the OCP ones, showing that a perturbative implementation of the NSE is sufficient. We have seen that a rearrangement term enters the expression of thermodynamic potential due to the self-consistency induced by the Coulomb part of the ion free energy, and we have proposed an approximation of this term which avoids solving a complex self-consistent problem, by imposing the most probable nucleus to coincide with the OCP solution in the OCP limit. As in the zero-temperature limit, we have chosen to use the CLD approach to model the nuclear free energy in the free neutron regime. Sommerfeld expansions, reliable at low temperature, have been employed to derive the expression of the nuclear matter free energy as well as chemical potential of nucleons. Because of the low values of the crystallization temperature expected in the crust, we have safely neglected the excitation of surface modes.

Using experimental masses supplemented with state-of-the-art microscopic theoretical mass tables, we have shown results relevant for the outer crust of PNS, that

is for low temperatures and more particularly at crystallization. We have calculated the crystallization temperature of a OCP throughout the outer crust. We have observed that neglecting the anharmonic contribution to the ion free energy in the solid phase lead to an underestimation of the crystallization temperature, which ranges from approximately $5 \times 10^7$ K at very low pressure to $2.8 \times 10^9$ K in the vicinity of the neutron-drip point, and exhibits a discontinuous behavior due to the shell effects. We have verified that the crystallization temperature is not strongly dependent on the mass model in the bottom layers of the outer crust, as long as realistic theoretical mass tables are employed. We have found that the composition of the outer crust at crystallization is very close to that calculated in the CCM hypothesis, and that the average value of mass number $A$ and charge number $Z$ in the MCP mixture follow closely the equilibrium OCP solutions throughout the outer crust. As pressure and temperature are increased, we have shown that the charge distributions become broader, making the OCP approximation less reliable. We have computed the so-called impurity parameter $Q_{\rm imp}$, which represents the variance of the charge distribution, at the crystallization temperature, and recovered the original results of [Fan+20]. Important oscillations of $Q_{\rm imp}$ have been observed, suggesting that the outer crust might consists of an alternation of highly resistive and highly conductive layers, and we have found that it can reach values as high as $\approx 50$ when the charge distribution exhibits a multimodal character. We have also evaluated the fraction of odd-mass and odd-charge nuclei present in the outer crust. We have shown that this quantity increases with temperature, and that, at crystallization, odd nuclei constitute $\approx 2\%$ of species in the outer crust, and contribute $\approx 2.4\%$ of the outer-crust baryonic mass.

Finally, using the latest BSk functionals, we have presented results relevant for the inner crust of PNS, particularly at the crystallization temperature. Following our work at zero temperature, we have added temperature-dependent shell corrections to the CLD free energy, and within the OCP approximation, we have demonstrated that the highest source of model dependence of the crystallization temperature and associated composition comes from the smooth part of the nuclear functional. In addition, we have seen that shell effects are strongly softened at the crystallization temperature in the inner crust, which we have estimated to lie between $\approx 3 \times 10^9$ K and $\approx 9 \times 10^9$ K. Concerning the composition at crystallization, we have observed deviations with respect to CCM at low density. Within the MCP treatment, we have shown that at the crystallization temperature the composition of the inner crust is dominated by clusters with charge number $Z \approx 40$, while the range of the charge distribution varies from about 20 near the neutron-drip point, to about 40 close to the transition to homogeneous matter. This reflects on the behavior of the impurity parameter that monotonically increases with average baryon density up to around 40 in the deeper regions of the inner crust. We have also observed that the inclusion of the rearrangement term is required to guarantee thermodynamic consistency.

# General conclusions and outlooks

The main aim of this thesis has been to make realistic predictions and to investigate the sources of uncertainties in the observables of nonaccreting cold NS and warm PNS, using a unified metamodeling approach for the description of stellar matter energetics, which allows to account for the present day constraints provided by nuclear experiments and astrophysical observations.

We have considered a unified metamodeling approach in order to calculate the composition and EoS of cold nonaccreting NS for any functional of NM using the associated empirical parameters as inputs, with an error which, in the representative case of the SLy4 EoS, is less than 1%. To model the energy of clusters in the inner crust, we have proposed a version of the well-known CLDM based on the metamodeling technique, with a parametrization of the surface tension suggested from TF calculations at extreme isospin ratios. The ground-state composition obtained follows closely the ETF results reported in the literature. The main drawback of the CLD approach is that quantum effects are lost, yet we have shown that magic numbers in the inner crust can be recovered by adding Strutinsky shell corrections to the CLD energy, leading to results in very good agreement with ETFSI calculations. The same sequence of nonspherical pasta phases in the deepest layers of the inner crust has been observed for all CLDM considered, yet we have stressed that it is sensitive to the behavior of the surface tension at high isospin, which remains poorly constrained to the present day. The uncertainty on the EoS induced by the treatment of the surface energy can be estimated to the order 10%, which corresponds to the difference between our results with the SLy4 functional and the DH EoS which uses the same functional but a different treatment of the surface energy. The same is true concerning the location of the transition point to homogeneous *npe* matter, which has been computed for several nuclear models from the crust side. We have shown that the anticorrelation between the slope of the symmetry energy at saturation $L_{sym}$ and the CC transition density, reported in many previous works, is obtained if the surface energy is only optimized on a limited set of spherical magic and semimagic nuclei. Conversely, if the surface tension is optimized on a large pool of data and curvature terms are added, this correlation disappears and the sensitivity to the EoS is limited to the poorly known high-order empirical parameters in the isovector sector, particularly the skewness $Q_{sym}$.

We have exploited the main asset of the metamodeling technique, namely the fact that no artificial correlations are introduced *a priori* among the empirical parameters, also to carry out the Bayesian determination of the empirical parameters, leading to realistic predictions for NS observables. We have considered a flat prior for the

empirical parameters whose boundaries are compatible with experimental constraints. The likelihood function that we have constructed takes into account recent chiral EFT calculations for SNM and PNM up to 0.20 $\mathrm{fm}^{-3}$, and the maximum mass constraint as well as basic physical requirements. It also includes a probability in which is encoded the ability of the CLDM to fit the masses of AME2016. We have shown that imposing the constraints associated to the *ab initio* calculations is very effective in constraining the empirical parameters in the isovector channel, and that it yields correlations among the symmetry energy derivatives at saturation. We have made general predictions for the static properties using the posterior distribution of empirical parameters and found that our results are compatible with constraints of the LIGO and Virgo collaborations inferred from GW170817. Since the only hypothesis of the metamodeling technique is the possibility of expanding the EoS into a power series, this result implies that we have no compelling evidence of a first order phase transition in the core of NS, though the latter can of course not be excluded. The fractional crust moment of inertia, which is strongly correlated with the location of the CC transition point, has been computed, allowing us to exclude a full crustal origin of pulsar glitches if we consider the largest present estimation of crustal entrainment. This opens interesting possibilities of the relevance of superfluid components in the core, particularly in the ${}^3P_2$ channel for $nn$ and $pp$ pairs.

Following a recent work on the outer crust, we have considered a full statistical equilibrium of ions in the crust at finite temperature allowing for the presence of an ambient neutron gas. We have evaluated the abundancies of odd-mass and odd-charge nuclei present in the outer crust at crystallization. Their presence is of interest, because it could be the cause for ferromagnetic phase transitions. We have considered a temperature dependence of proton shell corrections in the regime of the inner crust. The crystallization temperature and associated composition have been calculated in the OCP approximation, and our results suggest that the highest source of model dependence comes from the smooth part of the nuclear functional, the most important ingredient to be settled for a quantitative prediction of the inner crust properties being the surface tension at extreme isospin ratios. Deviations from CCM have been observed at low density and crystallization temperature. Finally, we have consistently calculated the impurity parameter in the inner crust at crystallization for four BSk functionals that span a relative large range in the symmetry energy parameters. This is the first calculation to date of the impurity factor with nuclear realistic functionals, and it has shown that contributions of impurities is nonnegligible, thus potentially altering transport properties in the NS crust.

Clearly, higher precision in the experimental determination of high-order isovector empirical parameters in the low-density EFT theoretical predictions and in the microscopic modeling of the surface energy at extreme isospin ratios are needed to reduce the uncertainties of crustal observables. Moreover, we have shown that constraints on dense matter properties can be inferred from astrophysical observations within the Bayesian framework. Many new measurements are expected in the near future, notably from LIGO/Virgo collaborations, thus we can hope to reduce the uncertainties on the high-order symmetry energy derivatives and on NS observables using Bayesian

inference or machine learning algorithms.

Various applications of the formalism introduced for the description of a MCP in a full statistical equilibrium can be envisaged in the future. For instance, one could investigate the presence of hyperons in the crust at crystallization. Nonspherical geometries can also be considered in the MCP treatment, allowing the evaluation of the impurity parameter in the bottom layers of the inner crust, and thus verifying the hypothesis of [PVR13] that the presence of a highly resistive layer in the inner crust, might lead to a higher limit to the spinning period of x-ray pulsars.

During the thesis, I have written an open-source C library, NSEoS, with the aim of providing useful tools related to the physics of NS [Car17a]. The library has been used to produce all the results presented in this thesis. Moreover, it was already used by different students to perform their internship under the joint supervision of my thesis advisor and myself, and we believe that it can be used as a basis for future studies.

# Appendix A

# Energy density of a relativistic electron gas

We give here the derivation of the energy density of a relativistic electron gas of density $n_e$ at zero temperature.

From $\approx 10^{14}$ g/cm$^3$, electrons are essentially free. In this case, the energy density is given by

$$\varepsilon_e = \frac{c}{\pi^2}\int_{k=0}^{k_e} dk k^2 \sqrt{\hbar^2 k^2 + m_e^2 c^2}, \tag{A.1}$$

$c$ being the speed of light, $\hbar$ the reduced Planck constant, and $m_e$ the electron mass. The electron Fermi wave number $k_e$ is related to the electron density via $k_e = (3\pi^2 n_e)^{1/3}$. Making a simple variable, $x = \hbar k/(m_e c)$, we can rewrite the energy density as

$$\varepsilon_e = \frac{m_e^4 c^5}{\pi^2 \hbar^3}\xi(x_r) \tag{A.2}$$

with $x_r = \hbar k_e/(m_e c)$ and

$$\xi = \int_{x=0}^{x_r} dx x^2 \sqrt{x^2+1}. \tag{A.3}$$

Integrating by parts, it follows

$$\begin{aligned}
\xi &= \left[\frac{x^3}{3}\sqrt{x^2+1}\right]_0^{x_r} - \int_0^{x_r} dx \frac{x^4}{3\sqrt{x^2+1}} \\
3\xi &= x_r^3\sqrt{x_r^2+1} - \int_0^{x_r} dx x^2 \left(\frac{x^2+1}{\sqrt{x^2+1}} - \frac{1}{\sqrt{x^2+1}}\right) \\
4\xi &= x_r^3\sqrt{x_r^2+1} + \int_0^{x_r} dx \frac{x^2}{\sqrt{x^2+1}}.
\end{aligned} \tag{A.4}$$

We have

$$\frac{d}{dx}\left(x\sqrt{x^2+1}\right) = \sqrt{x^2+1} + \frac{x^2}{\sqrt{x^2+1}}, \tag{A.5}$$

and

$$\frac{d}{dx}\left[\ln(x+\sqrt{x^2+1})\right] = \sqrt{x^2+1} - \frac{x^2}{\sqrt{x^2+1}}. \tag{A.6}$$

thus,

$$\frac{1}{2}\frac{d}{dx}\left[x\sqrt{x^2+1}-\ln\left(x+\sqrt{x^2+1}\right)\right]=\frac{x^2}{\sqrt{x^2+1}}. \tag{A.7}$$

Hence,

$$4\xi = x_r^3\sqrt{x_r^2+1}+\frac{1}{2}\left[x\sqrt{x^2+1}-\ln\left(x+\sqrt{x^2+1}\right)\right]_0^{x_r}, \tag{A.8}$$

which finally gives

$$\varepsilon_e(n_e)=\frac{m_e^4c^5}{8\pi^2\hbar^3}\left[x_r(2x_r^2+1)\gamma_r-\ln(x_r+\gamma_r)\right], \tag{A.9}$$

where we have introduced the parameter parameter $\gamma_r=\sqrt{x_r^2+1}$.

# Appendix B

# Neutron and proton chemical potentials in the metamodel

From the metamodeling of the nuclear matter energy, Eq. 1.38, we give here the complete expressions of the neutron and proton chemical potentials for a homogeneous system characterized by a neutron density $n_n$ and proton density $n_p$ at zero temperature. Let us introduce the variables $x = (n - n_{sat})/(3n_{sat})$ and $\delta = (n_n - n_p)/n$, $n = n_n + n_p$ being the total baryon density.

The neutron chemical potential, with the rest mass energy $m_n c^2$, is given by

$$\mu_{HM,n} = e_{HM}(n_n, n_p) + n\left(\frac{\partial e_{HM}}{\partial n_n}\right)_{n_p} + m_n c^2 \quad \text{(B.1)}$$

$$\mu_{HM,n} = e_{HM}(n, \delta) + \frac{1+3x}{3}\left(\frac{\partial e_{HM}}{\partial x}\right)_{\delta} + (1-\delta)\left(\frac{\partial e_{HM}}{\partial \delta}\right)_{x} + m_n c^2. \quad \text{(B.2)}$$

Equivalently, the proton chemical potential is given by

$$\mu_{HM,p} = e_{HM}(n, \delta) + \frac{1+3x}{3}\left(\frac{\partial e_{HM}}{\partial x}\right)_{\delta} - (1+\delta)\left(\frac{\partial e_{HM}}{\partial \delta}\right)_{x} + m_p c^2. \quad \text{(B.3)}$$

We first go through the derivative with respect to $x$, yielding

$$\begin{aligned}\left(\frac{\partial e_{HM}}{\partial x}\right)_{\delta} = & \frac{5}{1+3x} t_{HM}^{FG}(n, \delta) \\ & - \frac{3}{1+3x}\frac{1}{2} t_{sat}^{FG}(1+3x)^{2/3}\left[(1+\delta)^{5/3} + (1-\delta)^{5/3}\right] \\ & + \sum_{\alpha \geq 0}(v_\alpha^{is} + v_\alpha^{iv}\delta^2)\frac{1}{\alpha!}\left(\alpha x^{\alpha-1} u_\alpha(x) + x^\alpha \frac{du_\alpha}{dx}\right). \end{aligned} \quad \text{(B.4)}$$

Let us notice that is gives the expression for the total pressure,

$$P_{HM}(n, \delta) = n^2\left(\frac{\partial e_{HM}}{\partial n}\right)_{\delta} \quad \text{(B.5)}$$

$$= \frac{1}{3} n_{sat}(1+3x)^2\left(\frac{\partial e_{HM}}{\partial x}\right)_{\delta}. \quad \text{(B.6)}$$

We now turn to the derivative with respect to the asymmetry $\delta$,

$$\begin{aligned}\left(\frac{\partial e_{HM}}{\partial \delta}\right)_x &= \frac{1}{2}t_{sat}^{FG}(1+3x)^{5/3}\left[(1+\delta)^{5/3}-(1-\delta)^{5/3}\right] \\ &+\frac{5}{6}t_{sat}^{FG}(1+3x)^{2/3}\left[(1+\delta)^{2/3}\frac{m}{m_n^*}-(1-\delta)^{2/3}\frac{m}{m_p^*}\right] \\ &+2\delta\sum_{\alpha\geq 0}v_\alpha^{iv}\frac{x^\alpha}{\alpha!}u_\alpha(x). \end{aligned} \tag{B.7}$$

# Appendix C

# Partie en français

Dans cette annexe sont données les traductions en français de l'introduction générale, de la conclusion générale et des conclusions partielles.

## C.1 Introduction générale

L'existence des étoiles à neutrons a été proposée dès 1931 par Landau [Lan32], un an avant la découverte du neutron par Chadwick [Cha32]. Landau avait anticipé que la matière stellaire pouvait devenir « très dense, au point que les noyaux des atomes soient presque en contact, formant ainsi un gigantesque noyau ». En 1934, Baade et Zwicky introduisirent le terme *supernova* pour désigner un « type de remarquable de nova géante », un phénomène rare et très énergétique caractérisé par un éclat soudain et éphémère de la luminosité suivi par un lent déclin, et prédirent que « les supernovas représentent la transition des étoiles ordinaires en étoiles à *neutrons* » [BZ34]. La présence des étoiles à neutrons dans l'Univers est restée purement théorique jusqu'à 1968, lorsqu'une source rapidement pulsante, un *pulsar*, fut observée pour la première fois par Jocelyn Bell, une étudiante en thèse supervisée par Antony Hewish [Hew+68]. Plusieurs semaines après cette observation et suite à la découverte du pulsar du Crabe en 1968 (qui ne pouvait pas correspondre à une naine blanche étant donné sa période de pulsation trop courte [Com+69]), les pulsars furent identifiés comme des « des étoiles à neutrons rotatives »par Gold [Gol68], ouvrant alors la voie à des développements théoriques majeurs et à de nombreuses observations dans les décennies suivantes.

Au cours de leur vie, les étoiles de masse supérieure à $\sim 10 M_\odot$ ($M_\odot$ étant la masse du Soleil) peuvent fusionner les éléments du cœur jusqu'au silicium brûlant en fer. La fusion des éléments n'est alors plus possible dans la mesure où le fer est le nucléide le plus stable présent dans la nature. Dès lors, la chaîne de réactions dans le cœur se termine, et dans leur stade final les étoiles présentent une structure en forme d'oignon : leur cœur est composé de fer et de noyaux riches en neutrons du groupe du fer [Bet+79], entouré de couches d'éléments de moins en moins massifs jusqu'à l'hydrogène inerte à des températures et des densités plus basses [WHW02]. À ce stade, le cœur stratifié est essentiellement soutenu par la pression de dégénérescence des électrons et sa masse ne cesse d'augmenter par accrétion, en brûlant les couches de silicium, jusqu'à atteindre la

masse de Chandrashekar, $M_{Ch} \sim 1.44 M_{\odot}$, à partir de laquelle la force gravitationnelle dépasse la pression de dégénérescence des électrons [Cha31], déclanchant alors une explosion de supernova à effondrement de cœur [Jan+07]. Le résidu de l'explosion est une protoétoile à neutrons chaude ($\sim 10^{10}$ K) et deux finalités sont envisageables : soit la protoétoile à neutrons finira par évoluer en étoile à neutrons, soit en trou noir si sa masse est plus importante que la masse maximale des étoiles à neutrons, qui est encore incertaine à ce jour. Quelques minutes après la formation de la protoétoile à neutrons chaude, elle devient transparente aux neutrinos.

L'étoile se refroidit en émettant des neutrinos et des photons. À environ $10^8$ K, la matière est catalysée, c'est-à-dire dans son état fondamental. Une représentation schématique de la structure interne d'une étoile à neutrons froide est donnée en fig. 1. La surface externe d'une étoile à neutrons se compose d'une très fine atmosphère de seulement quelques centimètres et d'une enveloppe de quelques mètres, où le spectre du rayonnement électromagnétique thermique est formé. Ce rayonnement fournit des informations utiles sur les paramètres relatifs à la surface de l'étoile ainsi que sur les masses et rayons des étoiles à neutrons. La croûte inhomogène est située sous la surface extérieure et fait environ 1 km d'épaisseur. La croûte est généralement subdivisée en deux régions : la croûte externe et la croûte interne. La frontière entre ces deux régions se situe au niveau de la surface où la limite de stabilité neutron est franchie, à quelques centaines de mètres sous l'atmosphère. Au sein de la croûte, les atomes sont entièrement ionisés et forment un réseau cristallin immergé dans un gaz d'électrons relativistes ainsi que dans un gaz dans de neutrons si le potentiel chimique des neutrons est supérieur à la masse au repos des neutrons. De part la capture électronique, la matière s'enrichit en neutrons avec l'augmentation de la densité, c'est-à-dire lorsque l'on se rapproche du centre de l'étoile. Dans les couches profondes de la croûte interne, il est supposé que les noyaux présentent des formes non sphériques. Lorsque la température de la croûte interne devient inférieure à la température critique $T_c \sim 10^{10}$ K, les neutrons libres ayant des spins anti-alignés et un moment angulaire orbital nul forment des paires de Cooper et sont dans un état superfluide, caractérisé par l'absence de viscosité. À environ la moitié de la densité de saturation $n_{sat}$, correspondant à la la densité d'équilibre de la matière nucléaire homogène et symétrique, l'interface croûte-cœur est atteinte et les noyaux disparaissent. Par analogie avec la croûte, nous pouvons distinguer le cœur externe, correspondant aux densités baryoniques $0.5 n_{sat} \lesssim n_B \lesssim 2 n_{sat}$, et le cœur interne, où $n_B \gtrsim 2 n_{sat}$ ($n_B$ étant la densité de baryon). Dans le cœur externe, la matière est constituée d'un mélange de neutrons, protons, électrons et éventuellement muons. La composition du cœur interne est cependant incertaine et plusieurs hypothèses ont été avancées dans la littérature, notamment l'apparence des hypérons, de condensats de bosons, et/ou une transition de phase vers les quarks.

Les pulsars ont été identifiés comme des étoiles à neutrons en rotation produisant des émissions pulsées, peu de temps après leur découverte fortuite en 1967 par Jocelyn Bell [Hew+68]. Cinq décennies plus tard, nous en avons observé environ 3000 et de nombreuses techniques ont été développées pour mesurer leurs observables caractéristiques.

Il est plus facile pour les astronomes de mesurer la masse d'une étoile à neutrons appartenant à un système binaire. Il existe plusieurs types de binaires et, selon le type, différentes techniques sont utilisées pour déduire la masse de l'étoile [HPY07]. Par exemple, dans un pulsar binaire, divers phénomènes tels que l'effet Shapiro [Sha64] peuvent être exploités dans le but de mesurer la masse en surveillant régulièrement la rotation d'un pulsar sur de longues périodes. L'effet Shapiro est un phénomène à partir duquel des masses précises, tant pour un pulsar milliseconde que pour son compagnon, peuvent être déduites [Dem+10; Cro+20]. Les masses mesurées des étoiles à neutrons par le *timing* de pulsar sont affichées dans la fig. 2.

Mesurer le rayon des étoiles à neutrons avec une grande précision est une tâche plus difficile. Le principe de base de l'extraction du rayon repose sur la mesure du spectre des rayons X (flux et fréquence), à partir duquel la température à la surface et le rayon de l'étoile peuvent être extraits à l'aide de l'équation du rayonnement du corps noir. En particulier, des estimations précises du rayon de l'étoile pourraient être fournies par des ajustements du spectre dans les binaires X de faible masse pendant les phases avec peu ou sans accrétion [BBR98]. Plusieurs binaires X de faible masse au repos ont été étudiés avec l'observatoire de rayons X Chandra et/ou XMM-Newton [Hei+14; Ser+12; GR14; Gui+13]. Cependant, les résultats dépendent fortement des hypothèses faites sur la composition de l'atmosphère des étoiles à neutrons qui est peu connue à ce jour [Ste+18]. Une amélioration importante est attendue avec l'analyse des résultats de la mission NICER, dont les premiers résultats commencent à être disponibles [Bog+19a; Bog+19b; Mil+19; Raa+19; Ril+19], même si des complications dans l'interprétation des données interviennent à cause du manque d'uniformité de la température à la surface [Bog+19a; Bog+19b; Mil+19; Raa+19; Ril+19]. Les valeurs typiques pour les masses et rayons des étoiles à neutrons sont respectivement $M = 1.4 M_\odot$ et $R = 10 - 14$ km.

Très récemment, la première détection d'ondes gravitationnelles à partir de la coalescence de deux étoiles à neutrons, l'événement GW170817, a donné des contraintes importantes pour la déformabilité due aux effets de marée [Abb+18]. La déformabilité décrit l'ampleur de la déformation d'un corps par les forces de marée qui surviennent lorsque deux corps massifs sont en orbite l'un autour de l'autre. L'exemple le plus simple et le plus connu correspond à la Lune qui provoque les marées observées dans les océans sur Terre. La détection du rayonnement gravitationnel émis par le binaire d'étoiles à neutrons a été rendu possible par les détecteurs d'ondes gravitationnelles terrestres LIGO et Virgo. Peu avant la fusion, lorsque la distance relative entre les étoiles est suffisamment faible, la distortion due aux effets de marée devient si importante que, dans certains cas (pour les signaux les plus forts correspondant aux événements les plus proches), il est possible de déduire la déformabilité à partir du signal.

Le phénomène de *glitch* observé chez certains pulsars correspond à un sursaut soudain dans la fréquence de rotation de l'étoile compacte. Ce sursaut pourrait s'expliquer par un transfert abrupt de moment angulaire depuis les composants superfluides de l'étoile vers la croûte solide de l'étoile et tous les composants normaux des fluides qui sont fortement couplés à la croûte par dissipation mutuelle. Il a été suggéré que ce transfert soudain soit dû au détachement des vortex superfluides confinés dans

le réseau cristallin [AI75]. En effet, un superfluide en rotation, tel que les neutrons superfluides à l'intérieur de la croûte, produit des vortex individuels quantifiés, avec une densité proportionnelle au taux de rotation. En raison de la force centrifuge associée à la rotation de l'étoile, ces vortex migrent vers la surface et se fixent aux ions du réseau constituant la croûte solide. Le ralentissement de la rotation de l'étoile causé par l'émission de rayonnement électromagnétique induit un décalage différentiel entre les vortex superfluides et la croûte, plus lente, entraînant ainsi une tension. Lorsque le décalage entre la croûte solide et les vortex superfluides dépasse un certain seuil et ne peut plus être soutenu, les vortex se détachent soudainement des sites du réseau, cédant alors du moment angulaire à la croûte et au reste de l'étoile qui est y mêlé par friction mutuelle, rétablissant des conditions proches de l'équilibre entre les composants normales et superfluides. Étant donné que le ralentissement dû à l'émission de rayonnement électromagnétique est un processus continu, il ne s'agit pas d'une situation d'équilibre finale. La tension finira ainsi éventuellement par se reconstituer, provoquant alors un autre *glitch*. À ce jour, 555 *glitches* ont été observés dans 190 pulsars via le *timing* de pulsar de haute précision [Esp+11; Jod]. Le pulsar de Vela (PSR B0833-45) est connu pour être le siège d'un grand nombre de *glitches*, avec des évènements se produisant quatre fois par décennie en moyenne.

Une description théorique des différents phénomènes mentionnés ci-dessus nécessite la modélisation de la matière baryonique dense, en particulier de l'équation d'état nucléaire. L'équation d'état relie, dans des conditions connues de température et de densité, les propriétés thermodynamiques du système, telles que la densité massique et la pression, à l'équilbre. Elle permet notamment de déterminer la relation masse-rayon des étoiles à neutrons, obtenue en résolvant l'équation d'équilibre hydrostatique en relativité générale [Tol39; OV39]. Étant donné que la chromodynamique quantique ne peut pas être exactement résolue dans le régime non perturbatif, l'équation d'état est fortement dépendante du modèle, ce qui induit des incertitudes dans la prévision des observables astrophysiques. Dans cette thèse, nous nous intéressons particulièrement à la modélisation de la croûte des (proto)étoiles à neutrons, où la matière est inhomogène. Du point de vue de la modélisation, ce régime de matière sous-saturée constitue la partie la plus délicate de l'équation d'état nucléaire. En effet, les incertitudes ne concernent pas seulement la fonctionnelle d'énergie nucléaire mais aussi la méthode *many-body* utilisée pour modéliser la matière inhomogène. En effet, l'évaluation de l'équation d'état implique de connaître la composition microscopique à chaque point de l'étoile. À température finie, une complication supplémentaire se présente de part le traitement statistique du problème. Historiquement, l'équation d'état de la matière sous-saturée a d'abord été calculée dans le cadre de l'approximation de noyau unique [BBP71; NV73], basée sur l'hypothèse que la matière peut être représentée par le noyau le plus probable, déterminé par la minimisation de la densité d'énergie libre de la matière. Bien que cette approximation soit exacte à température nulle, une distribution complète des *clusters* doit être envisagée à température finie, comme c'est le cas dans les modèles d'équilibre statistique nucléaire. Une fois encore, la solution exacte du problème *many-body* à température finie étant hors de portée, la modélisation ne peut pas être évitée, ce qui implique une dépendance au modèle lors du calcul

des observables.

Nous pourrions naïvement considérer qu'un modèle nucléaire optimal peut être extrait en confrontant les prédictions théoriques aux données observationnelles. Or, un problème majeur avec les équations d'état caractéristiques est que certaines observables sont plus fidèlement reproduites par un modèle particulier (ou une classe de modèles), tandis que ce dernier ne parvient pas forcément à reproduire d'autres observables. En outre, chaque observable est associée à des incertitudes et la capacité de reproduire ou non une mesure déterminée n'a pas le même impact sur la fiabilité du modèle en fonction de l'observable considéré. En plus des contraintes astrophysiques, nous devons aussi tenir compte des contraintes fournies par les expériences de physique nucléaire et des développements récents dans les calculs *ab initio* basés sur la théorie des perturbations chirales [DHS16], consistant en la détermination de la fonctionnelle d'énergie nucléaire à partir d'une série entière respectant les symétries fondamentales de chromodynamique quantique [ME11] de basse énergie, c'est-à-dire la théorie des interactions fortes. Les différents modèles pouvant être envisagés n'ont pas été systématiquement confrontés à toutes ces contraintes. Dans ces conditions, il est très difficile de valider (ou d'invalider) un modèle. Une solution à cette impasse est assurée par l'utilisation du principe d'inférence bayésienne qui permet de mettre à jour nos croyances antérieures sur l'équation d'état en utilisant les contraintes découlant des multiples sources mentionnées précédemment. Il a été démontré que les observables des (proto)étoiles à neutrons sont sensibles à la microphysique entrant en jeu dans l'équation d'état, notamment aux dérivés d'ordres élevés de l'énergie de symétrie nucléaire et aux propriétés de surface des noyaux finis. Il est donc essentiel de contraindre ces quantités afin de contrôler les incertitudes sur les observables. Dans cette thèse, nous proposons de faire des prédictions réalistes et d'étudier les sources d'incertitudes associées aux observables des étoiles à neutrons froides non accrétantes et des protoétoiles à neutrons chaudes, en utilisant les contraintes actuelles fournies par les expériences de physique nucléaire, les développements en théorie des perturbations chirales et les observations astrophysiques. Cet argument général s'applique à la modélisation totale de l'étoile à neutrons mais aussi à la croûte de l'étoile, qui constitue l'objet principal de ce travail de thèse.

Alors que la croûte ne représente qu'un très faible pourcentage de la masse totale d'une étoile à neutrons, il est important de la modéliser correctement s'il on veut comprendre la dynamique de ces astres compacts, notamment le phénomène de *glitch* et les processus de refroidissement. En plus de l'équation d'état nucléaire, la détermination des observables de la croûte nécessite la connaissance de la densité et de la pression au point de transition entre la croûte solide et le cœur liquide [PFH14]. Afin de valider l'hypothèse que le phénomène de *glitch* tire son origine de la physique de la croûte, cette dernière doit être suffisamment épaisse pour contenir sufisamment de moment angulaire. Pour le pulsar de Vela, la fraction nécessaire de moment d'inertie contenu dans la croûte est actuellement estimée entre 1.6% et 15% [LEL99; And+12; Del+16], selon l'importance de l'effet d'entraînement de la croûte, encore activement débatu [MU16; WP17]. Une estimation fiable de l'épaisseur de la croûte et du moment d'inertie associé est donc indispensable. Pour toutes ces applications, il est essentiel de disposer de critères objectifs permettant de valider ou d'invalider les différents mod-

èles, et éventuellement de corréler l'incertitude résiduelle des prédictions du modèle à des paramètres bien définis qui peuvent être contraints à l'avenir par des expériences plus précises ou des calculs *ab initio*. La première partie de cette thèse visera a fournir un effort dans cette direction. Cela sera rendu possible par l'introduction d'une procédure de métamodélisation flexible qui nous permettra de confronter un très large ensemble de modèles de matière nucléaire catalysée aux différentes contraintes provenant de la physique nucléaire de basse énergie et des observations astrophysiques d'étoiles à neutrons matures.

La deuxième partie de cette thèse portera sur la modélisation de la croûte à température finie. Une fois de plus, l'accent sera mis sur la détermination de barres d'erreur fiables sur les observables astrophysiques en raison des incertitudes inhérentes à la modélisation. Cette modélisation à température finie n'est pas seulement essentielle pour décrire l'évolution des supernovas et la dynamique des protoétoiles à neutrons mais pourrait également être pertinente pour la prédiction des observables de la croûte des étoiles à neutrons matures. En effet, il est peu probable que la croûte d'une étoile à neutrons soit à l'équilibre thermodynamique complet à température nulle : les étoiles à neutrons naissent chaudes et si leur cœur se refroidit suffisamment rapidement, la composition pourrait être gelée à une température finie [Gor+11]. Des écarts par rapport à la composition de la croûte refroidie dans l'état fondamental autour de la limite de stablité neutron ont déjà été considérées dans [BC79]. Toutefois, de simples extrapolations de formules de masse semi-empiriques avaient été utilisées à cette époque. La valeur de la température à laquelle la composition se fige est difficile à évaluer. Cependant, une limite inférieure est donnée par la température de cristallisation car nous pouvons nous attendre à ce que les réactions nucléaires soient entièrement inhibées dans un cristal de Coulomb. Pour ces raisons, la dernière partie de cette thèse sera consacrée à l'étude de la structure de la croûte à la température de cristallisation. La présence éventuelle de phases amorphes et hétérogènes dans la croûte interne d'une étoile à neutrons devrait réduire la conductivité électrique de la croûte, avec des conséquences potentiellement importantes sur l'évolution magnéto-thermique de l'étoile. L'étude des processus de refroidissement est importante pour comparer les calculs théoriques et la température de surface mesurée par les satellites. Dans les simulations de refroidissement, le désordre est quantifié par un paramètre d'impureté, souvent considéré comme un paramètre libre. Ce paramètre est directement relié à la conductivité électron-impureté, qui contribue à la conductivité thermique totale [FI76].

La thèse est divisée en trois chapitres. Dans le premier chapitre, nous considérons une approche de métamodélisation unifiée afin de calculer la composition et l'équation d'état des étoiles à neutrons froides non accrétantes pour toute fonctionnelle de matière nucléaire. Dans la croûte interne, l'énergie des *clusters* est calculée dans l'approximation de la goutte liquide compressible. Dans le deuxième chapitre, nous effectuons la détermination bayésienne des paramètres de l'équation d'état conduisant à des prédictions réalistes sur les observables des étoiles à neutrons froides. Nous confrontons ces prédictions aux contraintes des collaborations LIGO et Virgo. Des informations issues d'expériences de physique nucléaire, de calculs en théorie des perturbations chirales et d'observations astrophysiques sont encodées dans la fonction

de vraisemblance. Les corrélations entre les paramètres de l'équation d'état sont explorées. La densité et pression au point de transition croûte-cœur ainsi que le moment d'inertie de la croûte sont calculés à partir de la distribution *posterior* des paramètres de l'équation d'état et nous discutons l'origine des *glitches* du pulsar de Vela. Dans le troisième chapitre, nous considérons une approche d'équilibre statistique nucléaire pour modéliser la croûte des protoétoiles à neutrons à température finie. La composition d'équilibre au point de cristallisation est calculée et le paramètre d'impureté, qui est une donnée importante dans les simulations de refroidissement des étoiles à neutrons, est évalué pour différentes fonctionnelles réalistes. La présence de noyaux de masse impaire et de charge impaire dans la croûte externe fait également l'objet d'une étude.

## C.2 Structure et équation d'état des étoiles à neutrons froides non accrétantes

Dans ce premier chapitre, nous avons d'abord évalué l'état fondamental de la croûte externe que nous obtenons par application de la méthode proposée par Baym, Pethick et Sutherland en 1971 [BPS71] en utilisant les plus récentes données sur les masses expérimentales[Hua+17; Wel+17] complétées par des tables de masses théoriques Hartree-Fock-Bogoliubov [Sam+02], basées sur la théorie de la fonctionnelle de la densité. Nous avons montré que la composition de la croûte externe (et donc l'équation d'état) est entièrement déterminée par les connaissances actuelles sur les masses expérimentales jusqu'à $n_B \approx 3 \times 10^{-5}$ fm$^{-3}$. À des densités plus élevées, nous avons observé la persistance de $N = 82$ pour chacun des quatre modèles de masse considérés : HFB-24, HFB-26, HFB-14 et FRDM.

Nous avons proposé une version du modèle de la goutte liquide compressible basée sur la technique de métamodélisation [MHG18a; MHG18b]. Nous avons vu que le métamodèle offre la possibilité de reproduire toute fonctionnelle de matière nucléaire très précisément, avec une unique forme fonctionnelle. La paramétrisation de la tension de surface a été suggérée par des calculs microscopiques dans le régime des neutrons libres [RPL83] et les paramètres de surface et de courbure sont ajustés sur les masses expérimentales. Nous avons utilisé notre modèle de la goutte liquide compressible pour calculer l'état fondamental de la croûte interne qui est obtenu en minimisant la densité d'énergie de la matière à densité baryonique constante sous la condition de neutralité de la charge globale. Nous avons ainsi abouti à un système de quatre équations différentielles couplées, correspondant à des conditions d'équilibre, que nous avons résolues numériquement en utilisant la méthode de Broyden [Bro65]. La composition de la croûte interne dans l'état fondamental, pour les paramètres empiriques de BSk24, a été présentée et un très bon accord avec des approches plus microscopiques a été observé concernant la valeur de $Z \approx 40$. Nous avons également vu que la fraction de protons diminue avec la densité de façon monotone, comme c'est le cas dans la croûte externe. L'équation d'état de la croûte interne a été calculée et une corrélation positive avec le paramètre empirique $E_{sym}$ a été révélée. Nous avons montré que les nombres magiques, qui disparaissent dans le cadre de l'approche classique de la goutte liquide

compressible, peuvent être retrouvés en ajoutant de manière perturbative des corrections de couches des protons calculées par la méthode de Strutinsky. De cette façon, un très bon accord avec les calculs Thomas-Fermi étendu avec corrections de couches Strutinksy a été observé pour les functionelles BSk récentes [Pea+18]. Avec notre modèle de la goutte liquide compressible, nous avons exploré la présence de phases non sphériques dans les couches profondes de la croûte interne. Nous avons trouvé la séquence sphères $\rightarrow$ cylindres $\rightarrow$ plaques $\rightarrow$ tubes pour chacun des quatre modèles considérés : BSk24, SLy4, BSk22 et DD-ME$\delta$. Nous avons montré que la localisation du point de transition vers la matière homogène est très sensible au comportement de la tension de surface pour des valeurs extrêmes de l'isospin, contrôlé par le paramètre de surface isovecteur $p$. Malheureusement, il est impossible d'accéder à la valeur de ce paramètre à partir des données empiriques actuelles de physique nucléaire qui sont limitées à $I \lesssim 0.3$. Nous avons vu que les résultats de la littérature sur la densité et la pression de transition croûte-cœur pour la dynamique spinodale [Duc+11] sont globalement bien reproduits par notre calcul depuis la croûte avec $p \approx 3$. Nous avons également confirmé la corrélation entre la densité de transition $n_t$ et le paramètre empirique $L_{sym}$, déjà observée dans de précédents travaux.

Nous avons déterminé les équations d'équilibre caractérisant l'état fondamental de la matière dans le cœur $npe\mu$ jusqu'à $n_B \approx 2n_{sat}$. La forte corrélation entre l'énergie de symétrie et la fraction de proton a été expliquée. Nous avons constaté que les muons apparaissent à approximativement $n_B = 0.12$ fm$^{-3}$ pour chaque modèle. Comme dans de précédents travaux [WFF88; DH01], nous avons extrapolé la matière $npe\mu$ à des densités plus élevées puisque les interactions hypéron-hypéron et hypéron-nucléon restent actuellement très peu connues.

Enfin, nous avons souligné que l'utilisation d'une équation d'état unifiée est essentielle pour déterminer les observables de la croûte. En ce sens, nous avons proposé une métamodélisation de l'équation d'état pour une étoile à neutrons froide non accrétante où la croûte et le cœur sont traités de manière uniforme, c'est-à-dire avec le même jeu de paramètres empiriques. En utilisant les paramètres empiriques de SLy4, nous avons montré que la différence relative avec l'équation d'état de Douchin et Haensel est inférieure à 10% dans la croûte interne et à 1% dans le cœur.

## C.3 Inférence bayésienne des observables des étoiles à neutrons

Dans ce chapitre, nous avons d'abord introduit les équations de base de l'équilibre hydrostatique en relativité générale pour les étoiles sphériques non rotatives. Nous avons résolu ces équations pour différentes équations d'état connues afin d'obtenir la relation entre la masse et le rayon de l'étoile. Dans le même esprit, nous avons calculé le moment d'inertie ainsi que la déformabilité due aux effets de marée dans l'approximation de la rotation lente qui devrait être valable pour la plupart des pulsars. La détermination de la densité et de la pression au point de transition entre la croûte et le cœur, discutée dans le premier chapitre, permet le calcul des observables de la croûte. Nous avons ainsi calculé son épaisseur et la fraction du moment d'inertie

résidant à l'intérieur. Nous avons expliqué en détail le lien entre le moment d'inertie de la croûte et le phénomène de *glitch* de pulsar dans le consensus actuel, où un *glitch* est observé lors du transfert de moment angulaire depuis les neutrons superfluides, confinés dans la croûte interne, vers le reste de l'étoile [AI75]. L'un des principaux problèmes exposés dans la section 2.1 est la sensibilité des résultats à l'équation d'état et plus particulièrement aux paramètres empiriques du secteur isovecteur. Nous avons montré que les équations d'état considérées ne réussissent pas toutes à dépasser la contrainte de masse maximale, $M_{max} \gtrsim 2M_\odot$ [Dem+10; Ant+13; Cro+20], favorisant une équation d'état *stiff*. De plus, nos résultats tendent à indiquer que le phénomène de *glitch* ne peut pas uniquement tirer son origine de la physique de la croûte compte tenu des estimations actuelles de l'effet d'entraînement [And+12; PFH14]. Inversement, la récente contrainte sur le paramètre de déformabilité due aux effets de marée $\Lambda_{1.4}$ déduit de GW170817 [Abb+18] tend à favoriser les équations d'état *soft*.

Nous avons rappelé le principe de l'inférence bayésienne avant d'effectuer la détermination bayésienne des paramètres de l'équation d'état en utilisant la technique de métamodélisation [MHG18a]. Nous avons utilisé une distribution *prior* uniforme pour les paramètres qui tient compte des contraintes empiriques actuelles. Les résultats et les analyses présentés dans ce chapitre sont proches mais ne sont pas identiques à nos résultats publiés [CGM19a; CGM19b]. En effet, une analyse bayésienne dépend de façon cruciale à la fois de la modélisation du *prior* et de celle de la fonction de vraisemblance. Dans ce travail de thèse, nous avons fait varier à la fois la distribution *prior* des paramètres de surface, en adoptant un protocole d'optimisation différent de celui de [CGM19a; CGM19b] et en introduisant des termes de courbure qui ont été négligées dans l'étude précédente, et les filtres, en explorant les effet de l'inclusion ou non des prédictions de la théorie des perturbations chirales concernant la pression de la matière nucléaire symétrique et la matière pure de neutrons. Les différents résultats sont compatibles à l'intérieur des barres d'erreur mais des corrélations différentes sont observées. L'analyse de ces différences nous a permis de mieux comprendre l'effet des différentes conditions. Une analyse de sensitivité sur le point de transition croûte-cœur a révélé que les paramètres empiriques du secteur isovecteur sont les plus importants pour déterminer précisément la densité $n_t$ et pression $P_t$ de transition. Nous avons calculé la fonction de vraisemblance en tenant compte de contraintes sur les observables de physique nucléaire (contraintes de basse densité), à savoir les masses expérimentales [Hua+17] et les calculs en théorie des perturbations chirales pour la matière nucléaire symétrique et la matière pure de neutrons [DHS16], et sur les observables des étoiles à neutrons (contraintes de haute densité). La distribution *posterior* des paramètres empiriques a été analysée. Nous avons observé que le filtre de basse densité est très efficace pour contraindre les paramètres dans le secteur isovecteur, en particulier si l'on impose la compatibilité avec les prédictions de la théorie des perturbations chirales pour la pression de la matière nucléaire. Nous avons montré que seules les contraintes en physique nucléaire donnent lieu à des corrélations entre les paramètres empiriques. Dans le secteur isovecteur, la corrélation entre $E_{sym}$ et $L_{sym}$ est retrouvée. Nous avons constaté que le paramètre $L_{sym}$ est corrélé avec $K_{sym}$ et avons trouvé de nouvelles corrélations intéressantes lors de l'ajout du filtre sur la pression : $r(L_{sym}, Q_{sym}) = -0.55$ et $r(K_{sym}, Q_{sym}) = 0.52$.

Enfin, nous avons fait des prédictions générales sur les propriétés statiques et les observables de la croûte des étoiles à neutrons à partir de la distribution *posterior* des paramètres calculée dans la section 2.2. Dans l'ensemble, nous avons constaté que nos prédictions des observables de l'étoile sont en assez bon accord avec les contraintes sur l'équation d'état, le rayon et la déformabilité déduites de l'événement GW170817 [De+18; Abb+18]. Nous avons obtenu $R_{1.4} = 12.88^{+0.53}_{-0.65}$ km et $\Lambda_{1.4} = 634^{+204}_{-190}$ avec un intervalle de confiance de 90%. Nous avons montré que la densité et la pression de transition sont corrélées avec les paramètres empiriques du secteur isovecteur, notamment avec $Q_{sym}$. En considérant l'incertitude expérimentale et théorique sur ces paramètres, nous avons estimé la densité et pression de transition à respectivement $n_t = 0.068^{+0.021}_{-0.021}$ fm$^{-3}$ et $P_t = 0.263^{+0.302}_{-0.149}$ MeV/fm$^3$ à $1\sigma$. Contrairement à nos travaux publiés [CGM19a], nous n'observons pas une forte influence des paramètres de surface sur les quantités au point de transition croûte-cœur. Ceci peut s'expliquer par un contrôle plus important de l'énergie de surface dans cette thèse. Nous avons observé que plus la croûte est épaisse, plus la quantité de moment angulaire confinée dans le superfluide, coexistant avec le réseau d'ions dans la croûte interne, est importante. La grande incertitude sur la pression de transition se reflète sur le moment d'inertie de la croûte. En effet, pour une étoile à neutrons de $1.4M_\odot$, nous avons obtenu $I_{crust,1.4}/I_{1.4} = 2.89^{+2.51}_{-1.68}\%$ à $1\sigma$. La distribution de probabilité pour la masse et le rayon du pulsar de Vela a été calculée pour deux estimations différentes de l'effet d'entraînement de la croûte. Ceci nous a permis de confirmer qu'une meilleure estimation quantitative de l'effet d'entraînement est le point clé pour associer le phénomène de *glitch* à la physique de la croûte, même si l'incertitude sur l'équation d'état brouille les résultats. Nous nous sommes intéressés à la variation du moment d'inertie de la croûte avec la masse de l'étoile et avons conclu que le phénomène de *glitch* démontré par certains pulsars ne peut pas uniquement tirer son origine de la physique de la croûte dans le cas où l'on considère la plus grande estimation actuelle de l'effet d'entraînement [Del+16].

## C.4 Cristallisation de la croûte des protoétoiles à neutrons

Dans ce dernier chapitre, nous nous sommes intéressés à la modélisation de la croûte à température finie. L'approximation de plasma à un composant, dans laquelle la distribution attendue de noyaux est remplacé par un noyau unique déterminé à partir de la minimisation du potentiel thermodynamique à une condition thermodynamique donnée, a été considérée. Nous avons donné les expressions des corrections entrant en jeu dans l'énergie libre des ions à température finie, à savoir le terme de mouvement de translation du centre de masse dans le liquide, le terme de vibrations quantiques de point zéro dans la phase solide ainsi que la contribution de l'interaction coulombienne qui diffère selon la phase de la matière. Nous avons discuté la définition de la transition de la phase liquide à la phase solide. Puis, nous avons inclus la distribution des ions en considérant un plasma à plusieurs composants à l'équilibre. Dans ce cadre, des effets de mélange non linéaires apparaissent car la position du centre de masse

de chaque ion n'est pas limitée au seul volume de la cellule de Wigner-Seitz associée mais peut explorer librement le volume total. Ceci est connu dans la littérature de la physique des plasmas sous le terme d'« entropie de mélange ». Les potentiels chimiques des neutrons et des protons dans le mélange se sont avérés être très proches de ceux dans le plasma à un composant, ce qui montre qu'une implémentation perturbative de l'équilibre statistique nucléaire est suffisante. Nous avons vu qu'un terme de réarrangement entre dans l'expression du potentiel thermodynamique de part l'auto-cohérence induite par la partie coulombienne de l'énergie libre de l'ion. Nous avons proposé une approximation de ce terme pour éviter de résoudre un problème auto-cohérent complexe en imposant la coïncidence du noyau le plus probable avec la solution obtenue dans la limite du plasma à un composant. Comme lors de notre étude à température nulle, nous avons choisi d'utiliser l'approche de la goutte liquide compressible pour modéliser l'énergie libre des *clusters* dans le régime des neutrons libres. L'expansion de Sommerfeld, fiable à basse température, a été employée pour dériver l'expression de l'énergie libre de le matière nucléaire ainsi que du potentiel chimique des nucléons. En raison des faibles valeurs de la température de cristallisation prédites dans la croûte, nous avons négligé l'excitation des modes de surface.

En utilisant la table de masses expérimentales AME2016, complétée par des tables de masses théoriques basées sur le modèle microscopique Hartree-Fock-Bogoliubov, nous avons obtenu des résultats pertinents pour la croûte externe des protoétoiles à neutrons, c'est-à-dire à basse température et plus particulièrement au point de cristallisation. Nous avons calculé la température de cristallisation du plasma à un composant dans la croûte externe. Nous avons constaté que le fait de négliger la contribution anharmonique dans l'énergie libre des ions dans la phase solide conduit à une sous-estimation de la température de cristallisation qui varie d'environ $5 \times 10^7$ K, à très basse pression, à $2.8 \times 10^9$ K, au voisinage de la limite de stabilité neutron et qui présente un comportement discontinu en raison des effets de couches. Nous avons vérifié que la température de cristallisation n'est pas fortement dépendante du modèle de masse utilisé dans les couches profondes de la croûte externe, tant que des tables de masses théoriques réalistes sont utilisées pour compléter les données expérimentales. Nous avons constaté que la composition de la croûte externe au point de cristallisation est très proche de celle calculée dans l'hypothèse de matière froide catalysée et que la valeur moyenne du nombre de masse $A$ et de charge $Z$ dans le plasma à plusieurs composants est très proche de la solution pour le plasma à un composant dans la croûte externe. À mesure que la pression et la température augmentent, nous avons montré que la distribution de charges s'étend, indiquant alors que l'approximation du plasma à un composant devient moins fiable. Nous avons calculé le paramètre d'impureté $Q_{\rm imp}$, qui représente la variance de la distribution de charges, à la température de cristallisation et nous avons retrouvé les résultats de [Fan+20]. D'importantes oscillations de $Q_{\rm imp}$ ont été observées, ce qui suggère que la croûte externe pourrait consister en une alternance de couches hautement isolantes et de couches hautement conductrices. Nous avons constaté que le facteur d'impureté pouvait atteindre des valeurs aussi élevées que $\approx 50$ lorsque la distribution de charges présente un caractère multimodal. La fraction des noyaux de masse impaire et de charge impaire présents dans la croûte externe a été évaluée. Ces quantités augmentent avec la température et, au point

de cristallisation, les noyaux impairs constituent environ 2% des espèces de la croûte externe et contribuent à hauteur d'environ 2.4% de la masse baryonique de la croûte externe.

Enfin, en utilisant les fonctionnelles BSk les plus récentes, nous avons obtenu des résultats pertinents pour la croûte interne des protoétoiles à neutrons, particulièrement à la température de cristallisation. Suite à notre travail à température nulle, nous avons ajouté les corrections de couches à l'énergie libre des *clusters*. En se plaçant dans l'approximation de plasma à un composant, il a été observé que la plus grande source de dépendance au modèle de la température de cristallisation et composition associée provient de la partie lisse de la fonctionnelle nucléaire. En outre, nous avons vu que les effets de couches sont fortement atténués à la température de cristallisation dans la croûte interne, que nous avons estimée entre $\approx 3 \times 10^9$ K et $\approx 9 \times 10^9$ K. En ce qui concerne la composition au point de cristallisation, nous avons observé, à faible densité, des déviations par rapport à la matière froide catalysée. À la température de cristallisation, la composition de la croûte interne est dominée par les *clusters* avec $Z \approx 40$, tandis que la largeur de la distribution de charges est d'environ 20, proche de la limite de stabilité neutron, et environ 40, près du point de transition vers la matière homogène. Cela se reflète dans le comportement du paramètre d'impureté qui de manière monotone augmente avec la densité baryonique moyenne jusqu'à environ 40 dans les couches les plus profondes de la croûte interne. Nous avons également observé que l'inclusion du terme de réarrangement est nécessaire pour garantir la cohérence thermodynamique.

## C.5 Conclusions générales et perspectives

L'objectif principal de cette thèse a été de fournir des prédictions réalistes et d'étudier les sources d'incertitudes sur les observables des étoiles à neutrons froides isolées et des protoétoiles à neutrons chaudes. Pour ce faire, nous avons considéré une métamodélisation unifiée pour décrire l'énergétique de la matière d'étoile qui permet de tenir compte des contraintes actuelles liées aux expériences nucléaires et des observations astrophysiques.

Nous avons envisagé une approche de métamodélisation unifiée afin de calculer la composition et l'équation d'état de l'étoile à neutrons froide isolée pour toute fonctionnelle de matière nucléaire en utilisant les paramètres empiriques associés comme seuls ingrédients. Nous avons obtenu une erreur qui, dans le cas de l'équation d'état basée sur SLy4, est inférieure à 1%. Pour modéliser l'énergie des *clusters* dans la croûte interne, nous avons proposé une version du célèbre modèle de la goutte liquide compressible basée sur la technique de métamodélisation, avec une paramétrisation de la tension de surface suggérée par des calculs Thomas-Fermi à des ratios d'isospins extrêmes. La composition obtenue dans l'état fondamental suit de près les résultats de calculs Thomas-Fermi étendu rapportés dans la littérature. Le principal inconvénient de l'approche de la goutte liquide compressible est que les effets quantiques sont perdus. Cependant, nous avons montré que les nombres magiques dans la croûte interne peuvent être retrouvés en ajoutant les corrections de couches calculées par la méth-

ode de Strutinsky, conduisant alors à un très bon accord avec les résultats de calculs Thomas-Fermi étendu avec corrections de couches Strutinsky. La même séquence de phases non sphériques dans les couches les plus profondes de la croûte interne a été observée pour tous les modèles considérés mais nous avons souligné qu'elle est sensible au comportement de la tension de surface à grand isospin, restant peu contrainte à ce jour. L'incertitude sur l'équation d'état induite par le traitement de l'énergie de surface peut être estimée à 10%, ce qui correspond à la différence entre nos résultats avec la fonctionnelle SLy4 et l'équation d'état de Douchin et Haensel qui utilise la même fonctionnelle mais un traitement différent de l'énergie de surface. Il en va de même pour la localisation du point de transition vers la matière homogène *npe* qui a été calculée pour plusieurs modèles nucléaires dans le sens croûte $\rightarrow$ cœur. Nous avons montré que l'anticorrélation entre la pente de l'énergie de symétrie à la densité de saturation $L_{sym}$ et la densité de transition croûte-cœur, signalée dans de nombreux travaux antérieurs, est retrouvée si l'énergie de surface est seulement optimisée sur un ensemble limité de noyaux magiques et semi-magiques sphériques. Inversement, si la tension de surface est optimisée sur un grand nombre de données et si des termes de courbure sont ajoutés, cette corrélation disparaît et la sensibilité à l'équation d'état est limitée aux paramètres empiriques d'ordres élevés dans le secteur isovecteur ($K_{sym}$, $Q_{sym}$), peu contraints à ce jour.

Nous avons exploité le principal atout de la technique de métamodélisation, à savoir le fait qu'aucune corrélation artificielle n'est introduite *a priori* entre les paramètres empiriques, pour effectuer la détermination bayésienne de ces derniers, conduisant à des prédictions réalistes des observables des étoiles à neutrons. Nous avons considéré *a priori* une distribution uniforme pour les paramètres empiriques dont les limites sont compatibles avec les contraintes expérimentales actuelles. La fonction de vraisemblance que nous avons construite tient compte de récents résultats en théorie des perturbations chirales, pour la matière nucléaire symétrique et la matière pure de neutrons jusqu'à 0.20 $\text{fm}^{-3}$, ainsi que de la contrainte de masse maximale de l'étoile et des principes physiques de base. Elle comprend également une probabilité dans laquelle est encodée la capacité du modèle de la goutte liquide compressible à reproduire les masses de l'AME2016. Nous avons montré que le fait d'imposer les contraintes associées aux calculs *ab initio* est très efficace pour contraindre les paramètres empiriques dans le secteur isovecteur et que cela donne lieu à des corrélations entre les dérivés de l'énergie de symétrie à la densité de saturation. Nous avons fait des prédictions générales pour les propriétés statiques en utilisant la distribution *posterior* des paramètres empiriques et avons constaté que nos résultats sont compatibles avec les contraintes des collaborations LIGO et Virgo déduites de l'événement GW170817. La seule hypothèse de la technique de métamodélisation étant la possibilité d'étendre l'équation d'état en une série de Taylor, ce résultat implique que nous n'avons pas de preuve irréfutable qu'une transition de phase de premier ordre ait lieu dans le cœur des étoiles à neutrons, bien que cela ne puisse évidemment pas être exclu. Le moment d'inertie de la croûte, qui est fortement corrélé avec la localisation du point de transition croûte-cœur, a été calculé et les résultats tendent à indiquer que le phénomène de *glitch* ne peut pas uniquement tirer son origine de la physique de la croûte. Cela ouvre des possibilités intéressantes concernant la pertinence des composants superfluides dans le cœur, en particulier dans

le canal ${}^3P_2$ pour les paires $nn$ et $pp$.

Dans la continuité d'un travail récent sur la croûte externe, nous avons envisagé un équilibre statistique complet des ions dans la croûte à température finie permettant la présence d'un gaz de neutrons. Nous avons évalué l'abondance des noyaux de masse impaire et des noyaux de charge impaire présents dans la croûte externe à la température de cristallisation. Leur présence est intéressante car elle pourrait causer des transitions de phase ferromagnétiques. Une dépendance en température des corrections de couches des protons dans le régime de la croûte interne a été implémentée. La température de cristallisation et la composition associée ont été calculées dans l'approximation de plasma à un composant et nos résultats suggèrent que la source la plus importante de dépendance au modèle provient de la partie lisse de la fonctionnelle, l'ingrédient le plus important à fixer pour la prédiction quantitative des propriétés de la croûte interne étant la tension de superface à des ratios d'isospins extrêmes. Des déviations par rapport à la matière froide catalysée ont été observées à faible densité au point de cristallisation. Enfin, nous avons calculé le paramètre d'impureté de manière systématique dans la croûte interne à la température de cristallisation pour quatre fonctionnelles BSk récentes qui tiennent compte des incertitudes actuelles sur l'énergie de symétrie. Il s'agit, à ce jour, du premier calcul du facteur d'impureté dans la croûte interne basé sur des fonctionnelles nucléaires réalistes. Ce dernier a permis de montrer que la contribution des impuretés est non négligeable, ce qui pourrait modifier les propriétés de transport dans la croûte.

Il est clair que la détermination expérimentale des paramètres empiriques d'ordres élevés du secteur isovecteur dans les prévisions théoriques de la théorie des perturbations chirales à basse densité et dans la modélisation microscopique de l'énergie de surface à des ratios d'isospins extrêmes sont nécessaires pour réduire les incertitudes sur les observables de la croûte des étoiles à neutrons. De plus, nous avons montré que les contraintes sur les propriétés de la matière dense peuvent être déduites des observations astrophysiques dans un cadre bayésien. De nombreuses nouvelles mesures sont attendues dans un futur proche de la part de NICER et de LIGO/Virgo. Nous pouvons donc espérer réduire les incertitudes sur les dérivés de l'énergie de symétrie d'ordres élevés et sur les observables de l'étoile en utilisant une méthode bayésienne ou des méthodes d'apprentissage automatique.

Diverses applications du formalisme introduit pour la description d'un plasma à plusieurs composants dans un équilibre statistique complet peuvent être envisagées à l'avenir. Par exemple, il serait intéressant d'étudier la présence des hypérons dans la croûte au point de cristallisation. Les géométries non sphériques pourraient également être prises en compte dans ce traitement, ce qui permettrait l'évaluation du paramètre d'impureté dans les couches profondes de la croûte. Il serait ainsi possible de vérifier l'hypothèse de [PVR13] selon laquelle la présence d'une couche hautement résistive dans la croûte interne pourrait conduire à une limite plus élevée de la période de rotation des pulsars X.

Durant cette thèse, j'ai écrit une bibliothèque *open source* en langage C, NSEoS, dans le but de fournir des outils utiles liés à la physique des étoiles à neutrons [Car17a]. Cette bibliothèque a été utilisée pour produire tous les résultats présentés dans cette

thèse. En outre, elle a été utilisée par différents étudiants pendant leur stage sous la supervision conjointe de ma directrice de thèse et de moi-même et nous pensons qu'elle peut servir de base à de futures études.

# Bibliography


[Abb+17] B. P. Abbott et al. "GW170817: Observation of Gravitational Waves from a Binary Neutron Star Inspiral". In: *Phys. Rev. Lett.* 119 (16 Oct. 2017), p. 161101. DOI: 10.1103/PhysRevLett.119.161101.

[Abb+18] B. P. Abbott et al. "GW170817: Measurements of Neutron Star Radii and Equation of State". In: *Phys. Rev. Lett.* 121 (16 Oct. 2018), p. 161101. DOI: 10.1103/PhysRevLett.121.161101.

[Abb+19] B. P. Abbott et al. "Properties of the Binary Neutron Star Merger GW170817". In: *Phys. Rev. X* 9 (1 Jan. 2019), p. 011001. DOI: 10.1103/PhysRevX.9.011001.

[AI75] P. W. Anderson and N. Itoh. "Pulsar glitches and restlessness as a hard superfluidity phenomenon". In: *Nature* 256 (1975), pp. 25–27. DOI: 10.1038/256025a0.

[Ala+16] N. Alam et al. "Strong correlations of neutron star radii with the slopes of nuclear matter incompressibility and symmetry energy at saturation". In: *Phys. Rev. C* 94 (5 Nov. 2016), p. 052801. DOI: 10.1103/PhysRevC.94.052801.

[And+12] N. Andersson et al. "Pulsar Glitches: The Crust is not Enough". In: *Phys. Rev. Lett.* 109 (24 Dec. 2012), p. 241103. DOI: 10.1103/PhysRevLett.109.241103.

[Ant+13] John Antoniadis et al. "A Massive Pulsar in a Compact Relativistic Binary". In: *Science* 340.6131 (2013). DOI: 10.1126/science.1233232. eprint: https://science.sciencemag.org/content/340/6131/1233232.full.pdf.

[Ant+19] Sofija Antić et al. "Quantifying the uncertainties on spinodal instability for stellar matter through meta-modeling". In: *Journal of Physics G: Nuclear and Particle Physics* 46.6 (May 2019), p. 065109. DOI: 10.1088/1361-6471/ab1a51.

[APR98] A. Akmal, V. R. Pandharipande, and D. G. Ravenhall. "Equation of state of nucleon matter and neutron star structure". In: *Phys. Rev. C* 58 (3 Sept. 1998), pp. 1804–1828. DOI: 10.1103/PhysRevC.58.1804.

[Aud+12] G. Audi et al. "The Ame2012 atomic mass evaluation". In: *Chinese Physics C* 36.12 (Dec. 2012), pp. 1287–1602. DOI: 10.1088/1674-1137/36/12/002.

[Ava+08] S. S. Avancini et al. “Warm and cold pasta phase in relativistic mean field theory”. In: *Phys. Rev. C* 78 (1 July 2008), p. 015802. DOI: 10.1103/PhysRevC.78.015802.

[Ava+10] Sidney S. Avancini et al. “Warm “pasta” phase in the Thomas-Fermi approximation”. In: *Phys. Rev. C* 82 (5 Nov. 2010), p. 055807. DOI: 10.1103/PhysRevC.82.055807.

[Bay+19] Gordon Baym et al. “New Neutron Star Equation of State with Quark-Hadron Crossover”. In: *Astrophys. J.* 885.1, 42 (Nov. 2019), p. 42. DOI: 10.3847/1538-4357/ab441e. arXiv: 1903.08963 [astro-ph.HE].

[BBP71] Gordon Baym, Hans A. Bethe, and Christopher J Pethick. “Neutron star matter”. In: *Nuclear Physics A* 175.2 (1971), pp. 225–271. DOI: https://doi.org/10.1016/0375-9474(71)90281-8.

[BBR98] Edward F. Brown, Lars Bildsten, and Robert E. Rutledge. “Crustal Heating and Quiescent Emission from Transiently Accreting Neutron Stars”. In: *The Astrophysical Journal* 504.2 (Sept. 1998), pp. L95–L98. DOI: 10.1086/311578.

[BC79] G S Bisnovatyĭ-Kogan and V M Chechetkin. “Nonequilibrium shells of neutron stars and their role in sustaining x-ray emission and nucleosynthesis”. In: *Soviet Physics Uspekhi* 22.2 (Feb. 1979), pp. 89–108. DOI: 10.1070/pu1979v022n02abeh005418.

[Bed+12] Bednarek, I. et al. “Hyperons in neutron-star cores and a $2M_{\odot}$ pulsar”. In: *A&A* 543 (2012), A157. DOI: 10.1051/0004-6361/201118560.

[Bet+79] H.A. Bethe et al. “Equation of state in the gravitational collapse of stars”. In: *Nuclear Physics A* 324.2 (1979), pp. 487–533. DOI: https://doi.org/10.1016/0375-9474(79)90596-7.

[BH80] Marc Baus and Jean-Pierre Hansen. “Statistical mechanics of simple coulomb systems”. In: *Physics Reports* 59.1 (1980), pp. 1–94. DOI: https://doi.org/10.1016/0370-1573(80)90022-8.

[BMG20] Celso C. Barros, Débora P. Menezes, and Francesca Gulminelli. “Fluctuations in the composition of nuclear pasta in symmetric nuclear matter at finite temperature”. In: *Phys. Rev. C* 101 (3 Mar. 2020), p. 035211. DOI: 10.1103/PhysRevC.101.035211.

[Bog+19a] Slavko Bogdanov et al. “Constraining the Neutron Star Mass–Radius Relation and Dense Matter Equation of State with NICER. I. The Millisecond Pulsar X-Ray Data Set”. In: *The Astrophysical Journal* 887.1 (Dec. 2019), p. L25. DOI: 10.3847/2041-8213/ab53eb.

[Bog+19b] Slavko Bogdanov et al. “Constraining the Neutron Star Mass–Radius Relation and Dense Matter Equation of State with NICER. II. Emission from Hot Spots on a Rapidly Rotating Neutron Star”. In: *The Astrophysical Journal* 887.1 (Dec. 2019), p. L26. DOI: 10.3847/2041-8213/ab5968.

[BPS71] Gordon Baym, Christopher Pethick, and Peter Sutherland. "The Ground state of matter at high densities: Equation of state and stellar models". In: *Astrophys. J.* 170 (1971), pp. 299–317. DOI: 10.1086/151216.

[BPY01] D. A. Baiko, A. Y. Potekhin, and D. G. Yakovlev. "Thermodynamic functions of harmonic Coulomb crystals". In: *Phys. Rev. E* 64 (5 Oct. 2001), p. 057402. DOI: 10.1103/PhysRevE.64.057402.

[Bro65] C. G. Broyden. "A Class of Methods for Solving Nonlinear Simultaneous Equations". In: *Mathematics of Computation* 19.92 (1965), pp. 577–593.

[BW39] Niels Bohr and John Archibald Wheeler. "The Mechanism of Nuclear Fission". In: *Phys. Rev.* 56 (5 Sept. 1939), pp. 426–450. DOI: 10.1103/PhysRev.56.426.

[BZ34] W. Baade and F. Zwicky. "Remarks on Super-Novae and Cosmic Rays". In: *Phys. Rev.* 46 (1 July 1934), pp. 76–77. DOI: 10.1103/PhysRev.46.76.2.

[Car+20] Carreau, T. et al. "Crystallization of the inner crust of a neutron star and the influence of shell effects". In: *A&A* 635 (2020), A84. DOI: 10.1051/0004-6361/201937236.

[Car17a] T. Carreau. https://github.com/thomascarreau/NSEoS. 2017.

[Car17b] T. Carreau. "Vers une description unifiée de la croûte et du coeur des étoiles à neutrons". MA thesis. Université de Caen-Normandie, 2017.

[CCH05] Brandon Carter, Nicolas Chamel, and Pawel Haensel. "Entrainment coefficient and effective mass for conduction neutrons in neutron star crust: simple microscopic models". In: *Nuclear Physics A* 748.3 (2005), pp. 675–697. DOI: https://doi.org/10.1016/j.nuclphysa.2004.11.006.

[CF16] N. Chamel and A. F. Fantina. "Binary and ternary ionic compounds in the outer crust of a cold nonaccreting neutron star". In: *Phys. Rev. C* 94 (6 Dec. 2016), p. 065802. DOI: 10.1103/PhysRevC.94.065802.

[CFG20] Carreau, T., Fantina, A. F., and Gulminelli, F. "Inner crust of a neutron star at the point of crystallization in a multicomponent approach". In: *A&A* 640 (2020), A77. DOI: 10.1051/0004-6361/202038347.

[CGM19a] Carreau, Thomas, Gulminelli, Francesca, and Margueron, Jérôme. "Bayesian analysis of the crust-core transition with a compressible liquid-drop model". In: *Eur. Phys. J. A* 55.10 (2019), p. 188. DOI: 10.1140/epja/i2019-12884-1.

[CGM19b] Thomas Carreau, Francesca Gulminelli, and Jérôme Margueron. "General predictions for the neutron star crustal moment of inertia". In: *Phys. Rev. C* 100 (5 Nov. 2019), p. 055803. DOI: 10.1103/PhysRevC.100.055803.

[CGS14] Colò, G., Garg, U., and Sagawa, H. "Symmetry energy from the nuclear collective motion: constraints from dipole, quadrupole, monopole and spin-dipole resonances". In: *Eur. Phys. J. A* 50.2 (2014), p. 26. DOI: 10.1140/epja/i2014-14026-9.

[Cha+07] N. Chamel et al. “Validity of the Wigner-Seitz approximation in neutron star crust”. In: *Phys. Rev. C* 75 (5 May 2007), p. 055806. DOI: 10.1103/PhysRevC.75.055806.

[Cha+17] D. Chatterjee et al. “Constraints on the nuclear equation of state from nuclear masses and radii in a Thomas-Fermi meta-modeling approach”. In: *Phys. Rev. C* 96 (6 Dec. 2017), p. 065805. DOI: 10.1103/PhysRevC.96.065805.

[Cha+97] E Chabanat et al. “A Skyrme parametrization from subnuclear to neutron star densities”. In: *Nuclear Physics A* 627.4 (1997), pp. 710–746.

[Cha+98] E. Chabanat et al. “A Skyrme parametrization from subnuclear to neutron star densities Part II. Nuclei far from stabilities”. In: *Nuclear Physics A* 635.1 (1998), pp. 231–256. DOI: https://doi.org/10.1016/S0375-9474(98)00180-8.

[Cha06] Nicolas Chamel. “Effective mass of free neutrons in neutron star crust”. In: *Nuclear Physics A* 773.3 (2006), pp. 263–278. DOI: https://doi.org/10.1016/j.nuclphysa.2006.04.010.

[Cha12] N. Chamel. “Neutron conduction in the inner crust of a neutron star in the framework of the band theory of solids”. In: *Phys. Rev. C* 85 (3 Mar. 2012), p. 035801. DOI: 10.1103/PhysRevC.85.035801.

[Cha13] N. Chamel. “Crustal Entrainment and Pulsar Glitches”. In: *Phys. Rev. Lett.* 110 (1 Jan. 2013), p. 011101. DOI: 10.1103/PhysRevLett.110.011101.

[Cha31] Subrahmanyan Chandrasekhar. “The maximum mass of ideal white dwarfs”. In: *The Astrophysical Journal* 74 (1931), p. 81.

[Cha32] James Chadwick. “Possible existence of a neutron”. In: *Nature* 129.3252 (1932), pp. 312–312.

[CLS06] L. G. Cao, U. Lombardo, and P. Schuck. “Screening effects in superfluid nuclear and neutron matter within Brueckner theory”. In: *Phys. Rev. C* 74 (6 Dec. 2006), p. 064301. DOI: 10.1103/PhysRevC.74.064301.

[Com+69] JM Comella et al. “Crab nebula pulsar NP 0532”. In: *Nature* 221.5179 (1969), pp. 453–454.

[Cro+20] H. T. Cromartie et al. “Relativistic Shapiro delay measurements of an extremely massive millisecond pulsar”. In: *Nature Astronomy* 4 (Jan. 2020), pp. 72–76. DOI: 10.1038/s41550-019-0880-2. arXiv: 1904.06759 [astro-ph.HE].

[CV16] Debarati Chatterjee and Isaac Vidana. “Do hyperons exist in the interior of neutron stars?” In: *The European Physical Journal A* 52.2 (2016), p. 29.

[DCG07] C. Ducoin, Ph. Chomaz, and F. Gulminelli. “Isospin-dependent clusterization of neutron-star matter”. In: *Nuclear Physics A* 789.1 (2007), pp. 403–425. DOI: https://doi.org/10.1016/j.nuclphysa.2007.03.006.

[De+18] Soumi De et al. “Tidal Deformabilities and Radii of Neutron Stars from the Observation of GW170817”. In: *Phys. Rev. Lett.* 121 (9 Aug. 2018), p. 091102. DOI: 10.1103/PhysRevLett.121.091102.

[Del+16] T. Delsate et al. “Giant pulsar glitches and the inertia of neutron star crusts”. In: *Phys. Rev. D* 94 (2 July 2016), p. 023008. DOI: 10.1103/PhysRevD.94.023008.

[Dem+10] P. B. Demorest et al. “A two-solar-mass neutron star measured using Shapiro delay”. In: *Nature Astronomy* 467.7319 (Oct. 2010), pp. 1081–1083. DOI: 10.1038/nature09466. arXiv: 1010.5788 [astro-ph.HE].

[DH00] F Douchin and P Haensel. “Inner edge of neutron-star crust with SLy effective nucleon-nucleon interactions”. In: *Physics Letters B* 485.1 (2000), pp. 107–114. DOI: https://doi.org/10.1016/S0370-2693(00)00672-9.

[DH01] Douchin, F. and Haensel, P. “A unified equation of state of dense matter and neutron star structure”. In: *A&A* 380.1 (2001), pp. 151–167. DOI: 10.1051/0004-6361:20011402.

[DHM00] F Douchin, P Haensel, and J Meyer. “Nuclear surface and curvature properties for SLy Skyrme forces and nuclei in the inner neutron-star crust”. In: *Nuclear Physics A* 665.3 (2000), pp. 419–446. DOI: https://doi.org/10.1016/S0375-9474(99)00397-8.

[DHS16] C. Drischler, K. Hebeler, and A. Schwenk. “Asymmetric nuclear matter based on chiral two- and three-nucleon interactions”. In: *Phys. Rev. C* 93 (5 May 2016), p. 054314. DOI: 10.1103/PhysRevC.93.054314.

[DL14] Pawel Danielewicz and Jenny Lee. “Symmetry energy II: Isobaric analog states”. In: *Nuclear Physics A* 922 (2014), pp. 1–70. DOI: https://doi.org/10.1016/j.nuclphysa.2013.11.005.

[DMC08] C. Ducoin, J. Margueron, and Ph. Chomaz. “Cluster formation in asymmetric nuclear matter: Semi-classical and quantal approaches”. In: *Nuclear Physics A* 809.1 (2008), pp. 30–64. DOI: https://doi.org/10.1016/j.nuclphysa.2008.05.015.

[DNR14] J Dobaczewski, W Nazarewicz, and P-G Reinhard. “Error estimates of theoretical models: a guide”. In: *Journal of Physics G: Nuclear and Particle Physics* 41.7 (May 2014), p. 074001. DOI: 10.1088/0954-3899/41/7/074001.

[Duc+07] C. Ducoin et al. “Anomalous thermodynamics and phase transitions in neutron star matter”. In: *Phys. Rev. C* 75 (6 June 2007), p. 065805. DOI: 10.1103/PhysRevC.75.065805.

[Duc+11] Camille Ducoin et al. “Core-crust transition in neutron stars: Predictivity of density developments”. In: *Phys. Rev. C* 83 (4 Apr. 2011), p. 045810. DOI: 10.1103/PhysRevC.83.045810.

[EH80] Mounib F El Eid and Wolfgang Hillebrandt. “A new equation of state of supernova matter”. In: *Astronomy and Astrophysics Supplement Series* 42 (1980), pp. 215–226.

[Esp+11] C. M. Espinoza et al. “A study of 315 glitches in the rotation of 102 pulsars”. In: *Monthly Notices of the Royal Astronomical Society* 414.2 (June 2011), pp. 1679–1704. DOI: 10.1111/j.1365-2966.2011.18503.x. eprint: https://academic.oup.com/mnras/article-pdf/414/2/1679/3015039/mnras0414-1679.pdf.

[Fan+20] Fantina, A. F. et al. “Crystallization of the outer crust of a non-accreting neutron star”. In: *A&A* 633 (2020), A149. DOI: 10.1051/0004-6361/201936359.

[FF18] G. Fiorella Burgio and Anthea F. Fantina. “Nuclear Equation of State for Compact Stars and Supernovae”. In: *The Physics and Astrophysics of Neutron Stars*. Ed. by Luciano Rezzolla et al. Cham: Springer International Publishing, 2018, pp. 255–335. DOI: 10.1007/978-3-319-97616-7_6.

[FH93] R. T. Farouki and S. Hamaguchi. “Thermal energy of the crystalline one-component plasma from dynamical simulations”. In: *Phys. Rev. E* 47 (6 June 1993), pp. 4330–4336. DOI: 10.1103/PhysRevE.47.4330.

[FI76] Elliott Flowers and Naoki Itoh. “Transport properties of dense matter”. In: *The Astrophysical Journal* 206 (1976), pp. 218–242.

[FMT49] R. P. Feynman, N. Metropolis, and E. Teller. “Equations of State of Elements Based on the Generalized Fermi-Thomas Theory”. In: *Phys. Rev.* 75 (10 May 1949), pp. 1561–1573. DOI: 10.1103/PhysRev.75.1561.

[FOP18] M Fortin, M Oertel, and C Providência. “Hyperons in hot dense matter: what do the constraints tell us for equation of state?” In: *Publications of the Astronomical Society of Australia* 35 (2018).

[For+10] M. Fortin et al. “Thermalization time and specific heat of the neutron stars crust”. In: *Phys. Rev. C* 82 (6 Dec. 2010), p. 065804. DOI: 10.1103/PhysRevC.82.065804.

[For+15] M. Fortin et al. “Neutron stars with hyperon cores: stellar radii and equation of state near nuclear density”. In: *Astron. Astrophys.* 576 (2015), A68. DOI: 10.1051/0004-6361/201424800. arXiv: 1408.3052 [astro-ph.SR].

[For+16] M. Fortin et al. “Neutron star radii and crusts: Uncertainties and unified equations of state”. In: *Phys. Rev. C* 94 (3 Sept. 2016), p. 035804. DOI: 10.1103/PhysRevC.94.035804.

[Gan+14] Gandolfi, S. et al. “The equation of state of neutron matter, symmetry energy and neutron star structure”. In: *Eur. Phys. J. A* 50.2 (2014), p. 10. DOI: 10.1140/epja/i2014-14010-5.

[GCP13] S. Goriely, N. Chamel, and J. M. Pearson. "Further explorations of Skyrme-Hartree-Fock-Bogoliubov mass formulas. XIII. The 2012 atomic mass evaluation and the symmetry coefficient". In: *Phys. Rev. C* 88 (2 Aug. 2013), p. 024308. DOI: 10.1103/PhysRevC.88.024308.

[GLY17] M. Grasso, D. Lacroix, and C. J. Yang. "Lee-Yang–inspired functional with a density-dependent neutron-neutron scattering length". In: *Phys. Rev. C* 95 (5 May 2017), p. 054327. DOI: 10.1103/PhysRevC.95.054327.

[Gol68] T. Gold. "Rotating Neutron Stars as the Origin of the Pulsating Radio Sources". In: *Pulsating Stars: A NATURE Reprint*. Boston, MA: Springer US, 1968, pp. 74–75. DOI: 10.1007/978-1-4899-6387-1_40.

[Gon+17] C. Gonzalez-Boquera et al. "Higher-order symmetry energy and neutron star core-crust transition with Gogny forces". In: *Phys. Rev. C* 96 (6 Dec. 2017), p. 065806. DOI: 10.1103/PhysRevC.96.065806.

[Gor+05] S. Goriely et al. "Further explorations of Skyrme–Hartree–Fock–Bogoliubov mass formulas. IV: Neutron-matter constraint". In: *Nuclear Physics A* 750.2 (2005), pp. 425–443. DOI: https://doi.org/10.1016/j.nuclphysa.2005.01.009.

[Gor+11] Goriely, S. et al. "The decompression of the outer neutron star crust and r-process nucleosynthesis". In: *A&A* 531 (2011), A78. DOI: 10.1051/0004-6361/201116897.

[GPA12] Fabrizio Grill, Constan ça Providência, and Sidney S. Avancini. "Neutron star inner crust and symmetry energy". In: *Phys. Rev. C* 85 (5 May 2012), p. 055808. DOI: 10.1103/PhysRevC.85.055808.

[GR14] Sebastien Guillot and Robert E Rutledge. "Rejecting proposed dense matter equations of state with quiescent low-mass x-ray binaries". In: *The Astrophysical Journal Letters* 796.1 (2014), p. L3.

[GR15] F. Gulminelli and Ad. R. Raduta. "Unified treatment of subsaturation stellar matter at zero and finite temperature". In: *Phys. Rev. C* 92 (5 Nov. 2015), p. 055803. DOI: 10.1103/PhysRevC.92.055803.

[Gra+17] Guilherme Grams et al. "Nuclear pasta phases within the quark-meson coupling model". In: *Phys. Rev. C* 95 (5 May 2017), p. 055807. DOI: 10.1103/PhysRevC.95.055807.

[Gra+18] G. Grams et al. "Distribution of nuclei in equilibrium stellar matter from the free-energy density in a Wigner-Seitz cell". In: *Phys. Rev. C* 97 (3 Mar. 2018), p. 035807. DOI: 10.1103/PhysRevC.97.035807.

[GSP07] S. Goriely, M. Samyn, and J. M. Pearson. "Further explorations of Skyrme-Hartree-Fock-Bogoliubov mass formulas. VII. Simultaneous fits to masses and fission barriers". In: *Phys. Rev. C* 75 (6 June 2007), p. 064312. DOI: 10.1103/PhysRevC.75.064312.

[Gui+13] Sebastien Guillot et al. "Measurement of the radius of neutron stars with high signal-to-noise quiescent low-mass X-ray binaries in globular clusters". In: *The Astrophysical Journal* 772.1 (2013), p. 7.

[Hae+16] P Haensel et al. “Rotating neutron stars with exotic cores: masses, radii, stability”. In: *The European Physical Journal A* 52.3 (2016), p. 59.

[Har+65] B Kent Harrison et al. “Gravitation theory and gravitational collapse”. In: *gtgc* (1965).

[Har67] James B. Hartle. “Slowly Rotating Relativistic Stars. I. Equations of Structure”. In: *Astrophys. J.* 150 (Dec. 1967), p. 1005. DOI: 10.1086/149400.

[Hei+14] Craig O Heinke et al. “Improved mass and radius constraints for quiescent neutron stars in $\omega$ Cen and NGC 6397”. In: *Monthly Notices of the Royal Astronomical Society* 444.1 (2014), pp. 443–456.

[Hes+06] Jason W. T. Hessels et al. “A Radio Pulsar Spinning at 716 Hz”. In: *Science* 311.5769 (2006), pp. 1901–1904. DOI: 10.1126/science.1123430. eprint: https://science.sciencemag.org/content/311/5769/1901.full.pdf.

[Hew+68] A. Hewish et al. “Observation of a rapidly pulsating radio source”. In: *Nature* 217 (1968), pp. 709–713. DOI: 10.1038/217709a0.

[Hin+10] Tanja Hinderer et al. “Tidal deformability of neutron stars with realistic equations of state and their gravitational wave signatures in binary inspiral”. In: *Phys. Rev. D* 81 (12 June 2010), p. 123016. DOI: 10.1103/PhysRevD.81.123016.

[Ho+15] Wynn C. G. Ho et al. “Pinning down the superfluid and measuring masses using pulsar glitches”. In: *Science Advances* 1.9 (2015). DOI: 10.1126/sciadv.1500578. eprint: https://advances.sciencemag.org/content/1/9/e1500578.full.pdf.

[Hor69] H.M. [Van Horn]. “Crystallization of a classical, one-component coulomb plasma”. In: *Physics Letters A* 28.10 (1969), pp. 706–707. DOI: https://doi.org/10.1016/0375-9601(69)90699-9.

[HP94] P. Haensel and B. Pichon. “Experimental nuclear masses and the ground state of cold dense matter”. In: *Astron. Astrophys.* 283 (1994), p. 313. arXiv: nucl-th/9310003 [nucl-th].

[HPY07] P. Haensel, A. Y. Potekhin, and D. G. Yakovlev. *Neutron stars 1: Equation of state and structure*. Vol. 326. 2007, pp.1–619. DOI: 10.1007/978-0-387-47301-7.

[HS10] Matthias Hempel and Jürgen Schaffner-Bielich. “A statistical model for a complete supernova equation of state”. In: *Nuclear Physics A* 837.3-4 (2010), pp. 210–254.

[Hu+20] Jinniu Hu et al. *Effects of symmetry energy on the radius and tidal deformability of neutron stars in relativistic mean-field model*. 2020. arXiv: 2002.00562 [nucl-th].

[Hua+17] W.J. Huang et al. “The AME2016 atomic mass evaluation (I). Evaluation of input data; and adjustment procedures”. In: *Chinese Physics C* 41.3 (Mar. 2017), p. 030002. DOI: 10.1088/1674-1137/41/3/030002.

[Jan+07] H.-Th. Janka et al. “Theory of core-collapse supernovae”. In: *Physics Reports* 442.1 (2007). The Hans Bethe Centennial Volume 1906-2006, pp. 38–74. DOI: https://doi.org/10.1016/j.physrep.2007.02.002.

[Ji+19] Fan Ji et al. “Effects of nuclear symmetry energy and equation of state on neutron star properties”. In: *Phys. Rev. C* 100 (4 Oct. 2019), p. 045801. DOI: 10.1103/PhysRevC.100.045801.

[Jod] Jodrell Bank Centre for Astrophysics. *Glitch Catalogue*. http://www.jb.man.ac.uk/pulsar/glitches.html.

[Koj+15] Toru Kojo et al. “Phenomenological QCD equation of state for massive neutron stars”. In: *Phys. Rev. D* 91 (4 Feb. 2015), p. 045003. DOI: 10.1103/PhysRevD.91.045003.

[Kor+12] M. Kortelainen et al. “Nuclear energy density optimization: Large deformations”. In: *Phys. Rev. C* 85 (2 Feb. 2012), p. 024304. DOI: 10.1103/PhysRevC.85.024304.

[Kub04] Sebastian Kubis. “Diffusive instability of a kaon condensate in neutron star matter”. In: *Phys. Rev. C* 70 (6 Dec. 2004), p. 065804. DOI: 10.1103/PhysRevC.70.065804.

[Kub07] Sebastian Kubis. “Nuclear symmetry energy and stability of matter in neutron stars”. In: *Phys. Rev. C* 76 (2 Aug. 2007), p. 025801. DOI: 10.1103/PhysRevC.76.025801.

[Lan32] Lev Davidovich Landau. “On the theory of stars”. In: *Phys. Z. Sowjetunion* 1.285 (1932), p. 152.

[Lat19] James M. Lattimer. “Neutron Star Mass and Radius Measurements”. In: *Universe* 5.7 (2019). DOI: 10.3390/universe5070159.

[LEL99] Bennett Link, Richard I. Epstein, and James M. Lattimer. “Pulsar Constraints on Neutron Star Structure and Equation of State”. In: *Phys. Rev. Lett.* 83 (17 Oct. 1999), pp. 3362–3365. DOI: 10.1103/PhysRevLett.83.3362.

[LH19] Lim, Y. and Holt, J. W. “Bayesian modeling of the nuclear equation of state for neutron star tidal deformabilities and GW170817”. In: *Eur. Phys. J. A* 55.11 (2019), p. 209. DOI: 10.1140/epja/i2019-12917-9.

[LHS19] Yeunhwan Lim, Jeremy W. Holt, and Robert J. Stahulak. “Predicting the moment of inertia of pulsar J0737-3039A from Bayesian modeling of the nuclear equation of state”. In: *Phys. Rev. C* 100 (3 Sept. 2019), p. 035802. DOI: 10.1103/PhysRevC.100.035802.

[Li+14] Bao-An Li et al. *Topical issue on nuclear symmetry energy*. 2014.

[Li17] Bao-An Li. “Origins and impacts of high-density symmetry energy”. In: *AIP Conference Proceedings* 1852.1 (2017), p. 030005. DOI: 10.1063/1.4984856. eprint: https://aip.scitation.org/doi/pdf/10.1063/1.4984856.

[Lon+04] Wenhui Long et al. "New effective interactions in relativistic mean field theory with nonlinear terms and density-dependent meson-nucleon coupling". In: *Phys. Rev. C* 69 (3 Mar. 2004), p. 034319. DOI: 10.1103/PhysRevC.69.034319.

[LPT03] D. Lunney, J. M. Pearson, and C. Thibault. "Recent trends in the determination of nuclear masses". In: *Rev. Mod. Phys.* 75 (3 Aug. 2003), pp. 1021–1082. DOI: 10.1103/RevModPhys.75.1021.

[LRP93] C. P. Lorenz, D. G. Ravenhall, and C. J. Pethick. "Neutron star crusts". In: *Phys. Rev. Lett.* 70 (4 Jan. 1993), pp. 379–382. DOI: 10.1103/PhysRevLett.70.379.

[LS08] Z. H. Li and H.-J. Schulze. "Neutron star structure with modern nucleonic three-body forces". In: *Phys. Rev. C* 78 (2 Aug. 2008), p. 028801. DOI: 10.1103/PhysRevC.78.028801.

[LS91] James M. Lattimer and Douglas F. Swesty. "A generalized equation of state for hot, dense matter". In: *Nuclear Physics A* 535.2 (Dec. 1991), pp. 331–376. DOI: 10.1016/0375-9474(91)90452-C.

[ME11] R. Machleidt and D.R. Entem. "Chiral effective field theory and nuclear forces". In: *Physics Reports* 503.1 (2011), pp. 1–75. DOI: https://doi.org/10.1016/j.physrep.2011.02.001.

[Mei+18] Zach Meisel et al. "Nuclear physics of the outer layers of accreting neutron stars". In: *Journal of Physics G: Nuclear and Particle Physics* 45.9 (July 2018), p. 093001. DOI: 10.1088/1361-6471/aad171.

[MG19] Jérôme Margueron and Francesca Gulminelli. "Effect of high-order empirical parameters on the nuclear equation of state". In: *Phys. Rev. C* 99 (2 Feb. 2019), p. 025806. DOI: 10.1103/PhysRevC.99.025806.

[MHG18a] Jérôme Margueron, Rudiney Hoffmann Casali, and Francesca Gulminelli. "Equation of state for dense nucleonic matter from metamodeling. I. Foundational aspects". In: *Phys. Rev. C* 97 (2 Feb. 2018), p. 025805. DOI: 10.1103/PhysRevC.97.025805.

[MHG18b] Jérôme Margueron, Rudiney Hoffmann Casali, and Francesca Gulminelli. "Equation of state for dense nucleonic matter from metamodeling. II. Predictions for neutron star properties". In: *Phys. Rev. C* 97 (2 Feb. 2018), p. 025806. DOI: 10.1103/PhysRevC.97.025806.

[MHT13] Kota Masuda, Tetsuo Hatsuda, and Tatsuyuki Takatsuka. "Hadron-quark crossover and massive hybrid stars with strangeness". In: *The Astrophysical Journal* 764.1 (2013), p. 12.

[Mil+19] M. C. Miller et al. "PSR J0030+0451 Mass and Radius from NICER Data and Implications for the Properties of Neutron Star Matter". In: *The Astrophysical Journal* 887.1 (Dec. 2019), p. L24. DOI: 10.3847/2041-8213/ab50c5.

[MN88] P. Möller and J.R. Nix. "Nuclear masses from a unified macroscopic-microscopic model". In: *Atomic Data and Nuclear Data Tables* 39.2 (1988), pp. 213–223. DOI: https://doi.org/10.1016/0092-640X(88)90022-8.

[Mol+95] P. Moller et al. "Nuclear Ground-State Masses and Deformations". In: *Atomic Data and Nuclear Data Tables* 59.2 (1995), pp. 185–381. DOI: https://doi.org/10.1006/adnd.1995.1002.

[Mon+17] C. Mondal et al. "Interdependence of different symmetry energy elements". In: *Phys. Rev. C* 96 (2 Aug. 2017), p. 021302. DOI: 10.1103/PhysRevC.96.021302.

[Mon+20] C. Mondal et al. "Structure and composition of the inner crust of neutron stars from Gogny interactions". In: *Phys. Rev. C* 102 (1 July 2020), p. 015802. DOI: 10.1103/PhysRevC.102.015802.

[MS65] W. D. Myers and W. J. Swiatecki. "unpublished". In: *UCRL Report* 11980 (May 1965).

[MS66] William D. Myers and Wladyslaw J. Swiatecki. "Nuclear masses and deformations". In: *Nuclear Physics* 81.1 (1966), pp. 1–60. DOI: https://doi.org/10.1016/0029-5582(66)90639-0.

[MTC09] Toshiki Maruyama, Toshitaka Tatsumi, and Satoshi Chiba. "Equation of state of nuclear matter in the first order phase transition". In: *AIP Conference Proceedings* 1120.1 (2009), pp. 129–134. DOI: 10.1063/1.3141634. eprint: https://aip.scitation.org/doi/pdf/10.1063/1.3141634.

[MU15] Noël Martin and Michael Urban. "Liquid-gas coexistence versus energy minimization with respect to the density profile in the inhomogeneous inner crust of neutron stars". In: *Phys. Rev. C* 92 (1 July 2015), p. 015803. DOI: 10.1103/PhysRevC.92.015803.

[MU16] Noël Martin and Michael Urban. "Superfluid hydrodynamics in the inner crust of neutron stars". In: *Phys. Rev. C* 94 (6 Dec. 2016), p. 065801. DOI: 10.1103/PhysRevC.94.065801.

[NGL12] W. G. Newton, M. Gearheart, and Bao-An Li. "A SURVEY OF THE PARAMETER SPACE OF THE COMPRESSIBLE LIQUID DROP MODEL AS APPLIED TO THE NEUTRON STAR INNER CRUST". In: *The Astrophysical Journal Supplement Series* 204.1 (Dec. 2012), p. 9. DOI: 10.1088/0067-0049/204/1/9.

[NS09] W. G. Newton and J. R. Stone. "Modeling nuclear "pasta" and the transition to uniform nuclear matter with the 3D Skyrme-Hartree-Fock method at finite temperature: Core-collapse supernovae". In: *Phys. Rev. C* 79 (5 May 2009), p. 055801. DOI: 10.1103/PhysRevC.79.055801.

[NV73] J.W. Negele and D. Vautherin. "Neutron star matter at sub-nuclear densities". In: *Nuclear Physics A* 207.2 (1973), pp. 298–320. DOI: https://doi.org/10.1016/0375-9474(73)90349-7.

[Oer+15] M Oertel et al. “Hyperons in neutron star matter within relativistic mean-field models”. In: *Journal of Physics G: Nuclear and Particle Physics* 42.7 (June 2015), p. 075202. DOI: 10.1088/0954-3899/42/7/075202.

[Oer+17] M. Oertel et al. “Equations of state for supernovae and compact stars”. In: *Rev. Mod. Phys.* 89 (1 Mar. 2017), p. 015007. DOI: 10.1103/RevModPhys.89.015007.

[OI07] Kazuhiro Oyamatsu and Kei Iida. “The Symmetry energy at subnuclear densities and nuclei in neutron star crusts”. In: *Phys. Rev. C* 75 (2007), p. 015801. DOI: 10.1103/PhysRevC.75.015801. arXiv: nucl-th/0609040.

[Ons+08] M. Onsi et al. “Semi-classical equation of state and specific-heat expressions with proton shell corrections for the inner crust of a neutron star”. In: *Phys. Rev. C* 77 (6 June 2008), p. 065805. DOI: 10.1103/PhysRevC.77.065805.

[OV39] J. R. Oppenheimer and G. M. Volkoff. “On Massive Neutron Cores”. In: *Phys. Rev.* 55 (4 Feb. 1939), pp. 374–381. DOI: 10.1103/PhysRev.55.374.

[Pap+13] P. Papakonstantinou et al. “Densities and energies of nuclei in dilute matter at zero temperature”. In: *Phys. Rev. C* 88 (4 Oct. 2013), p. 045805. DOI: 10.1103/PhysRevC.88.045805.

[PC00] Alexander Y. Potekhin and Gilles Chabrier. “Equation of state of fully ionized electron-ion plasmas. II. Extension to relativistic densities and to the solid phase”. In: *Phys. Rev. E* 62 (6 Dec. 2000), pp. 8554–8563. DOI: 10.1103/PhysRevE.62.8554.

[PC10] A. Y. Potekhin and G. Chabrier. “Thermodynamic Functions of Dense Plasmas: Analytic Approximations for Astrophysical Applications”. In: *Contributions to Plasma Physics* 50.1 (2010), pp. 82–87. DOI: 10.1002/ctpp.201010017. eprint: https://onlinelibrary.wiley.com/doi/pdf/10.1002/ctpp.201010017.

[PCP20] J. M. Pearson, N. Chamel, and A. Y. Potekhin. “Unified equations of state for cold nonaccreting neutron stars with Brussels-Montreal functionals. II. Pasta phases in semiclassical approximation”. In: *Phys. Rev. C* 101 (1 Jan. 2020), p. 015802. DOI: 10.1103/PhysRevC.101.015802.

[PCS19] L. Perot, N. Chamel, and A. Sourie. “Role of the symmetry energy and the neutron-matter stiffness on the tidal deformability of a neutron star with unified equations of state”. In: *Phys. Rev. C* 100 (3 Sept. 2019), p. 035801. DOI: 10.1103/PhysRevC.100.035801.

[PCS20] L. Perot, N. Chamel, and A. Sourie. “Role of the crust in the tidal deformability of a neutron star within a unified treatment of dense matter”. In: *Phys. Rev. C* 101 (1 Jan. 2020), p. 015806. DOI: 10.1103/PhysRevC.101.015806.

[Pea+12] J. M. Pearson et al. “Inner crust of neutron stars with mass-fitted Skyrme functionals”. In: *Phys. Rev. C* 85 (6 June 2012), p. 065803. DOI: 10.1103/PhysRevC.85.065803.

[Pea+14] Pearson, J. M. et al. “Symmetry energy: nuclear masses and neutron stars”. In: *Eur. Phys. J. A* 50.2 (2014), p. 43. DOI: 10.1140/epja/i2014-14043-8.

[Pea+18] J M Pearson et al. “Unified equations of state for cold non-accreting neutron stars with Brussels–Montreal functionals – I. Role of symmetry energy”. In: *Monthly Notices of the Royal Astronomical Society* 481.3 (Sept. 2018), pp. 2994–3026. DOI: 10.1093/mnras/sty2413. eprint: https://academic.oup.com/mnras/article-pdf/481/3/2994/25817956/sty2413.pdf.

[Pea+19] J M Pearson et al. “Erratum: Unified equations of state for cold non-accreting neutron stars with Brussels-Montreal functionals. I. Role of symmetry energy”. In: *Monthly Notices of the Royal Astronomical Society* 486.1 (Mar. 2019), pp. 768–768. DOI: 10.1093/mnras/stz800. eprint: https://academic.oup.com/mnras/article-pdf/486/1/768/28345283/stz800.pdf.

[Pea19] J. M. Pearson. Private communication. 2019.

[PF19] J. Piekarewicz and F. J. Fattoyev. “Impact of the neutron star crust on the tidal polarizability”. In: *Phys. Rev. C* 99 (4 Apr. 2019), p. 045802. DOI: 10.1103/PhysRevC.99.045802.

[PFH14] J. Piekarewicz, F. J. Fattoyev, and C. J. Horowitz. “Pulsar glitches: The crust may be enough”. In: *Phys. Rev. C* 90 (1 July 2014), p. 015803. DOI: 10.1103/PhysRevC.90.015803.

[Piz+17] P. M. Pizzochero et al. “Constraints on pulsar masses from the maximum observed glitch”. In: *Nature Astronomy* 1, 0134 (July 2017), p. 0134. DOI: 10.1038/s41550-017-0134. arXiv: 1611.10223 [astro-ph.HE].

[PR06] Dany Page and Sanjay Reddy. “Dense matter in compact stars: theoretical developments and observational constraints”. In: *Annu. Rev. Nucl. Part. Sci.* 56 (2006), pp. 327–374.

[PR95] C. J. Pethick and D. G. Ravenhall. “Matter at large neutron excess and the physics of neutron-star crusts”. In: *Ann. Rev. Nucl. Part. Sci.* 45 (1995), pp. 429–484. DOI: 10.1146/annurev.ns.45.120195.002241.

[PRL95] C.J. Pethick, D.G. Ravenhall, and C.P. Lorenz. “The inner boundary of a neutron-star crust”. In: *Nuclear Physics A* 584.4 (1995), pp. 675–703. DOI: https://doi.org/10.1016/0375-9474(94)00506-I.

[PVR13] José A. Pons, Daniele Viganò, and Nanda Rea. “A highly resistive layer within the crust of X-ray pulsars limits their spin periods”. In: *Nature Physics* 9.7 (July 2013), pp. 431–434. DOI: 10.1038/nphys2640. arXiv: 1304.6546 [astro-ph.SR].

[Raa+19] G. Raaijmakers et al. “A NICER View of PSR J0030+0451: Implications for the Dense Matter Equation of State”. In: *The Astrophysical Journal* 887.1 (Dec. 2019), p. L22. DOI: 10.3847/2041-8213/ab451a.

[RAG14] Ad R Raduta, F Aymard, and F Gulminelli. “Clusterized nuclear matter in the (proto-) neutron star crust and the symmetry energy”. In: *The European Physical Journal A* 50.2 (2014), p. 24.

[Ril+19] T. E. Riley et al. “A NICER View of PSR J0030+0451: Millisecond Pulsar Parameter Estimation”. In: *The Astrophysical Journal* 887.1 (Dec. 2019), p. L21. DOI: 10.3847/2041-8213/ab481c.

[Roc+11] X. Roca-Maza et al. “Relativistic mean-field interaction with density-dependent meson-nucleon vertices based on microscopical calculations”. In: *Phys. Rev. C* 84 (5 Nov. 2011), p. 054309. DOI: 10.1103/PhysRevC.84.054309.

[RPL83] D.G. Ravenhall, C.J. Pethick, and J.M. Lattimer. “Nuclear interface energy at finite temperatures”. In: *Nuclear Physics A* 407.3 (1983), pp. 571–591. DOI: https://doi.org/10.1016/0375-9474(83)90667-X.

[Sam+02] M. Samyn et al. “A Hartree–Fock–Bogoliubov mass formula”. In: *Nuclear Physics A* 700.1 (2002), pp. 142–156. DOI: https://doi.org/10.1016/S0375-9474(01)01316-1.

[Ser+12] Mathieu Servillat et al. “Neutron star atmosphere composition: the quiescent, low-mass X-ray binary in the globular cluster M28”. In: *Monthly Notices of the Royal Astronomical Society* 423.2 (2012), pp. 1556–1561.

[Sha64] Irwin I. Shapiro. “Fourth Test of General Relativity”. In: *Phys. Rev. Lett.* 13 (26 Dec. 1964), pp. 789–791. DOI: 10.1103/PhysRevLett.13.789.

[SKT95] K. Sumiyoshi, H. Kuwabara, and H. Toki. “Relativistic mean-field theory with non-linear $\sigma$ and $\omega$ terms for neutron stars and supernovae”. In: *Nuclear Physics A* 581.3 (1995), pp. 725–746. DOI: https://doi.org/10.1016/0375-9474(94)00335-K.

[SLL13] K Stovall, D R Lorimer, and R S Lynch. “Searching for millisecond pulsars: surveys, techniques and prospects”. In: *Classical and Quantum Gravity* 30.22 (Nov. 2013), p. 224003. DOI: 10.1088/0264-9381/30/22/224003.

[SS06] Devinderjit Sivia and John Skilling. *Data analysis: a Bayesian tutorial*. OUP Oxford, 2006.

[Ste+18] A W Steiner et al. “Constraining the mass and radius of neutron stars in globular clusters”. In: *Monthly Notices of the Royal Astronomical Society* 476.1 (Jan. 2018), pp. 421–435. DOI: 10.1093/mnras/sty215. eprint: https://academic.oup.com/mnras/article-pdf/476/1/421/24243755/sty215.pdf.

[TCV08] Luca Trippa, Gianluca Colò, and Enrico Vigezzi. “Giant dipole resonance as a quantitative constraint on the symmetry energy”. In: *Phys. Rev. C* 77 (6 June 2008), p. 061304. DOI: 10.1103/PhysRevC.77.061304.

[TMR19] Tews, I., Margueron, J., and Reddy, S. "Confronting gravitational-wave observations with modern nuclear physics constraints". In: *Eur. Phys. J. A* 55.6 (2019), p. 97. DOI: 10.1140/epja/i2019-12774-6.

[Tol39] Richard C. Tolman. "Static Solutions of Einstein's Field Equations for Spheres of Fluid". In: *Phys. Rev.* 55 (4 Feb. 1939), pp. 364–373. DOI: 10.1103/PhysRev.55.364.

[Vau96] D. Vautherin. "Many-Body Methods at Finite Temperature". In: *Advances in Nuclear Physics*. Ed. by J. W. Negele and Erich Vogt. Boston, MA: Springer US, 1996, pp. 123–172. DOI: 10.1007/0-306-47065-9_4.

[VB72] D Vautherin and DM t Brink. "Hartree-Fock calculations with Skyrme's interaction. I. Spherical nuclei". In: *Physical Review C* 5.3 (1972), p. 626.

[Vid+09] Isaac Vidaña et al. "Density dependence of the nuclear symmetry energy: A microscopic perspective". In: *Phys. Rev. C* 80 (4 Oct. 2009), p. 045806. DOI: 10.1103/PhysRevC.80.045806.

[Viñ+17] X. Viñas et al. "Crust-Core Transitions in Neutron Stars Revisited". In: *Bulg. J. Phys.* 44.S1 (2017), pp. 081–092.

[Wat+03] Gentaro Watanabe et al. "Structure of cold nuclear matter at subnuclear densities by quantum molecular dynamics". In: *Phys. Rev. C* 68 (3 Sept. 2003), p. 035806. DOI: 10.1103/PhysRevC.68.035806.

[Wel+17] A. Welker et al. "Binding Energy of $^{79}$Cu: Probing the Structure of the Doubly Magic $^{78}$Ni from Only One Proton Away". In: *Phys. Rev. Lett.* 119 (19 Nov. 2017), p. 192502. DOI: 10.1103/PhysRevLett.119.192502.

[WFF88] R. B. Wiringa, V. Fiks, and A. Fabrocini. "Equation of state for dense nucleon matter". In: *Phys. Rev. C* 38 (2 Aug. 1988), pp. 1010–1037. DOI: 10.1103/PhysRevC.38.1010.

[WHW02] S. E. Woosley, A. Heger, and T. A. Weaver. "The evolution and explosion of massive stars". In: *Rev. Mod. Phys.* 74 (4 Nov. 2002), pp. 1015–1071. DOI: 10.1103/RevModPhys.74.1015.

[WI03] Gentaro Watanabe and Kei Iida. "Electron screening in the liquid-gas mixed phases of nuclear matter". In: *Phys. Rev. C* 68 (4 Oct. 2003), p. 045801. DOI: 10.1103/PhysRevC.68.045801.

[WM11] Gentaro Watanabe and Toshiki Maruyama. *Nuclear pasta in supernovae and neutron stars*. 2011. arXiv: 1109.3511 [nucl-th].

[WP17] Gentaro Watanabe and C. J. Pethick. "Superfluid Density of Neutrons in the Inner Crust of Neutron Stars: New Life for Pulsar Glitch Models". In: *Phys. Rev. Lett.* 119 (6 Aug. 2017), p. 062701. DOI: 10.1103/PhysRevLett.119.062701.

[WS33] E. Wigner and F. Seitz. "On the Constitution of Metallic Sodium". In: *Phys. Rev.* 43 (10 May 1933), pp. 804–810. DOI: 10.1103/PhysRev.43.804.

[Xu +13] Xu, Y. et al. “Databases and tools for nuclear astrophysics applications - BRUSsels Nuclear LIBrary (BRUSLIB), Nuclear Astrophysics Compilation of REactions II (NACRE II) and Nuclear NETwork GENerator (NETGEN)”. In: *A&A* 549 (2013), A106. DOI: 10.1051/0004-6361/201220537.

[Yas+14] Nobutoshi Yasutake et al. “Finite-size effects at the hadron-quark transition and heavy hybrid stars”. In: *Phys. Rev. C* 89 (6 June 2014), p. 065803. DOI: 10.1103/PhysRevC.89.065803.

[YMT09] Nobutoshi Yasutake, Toshiki Maruyama, and Toshitaka Tatsumi. “Hot hadron-quark mixed phase including hyperons”. In: *Phys. Rev. D* 80 (12 Dec. 2009), p. 123009. DOI: 10.1103/PhysRevD.80.123009.

[YMT11] Nobutoshi Yasutake, Toshiki Maruyama, and Toshitaka Tatsumi. “Pasta Structures of Quark-Hadron Phase Transition in Proto-Neutron Stars”. In: *Journal of Physics: Conference Series* 312.4 (Sept. 2011), p. 042027. DOI: 10.1088/1742-6596/312/4/042027.

[ZFH17] Zdunik, J. L., Fortin, M., and Haensel, P. “Neutron star properties and the equation of state for the core”. In: *A&A* 599 (2017), A119. DOI: 10.1051/0004-6361/201629975.

[ZH13] J. L. Zdunik and P. Haensel. “Maximum mass of neutron stars and strange neutron-star cores”. In: *Astron. Astrophys.* 551 (2013), A61. DOI: 10.1051/0004-6361/201220697. arXiv: 1211.1231 [astro-ph.SR].

**Modeling the (proto)neutron star crust: toward a controlled estimation of uncertainties**

The main aim of this thesis is to make realistic predictions and to investigate the sources of uncertainties in the observables of nonaccreting cold neutron stars and warm protoneutron stars, using the present day constraints provided by nuclear experiments, developments in chiral effective field theory, and astrophysical observations. A unified metamodeling approach was introduced to calculate the stellar composition and equation of state of cold nonaccreting neutron stars for any functional of nuclear matter. A Bayesian determination of the equation of state parameters was carried out, leading to realistic predictions for neutron star observables. At finite temperature, a full statistical equilibrium of ions in the crust was considered, allowing in particular for the computation of the impurity parameter. The results are compatible with constraints inferred from GW170817, and suggest that a full crustal origin of pulsar glitches should be excluded. Deviations in the crust composition from cold catalyzed matter are observed at the crystallization temperature. Results show that the contribution of impurities is nonnegligible, thus potentially having an impact on transport properties in the crust. Higher precision in the determination of high-order isovector empirical parameters through nuclear experiments or low-density effective field theory predictions, and in the experimental and/or theoretical knowledge of the surface energy at extreme isospin ratios are needed to reduce the uncertainties of crustal observables. The numerical framework developed during this thesis can be used as a basis for future studies.

**Keywords:** neutron star, crust, nuclear physics, equation of state, Bayesian statistics, pulsar glitch, nuclear statistical equilibrium, crystallization

---

**Modélisation de la croûte des (proto)étoiles à neutrons : vers une estimation contrôlée des incertitudes**

L'objectif principal de cette thèse est de fournir des prédictions réalistes et d'étudier les sources d'incertitudes sur les observables des étoiles à neutrons froides isolées et des protoétoiles à neutrons chaudes. Ces prédictions doivent s'accorder avec les contraintes actuelles fournies par les expériences en physique nucléaire, les développements en théorie des perturbations chirales et les observations astrophysiques. Une approche unifiée de métamodélisation a été introduite pour calculer la composition et l'équation d'état des étoiles à neutrons froides isolées pour toute fonctionnelle de matière nucléaire. Une détermination bayésienne des paramètres de l'équation d'état a été effectuée, conduisant à des prédictions réalistes pour les observables de l'étoile. À température finie, l'équilibre statistique complet des ions dans la croûte a été considéré, permettant entre autres le calcul du paramètre d'impureté. Les résultats sont compatibles avec les contraintes déduites de GW170817 et tendent à indiquer que le phénomène de glitch ne peut pas uniquement tirer son origine de la physique de la croûte. Des déviations dans la composition de la croûte par rapport à la matière catalysée froide sont observées à la température de cristallisation. Les résultats montrent que la contribution des impuretés n'est pas négligeable, ce qui pourrait avoir un impact sur les propriétés de transport dans la croûte. Une plus grande précision dans la détermination des dérivées d'ordre élevé de l'énergie de symétrie dans les expériences et/ou la théorie des perturbations chirales, et dans la connaissance de l'énergie de surface à des isospins extrêmes est nécessaire pour réduire les incertitudes sur les observables de la croûte. Le cadre numérique développé au cours de cette thèse peut servir de base à des recherches futures.

**Mots clés :** étoile à neutrons, croûte, physique nucléaire, équation d'état, statistiques bayésiennes, glitch de pulsar, équilibre statistique nucléaire, cristallisation